Valentin L. Popov · Markus Heß

Method of Dimensionality Reduction in Contact Mechanics and Friction

Springer

Method of Dimensionality Reduction in Contact Mechanics and Friction

Valentin L. Popov · Markus Heß

Method of Dimensionality Reduction in Contact Mechanics and Friction

English translation by Joshua A.T. Gray

Springer

Valentin L. Popov
Institute of Mechanics
Technische Universität Berlin
Berlin
Germany

Markus Heß
Abteilung IC Studienkolleg
Technische Universität Berlin
Berlin
Germany

ISBN 978-3-642-53875-9 ISBN 978-3-642-53876-6 (eBook)
DOI 10.1007/978-3-642-53876-6

Library of Congress Control Number: 2014945961

Springer Heidelberg New York Dordrecht London

© Springer-Verlag Berlin Heidelberg 2015
This work is subject to copyright. All rights are reserved by the Publisher, whether the whole or part of the material is concerned, specifically the rights of translation, reprinting, reuse of illustrations, recitation, broadcasting, reproduction on microfilms or in any other physical way, and transmission or information storage and retrieval, electronic adaptation, computer software, or by similar or dissimilar methodology now known or hereafter developed. Exempted from this legal reservation are brief excerpts in connection with reviews or scholarly analysis or material supplied specifically for the purpose of being entered and executed on a computer system, for exclusive use by the purchaser of the work. Duplication of this publication or parts thereof is permitted only under the provisions of the Copyright Law of the Publisher's location, in its current version, and permission for use must always be obtained from Springer. Permissions for use may be obtained through RightsLink at the Copyright Clearance Center. Violations are liable to prosecution under the respective Copyright Law.
The use of general descriptive names, registered names, trademarks, service marks, etc. in this publication does not imply, even in the absence of a specific statement, that such names are exempt from the relevant protective laws and regulations and therefore free for general use.
While the advice and information in this book are believed to be true and accurate at the date of publication, neither the authors nor the editors nor the publisher can accept any legal responsibility for any errors or omissions that may be made. The publisher makes no warranty, express or implied, with respect to the material contained herein.

Printed on acid-free paper

Springer is part of Springer Science+Business Media (www.springer.com)

… it is more difficult to break a prejudice
than an atom.

A. Einstein

Foreword

Contact and friction are phenomena that are of extreme importance in uncountable technical applications. Simultaneously, they are phenomena which cause difficulties in their theoretical consideration and numerical simulation. This book presents a method that trivializes two classes of contact problems to such a degree that they become accessible even for first semester engineering students who possess an elementary understanding of mathematics and physics. Furthermore, this method presents a very simple way to numerically simulate contact and frictional forces.

The "trivialization" occurs with the help of the method of dimensionality reduction, which is the primary focus of this book. This method is based on the analogy between certain classes of three-dimensional contacts and contacts with one-dimensional elastic or viscoelastic foundations. Within the framework of the method of dimensionality reduction, three-dimensional contacts are replaced by a series of one-dimensional elastic or viscoelastic elements. In doing this, we would like to strongly accentuate the fact that this *is not an approximation*: Certain macroscopic contact properties correspond *exactly* with those of the original three-dimensional contact.

The method of dimensionality reduction offers a *two-fold* reduction: First, a three-dimensional system is replaced by a one-dimensional system, and second, the resulting degrees of freedom for the one-dimensional system are independent of one another. Both of these properties lead to an enormous simplification in the treatment of contact problems and a qualitative acceleration of numerical simulations.

The method of dimensionality reduction distinguishes itself by four essential properties: It is *powerful*, it is *simple*, it is *proven*, and it is *counterintuitive*. It is difficult to be convinced of its validity. Every expert in the field of contact mechanics who has not yet engaged himself in the detailed proofs of the reduction method would immediately form the opinion that it cannot possibly work. It appears to completely contradict a healthy intuition that a system with another spatial dimension, and furthermore, independent degrees of freedom can correctly agree with a three-dimensional system with spatial interactions. And nevertheless, it works! This book is dedicated to the reasons for and under which limitations this is the case.

In writing this book, we have followed two main goals. The first is the simplest possible presentation of the rules of application of the method. The second is to prove the assertions of the reduction method with strict mathematical evidence, so that even the most rigorous practitioner in contact mechanics may be convinced of the correctness of this method. We have attempted to keep these two goals separated. We attempted to keep the mathematical proofs to a minimum in the chapters in which the fundamentals of practical application are explained. This is primarily in Chap. 3, but also in the immediately following Chaps. (4–7) as well as Chap. 10, which is dedicated to the contact mechanics of rough surfaces. It is clear to us that this has not been possible at every point.

Above all, the method of dimensionality reduction offers the engineer a practical tool. In order to stress the practicality of the method even more, we have included many problems at the end of most chapters, which serve for a better understanding of the use of the reduction method and its areas of application. Therefore, this book can also be used as a textbook in a tribologically oriented course of studies.

Acknowledgments

This book would not have been possible were it not for the active support of our colleagues at the Institute of Mechanics at the Berlin University of Technology. Many chapters were written in direct cooperation with these colleagues:

Chapter 6: Rolling Contact—together with R. Wetter
Chapter 7: Contact with Elastomers—together with S. Kürschner
Chapter 10: Normal Contact of Rough Surfaces—together with R. Pohrt
Chapter 11: Frictional Force—together with S. Kürschner
Chapter 12: Frictional Damping—together with E. Teidelt
Chapter 13: The Coupling of Macroscopic Dynamics—together with E. Teidelt
Chapter 14: Acoustic Emission in Rolling Contacts—together with M. Popov und J. Benad
Chapter 15: Coupling on the Microscale—together with R. Pohrt
Chapter 19: Appendix 3: Replacing the Material Properties with Radok's Method of Functional Equations—together with S. Kürschner

We are very thankful for the many valuable discussions with our colleagues and guests at the Institute of Mechanics: A. Dimaki, A.E. Filippov, T. Geike, R. Heise, Q. Li, S.G. Psakhie, J. Starcevic, E. Teidelt, and E. Willert. We would like to convey our heartfelt thanks to Dr. J. Starcevic for her extensive support in the composition of this book. We also thank Ms. Ch. Koll for her patience in the creation of the many figures.

Berlin, May 2014

Valentin L. Popov
Markus Heß

Contents

Author Biographies

Prof. Dr. rer. nat. Valentin L. Popov studied physics (1976–1982) and obtained his doctorate in 1985 from the Moscow State Lomonosov University. He worked at the Institute of Strength Physics of the Russian Academy of Sciences. After a guest-professorship in the field of theoretical physics at the University of Paderborn (Germany) from 1999 to 2002, he has headed since 2002 the Department of System Dynamics and the Physics of Friction in the Institute of Mechanics at the Berlin University of Technology.

Address: Technische Universität Berlin, Institute of Mechanics, Sekr. C8-4, Str. des 17. Juni 135, 10623 Berlin, Germany.
E-mail: v.popov@tu-berlin.de

Dr. Markus Heß studied physical engineering sciences at TU Berlin. He obtained his doctorate in 2011, receiving in the same year the Research Prize from the German Tribological Society for his dissertation. Since 2011, he has worked for the Studienkolleg at TU Berlin, where he teaches engineering mathematics.

Address: Technische Universität Berlin, IC Studienkolleg, Sekr. EB15, Str. des 17. Juni 145, 10623 Berlin, Germany.
E-mail: markus.hess@tu-berlin.de

Chapter 1
Introduction

Valentin L. Popov and Markus Heß

1.1 Goal of This Book

The goal of this book is to describe the *method of dimensionality reduction* in contact mechanics and friction. Contacts between three-dimensional bodies arise in a wide variety of applications. Therefore, their simulation, both analytically and numerically, are of major importance. From a mathematical point of view, contacts are described using integral equations having mixed boundary conditions. Furthermore, the stress distribution, the displacements of the surface, and even the shape of the contact domain are generally not known in such problems [1]. It is, therefore, astounding that a large number of classical contact problems can be mapped to one-dimensional models of contacts with a properly defined linearly elastic foundation (Winkler foundation). This means that the results of the one-dimensional model correspond *exactly* to those of a three-dimensional model. According to this mapping concept, solving contact-mechanical problems is trivialized is such a way as to require no special knowledge other than the fundamentals of algebra and calculus.

The healthy intuition of a specialist in contact mechanics completely discards the possibility of such an *exact* mapping of a three-dimensional problem with extensive interactions to the banal one-dimensional foundation of independent elements (spring or spring–dashpot combinations). Yet even the finest intuition must come to terms with mathematical truths: It has been rigorously proven mathematically for a large variety of contact problems that the one-dimensional mapping of three-dimensional contact problems results in an exact solution [2]. This book offers the required evidence for interested readers.

Just like every model, the method of dimensionality reduction has its domain of application. There are problems which cannot be exactly solved with this method as well as domains for which the method is not exact, but provides a very good approximation. Of course, there are also boundaries beyond which this

V.L. Popov and M. Heß, *Method of Dimensionality Reduction in Contact Mechanics and Friction*, DOI 10.1007/978-3-642-53876-6_1

method is no longer applicable. The method of dimensionality reduction provides exact solutions for normal and tangential contacts with *arbitrary axially-symmetric* bodies. Already here, the following argument may be voiced: “That may well be, but contact problems with axially-symmetric bodies can also be solved in three-dimensions. The method of dimensionality reduction does not present anything new!” This statement is fundamentally correct. However, the abundance of exact solutions for three-dimensional problems is strewn throughout the one-hundred year development of contact mechanics in hundreds of original publications. The authors of this book deal with contact mechanics on a daily basis and still we must admit that it took us months and years to gather and assemble the necessary solutions. The method of dimensionality reduction places this abundance of knowledge at the disposal of every engineer in a simple form, here and now, effectively and without reservation. It is, therefore, correct to say that “the method of dimensionality reduction is *nothing new* for axially-symmetric bodies.” However, it reproduces the results of a three-dimensional contact problem exactly, thereby, lending itself to being a kind of pocket edition of contact mechanics.

We would like to add that many contact problems with axially symmetric bodies are solved “in principle,” however, their application is extremely difficult when, for example, it comes to dynamic contacts. Also here, the method of reduction of dimensionality can be helpful, because due to its trivial formulation, it can be applied very easily either analytically or numerically and provides a convenient “thinking tool.”

A second large field of application for this method is the contact between rough surfaces. Not all problems involving rough surfaces can be solved with the reduction method, but only those that deal with forces and relative displacements, such as problems dealing with contact stiffness, electrical or heat conduction, and frictional force. The area of application is limited but very large and includes many problems which have meaningful implications in engineering. There are no exact solutions when it comes to rough surfaces. Therefore, we are dependent on comparisons with three-dimensional numerical solutions for the purpose of verification. Due to the fact that this method is meant to be an engineering tool, it was very important for us to ensure its applicability for rough surfaces. For this purpose, extensive three-dimensional simulations of rough surfaces with elastic [3] and viscous [4] media were conducted in the Department of System Dynamics and the Physics of Friction at the Technische Universität Berlin. In doing this, we have investigated the entire spectrum of rough surfaces, from “white noise” to smooth single contacts (see Chap. 10). Over this span, the reduction method results in either an (asymptotically) exact solution or a very good approximation. Here as well, the book presents evidence to these findings.

The mapping of real contact area remains *beyond* the realm of application. The method of dimensionality reduction is able to map contact areas for the very short initial stage of indentation, but not in a general case [5].

With this book, we wish to introduce practitioners to methods which are in our opinion extremely simple, elegant, and effective. We are certain that they will find direct application in numerical simulation methods in the future.

The prospective primary application of this method lies not in the field where it yields exact solutions, but rather in the field of the contact mechanics and friction of rough surfaces. The most important advantage is the speed at which the calculations may be carried out, due to the one-dimensionality and the independent degrees of freedom. Therefore, it allows for a direct simulation of multi-scaled systems for which both the macroscopic system dynamics as well as the microscopic contact mechanics can be combined into one model.

1.2 Method of Dimensionality Reduction as the Link Between the Micro- and Macro-Scales

Since the classical works of Bowden and Tabor [6], it is generally known that the surface roughness has a deciding influence on tribological contacts. Without roughness, these contacts would have completely different properties. If this were the case, Coulomb's law would not even be approximately valid. Furthermore, adhesive forces would be orders of magnitude larger than those typically observed in macroscopic tribological systems. The world of atomically smooth surfaces exhibits an entirely different nature than that of the real world with rough surfaces! As early as the 1950s, it was determined that the roughness of real surfaces features a complicated multi-scaled structure, which can be characterized as being "fractal." Many physical surfaces (e.g., fractured or worn surfaces or surfaces produced using current technologies) have fractal characteristics, meaning they exhibit roughnesses on all scales from the atomic to the macroscopic. Above all, it became clear through the works of Archard [7] that this fractality has a significant influence on the properties of real contacts and is the actual cause for the approximate validity of Coulomb's law. Contact mechanics is, therefore, a multi-scaled phenomenon. This multi-scaled nature begs the question: Which methods can be used to take *all* relevant scales of a dynamic system into account? One of the possibilities consists of dividing the considered scales into three domains: Micro, Meso, and Macro. On the macroscopic scales, the system is simulated explicitly with a typical "mono-scale method," for instance, finite element methods. On the smallest microscales, the approach remains the same as in the past and a "microscopic law of friction" is defined. This can either be determined through molecular-dynamic simulations or through empirical observation. The scales between micro and "macro" must somehow be bridged with a method which reproduces these scales with sufficient accuracy but is no more extensive than necessary so that the respective simulations are able to be carried out on realistic time scales. For this, the method of dimensionality reduction described in this book is an excellent candidate.

1.3 Structure of the Book

The method of dimensionality reduction is relatively new. The most important goal of this book is initially to present the method as clear and simply as possible so that a large number of engineers can become familiar with the constructs of the method as well as its application. The book is structured in a way as to accomplish this goal.

In Chap. 2, all general prerequisites for the application of the reduction method are discussed. Those who wish to gain a general idea immediately and what opportunities this method has to offer may begin reading in Chap. 3, where the fundamental concepts and rules of its use are illustrated with many examples. The ideas formulated in Chap. 3 for normal contact problems without adhesion are generalized in Chap. 4 to contacts with adhesion. Chap. 5 follows with the treatment of the tangential contact.

Chapters 3–5 initially handle only axially-symmetric profiles. The advantage is that the functionality of the reduction method can be more simply understood using these profiles. All methods in these chapters are absolutely *exact*. The pure mathematical arguments for the validity of this method are very important to us. However, we do not want to immediately assail the reader, who may be most interested in the practical application of the method, with formal mathematical proofs. Those interested in the strict mathematical proofs may find them in the appendix (Chaps. 17 and 18).

After Chap. 6, which is dedicated to the rolling contact, comes a chapter which describes one of the central aspects of the reduction method: In Chap. 7, the rules of use for the method of dimensionality reduction are described for the application to elastomers, the mathematical derivations of which can be found in Chap. 19 in the appendix. Also in this chapter, we are dealing with an *exact* mapping of three-dimensional bodies onto one dimension.

In addition to purely mechanical properties, the method of dimensionality reduction can be used to describe the electrical and thermal conduction of contacts. These aspects are discussed in Chap. 8. In Chap. 9, the contact between elastomers is extended to include adhesion effects.

The chapters dedicated to axially-symmetric profiles should not merely be seen as a preparation for the more complex topics: Axially-symmetric profiles appear very often in engineering applications and are of outstanding independent importance. Nevertheless, the primary concern of this method is the description of rough surfaces, which Chap. 10 covers in detail. This chapter belongs likewise to the core of the book. In contrast to the axially-symmetric profiles, however, the solutions in this case cannot be verified by comparison with an analytical solution because these solutions are unknown. Therefore, in the case of rough surfaces, we have used comparisons to numerical solutions of respective three-dimensional problems.

In Chap. 11, the simulation of friction is explained and illustrated within the framework of the method of dimensionality reduction. Chapters 12–15 serve simultaneously as case studies and exemplifications of important general topics. For example, it is illustrated in Chap. 12 that also *dynamic* tangential contacts are exactly mapped by the method of dimensionality reduction. Chapter 13 explains the important idea of the "hybrid model." As we already mentioned in Sect. 1.2, an explicit scheme of the multi-scale mechanics must be inserted between the macroscopic system dynamics and the microscopic law of friction. The role of this middle domain is assumed by the method of dimensionality reduction. However, for the entire construction to work properly, the middle domain must be coupled on one side to the macroscopic system dynamics and on the other, to the microscales. In Chap. 13, the coupling to the macroscales is described and supported by an example. A further example follows in Chap. 14. Several ideas as to the coupling to the microscales are discussed in Chap. 15. This topic, however, is still widely open.

Because the method of dimensionality reduction is, above all, an engineering tool, we have given ourselves the liberty of addressing several questions with respect to potential extension and simplification of the practical applications of the method in Chap. 16. In doing so, we have ventured into such topics as plastic deformation, fracturing, and the description of non-isotropic and non-randomly rough surfaces or heterogeneous materials. With this chapter, we would like to show that the method of dimensionality reduction has quite a large potential for further development.

References

1. V.L. Popov, *Contact Mechanics and Friction. Physical Principles and Applications* (Springer, Heidelberg, 2010), p. 362
2. M. Heß, *Über die exakte Abbildung ausgewählter dreidimensionaler Kontakte auf Systeme mit niedrigerer räumlicher Dimension* (Cuvillier-Verlag, Göttingen, 2011)
3. R. Pohrt, V.L. Popov, A.E. Filippov, Normal contact stiffness of elastic solids with fractal rough surfaces for one- and three-dimensional systems. Phys. Rev. E **86**, 026710 (2012)
4. S. Kürschner, V.L. Popov, Penetration of self-affine fractal rough rigid bodies into a model elastomer having a linear viscous rheology. Phys. Rev. E **87**, 042802 (2013)
5. V.L. Popov, Method of reduction of dimensionality in contact and friction mechanics: a linkage between micro and macro scales. Friction **1**(1), 41–62 (2013)
6. F.P. Bowden, D. Tabor, *The Friction and Lubrication of Solids* (Clarendon Press, Oxford, 1986)
7. J.F. Archard, Elastic deformation and the laws of friction. Proc. R. Soc. A **243**, 190 (1957)

Chapter 2
Separation of the Elastic and Inertial Properties in Three-Dimensional Systems

Valentin L. Popov and Markus Heß

2.1 Introduction

For a wide class of "typical tribological systems," there are a number of properties that allow for the significant simplification of contact problems and, in this way, make fast calculations of multi-scalar systems possible. These simplified properties, which are used by the method of dimensionality reduction include

1. The ability to separate the elastic and inertial properties in three-dimensional systems
2. The close analogy between three-dimensional contacts and certain one-dimensional problems.

The first of these will be discussed in this chapter, while further chapters are dedicated to the second. The first property can be formulated into three statements:

(a) For sufficiently small velocities, deformations may be considered to be quasi-static.
(b) The potential energy, and therewith, the force–displacement ratio, is a *local* property which is only dependent on the configuration of the contact area and not on the form or size of the body as a whole.
(c) The kinetic energy, on the other hand, is a *global* property which is only dependent on the form and size of the body and not on the configuration of the micro-contacts.

These three listed statements are met in many macroscopic systems. In the following, we will consider them in detail individually.

V.L. Popov and M. Heß, *Method of Dimensionality Reduction in Contact Mechanics and Friction*, DOI 10.1007/978-3-642-53876-6_2

2.2 The Quasi-Static State

The separation of the elastic and inertial properties is only valid under the condition that the characteristic loading time T of a contact is much larger than the time that elastic waves in the continuum require to travel a distance on the order of magnitude of the diameter D of the contact area:

$$T > D/c, \tag{2.1}$$

where c is the speed of sound. For instance, if the characteristic time of changes in force in a wheel–rail contact is larger than the characteristic time of $T = 1\ \text{cm}/\left(5 \times 10^3\ \text{m/s}\right) = 2 \times 10^{-6}\ \text{s}$ (or the frequency is below 500 kHz), then they may be considered quasi-static. If this condition is met, then the deformation near the contact area is practically the same as in a static contact. This is, of course, the same for the contact forces.

If an even more stringent condition is met, namely,

$$T > R/c, \tag{2.2}$$

where R is the size of the entire system, then all particles in the continuum, with the exception of a small volume near the contact, move as a rigid body. In other words, the condition (2.2) means that the characteristic contact time is much larger than the period of the normal modes of the system. For a wheel–rail contact, this condition is met for frequencies below approximately 2 kHz.

If we continue with the example of a rolling wheel, then the characteristic contact time can be approximated as $T \approx D/v$, where v is the linear velocity (driving speed). Then, the quasi-static state condition simply means

$$v < c. \tag{2.3}$$

For a rough contact with a characteristic wavelength of λ, the characteristic time is $T \approx \lambda/v$, so that condition for the quasi-static state is much more restrictive: $\lambda/v > D/c$ or

$$v < c\frac{\lambda}{D}. \tag{2.4}$$

In most tribological systems, we are dealing with the movements of components whose relative velocities (e.g., a train at around 50 m/s) are orders of magnitude smaller than the speed of sound in these components (this is around 5×10^3 m/s for steel). Under these conditions, one can consider the problem to be *quasi-static* if one is interested in the wavelengths of the roughness that are roughly two orders of magnitude smaller than the diameter of the contact area.

2.3 Elastic Energy as a Local Property

Elastic interactions are local in the sense that they play a role only within a volume on the same order of magnitude as the diameter of the contact area and, therefore, are not dependent on the size or form of the body as a whole. Let us investigate

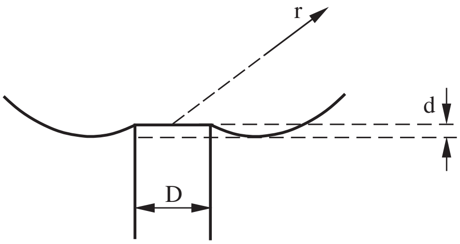

Fig. 2.1 Flat cylindrical indenter being pressed into an elastic body by a distance of *d*

this somewhat more closely by calculating the potential energy of a deformed contact area. We observe a cylindrical indenter that is pressed into a body by the distance d (Fig. 2.1).

For the displacement inside the elastic body at a large distance r from the indentation point, the following is valid:

$$u \approx \frac{D \cdot d}{r}. \tag{2.5}$$

The deformation can be estimated as $\varepsilon \approx \frac{\mathrm{d}u}{\mathrm{d}r} \approx -\frac{D \cdot d}{r^2}$ and the energy density, as $\mathcal{E} \approx \frac{1}{2}G\varepsilon^2 \approx \frac{1}{2}G\frac{D^2 \cdot d^2}{r^4}$. Through integration, the elastic energy is

$$U \simeq \int G\frac{D^2 \cdot d^2}{r^4}\pi r^2 \mathrm{d}r = \pi G D^2 \cdot d^2 \int \frac{\mathrm{d}r}{r^2}, \tag{2.6}$$

where G is shear modulus of the medium. This integral converges at the upper boundary (therefore, it can be set to infinity) and diverges at the lower limit. However, because the asymptote (2.5) is only valid for $r > D$, the elastic energy of the deformation within a volume with a linear dimension on the order of magnitude D dominates. In other words, the elastic energy is a local value that is only dependent on the configuration and deformation in the vicinity of the microcontact. The size and form of the macroscopic body is irrelevant for the contact mechanics of this problem.

Incidentally, this property is not self-evident and would not, for example, be valid in a two-dimensional system. Instead of having Eq. (2.6), we would have the integral $\int \mathrm{d}r/r$ in the two-dimensional case, which diverges logarithmically on both boundaries. The elastic contact energy for the two-dimensional case is, therefore, dependent on the contact configuration as well as the size and form of the body as a whole.

2.4 Kinetic Energy as a Global Property

Exactly the opposite is true for the kinetic energy of the body. To illustrate this, let us consider a sphere landing on an indenter with a diameter of D (the contact radius remains the same) at a velocity of v (Fig. 2.2).

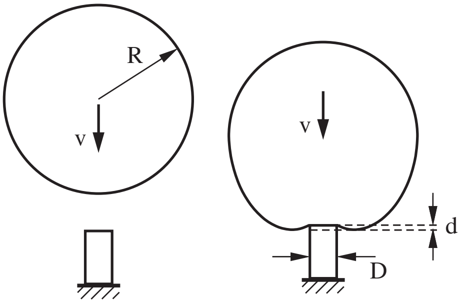

Fig. 2.2 Illustrating the kinetic energy of an elastic body landing on a rigid cylindrical indenter at a velocity of *v*

We assume that the condition (2.2) is met so that the elastic deformation in the entire body may be considered to be quasi-static. The center of gravity of the sphere x and the coordinate of the point of contact ξ are chosen as the generalized coordinates of the sphere. Accordingly, the indentation depth is equal to

$$d = x - \xi + R. \tag{2.7}$$

The potential energy of the sphere is a function of the indentation depth:

$$U = \frac{kd^2}{2} = \frac{k}{2}(x - \xi + R)^2, \tag{2.8}$$

where $k = E^* D$. E^* is here the effective Young modulus defined in the next Chapter [Eq. (3.2)]. The velocity field for a quasi-static indentation is obtained from (2.5) by differentiating the indentation depth with respect to time:

$$\dot{u} \approx \frac{D \cdot \dot{d}}{r} = \frac{D \cdot \left(\dot{x} - \dot{\xi}\right)}{r}. \tag{2.9}$$

The total kinetic energy is then composed of the kinetic energy of the movement of the center of mass and the kinetic energy of the deformation relative to the center of mass:

$$K = \frac{m\dot{x}^2}{2} + \frac{\rho}{2}\left(\dot{x} - \dot{\xi}\right)^2 \int \left(\frac{D}{r}\right)^2 \mathrm{d}V = \frac{m\dot{x}^2}{2} + \frac{m_1}{2}\left(\dot{x} - \dot{\xi}\right)^2, \tag{2.10}$$

with

$$m_1 \approx \rho D^2 \int \left(\frac{1}{r}\right)^2 2\pi r^2 \mathrm{d}r = 2\pi \rho D^2 R \approx m\left(\frac{D}{R}\right)^2. \tag{2.11}$$

A more accurate derivation leads to the result of $m_1 \approx 0.3\, m(D/R)^2$ for materials with $\nu = 1/3$ (see Problem 3 in this chapter). Note that this mass is on the same order of magnitude as the mass of a rod with the diameter D and the length R.

We now would like to illustrate the separation of the elastic and inertial properties of a contact and their accuracy using several concrete dynamic examples. The dynamic treatment of the system makes use of the Lagrange function, which

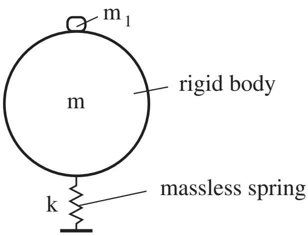

Fig. 2.3 Model for the impact of a sphere on a rigid cylindrical rod

is calculated as the difference between the kinetic energy (2.10) and the potential energy (2.8):

$$L = K - U = \frac{m\dot{x}^2}{2} + \frac{m_1}{2}\left(\dot{x} - \dot{\xi}\right)^2 - \frac{k}{2}(x - \xi + R)^2$$
$$= \frac{m\dot{x}^2}{2} + \frac{m_1}{2}\left(\dot{x} - \dot{\zeta}\right)^2 - \frac{k}{2}(x - \zeta)^2, \tag{2.12}$$

where we have introduced a new variable $\zeta = \xi - R$.

We consider three cases:

1. *Impact of the body with a stationary, rigid rod.* In this case, $\zeta = 0$ is valid for the entirety of the impact time and the Lagrange function takes the form

$$L = \frac{(m + m_1)\dot{x}^2}{2} - \frac{k}{2}x^2. \tag{2.13}$$

Therefore, the system is equivalent to a rigid body with the mass $(m + m_1)$ on a spring with the stiffness k, which is equal to the static contact stiffness (Fig. 2.3). The mass correction m_1 is on the order of magnitude of $m(D/R)^2$ and may be neglected for small contact diameters.

2. *"Base excitation."* We now assume that the coordinate of the contact area, and therefore, the coordinate ζ, is a given function of time: $\zeta = \zeta(t)$. The Lagrange function is then equal to

$$L = \frac{m\dot{x}^2}{2} + \frac{m_1}{2}\left(\dot{x} - \dot{\zeta}(t)\right)^2 - \frac{k}{2}(x - \zeta(t))^2 \tag{2.14}$$

and the Euler–Lagrange equation for the coordinate of the center of gravity is

$$(m + m_1)\,\ddot{x} + kx = k\zeta(t) + m_1\ddot{\zeta}(t) = \Delta F_N(t). \tag{2.15}$$

The acceleration term on the right-hand side of this equation is on the order of magnitude of $m_1\zeta/T^2$. Within the validity regime of the condition (2.2), we have the equation

$$\frac{m_1}{T^2}\zeta < \frac{m_1c^2}{R^2}\zeta \approx \frac{mc^2D^2}{2R^4}\zeta = k\frac{mc^2D^2}{2kR^4}\zeta \approx k\frac{2\pi R^3\rho c^2D^2}{EDR^4}\zeta = k\frac{2\pi D}{R}\zeta \ll k\zeta, \tag{2.16}$$

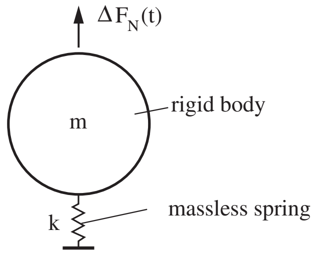

Fig. 2.4 Model of a non-stationary contact (e.g., a rolling sphere on a rough substrate)

where $c^2 = E/\rho$ has been substituted, E being Young's modulus. Therefore, the acceleration contribution can always be neglected with respect to the elastic contribution for small contact diameters. As in the first case, for sufficiently small contact diameter, the system can be modeled as a rigid body with the mass m bound to a spring (see Fig. 2.4).

3. *Freely oscillating surface.* If the body is held and a contact area with the diameter D indented and then instantaneously let free, then we obtain the Lagrange function by substituting $x = 0$ into (2.12):

$$L = \frac{m_1}{2}\dot{\zeta}^2 - \frac{k}{2}\zeta^2. \tag{2.17}$$

The movement of the surface would be an oscillation with the angular frequency ω_1:

$$\omega_1^2 = \frac{k}{m_1} \approx \frac{ED}{2\pi\rho D^2 R} \approx \frac{c^2}{2\pi DR}. \tag{2.18}$$

This frequency, however, is much larger than the natural frequency of the body $\omega_0^2 \approx c^2/R^2$. Therefore, the condition of validity for the Lagrange function (2.17) is not met: Resonance oscillations of a free surface *cannot* be dealt with using this approximation.

If the diameter of the contact is dependent on the indentation depth, then the corresponding potential energy of the contact $U(d)$ must be used in the Lagrange function:

$$L = \frac{m\dot{x}^2}{2} + \frac{m_1(t)}{2}\left(\dot{x} - \dot{\zeta}\right)^2 - U(x - \zeta), \tag{2.19}$$

where, as before,

$$m_1 \approx \frac{m}{2}\left(\frac{D(t)}{R}\right)^2. \tag{2.20}$$

As explained above, the second term in (2.19) can always be neglected as long as condition (2.2) is met. The model shown in Fig. 2.5 is the result.

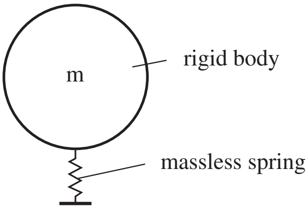

Fig. 2.5 Dynamic model for a non-linear (e.g., Hertzian) contact

Now, we will concentrate on the procedure for non-stationary force effects on a small contact area. As an example, we consider a rough sphere rolling on a rigid rough surface (although nominally flat) so that the potential energy is not only a function of indentation depth, but also an explicit function of time:

$$L = \frac{m\dot{x}^2}{2} + \frac{m_1(t)}{2}\left(\dot{x} - \dot{\zeta}\right)^2 - U(x - \zeta, t). \tag{2.21}$$

Due to the fact that the rolling takes place on a rigid surface, $\zeta = 0$ and the Lagrange function takes the form

$$L \approx \frac{m\dot{x}^2}{2} - U(x, t), \tag{2.22}$$

where we have neglected the mass correction. The corresponding Euler-Lagrange equation is then

$$m\ddot{x} = -\frac{\partial U}{\partial x} = F_N(x, t). \tag{2.23}$$

In this case, the system is equivalent to a rigid body on which the time-dependent contact forces act. If it is possible to divide the force into the part for the "smooth surface" and a stochastic part, according to the equation

$$F_N(x, t) = F_{N,0}(x) + \Delta F_N(t), \tag{2.24}$$

then the equation of motion takes the form

$$m\ddot{x} = F_{N,0}(x) + \Delta F_N(t). \tag{2.25}$$

This equation describes a rigid mass m coupled to the surface with a non-linear contact force $F_{N,0}(x)$ being acted upon by the exciting force $\Delta F_N(t)$. The corresponding model is the same as that in Fig. 2.4 with the exception that a non-linear spring is used here.

If the condition (2.2) is not met, but the condition (2.1) is still valid, then the body can no longer be treated as a rigid mass, such as in the case of high-frequency oscillations; however, the static equations can still be used to determine the contact forces. In this case, there is no simple model to describe the entire dynamics of the system, because the frequency is too high for the body to be assumed to be rigid. Therefore, the complete dynamic problem must be solved. The contact problem, however, remains quasi-static and provides a boundary condition for the elastic problem (Fig. 2.6). An example of such a dynamic case is presented in Problem 4.

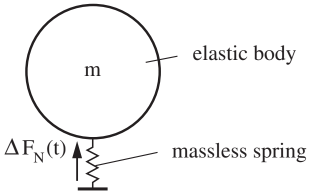

Fig. 2.6 Model for the case of high-frequency contact forces, for which condition (2.2) is not met, but the weaker condition (2.1) still holds true

2.5 Problems

Problem 1 Determine the contact time for an elastic sphere (radius R) impacting a rigid wall. (Hertz 1881, [1]).

Solution The approaching distance between the center of the sphere and the wall, starting at the moment of impact, is defined as x. The potential energy of the system is given by[1] $U = (8/15)E^*R^{1/2}d^{5/2}$, while the kinetic energy is equal to that of a rigid body. During the time of impact, the energy is conserved:

$$\frac{m}{2}\left(\frac{\mathrm{d}x}{\mathrm{d}t}\right)^2 + \frac{8}{15}E^*R^{1/2}x^{5/2} = \frac{mv_0^2}{2}, \tag{2.26}$$

where v_0 is the impact velocity. The minimum distance between the center of the sphere and the wall x_0 corresponds to the time at which the velocity $\mathrm{d}x/\mathrm{d}t$ disappears, and is equal to

$$x_0 = \left(\frac{15}{16}\frac{mv_0^2}{E^*R^{1/2}}\right)^{2/5}. \tag{2.27}$$

The length of impact τ (while x increases from 0 to x_0 and then decreases back to 0) is

$$\tau = \frac{2}{v_0}\int_0^{x_0}\frac{\mathrm{d}x}{\sqrt{1-(x/x_0)^{5/2}}} = \frac{2x_0}{v_0}\int_0^1\frac{\mathrm{d}\xi}{\sqrt{1-\xi^{5/2}}} \approx \frac{2.94x_0}{v_0}. \tag{2.28}$$

Problem 2 Solve Problem 1 assuming that the sphere is glued to a hard cylindrical foot, much like a golf tee, with a diameter of D so that the contact radius does not change.

Solution The contact stiffness of a contact with a diameter of D is equal to $k = E^*D$ [2] (definition of material parameters see next Chapter) and the sphere can be considered to be a rigid mass as a first approximation. During the entire contact process, the differential equation

---

[1] Definition of the material parameter E see next chapter.

$$m\ddot{x} + kx = 0 \tag{2.29}$$

is sufficient to describe the motion. The solution for the initial conditions $x(0) = 0$ and $\dot{x}(0) = v_0$ is $x = \frac{v_0}{\omega}\sin(\omega t)$, with $\omega^2 = k/m$. The length of time of the contact is equal to half of the period of the oscillation

$$\tau = \frac{\pi}{\omega} = \pi\sqrt{\frac{m}{E^* D}}. \tag{2.30}$$

Problem 3 Calculate the mass m_1 in Eq. (2.10) in the case of an elastic sphere.

Solution We will assume that the displacement relative to the center of mass in the entire volume of the sphere is the same as that in a half-space. If a round area with the diameter D is pressed into an elastic half-space by the distance u, then displacements result whose asymptotic forms (for $r \gg D$) appear as follows [3]:

$$u_x = \frac{1+\nu}{2\pi E}\left[\frac{xz}{r^3} - \frac{(1-2\nu)x}{r(r+z)}\right]F_z, \tag{2.31}$$

$$u_y = \frac{1+\nu}{2\pi E}\left[\frac{yz}{r^3} - \frac{(1-2\nu)y}{r(r+z)}\right]F_z, \tag{2.32}$$

$$u_z = \frac{1+\nu}{2\pi E}\left[\frac{2(1-\nu)}{r} + \frac{z^2}{r^3}\right]F_z \tag{2.33}$$

with

$$F_z = uE^* D. \tag{2.34}$$

Substitution of (2.34) into the equations for displacements results in

$$u_x = \frac{uD}{2\pi(1-\nu)}x\left[\frac{z}{r^3} - \frac{(1-2\nu)}{r(r+z)}\right], \tag{2.35}$$

$$u_y = \frac{uD}{2\pi(1-\nu)}y\left[\frac{z}{r^3} - \frac{(1-2\nu)}{r(r+z)}\right], \tag{2.36}$$

$$u_z = \frac{uD}{2\pi(1-\nu)}\left[\frac{2(1-\nu)}{r} + \frac{z^2}{r^3}\right]. \tag{2.37}$$

The corresponding velocities, under the assumption that the deformation is quasi-static, are equal to

$$\dot{u}_x = \frac{\dot{u}D}{2\pi(1-\nu)}x\left[\frac{z}{r^3} - \frac{(1-2\nu)}{r(r+z)}\right], \tag{2.38}$$

$$\dot{u}_y = \frac{\dot{u}D}{2\pi(1-\nu)} y\left[\frac{z}{r^3} - \frac{(1-2\nu)}{r(r+z)}\right], \tag{2.39}$$

$$\dot{u}_z = \frac{\dot{u}D}{2\pi(1-\nu)}\left[\frac{2(1-\nu)}{r} + \frac{z^2}{r^3}\right]. \tag{2.40}$$

With the spherical coordinates

$$x = r\cos\theta\cos\varphi, \tag{2.41}$$

$$y = r\cos\theta\sin\varphi, \tag{2.42}$$

$$z = r\sin\theta, \tag{2.43}$$

The equations (2.38)–(2.40) can be written as follows:

$$\dot{u}_x = \frac{\dot{u}D}{2\pi(1-\nu)}\frac{1}{r}\left\{\cos\theta\cos\varphi\left[\sin\theta - \frac{(1-2\nu)}{(1+\sin\theta)}\right]\right\}, \tag{2.44}$$

$$\dot{u}_y = \frac{\dot{u}D}{2\pi(1-\nu)}\frac{1}{r}\left\{\cos\theta\sin\varphi\left[\sin\theta - \frac{(1-2\nu)}{(1+\sin\theta)}\right]\right\}, \tag{2.45}$$

$$\dot{u}_z = \frac{\dot{u}D}{2\pi(1-\nu)}\frac{1}{r}\left[2(1-\nu) + \sin^2\theta\right]. \tag{2.46}$$

The kinetic energy of the deformation is now calculated as

$$\begin{aligned}
K &\approx \frac{\rho}{2}2\pi\int\limits_0^{\pi/2} \mathrm{d}\theta \int\limits_0^{2R\sin\theta} \left(\dot{u}_x^2 + \dot{u}_y^2 + \dot{u}_z^2\right) r^2\cos\theta \mathrm{d}r \\
&= \frac{\pi\rho\dot{u}^2D^2R}{2\pi^2(1-\nu)^2}\int\limits_0^{\pi/2}\left\{\cos^2\theta\left[\sin\theta - \frac{(1-2\nu)}{(1+\sin\theta)}\right]^2\right. \\
&\quad \left. + \left[2(1-\nu) + \sin^2\theta\right]^2\right\}\sin\theta\cos\theta \mathrm{d}\theta \\
&= \frac{\pi\rho\dot{u}^2D^2R}{2\pi^2(1-\nu)^2}\left(\frac{55}{12} - \frac{32}{3}\nu + 8\nu^2 - 2\ln 2\cdot(1-2\nu)^2\right) \\
&= \frac{1}{2}\cdot\frac{4\pi\rho R^3}{3}\frac{3\dot{u}^2D^2}{4\pi^2R^2}\cdot\frac{\frac{55}{12} - \frac{32}{3}\nu + 8\nu^2 - 2\ln 2\cdot(1-2\nu)^2}{(1-\nu)^2}.
\end{aligned} \tag{2.47}$$

From this, it follows that

$$m_1 = m\left(\frac{D}{R}\right)^2\frac{3}{4\pi^2}\cdot\frac{\frac{55}{12} - \frac{32}{3}\nu + 8\nu^2 - 2\ln 2\cdot(1-2\nu)^2}{(1-\nu)^2} = m\left(\frac{D}{R}\right)^2\delta(\nu). \tag{2.48}$$

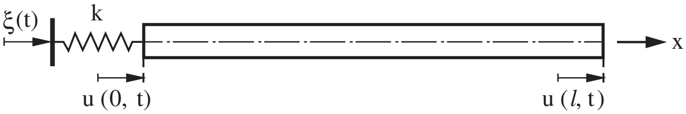

Fig. 2.7 Diagram for the contact described in Problem 4

For metallic materials ($\nu \approx 1/3$) and incompressible media ($\nu \approx 1/2$), $\delta(1/3) \approx 0.3$ and $\delta(1/2) \approx 0.38$, respectively.

Problem 4 A round rod with the diameter D_1 is excited in an area of constant diameter $D_2 \ll D_1$ by the harmonic oscillation $\xi = \xi_0 \cos \omega t$. Calculate the motion of the system.

Solution The system diagram is shown in Fig. 2.7, where $k = E^* D_2$.
The equation of motion for the elastic rod is

$$\frac{\partial^2 u(x,t)}{\partial t^2} = c^2 \frac{\partial^2 u(x,t)}{\partial x^2}. \tag{2.49}$$

Here, $u(x,t)$ is the displacement of the point with the initial coordinate x and $c^2 = E/\rho$. The displacement of the "base point" we describe with ξ. The boundary condition at the left side of the rod is then

$$k[u(0,t) - \xi(t)] = AE \left.\frac{\partial u}{\partial x}\right|_{x=0}. \tag{2.50}$$

$A = \pi D_1^2/4$ is the cross section of the rod. The solution of Eq. (2.49), taking under consideration the unloaded end at the point $x = l$ and the boundary condition (2.50) with $\xi = \xi_0 \cos \omega t$ is

$$u(x,t) = \frac{k\xi_0 \cos \frac{\omega}{c}(x-l)}{k \cos \frac{\omega}{c} l - AE\frac{\omega}{c} \sin \frac{\omega}{c} l} \cos(\omega t). \tag{2.51}$$

If condition (2.2) is met, and therefore $\omega l/c \ll 1$, then the solution takes the form

$$u(x,t) = \frac{k\xi_0 \cos(\omega t)}{k - \frac{AlE\omega^2}{c^2}} = \frac{k\xi_0 \cos(\omega t)}{k - m\omega^2}, \tag{2.52}$$

where $m = \rho A l$ is the mass of the rod. In this limiting case, the displacement is not dependent of the coordinate x: The rod moves as a rigid structure with the mass m. The deviation from the approximation as a rigid mass, in this case, is of the second order of magnitude for $\omega l/c$.

References

1. H. Hertz, Über die Berührung fester elastischer Körper. J. für die reine und angewandte Mathematik **92**, 156–171 (1881)
2. V.L. Popov, Contact Mechanics and Friction. Physical Principles and Applications (Springer-Verlag 2010), p. 362
3. L.D. Landau, E.M. Lifschitz, Elastizitätstheorie, (Lehrbuch der Theoretischen Physik, Band VII). 7., überarb. Auflage, Akademie Verlag (Berlin 1991), §§ 8, 9

Chapter 3
Normal Contact Problems with Axially-Symmetric Bodies Without Adhesion

Valentin L. Popov and Markus Heß

3.1 Mapping of Three-Dimensional Contact Problems onto One Dimension: The Basic Idea

The *method of dimensionality reduction* is based on the observation that certain types of three-dimensional contacts can be *exactly* mapped to one-dimensional linearly elastic foundations. Even one of the simplest contact problems offers us a taste of this method: If a flat cylindrical indenter is pressed into the surface of an elastic half-space (Fig. 3.1a), then the normal stiffness of the contact is *proportional to its diameter* D:

$$k_z = DE^*, \tag{3.1}$$

where E^* is the effective Young's modulus and is calculated from

$$\frac{1}{E^*} = \frac{1-\nu_1^2}{E_1} + \frac{1-\nu_2^2}{E_2}, \tag{3.2}$$

using the Young's moduli of the contacting bodies E_1 and E_2 as well as their shear moduli ν_1 and ν_2.[1] The proportionality of the stiffness to the diameter can also be reproduced quite trivially by a *one-dimensional* linearly elastic foundation.

The linearly elastic foundation (Fig. 3.1b) is a series of independent, identical springs that are fixed to a rigid substrate separated from one another by a distance of Δx. In order to represent continua, the "discretization step" Δx must, of course, be sufficiently small, which we always silently imply. The number of springs that are in contact with the indenter is equal to $D/\Delta x$. If we denote the stiffness of a single spring as Δk_z, then the total stiffness of the contact is

$$k_z = \Delta k_z \frac{D}{\Delta x}. \tag{3.3}$$

---

[1] This result can be found in any book dealing with contact mechanics (see, for example [1]).

V.L. Popov and M. Heß, *Method of Dimensionality Reduction in Contact Mechanics and Friction*, DOI 10.1007/978-3-642-53876-6_3

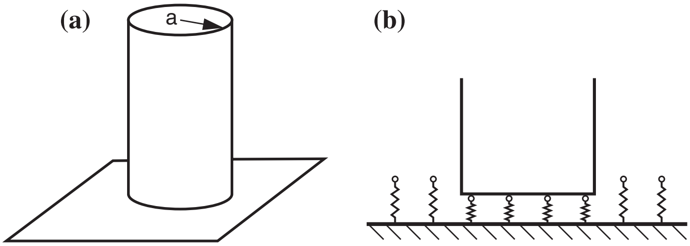

Fig. 3.1 (**a**) Contact between a flat, cylindrical indenter and an elastic half-space and (**b**) the one-dimensional model

In order for Eq. (3.1) to also be valid for the indentation into a linearly elastic foundation, the stiffness per unit length must be chosen to be equal to effective modulus E^*:

$$\frac{\Delta k_z}{\Delta x} = E^*. \tag{3.4}$$

According to this, the stiffness of every individual spring is

$$\Delta k_z = E^* \Delta x. \tag{3.5}$$

The proportionality of the stiffness to the diameter of the indenter is then met rather trivially in the case of an elastic foundation. In the following, it will be shown that the defined elastic foundation is also suitable for the mapping of a large number of other contact problems.

3.2 The Rules of Geike and Popov and the Rules of Heß for Normal Contact Problems

The relationship between normal force, the indention depth, and the contact radius can be reproduced exactly for a broad range of profiles by the reduced contact problem of a one-dimensional linearly elastic foundation. Thereby, the surface profile must merely be modified according to a few simple rules.

Let us first consider the contact between an elastic sphere with the radius R and an elastic half-space (the Herzian contact problem, Fig. 3.2a).[2] As early as 2005, Popov pointed out in a lecture[3] that also for a sphere (or a parabolic indenter) the relationship between normal force, the indentation depth, and the contact radius

---

[2] Strictly speaking, a parabolic profile with the radius of curvature R is considered.

[3] German–Russian Workshop "Numerical simulation methods in tribology: possibilities and limitations", Berlin University of Technology, March 14–17, 2005. Published in [2].

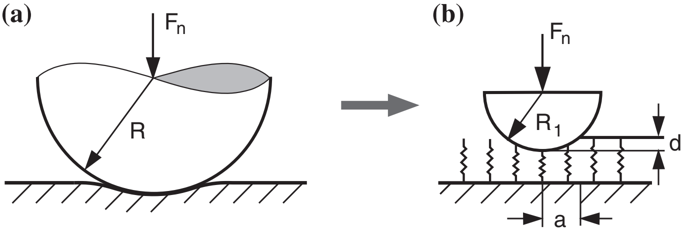

Fig. 3.2 (**a**) Contact between a sphere and an elastic half-space and (**b**) the one-dimensional model

can be *exactly* described by a one-dimensional model (Fig. 3.2b), provided that the radius is scaled by a factor of 1/2. At this point, we will describe the solution for a sphere in detail. In the following chapters, however, we will dispense with the details of the calculation due to their simplicity and only state the results.

The one-dimensional substitution profile should have the radius of curvature of R_1 and is given by the equation

$$\tilde{z} = g(x) = \frac{x^2}{2R_1}. \tag{3.6}$$

If this profile is pressed into the elastic foundation to a depth of d, then we obtain the vertical displacement of the foundation at the point x:

$$u_z(x) = d - g(x) = d - \frac{x^2}{2R_1}. \tag{3.7}$$

The semi-span of the contact area (the "contact radius") a is given by requiring that $u_z(a) = 0$ and is

$$a = \sqrt{2R_1 d}. \tag{3.8}$$

The contribution of a single spring with a coordinate x to the normal force is

$$f_N = \Delta k_z \cdot u_z(x) = E^* \left(d - \frac{x^2}{2R_1} \right) \Delta x. \tag{3.9}$$

The total normal force is obtained by integration over the contact area:

$$F_N = \int_{-a}^{a} E^* \left(d - \frac{x^2}{2R_1} \right) dx = \int_{-\sqrt{2R_1 d}}^{\sqrt{2R_1 d}} E^* \left(d - \frac{x^2}{2R_1} \right) dx = \frac{4\sqrt{2}E^*}{3} \sqrt{R_1 d^3}. \tag{3.10}$$

If we now choose the radius of the "two-dimensional sphere" according to

$$R_1 = R/2, \tag{3.11}$$

("rule of Popov"), then we obtain the *exact* Herzian relationships for the contact radius and the normal force:

$$a = \sqrt{Rd}, \tag{3.12}$$

$$F_N(d) = \frac{4}{3}E^*\sqrt{Rd^3}. \tag{3.13}$$

In other words, the rule (3.11) means that the cross-section of the original three-dimensional profile (in our case, the sphere with the radius R) is stretched by a factor of 2 in the vertical direction.

In his dissertation from 2011, Heß [3] showed that a similar *exact* mapping is possible for an *arbitrary* axially-symmetric profile. In this chapter, we will apply the mapping rules determined by Heß without providing proof of their validity. A detailed derivation of these rules is provided in Chap. 17.

The focus of the following investigation is the contact between axially-symmetric bodies and an elastic half-space. Let the axis of symmetry be z and the surface of the elastic half-space be given by $z = 0$. We parameterize the surface of the half-space using the Cartesian coordinates x and y. Now, we consider an axially-symmetric body with the profile

$$\tilde{z} = f_n(r) = c_n r^n, \tag{3.14}$$

where $r = \sqrt{x^2 + y^2}$, C_n is a constant, and n represents an arbitrary positive number (not necessarily an integer). We now define a one-dimensional profile according to[4]

$$\tilde{z} = g_n(x) = \tilde{c}_n |x|^n. \tag{3.15}$$

As shown in Chap. 17, the contact between the three-dimensional profile (3.14) and the elastic half-space is equivalent to that of the two-dimensional profile (3.15) and the linearly elastic foundation (3.4) if the following *rule of Heß* is applied:

$$\tilde{c}_n = \kappa_n c_n, \quad \kappa_n = \frac{\sqrt{\pi}}{2}\frac{n\Gamma(\frac{n}{2})}{\Gamma(\frac{n}{2}+\frac{1}{2})}, \tag{3.16}$$

where $\Gamma(n)$ is the gamma function:

$$\Gamma(n) = \int_0^\infty t^{n-1}e^{-t}\mathrm{d}t. \tag{3.17}$$

---

[4] Let it be pointed out here that, as in the introductory examples, a one-dimensional profile is generally denoted with $g(x)$ and a three-dimensional profile with $f(r)$. Both are defined as being positive from the tip of the indenter upwards, which is additionally introduced as the coordinate $\tilde{z}$ (see Fig. 3.4).

The exact equivalence between the three-dimensional and one-dimensional problem is valid for the relationships between the normal force, the contact radius, and the indentation depth. In Table 3.1, the values of the scaling factor κ_n are presented for various values of n and in Fig. 3.3 for $0 < n \leq 5$, they are shown graphically.

Here, the values for a conical and a parabolic indenter are pointed out. The corresponding scaling factors are $\kappa_1 = \frac{1}{2}\pi$ and $\kappa_2 = 2$. The latter is, of course, consistent with the *rule of Popov*, which requires dividing the radius of curvature by 2.

The fact that it is possible to exactly map a three-dimensional contact problem to a one-dimensional linearly elastic foundation not only for profiles of the form (3.14), but rather *for arbitrary superpositions* of such forms is extremely important. We now consider a superposition of multiple profiles:

$$f(r) = \sum_{n=1}^{\infty} f_n(r) = \sum_{n=1}^{\infty} c_n r^n. \tag{3.18}$$

In this case, the rule of Heß is applied as follows: From the profile (3.18), a one-dimensional profile is generated

$$f(r) = \sum_{n=1}^{\infty} c_n r^n \Rightarrow g(x) = \sum_{n=1}^{\infty} \tilde{c}_n |x|^n. \tag{3.19}$$

In Chap. 17, it is shown that by indenting the profile (3.19) into a linearly elastic foundation with a stiffness according to (3.4), the relationships between the normal force, contact radius, and the indentation depth remain the same as those in the three-dimensional case.

Table 3.1 Scaling factor κ_n for various exponents of the form function

n	0.5	1	2	3	4	5	6	7	8	9	10
κ_n	1.311	1.571	2	2.356	2.667	2.945	3.2	3.436	3.657	3.866	4.063

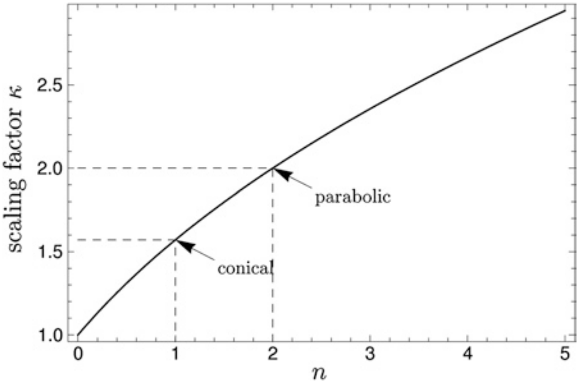

Fig. 3.3 Dependence of the scaling factor κ on the exponent n

The ability to map contacts between three-dimensional, axially-symmetric bodies of the form (3.14) to one-dimensional systems results from simple general scaling arguments and it is informative to discuss these briefly at this point. From dimensional analysis and self-affinity[5] of the profile (3.14), it arises that the contact radius and the indentation depth are related by the same exponential power n as $\tilde{z}$ and R:

$$d = \kappa_n c_n a^n, \tag{3.20}$$

where κ_n is a dimensionless constant. By pressing the one-dimensional profile (3.15) into the linearly elastic foundation, the indentation depth is trivially determined according to

$$d = \tilde{c}_n a^n. \tag{3.21}$$

By choosing a suitable $\tilde{c}_n = \kappa_n c_n$, one can always guarantee that the relationship between the indentation depth and the contact radius is correct in both cases. Furthermore, the differential contact stiffness is given in both the one-dimensional case as well as the three-dimensional case by

$$\frac{\partial F_N}{\partial d} = 2aE^* \tag{3.22}$$

(proof is given by Pharr et al. [4] or Popov [5]). By integrating this equation and taking (3.21) into consideration, the following relationship is obtained for both the one-dimensional and three-dimensional case:

$$F_N = \int \mathrm{d}F_N = 2E^* \int a\mathrm{d}(d) = 2E^* \int a\tilde{c}_n n a^{n-1} \mathrm{d}a = 2E^* \tilde{c}_n \frac{n}{n+1} a^{n+1}. \tag{3.23}$$

Inarguably, the force as a function of indentation depth must be the same in both cases:

$$F_N = \frac{2n}{n+1} E^* \tilde{c}_n^{-1/n} d^{\frac{n+1}{n}}. \tag{3.24}$$

If we constrain ourselves to the force–displacement relationship, then the ability to map three-dimensional systems to one-dimensional systems becomes even more general and is possible for arbitrary self-affine surfaces, regardless if they are axially-symmetric or not: The exponential dependence (3.24) is only contingent on the self-affinity and is valid for arbitrary surfaces with given Hurst exponents. Obviously, the correct coefficient can always be found by stretching the profile by the appropriate factor if the exponent in the force–displacement relationship is correct. As we will see in Chap. 10, this is also valid for self-affine, fractally rough surfaces. This paves the way for the fast calculation of contacts with rough surfaces and is, therefore, especially interesting.

Also, the superposition rule (3.19) has a simple physical meaning and requires only that the medium exhibits a linear behavior. Let us consider the two profiles

---

[5] For self-affinity, the following property is understood: If the profile (3.14) is stretched in the horizontal direction by the factor C and simultaneously in the vertical direction by a factor C^n, then one obtains the original profile. The exponent n is known as the *Hurst exponent*.

$f_1(r)$ and $f_2(r)$ being pressed into an elastic half-space. The first profile requires the indentation force $F_1(a)$ in order to obtain the contact radius a. The second profile, on the other hand, requires the force $F_2(a)$ in order to reach the *same contact radius a*. We denote the corresponding indentation depths with $d_1(a)$ and $d_2(a)$. If we initially consider the indention of $f_1(r)$ and then *additionally* apply $f_2(r)$ to the *same contact area,* with the radius a, then it directly follows from the linearity of the medium that the necessary force is

$$F_N(a) = F_1(a) + F_2(a). \tag{3.25}$$

The indentation depth, thereby, is

$$d(a) = d_1(a) + d_2(a). \tag{3.26}$$

These are exactly the two properties that are necessary for the mapping of superimposed profiles according to Eq. (3.19). In order to prevent confusion, we would like to stress that the principle of superposition is not valid (or is not exact) if the areas of application of both profiles are not the same.

3.3 General Mapping of Axially-Symmetric Profiles

The previous considerations dealt with the simplest mapping rules which are valid for contact profiles in the form of power functions. By choosing an arbitrary, positive real exponent and using the principle of superposition due to linearity, a large number of axially-symmetric contacts are able to be exactly mapped. The equivalence between one-dimensional and three-dimensional systems, however, is in no way restricted to such systems, but is generally valid for *all* axially-symmetric contacts with a simply connected contact area. The calculation of an equivalent profile using the profile function of the three-dimensional contact is conducted using the following formula:

$$g(x) = |x| \int_0^{|x|} \frac{f'(r)}{\sqrt{x^2 - r^2}} \mathrm{d}r, \tag{3.27}$$

the validity of which will be proven in Chap. 17. The fact that in the case of the power function (3.14), this rule leads to the simple scaling relation (3.16) is also explained here. Except for the explicit application of the formula (3.27), nothing changes in the procedure of the reduction method in order to determine the relationships between contact radius, indentation depth, and normal force. In the following, we would like to explain the procedure step by step using an example. For this, we consider the indentation of the following piecewise-defined profile into an elastic half-space:

$$f(r) = \begin{cases} 0 & \text{for } 0 \le r < b \\ \frac{r^2 - b^2}{2R} & \text{for } b \le r \le a \end{cases}. \tag{3.28}$$

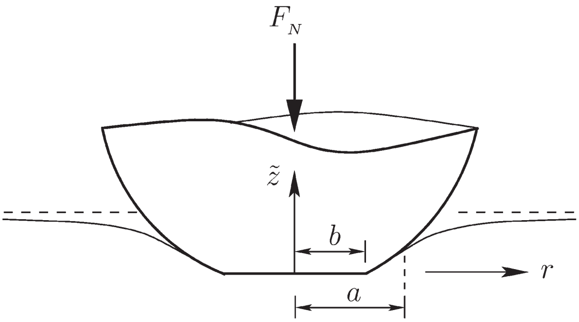

Fig. 3.4 Qualitative presentation of the indentation of a parabolic profile with a flattened tip into an elastic half-space

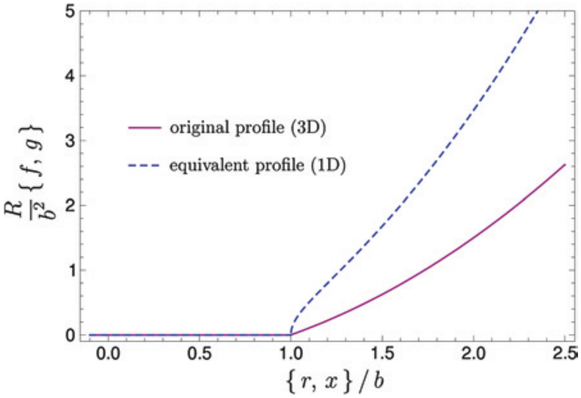

Fig. 3.5 Parabolic indenter with "worn" tip: comparison between original and equivalent profile

As can be gathered from Fig. 3.4, we can interpret the profile as an asperity which was originally parabolic, the tip of which, however, has been worn down through time.

The application of (3.27) requires the derivative of the original profile (3.28)

$$f'(r) = \begin{cases} 0 & \text{for } 0 \leq r < b \\ \frac{r}{R} & \text{for } b \leq r \leq a \end{cases}, \tag{3.29}$$

which, after insertion into (3.27) and subsequent integration, leads to the equivalent one-dimensional profile[6]

$$g(x) = \begin{cases} 0 & \text{for } 0 \leq |x| < b \\ \frac{|x|}{R}\sqrt{x^2 - b^2} & \text{for } b \leq |x| \leq a \end{cases}. \tag{3.30}$$

This profile is compared to the original in Fig. 3.5.

---

[6] Frequently, the one-dimensional profile is referred to in the following; this is to be understood, of course, as the profile in the one-dimensional model.

Naturally, the special case of $b = 0$ coincides with the mapping rule of Popov, of which one may be convinced by comparing (3.28) and (3.30) for this case.

For a known equivalent profile, we can now proceed to the solution of the contact problem using the aforementioned reduction process. In order to accomplish this, we must merely press the rigid profile described by (3.30) into the one-dimensional linearly elastic foundation, which results in a surface displacement of

$$u_z(x) = d - g(x) = d - \frac{|x|}{R}\sqrt{x^2 - b^2}. \tag{3.31}$$

The indentation depth, contact radius, and normal force must reveal the exact three-dimensional dependencies. The indentation depth as a function of contact radius results from requiring that the displacement at the edge of the contact approaches zero:

$$u_z(a) = 0 \quad \Rightarrow \quad d = g(a) = \frac{a}{R}\sqrt{a^2 - b^2}. \tag{3.32}$$

The normal force is the sum of the spring forces

$$F_N = E^* \int_{-a}^{a} \left[d - g(x)\right] \mathrm{d}x = 2E^* \int_{0}^{a} d \, \mathrm{d}x - \frac{2E^*}{R} \int_{b}^{a} x \sqrt{x^2 - b^2} \, \mathrm{d}x, \tag{3.33}$$

which provides

$$F_N(a) = \frac{2E^*}{3R}\left(2a^2 + b^2\right) \cdot \sqrt{a^2 - b^2}. \tag{3.34}$$

after integration and rearranging with the help of (3.32). The results (3.32) and (3.34) obtained by using the reduction method are exactly those derived by Ejike [6] for the three-dimensional problem. For the sake of completeness, let us state the relationship between normal force and indentation depth, which after solving (3.32) with respect to a and subsequently inserting this into (3.34), results in

$$F_N(d) = \frac{\sqrt{2}E^* b^3}{3R}\left(2 + \sqrt{1 + \left(\frac{2R}{b^2}d\right)^2}\right) \cdot \sqrt{-1 + \sqrt{1 + \left(\frac{2R}{b^2}d\right)^2}}. \tag{3.35}$$

Further contact problems that require the explicit application of formula (3.27) for the calculation of the equivalent profile can be found in the practice exercises at the end of this and the following two chapters.

3.4 The Mapping of Stress

In the one-dimensional contact problem with the linearly elastic foundation, the stresses are not able to be directly determined. Although the relationships between the force, displacement, and contact radius may be correctly obtained, it seems as if the contact-mechanical information dealing with the stress is lost. In reality, however, this is not the case. In the aforementioned dissertation by Heß [3], it was shown that the stress distribution for an arbitrary three-dimensional contact is able to be reproduced for a corresponding one-dimensional problem. The required derivations can be found in Chap. 17. In the present chapter, we will explain the rules for the calculation without the necessary evidence.

For the linearly elastic foundation, the spring forces $f_N(x)$ are directly given for every contact configuration. The distributed load $q(x)$ (or linear force density) is also able to be directly defined:

$$q(x) = \frac{f_N(x)}{\Delta x}. \tag{3.36}$$

Among others properties, it will be shown in Chap. 17 that the normal stress $\sigma_{zz}(r)$ in the contact area of a three-dimensional contact problem may be found from the distributed load $q(x)$ using the following integral transformation (the Abel transformation):

$$\sigma_{zz}(r) = \frac{1}{\pi}\int\limits_r^\infty \frac{q'(x)}{\sqrt{x^2 - r^2}}\mathrm{d}x. \tag{3.37}$$

As an example of the application of this procedure, we once again consider the Hertzian contact problem. For the distributed load, it follows from (3.9) that

$$\begin{aligned} &q(x) = E^*\left(d - \tfrac{x^2}{2R_1}\right), && \text{for} \quad |x| < a = \sqrt{2R_1 d}. \\ &q(x) = 0, && \text{for} \quad |x| > a = \sqrt{2R_1 d} \end{aligned} \tag{3.38}$$

The derivative is $q'(x) = -E^* x/R_1$ within the contact area and zero outside of it. Insertion into (3.37) leads to

$$\sigma_{zz}(r) = -\frac{E^*}{\pi R_1}\int\limits_r^\infty \frac{x\mathrm{d}x}{\sqrt{x^2 - r^2}} = -\frac{E^*}{\pi R_1}\int\limits_r^a \frac{x\mathrm{d}x}{\sqrt{x^2 - r^2}} = -\frac{2}{\pi}E^*\left(\frac{d}{R}\right)^{1/2}\sqrt{1 - \left(\frac{r}{a}\right)^2}, \tag{3.39}$$

which corresponds exactly with the known Herzian solution.

Further examples to the calculation of the stress in axially-symmetric contacts according to Eq. (3.37) will be considered in the exercises at the end of this chapter.

3.5 The Mapping of Non-Axially-Symmetric Bodies

The equation for contact stiffness written in the form

$$k_z = 2E^*\beta\sqrt{\frac{A}{\pi}} \tag{3.40}$$

is also valid for non-circular cross-sections (A is the contact area). The constant β is always on the order of magnitude of 1 for "simple" profiles (see [7]):

$$\begin{array}{ll} \text{circular cross-section:} & \beta = 1.000 \\ \text{triangular cross-section:} & \beta = 1.034 \\ \text{square cross-section:} & \beta = 1.012 \end{array} \tag{3.41}$$

Equation (3.40) can be written in the form (3.1), if we define the effective diameter D as

$$D = 2\beta\sqrt{\frac{A}{\pi}}. \tag{3.42}$$

This rule allows for non-axially symmetric contacts to be mapped to a one-dimensional contact with a linearly elastic foundation.

3.6 Problems

Problem 1 Solve the problem of the contact between a cone and an elastic half-space (Fig. 3.6a) using the reduction method. Calculate the contact radius and the normal force as a function of the indentation depth.

Solution The form of the cone is described by the equation $f(r) = \tan\theta \cdot r$. The corresponding scaling factor has the value $\kappa_1 = \pi/2$, so that the one-dimensional profile is given by $g(x) = (\pi/2)\tan\theta \cdot |x|$. If the indenter is pressed to a depth of d, then the vertical displacement of the foundation at point x is given by $u_z(x) = d - (\pi/2)\tan\theta \cdot |x|$. We calculate the contact radius by demanding that $u_z(a) = 0$ and in this way, obtain the desired dependence on the indentation depth:

$$a = \frac{2}{\pi}\frac{d}{\tan\theta}. \tag{3.43}$$

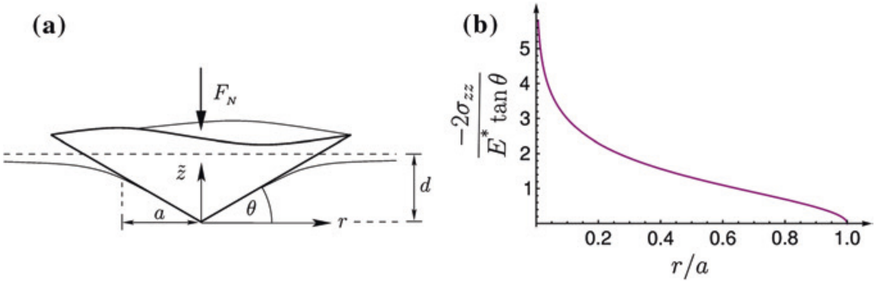

Fig. 3.6 (**a**) Contact between a rigid conical indenter and an elastic half-space. (**b**) Pressure distribution for the normal contact between a conical indenter and an elastic half-space

The normal force is obtained by "summing the spring forces":

$$F_N = 2E^* \int_0^a u_z(x)\mathrm{d}x = 2E^* \int_0^a (d - (\pi/2)\tan\theta \cdot x)\mathrm{d}x = \frac{2}{\pi} E^* \frac{d^2}{\tan\theta}. \quad (3.44)$$

Both results correspond *exactly*, of course, with those of the three-dimensional contact problem [8].

Problem 2 Let the profile $f(r) = C \cdot r^n$ be given for a rigid axially-symmetric indenter that is pressed into an elastic half-space. Determine the contact radius and the normal force in dependence on the indentation depth by using the reduction method.

Solution The equivalent one-dimensional profile is $g(x) = C\kappa_n|x|^n$. The contact radius is calculated from the condition $g(a) = d$ as

$$a = \left(\frac{d}{C\kappa_n}\right)^{1/n}. \quad (3.45)$$

The displacement field is determined by $u_z(x) = d - C\kappa_n|x|^n$ and for the normal force, we obtain

$$F_N = 2E^* \int_0^a u_z(x)\mathrm{d}x = 2E^* \int_0^a \left(d - C\kappa_n x^n\right)\mathrm{d}x = \frac{2n}{n+1} \frac{E^* d^{\frac{n+1}{n}}}{(C\kappa_n)^{1/n}}. \quad (3.46)$$

Once again, the results provide the *exact* dependencies of the three-dimensional problem (see Chap. 17).

Problem 3 Analyze the contact between a half-space and a superimposed profile of the form $f(r) = \frac{r^2}{2R} + |r|\tan\theta$ using the reduction method. Determine the contact radius and the normal force with respect to indentation depth.

Solution The equivalent one-dimensional profile is

$$g(x) = \kappa_2 \frac{x^2}{2R} + \kappa_1 |x| \tan\theta = \frac{x^2}{R} + \frac{\pi}{2}|x|\tan\theta. \quad (3.47)$$

The contact radius is determined using the condition

$$g(a) = \frac{a^2}{R} + \frac{\pi}{2} a \tan\theta = d, \quad (3.48)$$

so that the following relationship between the contact radius and displacement results:

$$a = \sqrt{\left(\frac{\pi}{4} R \tan\theta\right)^2 + Rd} - \frac{\pi}{4} R \tan\theta. \quad (3.49)$$

The one-dimensional displacement field is given by $u_z(x) = d - \frac{x^2}{R} - \frac{\pi}{2}|x|\tan\theta$, where we obtain the equation

$$F_N = 2E^* \int_0^a u_z(x)\mathrm{d}x = 2E^* \int_0^a \left(d - \frac{x^2}{R} - \frac{\pi}{2}|x|\tan\theta \right)\mathrm{d}x \tag{3.50}$$

for the normal force, which leads to the following equation after integration:

$$F_N = 2E^* \left(da - \frac{a^3}{3R} - \frac{\pi}{4}a^2 \tan\theta \right). \tag{3.51}$$

Insertion of (3.49) and simple rearrangement with respect to the desired relationship between normal force and indentation depth leads to

$$\begin{aligned} F_N = \frac{\pi^3 R^2 (\tan\theta)^3 E^*}{96} &\left(\sqrt{1 + \frac{16d}{\pi^2 R (\tan\theta)^2}} - 1 \right) \\ &\left(1 + \frac{32d}{R\pi^2 (\tan\theta)^2} - \sqrt{1 + \frac{16d}{\pi^2 R (\tan\theta)^2}} \right). \end{aligned} \tag{3.52}$$

Problem 4 Calculate the stress distribution between a flat cylindrical indenter and an elastic half-space with the help of the Abel transformation.

Solution We begin by calculating the distributed load in the one-dimensional case. For a flat cylindrical indenter, the distributed load is constant and equal to

$$q(x) = \begin{cases} F_N/(2a), & \text{for } |x| < a \\ 0, & \text{for } |x| > a \end{cases}. \tag{3.53}$$

We obtain the derivative

$$q'(x) = \frac{F_N}{2a}(\delta(x+a) - \delta(x-a)), \tag{3.54}$$

where $\delta(x)$ denotes the Dirac delta function. The integral (3.37) takes the form

$$\sigma_{zz}(r) = \frac{1}{\pi} \int_r^\infty \frac{q'(x)}{\sqrt{x^2 - r^2}}\mathrm{d}x = \frac{1}{\pi}\frac{F_N}{2a} \int_r^\infty \frac{(\delta(x+a) - \delta(x-a))}{\sqrt{x^2 - r^2}}\mathrm{d}x. \tag{3.55}$$

For the Dirac delta function equation $\int f(x)\delta(x-a)\mathrm{d}x = f(a)$ is valid if the integration area contains the point $x = a$ and is otherwise zero. Thus, the integration in (3.55) results in

$$\sigma_{zz}(r) = \frac{1}{\pi}\frac{F_N}{2a} = \begin{cases} -\frac{1}{\sqrt{a^2 - r^2}}, & \text{for } |r| < a \\ 0, & \text{for } |r| > a \end{cases}. \tag{3.56}$$

This is the *exact* stress distribution that exists in the three-dimensional contact between a rigid flat cylindrical indenter and an elastic half-space [1].

Problem 5 Calculate the stress distribution in a contact between a rigid cone and an elastic half-space with the help of the Abel transformation.

Solution We consider the equivalent one-dimensional model from Problem 1. The vertical displacement of the foundation at the point x is $u_z(x) = d - (\pi/2)\tan\theta \cdot |x|$, from which we obtain the distributed load $q(x) = E^* \cdot u_z(x) = E^*(d - (\pi/2)\tan\theta \cdot |x|)$. In order to calculate the normal stress, we insert the derivative $q'(x) = -(\pi/2)E^*\tan\theta \cdot \operatorname{sign}(x)$ into Eq. (3.37)

$$\sigma_{zz}(r) = \frac{1}{\pi}\int_r^\infty \frac{q'(x)}{\sqrt{x^2 - r^2}}\mathrm{d}x = -\frac{1}{2}E^*\tan\theta \int_r^a \frac{\mathrm{d}x}{\sqrt{x^2 - r^2}}. \tag{3.57}$$

Taking the integral results in

$$\sigma_{zz}(r) = \begin{cases} -\frac{1}{2}E^*\tan\theta \cdot \ln\left(\frac{a}{r} + \sqrt{\left(\frac{a}{r}\right)^2 - 1}\right), & \text{for } r < a \\ 0, & \text{for } r > a \end{cases}, \tag{3.58}$$

which is, of course, also in this case the *exact* three-dimensional stress distribution. This is shown graphically in Fig. 3.6b.

Problem 6 Determine the normal force and normal stress for the contact between a rigid cylindrical indenter and a concave, parabolic profile (see Fig. 3.7) with the help of the reduction method. Instead of using the indentation depth d, the displacement should be formulated based on the geometric values of d_o and h. It is assumed that a complete contact is present.

Solution First, we define the surface displacement within the contact area for the axially-symmetric contact. For this, we use the average displacement d_o in place of

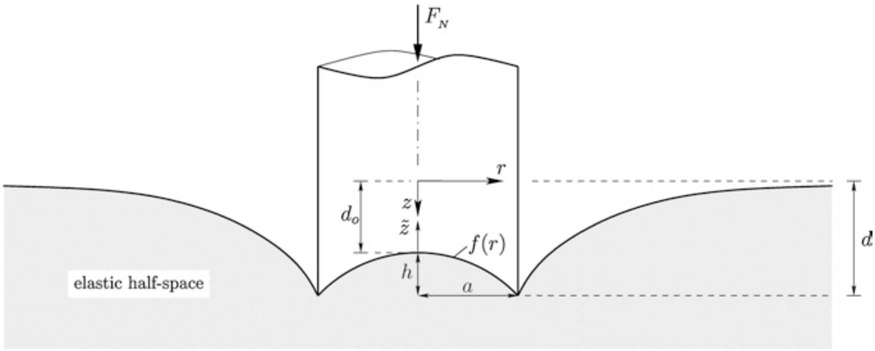

Fig. 3.7 Qualitative presentation of a (complete) indentation of a rigid cylindrical indenter with a concave, parabolic profile into an elastic half-space

the indentation depth d, so that $f(0) = 0$ is guaranteed for the concave profile in the same way as for the convex profile. Then, the following is valid:

$$u_z(r) = d_o - f(r) = d_o + \frac{h}{a^2} r^2. \tag{3.59}$$

The original profile contains a quadratic term, which we must simply multiply with the corresponding scaling factor in order to arrive at the geometry of the equivalent system:

$$g(x) = \kappa_2 f(|x|) = -2\frac{h}{a^2} x^2. \tag{3.60}$$

From the corresponding surface displacement in the one-dimensional model, we obtain a normal force of

$$F_N = 2E^* \int_0^a \left[d_o - g(x)\right] \mathrm{d}x = 2E^* \int_0^a \left(d_o + 2\frac{h}{a^2} x^2\right) \mathrm{d}x = 2E^* a\left(d_o + \frac{2}{3}h\right). \tag{3.61}$$

In order to calculate the normal stress in the original contact, we require the derivative of the distributed load $q'(x)$ in the reduced dimensions as well as the boundary condition $q(a)$:

$$q(x) = E^*\left(d_o + 2\frac{h}{a^2} x^2\right) \quad \Rightarrow \quad q'(x) = 4E^* \frac{h}{a^2} x \text{ and } q(a) = E^*(d_o + 2h). \tag{3.62}$$

Insertion of (3.62) into (3.37) leads to the desired normal stresses after integration and elementary rearrangement:

$$\sigma_{zz}(r) = -\frac{E^*}{\pi} \cdot \frac{d_o - 2h + 4h\left(\frac{r}{a}\right)^2}{\sqrt{a^2 - r^2}}. \tag{3.63}$$

Naturally, the results (3.61) and (3.63) correspond exactly to those of the three-dimensional, axially-symmetric contact, which is confirmed by comparison with the results given by Barber [9], if one takes into account the conversion $d_o = d - h$. Let it be once again insistently pointed out that a complete contact is assumed, which must satisfy the requirement of $\sigma_{zz}(0) \leq 0$. Then, from Eq. (3.63), the condition $d_o \geq 2h$ follows. Due to the fact that the reduction method in the form shown here is only suitable for the mapping of complete contacts (and not ring-shaped contact areas), this condition does not follow directly from the one-dimensional model. Furthermore, the exact mapping is only guaranteed for $F_N(d_o)$ and not for $F_N(d)$, because the maximum displacement (indentation depth) for concave profiles occurs on the boundary and not in the middle.

Problem 7 Formulate the method of dimensionality reduction for a transversally-isotropic medium.

Solution A transversally-isotropic medium is a medium that is isotropic in one plane. For crystalline bodies, this includes bodies in the hexagonal class of crystals. Also, a fiber composite with all fibers oriented in parallel is a transversally-isotropic medium. A linearly transversally-isotropic medium can be completely defined by 5 elastic moduli. If we denote the axis of symmetry to be "3," then the axes "1" and "2" are "equivalent" and can be chosen arbitrarily within the plane which they define. Hooke's law for such a medium is as follows:

$$\begin{aligned}
\sigma_{11} &= C_{11}\varepsilon_{11} + C_{12}\varepsilon_{22} + C_{13}\varepsilon_{33} \\
\sigma_{22} &= C_{12}\varepsilon_{11} + C_{11}\varepsilon_{22} + C_{13}\varepsilon_{33} \\
\sigma_{33} &= C_{13}(\varepsilon_{11} + \varepsilon_{22}) + C_{33}\varepsilon_{33} \\
\sigma_{12} &= (C_{11} - C_{12})\varepsilon_{12} \\
\sigma_{23} &= 2C_{44}\varepsilon_{23} \\
\sigma_{31} &= 2C_{44}\varepsilon_{31}\,.
\end{aligned} \tag{3.64}$$

The applicability of the method of dimensionality reduction is based solely on the fact that the differential stiffness of a medium is determined exclusively by the current contact area. For axially-symmetric profiles, it is given by the stiffness of the contact between a flat, rigid cylindrical indenter and the elastic half-space. Therefore, the rule for the application of the method of dimensional reduction to an arbitrary linearly elastic medium is as follows: First, the stiffness k_z of the contact with a flat cylindrical indenter with the diameter D and the equivalent one-dimensional system as a linearly elastic foundation with a stiffness per unit length of k_z/D are determined. This method can be applied to any medium for which a solution with a rigid cylinder is known.

The solution for the stiffness of a contact between a flat, cylindrical indenter and a transversally-isotropic medium (with an axis of symmetry parallel to the normal vector) can be directly taken from the work of Yu [10]. It is given by Eq. (3.1) with

$$E^* = \frac{2\left(\bar{C}_{13}^2 - C_{13}^2\right)}{\bar{C}_{13}(\nu_1 + \nu_2)}, \tag{3.65}$$

where the following relationships are introduced:

$$\nu_1 = \left[\frac{\left(\bar{C}_{13} - C_{13}\right)\left(2\bar{C}_{13} - I_0\right)}{4C_{33}C_{44}}\right]^{1/2} + \left[\frac{\left(\bar{C}_{13} + C_{13}\right)I_0}{4C_{33}C_{44}}\right]^{1/2} \tag{3.66}$$

$$\nu_2 = \left[\frac{\left(\bar{C}_{13} - C_{13}\right)\left(2\bar{C}_{13} - I_0\right)}{4C_{33}C_{44}}\right]^{1/2} - \left[\frac{\left(\bar{C}_{13} + C_{13}\right)I_0}{4C_{33}C_{44}}\right]^{1/2} \tag{3.67}$$

$$\bar{C}_{13} = (C_{11}C_{33})^{1/2} \tag{3.68}$$

$$I_0 = \bar{C}_{13} - C_{13} - 2C_{44}. \tag{3.69}$$

Insertion of (3.66)–(3.69) into (3.65) results in

$$E^* = \frac{2\sqrt{C_{44}}\left(C_{11}C_{33} - C_{13}^2\right)}{\sqrt{C_{11}}\sqrt{\left(\sqrt{C_{11}C_{33}} - C_{13}\right)\left(C_{13} + 2C_{44} + \sqrt{C_{11}C_{33}}\right)}}. \tag{3.70}$$

Problem 8 Determine the indentation depth and the normal force as a function of contact radius for the normal contact between a sphere of radius R and a linearly elastic half-space with the help of the reduction method. Contrary to the parabolic approximation of Hertz, here the exact spherical form should be taken into account and the equivalent profile should be calculated with the general Eq. (3.27).

Solution The exact profile of a sphere with a radius of R is given by the function

$$f(r) = R - \sqrt{R^2 - r^2}. \tag{3.71}$$

The first derivative of (3.71) is

$$f'(r) = \frac{r}{\sqrt{R^2 - r^2}}. \tag{3.72}$$

Inserting (3.72) into the general formula (3.27) leads to the equation

$$g(x) = x \int_0^x \frac{r}{\sqrt{R^2 - r^2} \cdot \sqrt{x^2 - r^2}} \mathrm{d}r = -x \int_{z(0)}^{0} \frac{\mathrm{d}z}{\sqrt{1 + z^2}}, \tag{3.73}$$

for which the elementary integral on the right results by using the substitution $z(r) = \dfrac{\sqrt{x^2 - r^2}}{\sqrt{R^2 - x^2}}$. The equivalent profile is

$$g(x) = x \cdot \operatorname{arsinh}\left(\frac{x}{\sqrt{R^2 - x^2}}\right) = \frac{1}{2} x \ln\left(\frac{R + x}{R - x}\right). \tag{3.74}$$

Figure 3.8 shows both of the “equivalent” profiles as well as their parabolic approximations. The dashed lines confirm the rule of Popov.

Simultaneously, the surface displacement of the linearly elastic foundation may be found with (3.74), which must tend to zero at the contact boundary and in this way, determines the indentation depth:

$$u_z(a) = 0 \quad \Rightarrow \quad d = g(a) = \frac{1}{2} a \ln\left(\frac{R + a}{R - a}\right). \tag{3.75}$$

The spring forces, which are proportional to the surface displacement, must be in equilibrium with the normal force

$$F_N = E^* \int_{-a}^{a} \left[d - g(x)\right] \mathrm{d}x = 2E^* da - E^* \int_0^a x \ln\left(\frac{R + x}{R - x}\right) \mathrm{d}x. \tag{3.76}$$

Fig. 3.8 Exact spherical form and parabolic approximation (Hertz) including the one-dimensional equivalents

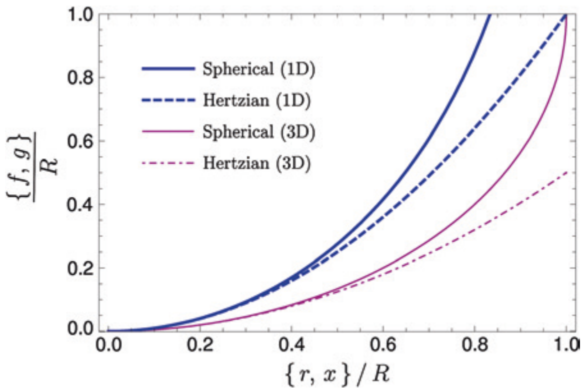

A suitable partial integration initially provides

$$F_N = 2E^*a\left[d - \frac{R}{2} + \frac{R^2 - a^2}{4a}\ln\left(\frac{R+a}{R-a}\right)\right] \tag{3.77}$$

and after insertion of (3.75), the contact force is finally obtained as a function of contact radius:

$$F_N(a) = E^*\frac{R^2 + a^2}{2}\ln\left(\frac{R+a}{R-a}\right) - E^*Ra. \tag{3.78}$$

The indentation depth from (3.75) and the normal force from (3.78) correspond exactly to the three-dimensional contacts based on the solutions of Segedin [11], which are obtained using the Area-functions. Finally, let it be known that we could have just as well developed the spherical profile as a series. After multiplying the individual terms with the corresponding scaling factor, according to the rules of Heß, the equivalent profile (3.74) would have been given in the form of a power series. If the integral for the general formula (3.27) is not known, we have, in fact, no choice but to use this strategy.

References

1. K.L. Johnson, *Contact Mechanics*, Nachdruck der 1. Auflage (s.l.: Cambridge University Press, Cambridge, 2001), p. 6
2. V.L. Popov, S.G. Psakhie, Numerical simulation methods in tribology. Tribol. Int. **40**(6), 916–923 (2007)
3. M. Heß, *Über die exakte Abbildung ausgewählter dreidimensionaler Kontakte auf Systeme mit niedrigerer räumlicher Dimension* (Cuvillier, Berlin, 2011)
4. G.M. Pharr, W.C. Oliver, F.R. Brotzen, On the generality of the relationship among contact stiffness, contact area, and elastic modulus during indentation. J. Mater. Res. **7**(3), 613–617 (1992)

5. V.L. Popov, Contact Mechanics and Friction. Physical Principles and Applications (Springer, Berlin Heidelberg 2010), pp. 69–70.
6. U.B.C.O. Ejike, The stress on an elastic half-space due to sectionally smooth-ended punch. J. Elast. **11**(4), 395–402 (1981)
7. R.B. King, Elastic analysis of some punch problems for a layered medium. Int. J. Solids Struct. **23**(12), 1657–1664 (1987)
8. A.E.H. Love, Boussinesq's problem for a rigid cone. Q. J. Math. **10**, 161–175 (1939)
9. J.R. Barber, Indentation of the semi-infinite elastic solid by a concave rigid punch. J. Elast. **6**(2), 149–159 (1976)
10. H.Y.A. Yu, Concise treatment of indentation problems in transversely isotropic half-spaces. Int. J. Solids Struct. **38**(10), 2213–2232 (2001)
11. C.M. Segedin, The relation between load and penetration for a spherical punch. Mathematika **4**, 156–161 (1957)

Chapter 4
Normal Contact with Adhesion

Markus Heß and Valentin L. Popov

4.1 Introduction

The miniaturization of components and the manufacturing of ever smoother surfaces are a mark of the constant improvements in micro and nano-technologies today. For the length scales associated herewith, the adhesion forces must be doubtlessly taken into account. However, adhesion is also important for contacts in which one partner is composed of a very soft material. Above all, the adhesion between rough surfaces is a central research topic in this respect, as it deals with the friction of rubbers and the contact between biological structures.

From a theoretical point of view, one can name two main ansätze which were developed in order to describe adhesive contacts for *elastic*, parabolic bodies. The first is the theory of Johnson et al. [1] (JKR theory), which takes adhesion forces within the contact area into account. In this case, the contact radius in the equilibrium state is calculated from the minimum in the total energy, which in turn, is obtained from the elastic deformation energy, the potential of external forces, and the surface energy of the contacting bodies. On the other hand, in the theory developed by Derjagin et al. [2] (DMT theory), the molecular forces of attraction act only within a ring outside of the contact area. They naturally contribute to the normal force, however, it is assumed that they cause no deformation. Within the framework of DMT theory, the maximum magnitude of the adhesion force corresponds to that which Bradley derived in 1932 [3] for the adhesive contact between rigid spheres. Because the JKR theory diverges from the DMT theory, it appears at first that the two theories contradict each other. Tabor [4] was able to successfully explain this discrepancy by investigating the areas of validity of both theories in greater detail and defining them based on a dimensionless parameter. According to his findings, DMT theory is suitable for describing the contact of small, rigid spheres, while JKR theory is more adept at describing large, soft spheres. Johnson and Greenwood [5] created a map of adhesion, which graphically depicts the areas

V.L. Popov and M. Heß, *Method of Dimensionality Reduction in Contact Mechanics and Friction*, DOI 10.1007/978-3-642-53876-6_4

of validity for various adhesion theories. Furthermore, they pointed out the fact that the JKR theory still provides good results outside of its actual area of validity. It is possible that this is the reason that the JKR theory is primarily used to describe adhesion.

In this chapter, we will discuss how the leading adhesion theory from Johnson, Kendall, and Roberts is able to be exactly mapped using the method of dimensionality reduction. To begin, we will concentrate on a pure formulation of the simple rules of application for the adhesive normal contact and refrain from presenting the required evidence. Subsequently, these rules will be explained in more detail, which requires a certain understanding of the theoretical background on the adhesion in three-dimensional contacts, which we will also provide. For those not satisfied with these short explanations, the entirety of the necessary evidence may be found in Chap. 17.

4.2 Rule of Heß for the Adhesive Contact Between Axially-Symmetric Bodies

Adhesive contacts of axially-symmetric bodies can also be exactly mapped to a one-dimensional equivalent model. The rule for this mapping was developed by one of the authors (Heß) [6]. It is based on the basic idea of Johnson, Kendall, and Roberts that *the contact with adhesion arises from the contact without adhesion plus a rigid-body translation*. Because both parts of the contact problem can be mapped to a one-dimensional equivalent model with a modified geometry, then this is true of the entire problem. The rule of Heß is as follows: If an indenter with the modified form described in Chap. 3 is initially pressed into a linearly elastic foundation and then pulled out, as shown in Fig. 4.1, then the springs on the edge of the profile will detach upon reaching a critical length

$$\Delta\ell_{\max}(a) = \sqrt{\frac{2\pi a\,\Delta\gamma}{E^*}}, \tag{4.1}$$

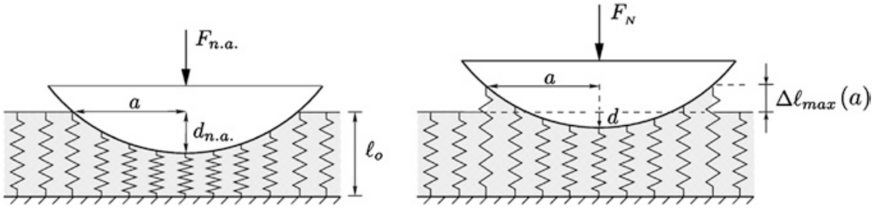

Fig. 4.1 Qualitative presentation of the indentation and separation process for the reduction method. The model shown exactly maps the adhesive contact of parabolic bodies and therefore, exactly mirrors JKR theory

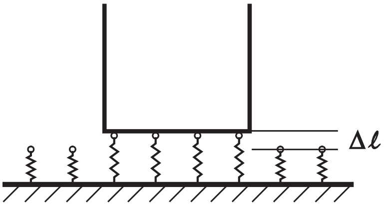

Fig. 4.2 Equivalent one-dimensional system for the adhesive contact between a flat, cylindrical indenter and an elastic half-space

where $\Delta\gamma$ is the separation energy of the bodies per unit area, which will be explained later in more detail. Here, it is worth noting that the separation criterion is not local, due to its dependence on the changing contact radius.

In order to illustrate the simple application of this rule, we will consider the adhesive contact between a flat, cylindrical indenter with the radius a and an elastic half-space (Fig. 4.2).

In this case, all springs will simultaneously detach as soon as the critical length (4.1) is reached. The total normal force required to separate the indenter from the substrate is then

$$F_A = 2E^*a\sqrt{\frac{2\pi a\,\Delta\gamma}{E^*}} = \sqrt{8\pi a^3 E^* \Delta\gamma}, \tag{4.2}$$

which corresponds exactly to the three-dimensional result [7]. For the problems at the end of this chapter, we will consider this type of contact problem once again by supplementing the general structure with relevant alterations. There, as well as in Sects. 4.4 and 4.5, there are numerous examples provided. However, before we proceed with these examples, we would like to explain the theoretical considerations that lead to Rule (4.1) in more detail. This is done primarily in Sect. 4.4, which contains further simple rules which help to determine the normal stress and the stability of the system. In this way, critical quantities can be determined very simply. We begin the theoretical consideration with the compatibility of the JKR theory with the ansätze from linear fracture mechanics. Those only interested in the practical application of the method of dimensionality reduction to adhesive contacts may continue directly with Sect. 4.4.

4.3 The Adhesive Contact and Griffith Crack

In the theory of Johnson, Kendall, and Roberts, the contact radius of an adhesive contact arises from the minimum total energy, which consists of the elastic deformation energy U_E, the potential of external forces U_P, and the surface energy U_S. In the original publication [1], it was already indicated that this energy ansatz is the same as that of Griffith [8, 9], which was once used to investigate fractures in

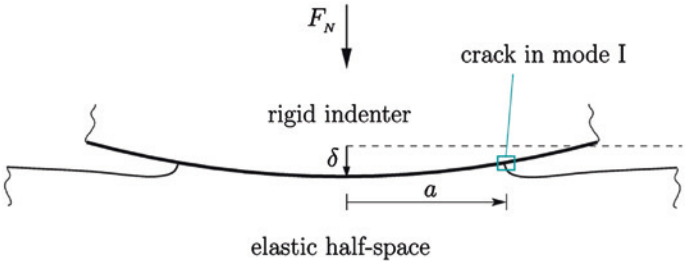

Fig. 4.3 Qualitative presentation of an adhesive contact between a rigid, curved body and an elastic half-space; the boundary of the contact can be referred to as the crack tip

brittle material[1] and is nothing more than the first law of thermodynamics. Maugis et al. [10, 11] conducted more penetrating thermodynamic considerations and proved, among other things, the compatibility of the JKR theory with that of linearly elastic fracture mechanics. The free boundary of the adhesive contact may, therefore, be referred to as a mode I crack,[2] which propagates either inwards or outwards based on changes in the contact surface. The decisive steps for the energy ansatz are very quickly explained. For this, we consider the adhesive contact between a rigid, curved body and an elastic half-space, according to Fig. 4.3. The indenter is loaded by an external force of F_N and, with the half-space, forms a contact area with a radius of a; in order to avoid confusion with differentials, the indentation depth will be denoted by δ in this section.

Initially, we assume that the indentation depth δ and the contact area A which describe the equilibrium state of the system are extensive properties. According to the first law of thermodynamics, a contribution of work from the external load, causes a change in the sum of the elastic deformation energy U_E and the surface energy U_S:

$$\mathrm{d}U_E(A,\delta) + \mathrm{d}U_S(A) = F_N(A,\delta)\mathrm{d}\delta. \tag{4.3}$$

The surface energy is not dependent on the indentation depth and is given by

$$U_S(A) = -\Delta\gamma \cdot A. \tag{4.4}$$

Here, $\Delta\gamma$ is the work that must be done per unit area against interatomic forces in order to separate the two solids, which is also known under the name of the Dupré energy of adhesion. It is dependent on the (specific) surface energies γ_1 and γ_2 of both bodies as well as the energy of the interface γ_{12}:

$$\Delta\gamma := \gamma_1 + \gamma_2 - \gamma_{12} \tag{4.5}$$

---

[1] More specifically, Griffith investigated the stability of a crack in the middle of a disc loaded in tension.

[2] The opening mode (mode I crack) is the separation mode for which the tensile stress acts *perpendicular* to the plane of the crack.

and can be interpreted as the "effective" interface energy. Insertion of (4.4) into (4.3) results in

$$\mathrm{d}U_E(A,\delta) - \Delta\gamma \cdot \mathrm{d}A = F_N(A,\delta)\ \mathrm{d}\delta. \tag{4.6}$$

By means of the Legèndre transformation, we can switch the independent extensive variables δ and F_N. In this way, we obtain

$$-\mathrm{d}U_E^K(A,F_N) - \Delta\gamma \cdot \mathrm{d}A = -\delta(A,F_N)\ \mathrm{d}F_N \quad \text{with} \quad U_E^K := F_N\delta - U_E, \tag{4.7}$$

in which U_E^K stands for the complementary elastic energy. By separating the total derivatives with respect to the corresponding variables, we obtain the laws of Castigliano and Engesser:

$$\left(\frac{\partial U_E}{\partial \delta}\right)_A = F_N \ \text{ or } \ \left(\frac{\partial U_E^K}{\partial F_N}\right)_A = \delta\,. \tag{4.8}$$

Furthermore, we now have two different possibilities for calculating the elastic energy release rate $\mathcal{G}$:

$$\mathcal{G} := \left(\frac{\partial U_E}{\partial A}\right)_\delta = -\left(\frac{\partial U_E^K}{\partial A}\right)_{F_N}. \tag{4.9}$$

In equilibrium, the mechanical energy released by a decrease in contact area must correspond to the energy required to form the new surface:

$$\mathcal{G} = \Delta\gamma =: \mathcal{G}_c. \tag{4.10}$$

Equation (4.10) once again provides the energetic fracture criterion of Griffith. Here, the effective interface energy $\Delta\gamma$ can be interpreted as the critical energy release rate $\mathcal{G}_c$ at which quasi-static fracture progression begins. The difference $\mathcal{G} - \Delta\gamma$ is occasionally called the *driving force* (with the units of linear force density) for the tip of the fracture and allows for the kinetic adhesive process to be investigated.

The energetic fracture criterion from Griffith in the form of (4.10) contains the energy release rate as a parameter and, as a result, is seen as a *global* fracture criterion. An equivalent criterion, and for our purposes more appropriate due to its *local* characteristic, is found using the concept of stress intensity. Irwin [12] recognized the fundamental fact that the singularities of all stress fields for all fracture types are similar in the fracture near field, and therefore, used their intensities for the investigation of fracture mechanics. The ligament stresses and the displacements which exist, for example, in the near field of the fracture shown in Fig. 4.4 with the separation mode I are

$$\sigma_{zz}(\eta,\beta=0) = \tfrac{K_I}{\sqrt{2\pi\eta}} \ \text{ and } \ u_z(\eta,\beta=\pm\pi) = \pm\tfrac{2}{E^*}K_I\sqrt{\tfrac{\eta}{2\pi}}\,. \tag{4.11}$$

Fig. 4.4 Qualitative presentation of the ligament stress and the opening form of a mode I crack

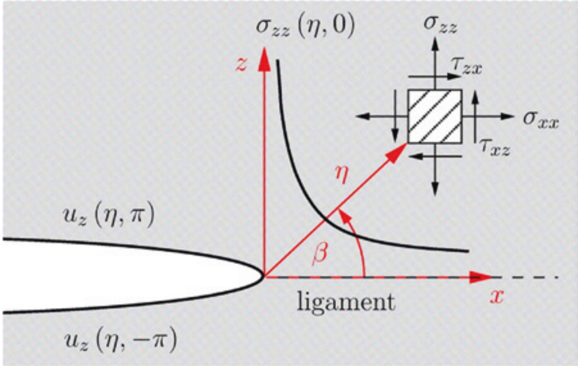

The stress intensity factor K_I, which is dependent on the material as well as the geometry, length, and loading of the fracture, can be obtained if the ligament stress is known:

$$K_I := \lim_{\eta \to 0} \sqrt{2\pi\eta}\, \sigma_{zz}(\eta, 0). \tag{4.12}$$

According to Irwin, fracture propagation occurs only after K_I reaches the so-called fracture toughness K_{Ic} of the material, which must, in turn, be determined experimentally on standardized fracture experiments. Therefore, the *local* fracture criterion from Irwin for a mode I crack is

$$K_I = K_{Ic}. \tag{4.13}$$

Of course, no real material can withstand the (theoretically) infinitely large stress. Except for very brittle materials, a relaxation in stress occurs in the area near the fracture tip due to inelastic deformation. Furthermore, regardless of the material, a small zone always exists in which non-linear microscopic processes occur. As long as the combination of the plastic and microscopic zones is much smaller than the zone in which K_I dominates, the elastic near field will control the processes occurring in this field, allowing the use of the concept of stress intensity. The fact that the K concept and the fracture criterion from Griffith are equivalent was proven by Irwin for which he calculated the work required to close a fracture of length Δa[3]:

$$\mathcal{G} = \frac{K_I^2}{2E^*}. \tag{4.14}$$

Equation (4.14) is for a mode I crack. If a combined fracture load is present for which all three separation modes occur, then the individual energy release rates

---

[3] The equation is based on a fracture in a planar state of deformation; we may assume that locally in an axially-symmetric contact with adhesion, every point on the contact boundary exhibits this state.

must be summed. In the case of a fracture interface between two elastically similar materials, the following is then valid:

$$\mathcal{G} = \frac{1}{2E^*}\left(K_I^2 + K_{II}^2\right) + \frac{1}{4}\left(\frac{1}{G_1} + \frac{1}{G_2}\right)K_{III}^2. \tag{4.15}$$

With the help of this generalized presentation, the interaction between adhesion and friction can be determined [13].

It may have been the equivalence of the concepts of the fracture mechanism that motivated Maugis and Barquins [14, 15] to use Sneddons theory [16] for the mapping of adhesive contacts; the analogy between JKR theory and the Griffith theory of fracture mechanics was already proven at this time. Thus, the concept of the stress intensity factor must also exist in Sneddons theory. The original equations from Sneddon contain a (still arbitrary) rigid body translation, which is responsible for a singularity in the stress at the contact boundary. The translation is that which results from pressing a flat cylindrical indenter into a half-space and corresponds to that of the initial approximation for a mode I crack. Furthermore, the difference in the normal displacement between the indenter and surface of the half-space outside of the contact area is the same as the shape of the fracture in Eq. (4.11), so that a connection exists between the rigid body degree of freedom and the intensity factor. For contacts without adhesion, with the assumption that the profile is convex, the Boussinesq condition must be met, meaning that the singularity at the contact boundary disappears. The only difference between the two theories is the rigid body translation. This causes a tensile stress for which the distribution is the same as that under a flat cylindrical indenter. This is an essential relationship, which we would like to stress:

> *The contact with adhesion results from the contact without adhesion plus a rigid body translation.*

Even the original theory of Johnson, Kendall, and Roberts touches on this principle, which extends the Hertzian contact by adding adhesion. This theory was discussed in a generalized form at the beginning of this chapter. It requires, among other things, that the energy of the elastic deformation be known, which in turn, can be determined in two parts. One of these comes from the non-adhesive indentation process, while the other results from the decompression at a constant contact area. Figure 4.5 explains the superposition of the two loading cases. The indentation process with a force $F_{n.a.}$ occurs without adhesion, so that the resulting stresses and surface displacements are for a Hertzian contact. Due to the successive increase in the relative interface energy, the subsequent unloading from $F_{n.a.}$ to F_N occurs for a constant contact area. Because of this, all points in the contact area must undergo a constant displacement. Therefore, the unloading is the same as for the contact with a flat indenter, the characteristic stress distribution for which is responsible for the infinitely large tensile stress at the contact boundary.

This singularity can be seen in Fig. 4.5b, the stresses for which are shown with respect to their mean in the non-adhesive contact. Interestingly, Johnson [17] had already recognized the ability to use superposition to describe a contact with adhesion in 1958. The non-physical excess in stress on the boundary, however, led him

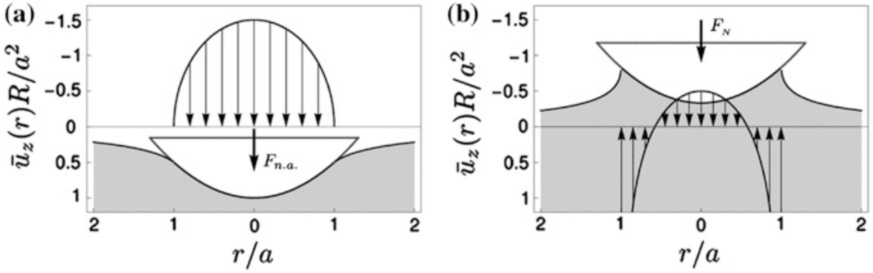

Fig. 4.5 **a** Hertzian spherical contact caused by the normal force $F_{n.a.}$, which leads to the same contact radius as in the adhesive case under the load of F_N; **b** Equilibrium state of the adhesive contact; more exactly, the critical state under a *fixed-load* condition is actually shown here

to *rule out* adhesion, which was in accord with the experimental works of Bowden and Tabor at the time.

4.4 Full Reduction of the Adhesive, Elastic Contact

The central notion of the exact mapping of axially-symmetric contacts with adhesion is the superposition concept described in the last section. According to this, the contact without adhesion must merely be superimposed with a rigid body translation. This means that the normal stress distribution in the contact area is

$$\sigma_{zz}(r) = \sigma_{n.a.}(r) + \frac{\Delta F}{2\pi a\sqrt{a^2 - r^2}} \quad \text{with} \quad \Delta F := F_{n.a.} - F_N = 2E^* a(d_{n.a.} - d), \tag{4.16}$$

where the second term is the stress distribution under a flat indenter described by Boussinesq. Remember that the values with the index “n.a.” are those for a contact without adhesion for which the same contact radius is reached as that in a contact with adhesion. They belong to the (fictitious) indentation process for the JKR theory, which was shown in Fig. 4.5a. The stress intensity factor for the distribution in (4.16) can be easily calculated using Eq. (4.12):

$$K_I(a) = \frac{\Delta F}{2a\sqrt{\pi a}}. \tag{4.17}$$

By taking into consideration the fact that the concepts of Griffith and Irwin (4.14) are equivalent and that the equilibrium condition (4.10) is met, then

$$\Delta F = \sqrt{8\pi E^* a^3 \Delta\gamma}, \tag{4.18}$$

with which the indentation depth and the normal force can be directly determined for the adhesive case:

$$d(a) = d_{n.a.}(a) - \sqrt{\frac{2\pi a\,\Delta\gamma}{E^*}}, \tag{4.19}$$

$$F_N(a) = F_{n.a.}(a) - \sqrt{8\pi E^* a^3 \Delta\gamma}. \tag{4.20}$$

The validity of Eqs. (4.19) and (4.20) is in no way limited to the parabolic contact. They are generally valid for arbitrary axially-symmetric contacts with a simply connected contact area [18].

No additional proof is needed to show that the results of the generalized JKR theory can be mapped to one-dimensional models. This is because if arbitrary axially-symmetric contacts without adhesion (for simply connected contact areas) satisfy the requirements of the reduction method (see Chap. 3), including the flat indenter, then this must also be true for their superposition. The adhesive contact forms a sort of special case of the rule of superposition described in Sect. 3.2, which is valid for the same contact areas. Nevertheless, Sect. 17.3 contains a step-by-step derivation, including information dealing with stability, which is based on the fracture mechanical analogy found by Maugis and Barquins.

The model for the adhesive contact between a parabolic indenter and an elastic half-space is sketched in Fig. 4.1. The loading and unloading process for the one-dimensional model, which exactly describes the equilibrium state of the adhesive contact in three dimensions, is simple. As in the case without adhesion, the equivalent profile g is first calculated and an appropriately formed indenter is subsequently pressed into a one-dimensional linearly elastic foundation with a force $F_{n.a.}$. The springs at the contact boundary $x = \pm a$ exhibit the non-loaded initial length ℓ_o, while the springs within the contact area are under load. Let us now assume that all springs in contact with the indenter adhere to it and for a subsequent decrease in normal force, the contact radius remains unchanged. Going from the contact boundary towards the center, more and more springs are placed under tensile loading. As soon as the change in length of the outer springs reach the maximum allowable value

$$\Delta\ell(\pm a) = \Delta\ell_{\max}(a) := \sqrt{\frac{2\pi a\,\Delta\gamma}{E^*}}, \tag{4.21}$$

there exists an indifference between the states of adhesion and separation. At the points $x = \pm a$, the surface displacement for the one-dimensional model is

$$u_z(\pm a) = -\Delta\ell_{\max}(a). \tag{4.22}$$

This state corresponds exactly to that of the equilibrium state in the three-dimensional case of adhesive contact. The separation condition (4.21) is a type of *local* fracture criterion for the equivalent model, which is also known as the *rule of Heß for the adhesive contact* [6, 19]. Alternately, we can define a maximum spring force instead of a maximum change in length. Upon exceeding this force, the springs at the boundary separate. Especially for the numerical application, the dependence of the separation condition on the contact half-width should be taken into account.

Even the stability of the equilibrium state can be investigated very trivially under various boundary conditions within the framework of the reduction method. For this (referring to Sect. 17.3), the following inequality is used:

$$\frac{\Delta\ell_{\max}(a)}{a} \le k\frac{\partial g(a)}{\partial a} \quad \text{with } k = \begin{cases} 2/3 & \text{for } F_N = const. \\ 2 & \text{for } \; d = const. \end{cases} . \tag{4.23}$$

The equals sign in (4.23) defines the state of marginal stability, which allows for the critical values to be calculated. According to (4.23), the slope of the equivalent profile at the point $x = a$ determines the stability of the system. Depending on the boundary condition (*fixed-load* or *fixed-grips*), it is to be multiplied with the corresponding factor k and compared with the quotient of the separation length and contact radius.

With the exception of the stability considerations named above, the implementation of adhesion using the reduction method requires no additional effort whatsoever. In contrast to the non-adhesive contact, only the displacement in the one-dimensional model must be extended by the rigid-body portion (see Fig. 4.1)

$$u_z(x) := d(a) - g(x) = g(a) - g(x) - \Delta\ell_{\max}(a) \quad \text{for } \; 0 \le |x| \le a. \tag{4.24}$$

The indentation depth is defined by the displacement at $x = 0$:

$$d(a) := u_z(0) = g(a) - \Delta\ell_{\max}(a). \tag{4.25}$$

By taking (4.24) and (4.25) into account, the normal force is obtained as a function of the contact radius in the same way as before, from the sum of the spring forces:

$$F_N(a) := E^* \int_{-a}^{a} u_z(x)\mathrm{d}x. \tag{4.26}$$

The normal stresses in the contact area are obtained also in the same way as in the contact without adhesion, from the modified Abel integral of the vertical distributed load:

$$\sigma_{zz}(r) = \frac{1}{\pi}\int_{r}^{a} \frac{q'(x)}{\sqrt{x^2 - r^2}}\mathrm{d}x - \frac{1}{\pi}\frac{q(a)}{\sqrt{a^2 - r^2}} \quad \text{with} \quad q(x) = E^* u_z(x). \tag{4.27}$$

In order to make the simple steps of the reduction method clear to the reader, we will show the complete mapping of the original theory from Johnson, Kendall, and Roberts as an example. In the typical way, the equivalent profile g of the parabolic indenters with the radius of curvature must first be determined. According to the *rule of Popov*, we must simply divide the radius of curvature by two:

$$f(r) = \frac{r^2}{2R} \Rightarrow g(x) = \frac{x^2}{R}\,. \tag{4.28}$$

The surface displacement in the equivalent model, according to Eq. (4.24), is

$$u_z(x) = \frac{a^2 - x^2}{R} - \Delta\ell_{\max}(a), \tag{4.29}$$

from which we can determine the indentation depth with respect to contact radius according to (4.25). Taking the separation condition (4.21) into account, we obtain

$$d(a) = \frac{a^2}{R} - \sqrt{\frac{2\pi a\,\Delta\gamma}{E^*}}. \tag{4.30}$$

The normal force is the sum of the spring forces

$$F_N(a) = E^* \int_{-a}^{a} u_z(x)\mathrm{d}x = 2E^* \int_{0}^{a} \left(d - \frac{x^2}{R}\right)\mathrm{d}x = \frac{4}{3}E^*\frac{a^3}{R} - \sqrt{8\pi a^3 E^* \Delta\gamma}. \tag{4.31}$$

Equations (4.30) and (4.31) will seem familiar to the reader, for they are exactly those developed by Johnson, Kendall, and Roberts using the minimum in the total energy.

We investigate the stability of the system with the criterion (4.23). For this, let k not be fixed for the time being. The slope of the equivalent profile at the point $x = a$ is

$$g(a) = \frac{a^2}{R} \Rightarrow \frac{\partial g(a)}{\partial a} = \frac{2a}{R}. \tag{4.32}$$

Insertion of (4.32) into (4.23) and taking the separation condition (4.21) into account, results in

$$\sqrt{\frac{2\pi a\,\Delta\gamma}{E^*}}\frac{1}{a} \leq k\frac{2a}{R}, \tag{4.33}$$

and after simple rearrangement, the contact radii for which the system is stable are obtained:

$$a \geq \left(\frac{\pi R^2 \Delta\gamma}{2k^2 E^*}\right)^{1/3} \quad \text{marginal stability: } a_c(k) = \left(\frac{\pi R^2 \Delta\gamma}{2k^2 E^*}\right)^{1/3}. \tag{4.34}$$

The marginally stable case characterizes the critical state at which the calculation of the critical values is possible: the minimum normal force and minimum indentation depth. In order to accomplish this, the contact radius in Eq. (4.34) must be take into account in Eqs. (4.30) and (4.31), from which we obtain

$$F_c(k) = \left(\frac{1}{3k} - 1\right)\frac{2\pi R\,\Delta\gamma}{k} \quad \text{and} \quad d_c(k) = \left(\frac{1}{k} - 2\right)\left(\frac{\pi^2 R\,\Delta\gamma^2}{4k\,E^{*2}}\right)^{1/3}. \tag{4.35}$$

Until now, we have left the type of boundary condition open. Now, we will assign the variable k a value. Under the *fixed-load* condition, we must set $k = \frac{2}{3}$ and obtain the known results:

$$a_c = \left(\frac{9\pi R^2 \Delta\gamma}{8E^*}\right)^{1/3}, \; F_c = -\tfrac{3}{2}\pi R\,\Delta\gamma\,, \; d_c = -\left(\frac{3\pi^2 R\,\Delta\gamma^2}{64E^{*2}}\right)^{1/3} . \tag{4.36}$$

The critical force in (4.36) is also called the *adhesion force* and corresponds to the minimum in the normal force. Its magnitude, however, is called the *maximum separation force.* Under the *fixed-grips* condition ($k = 2$), the indentation depth is actually able to be *stably* decreased even further, until the following three relationships are reached:

$$a_{c,d} = \left(\frac{\pi R^2 \Delta\gamma}{8E^*}\right)^{1/3}, \; F_{c,d} = -\tfrac{5}{6}\pi R\,\Delta\gamma\,, \; d_{c,d} = -\tfrac{3}{4}\left(\frac{\pi^2 R\,\Delta\gamma^2}{E^{*2}}\right)^{1/3} , \tag{4.37}$$

The additional index "*d*" denotes the fixed-grips condition.

For the sake of completeness, let the equilibrium curves (4.30) and (4.31) be expanded by a normalized representation. With the respect to the magnitude, the critical values are

$$\tilde{F}_N(\tilde{a}) = \tilde{a}^3 - 2\tilde{a}^{3/2} \text{ and } \tilde{d}(\tilde{a}) \; = 3\tilde{a}^2 - 4\tilde{a}^{1/2}, \tag{4.38}$$

with $\tilde{F}_N := F_N/|F_c|$, $\tilde{d} := d/|d_c|$, and $\tilde{a} := a/a_c$. Because of their complexity due to the normal force as a function of the indentation depth, they will not be specified explicitly, but their trends will be graphically shown with the help of the parametric form (4.38). Figure 4.6a shows the trend compared to the adhesive contact of a conical profile (shown in Fig. 4.6b). The dashed ends of the functions mark the extended domain of stability under the *fixed-grips* condition.

Comparing the curves reveals that the adhesion forces are negative in both cases, but the critical indentation depths (at a constant force) have different signs. The solution of the adhesive conical contact and the confirmation of the corresponding curves from Fig. 4.6b is one of the problems at the end of this chapter.

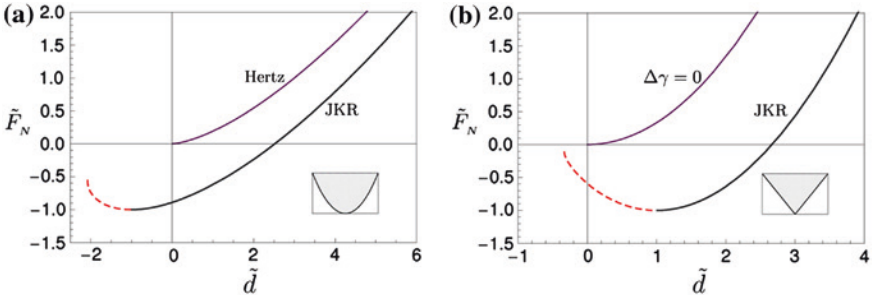

Fig. 4.6 Dependence of the normalized force on the normalized indentation depth for the adhesive contact for a parabolic (**a**) and a conical indenter (**b**); for comparison purposes, the trends of the respective contacts without adhesion are shown

Only the calculation of the stress is now needed to completely solve the adhesive contact problem for parabolic profiles. For this, we need the linear force density in the equivalent model:

$$q(x) = E^* u_z(x) = E^* \left[\frac{a^2 - x^2}{R} - \Delta\ell_{\max}(a) \right]. \tag{4.39}$$

By differentiating this with respect to x and then inserting the value at $x = a$, we obtain

$$q'(x) = -\frac{2E^*}{R} x \text{ and } q(a) = -E^* \Delta\ell_{\max}(a)\,. \tag{4.40}$$

Insertion of (4.40) into (4.27) results initially in

$$\sigma_{zz}(r) = -\frac{2E^*}{\pi R} \int_r^a \frac{x}{\sqrt{x^2 - r^2}}\,\mathrm{d}x + \frac{E^*}{\pi} \frac{\Delta\ell_{\max}(a)}{\sqrt{a^2 - r^2}}, \tag{4.41}$$

which is then integrated and suitably normalized, resulting in

$$\frac{\sigma_{zz}(s)}{\bar{p}_{n.a.}} = -\frac{3}{2}\sqrt{1 - s^2} + \frac{1}{2}\left(1 - \frac{F_N}{F_{n.a.}}\right) \frac{1}{\sqrt{1 - s^2}} \text{ with } s := \frac{r}{a} \text{ and } \bar{p}_{n.a.} := \frac{F_{n.a.}}{A}\,. \tag{4.42}$$

For the critical state of $F_c := F_N(a_c) = -F_{n.a.}$, this stress curve is presented in Fig. 4.5b.

The process for mapping the classical contact problems described by Johnson, Kendall, and Roberts within the reduction method may seem a bit challenging at first. However, the reader will quickly be convinced that, in reality, the opposite is the case. The method is composed primarily of just a few steps, which are formulated in Eqs. (4.21)–(4.27) and cannot be simpler. In the next section, the method will be used on a more complicated contact problem, which occasionally allows for commentary on the influence of roughness on adhesion.

4.5 Example: Adhesion of a Sphere with a Superimposed Radial Waveform

It is generally known that the adhesion between (visco-) elastic bodies is significantly influenced by the roughness of their surfaces. In the most general cases, the adhesion decreases rapidly with an increase in roughness, however, there are well-founded experimental results [20, 21], which show effects to the contrary. According to this, very soft materials having small scales of roughness exhibit a temporary increase in adhesion before a continuous decrease begins. An established theoretical reason for this increase is based on the increase in the real contact area, which occurs due to viscoelastic creep processes. A further cause for the increase in adhesion was brought to attention by Guduru [22] by theoretically

Fig. 4.7 Profile cross-section of a parabolic body superimposed with a radial waveform and its one-dimensional equivalent

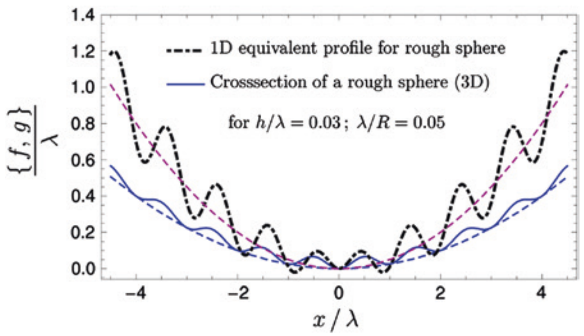

investigating the adhesive, elastic contact between a half-space and a parabolic body with superimposed axially-symmetric waveforms. Due to the waveform, defined oscillations occur in the equilibrium curves, bringing about instabilities during the separation process. These instabilities can lead to a significant increase in the separation force. Experimental investigations [23] confirm the validity of the theoretical ansatz from Guduru, which requires a simply connected contact area at the beginning of the separation process. This last condition, along with that of axial-symmetry, allow this example for a rough contact to be *exactly* mapped using the method of dimensionality reduction, which will be the subject of the following considerations.

The axially-symmetric profile is composed of a parabolic base profile with a radius of curvature of R and a radially harmonic profile with the wavelength λ and the (roughness) amplitude h according to the equation[4]

$$f(r) = \frac{r^2}{2R} + h\left[1 - \cos\left(\frac{2\pi}{\lambda} r\right)\right]. \tag{4.43}$$

The cross-section of the profile in the x-z plane for $h/\lambda = 0.03$ and $\lambda/R = 0.05$ is shown in Fig. 4.7. A simply connected contact area at *every* point in time for the indentation and separation process requires a monotonically increasing profile for $r \geq 0$, which with the help of the derivative

$$f'(r) = \frac{r}{R} + h\frac{2\pi}{\lambda} \sin\left(\frac{2\pi}{\lambda} r\right), \tag{4.44}$$

is expressed by the following condition:

$$f'(r) \geq 0 \Rightarrow \alpha := \frac{\lambda^2}{hR} \geq 4\pi^2 \sup\left[\frac{-\sin\left(\frac{2\pi}{\lambda} r\right)}{\frac{2\pi}{\lambda} r}\right] \approx 8.576. \tag{4.45}$$

---

[4] It is irrelevant if the superimposed profile is pressed into a planar elastic half-space or a parabolic body is pressed into an elastic half-space with the corresponding waveform.

Although the monotonic requirement (4.45) is obviously not met by the profile in Fig. 4.7 ($\alpha \approx 1.667 < 8.576$), a simply connected contact area can nevertheless be realized for a sufficiently large normal force. The reason for this is the decrease in the least upper bound (supremum) in (4.45), if we constrict ourselves to sufficiently large $r > r_{crit}$.

In order to determine the one-dimensional equivalent profile, we must make use of the conversion formula (see Sect. 3.3).

$$g(x) := |x| \int_0^{|x|} \frac{f'(r)}{\sqrt{x^2 - r^2}} \mathrm{d}r = \frac{x^2}{R} + s(x)h \int_0^{s(x)} \frac{\sin(u)}{\sqrt{s(x)^2 - u^2}} \mathrm{d}u \quad \text{with} \quad s(x) = \frac{2\pi}{\lambda}|x|. \tag{4.46}$$

The integral on the right side leads to the Struve function, so that we obtain

$$g(x) = \frac{x^2}{R} + \frac{\pi^2}{\lambda}|x|h \cdot H_0\left(\frac{2\pi}{\lambda}|x|\right) \tag{4.47}$$

for the equivalent profile. Let us here mention that the series representation of the Struve function is

$$H_n(x) = \sum_{k=0}^{\infty} \frac{(-1)^k}{\Gamma\left(k + \frac{3}{2}\right)\Gamma\left(k + n + \frac{3}{2}\right)} \left(\frac{x}{2}\right)^{2k+n+1}. \tag{4.48}$$

The one-dimensional equivalent profile according to Eq. (4.47) is likewise presented in Fig. 4.7. Moreover, the original and equivalent profiles are shown for a roughness of zero (dashed lines) and present, of course, a constant vertical scaling relationship based on the rule of Popov.

Upon obtaining the one-dimensional profile, the three-dimensional problem is as good as solved, because now the modified profile must simply be pressed with sufficient force into the one-dimensional layer of springs and then the force reduced while taking the equilibrium condition (4.22) and the accompanying stability test (4.23) into account. The numerical implementation is trivial due to the independence of the spring displacement, but nevertheless, agrees exactly with the three-dimensional theory! In the following, we conduct an analytical approach, which leads to the indentation depth when Eq. (4.47) is taken into account:

$$d(a) := g(a) - \Delta\ell_{\max}(a) = \frac{a^2}{R} + \frac{\pi^2 ah}{\lambda} H_0\left(\frac{2\pi}{\lambda}a\right) - \sqrt{\frac{2\pi a\,\Delta\gamma}{E^*}}. \tag{4.49}$$

The surface displacement of the linearly elastic foundation is defined by the difference between the indentation depth d and the equivalent profile g. Except for the sign, this displacement corresponds to the change in length of the springs. The resulting spring forces must maintain equilibrium by summation with the normal force:

$$F_N(a) = E^* \int_{-a}^{a} \left[d - g(x)\right] \mathrm{d}x. \tag{4.50}$$

Insertion of (4.47) and (4.49) into (4.50) results in

$$F_N(a) = \frac{4}{3} E^* \frac{a^3}{R} + E^* \pi a h \left[\frac{2\pi a}{\lambda} H_0\left(\frac{2\pi a}{\lambda}\right) - H_1\left(\frac{2\pi a}{\lambda}\right) \right] - \sqrt{8\pi a^3 E^* \Delta\gamma} \tag{4.51}$$

after integration and simple rearrangement. By taking the normalized values suggested by Guduru [22] into account:

$$\bar{F}_N := \frac{2F_N}{3\pi R \Delta\gamma}\,, \ \bar{d} := \frac{d}{\lambda}\,, \ \bar{a} := \frac{a}{\lambda}\,, \ \bar{\lambda} := \frac{\lambda}{R}\,, \ \bar{h} := \frac{h}{\lambda}\,, \ \overline{\Delta\gamma} := \frac{2\pi \Delta\gamma}{E^* R}$$

the equilibrium relations (4.49) and (4.51) can be expressed in dimensionless form:

$$\bar{d}\left(\bar{a}; \bar{\lambda}; \bar{h}; \overline{\Delta\gamma}\right) = \bar{a}^2 \bar{\lambda} + \pi^2 \bar{a}\,\bar{h} \cdot H_0(2\pi\bar{a}) - \sqrt{\frac{\bar{a}\,\overline{\Delta\gamma}}{\bar{\lambda}}}, \tag{4.52}$$

$$\bar{F}_N\left(\bar{a}; \bar{\lambda}; \bar{h}; \overline{\Delta\gamma}\right) = \frac{16}{9} \frac{\bar{a}^3 \bar{\lambda}^3}{\overline{\Delta\gamma}} + \frac{4\pi}{3} \frac{\bar{a}\,\bar{h}\bar{\lambda}^2}{\overline{\Delta\gamma}} \left[2\pi\bar{a} \cdot H_0(2\pi\bar{a}) - H_1(2\pi\bar{a})\right] - \frac{8}{3} \sqrt{\frac{\bar{a}^3 \bar{\lambda}^3}{\overline{\Delta\gamma}}}. \tag{4.53}$$

With the normalized contact radius $\bar{a}$ as a parameter, the (normalized) normal force can be plotted as a function of the (normalized) indentation depth. Figure 4.8 shows this plot for the parameters

$$\bar{h} = 0.005\,, \ \bar{\lambda} = 0.05\,, \ \overline{\Delta\gamma} = 0.05, \tag{4.54}$$

which only exhibits slight oscillating deviations in the equilibrium curve compared to the parabolic contact without roughness. The monotonic condition (4.45) is satisfied regardless of the load at any point in time.

If we now increase the size of the roughness and keep all other values the same, then a significant change occurs in the equilibrium curve. Oscillations of strong amplitude occur and can lead to an increase in the maximum separation force. Figure 4.9 presents this curve for the profile discussed at the beginning of this section (see Fig. 4.7), which is characterized by a roughness six times larger. The maximum separation force is increased by about 19 % with respect to the parabolic base profile. The critical indentation depth can be decreased by a further 10 % by using the fixed grips condition. Furthermore, the equilibrium curves are

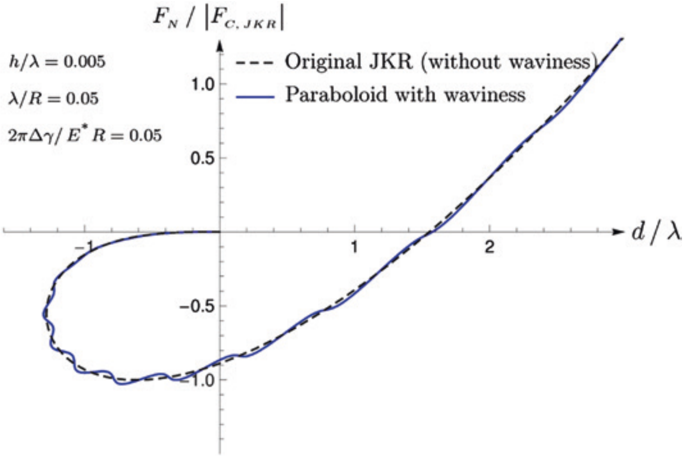

Fig. 4.8 Normal force with respect to the indentation depth for the adhesive contact of a parabolic profile with a superimposed radial waveform. The (small) roughness $h = 0.005\,\lambda$ causes only a minor difference from the original trend of the JKR theory

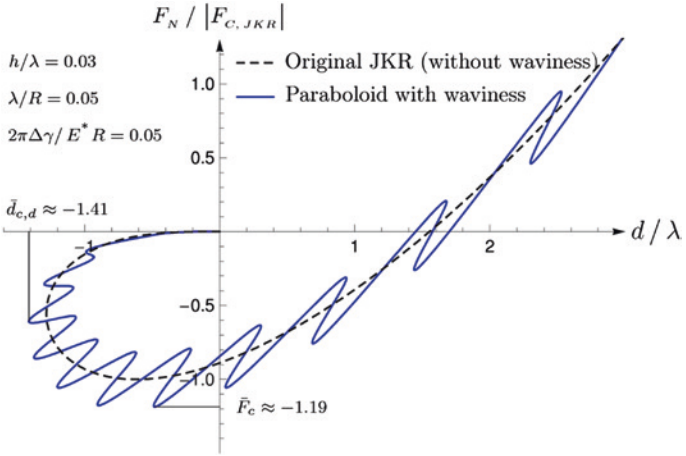

Fig. 4.9 Normal force with respect to the indentation depth for the adhesive contact with a superimposed radial waveform. The assumed roughness of $h = 0.03\,\lambda$ causes strong oscillations, resulting in an additional increase in the adhesion force of about 19 % compared to the original JKR theory

not continuous throughout the separation process. Due to the constant switching from stable to unstable domains, finite jumps occur, which result in energy loss.

As mentioned earlier, the exact solution of contact problems using the method of dimensionality reduction requires a simply-connected contact area and cannot be immediately transferred to partial contacts. Furthermore, the superimposed waveforms must be axially-symmetric. If one of these requirements is not met, significantly divergent results can result. For example, if a planar waveform instead of a radial waveform is present, then there will be no jumps in the equilibrium curve [24].

4.6 Problems

Problem 1 Investigate the contact between an elastic half-space and a conical body defined by $f(r) = \tan\theta \cdot r$. Adhesion forces should be taken into account. Determine the indentation depth and the normal force with respect to the contact radius. Furthermore, determine the critical values under the *fixed-load* conditions and the equilibrium relations in dimensionless parameters.

Solution The equivalent one-dimensional profile is obtained by vertically scaling the original profile by a factor of $\kappa_1 = \pi/2$ and is equal to $g(x) = (\pi/2)\tan\theta \cdot |x|$. From (4.24), the surface displacement can be obtained for the equivalent profile:

$$u_z(x) = g(a) - g(x) - \Delta\ell_{\max}(a) = \frac{\pi}{2}\tan\theta \cdot (a - |x|) - \Delta\ell_{\max}(a). \tag{4.55}$$

The indentation depth is the displacement at the point $x = 0$:

$$d(a) := u_z(0) = \frac{\pi}{2}\tan\theta \cdot a - \Delta\ell_{\max}(a) = \frac{\pi}{2}\tan\theta \cdot a - \sqrt{\frac{2\pi a\,\Delta\gamma}{E^*}}. \tag{4.56}$$

The sum of the spring forces must counteract the normal force:

$$F_N(a) = E^* \int_{-a}^{a} u_z(x)\mathrm{d}x = 2E^* \int_{0}^{a} \left[d - g(x)\right]\mathrm{d}x = \frac{1}{2}\pi E^* \tan\theta \cdot a^2 - \sqrt{8\pi a^3 E^* \Delta\gamma}. \tag{4.57}$$

We take the condition for calculating the critical contact radius a_c at a constant contact radius from Eq. (4.23):

$$\frac{\Delta\ell_{\max}(a_c)}{a_c} = \frac{2}{3}\frac{\partial g(a)}{\partial a}\bigg|_{a=a_c} \quad \text{with} \quad \frac{\partial g(a)}{\partial a} = \frac{\pi}{2}\tan\theta\,, \tag{4.58}$$

for which the right hand side is already extended by the slope of the profile at hand. By using the rule of Heß, the critical contact radius is obtained. Insertion of this value into the equilibrium relationships (4.56) and (4.57) and then rearranging the equations results in the adhesion force and the critical indentation depth:

$$a_c = \frac{18\,\Delta\gamma}{\pi\tan^2\theta \cdot E^*},\; F_c = -\frac{54\,\Delta\gamma^2}{\pi\tan^3\theta \cdot E^*},\; d_c = \frac{3\,\Delta\gamma}{\tan\theta \cdot E^*}\cdot \tag{4.59}$$

By introducing the normalized values $\tilde{F}_N := F_N/|F_c|$, $\tilde{d} := d/|d_c|$, and $\tilde{a} := a/a_c$, we obtain the equilibrium relationships (4.56) and (4.57) in dimensionless form:

$$\tilde{F}_N(\tilde{a}) = 3\tilde{a}^2 - 4\tilde{a}^{3/2} \text{ and } \tilde{d}(\tilde{a}) = 3\tilde{a} - 2\tilde{a}^{1/2}. \tag{4.60}$$

With the help of the parametric equations in (4.60), the normalized force can be easily plotted as a function of normalized indentation depth, which is shown in Fig. 4.6b. The comparison with the parabolic contact shows, above all, a striking difference in the critical indentation depth (under *fixed-load* conditions), which have opposing signs. All of the results for this exercise mirror the three-dimensional theory exactly (see [14]).

Problem 2 Determine the maximum separation force for the elastic contact between a flat, cylindrical indenter with the radius a and a half-space.

Solution From the original profile $\mathrm{f}(r) = 0$, the equivalent profile $g(x) = 0$ is directly obtained, so that the surface displacement within the contact area corresponds everywhere to the indentation depth according to (4.24). This means that

$$u_z(x) = d(a) = -\Delta\ell_{\max}(a) = -\sqrt{\frac{2\pi a\,\Delta\gamma}{E^*}}\,. \tag{4.61}$$

Because all of the springs exhibit the same change in length based on (4.61), the calculation of the normal force is trivial:

$$F_N(a) = -2E^* a\,\Delta\ell_{\max}(a) = -\sqrt{8\pi a^3 E^* \Delta\gamma}. \tag{4.62}$$

The verification of the condition (4.23), however, uncovers the fact that a stable, quasi-static equilibrium in the form of a controlled fracture is not possible. Therefore, all of the springs will adhere to the indenter until they reach the change in length of (4.61) and then simultaneously separate (*complete rupture)*. The normal force according to (4.62) presents simultaneously the adhesion force and the magnitude of the maximum separation force

$$F_A := |F_N(a_c)| = \sqrt{8\pi a^3 E^* \Delta\gamma}, \tag{4.63}$$

which corresponds with the known result of Kendall [7].

Problem 3 Analyze the influence of the profile form on the adhesion force for a single contact within a biological system. For this, assume an axially-symmetric profile in the form of a power function with a positive real exponent according to

$$f(r) = C \cdot r^n \text{ with } n \in \mathbb{R}^+. \tag{4.64}$$

In the first step, identify the equilibrium relationships $F_N(a)$ and $d(a)$. Then, calculate the critical values for marginal stability from (4.23) for a *constant normal force* and non-dimensionalize the equilibrium relationships.

Solution We obtain the one-dimensional equivalent profile by using the generalized rule of Heß (see Sect. 3.2):

$$g(x) = \kappa_n f(|x|) = \kappa_n C|x|^n \text{ with } \kappa_n = \frac{\sqrt{\pi}}{2} \frac{n\Gamma(\frac{n}{2})}{\Gamma(\frac{n+1}{2})} . \tag{4.65}$$

The difference between the value of the function for the equivalent profile at the contact boundary and the separation length provides the indentation depth

$$d(a) = g(a) - \Delta\ell_{\max}(a) = \kappa_n C a^n - \sqrt{\frac{2\pi a\, \Delta\gamma}{E^*}}. \tag{4.66}$$

The surface displacement in the one-dimensional model is then

$$u_z(x) := d - g(x) = \kappa_n C\left(a^n - |x|^n\right) - \sqrt{\frac{2\pi a\, \Delta\gamma}{E^*}}, \tag{4.67}$$

which expresses, except for the sign, the change in length of the individual springs. After multiplication with the stiffness and summation over the contact length, the normal force is found:

$$F_N(a) = 2E^* \int\limits_0^a \left[d - g(x)\right] dx = 2E^* \frac{n}{n+1} \kappa_n C a^{n+1} - \sqrt{8\pi a^3 E^* \Delta\gamma}. \tag{4.68}$$

The critical contact radius is obtained from the (transformed) stability equation for the one-dimensional model. It requires only (!) that the profile slope at the contact boundary be known, which is given here by

$$\frac{\partial g(a)}{\partial a} = n\,\kappa_n C a^{n-1}. \tag{4.69}$$

Insertion into (4.23) leads to the critical contact radius

$$\frac{\Delta\ell_{\max}(a_c)}{a_c} = \frac{2}{3} n\,\kappa_n C a_c^{n-1} \Rightarrow a_c = \left(\frac{9\pi\,\Delta\gamma}{2n^2 \kappa_n^2 C^2 E^*}\right)^{\dfrac{1}{2n-1}}, \tag{4.70}$$

which provides the adhesion force and the critical indentation depth when inserted into the equilibrium relationships:

$$F_c = \frac{1-2n}{n+1} \left[\left(\frac{3}{2n\kappa_n C}\right)^3 (2\pi\,\Delta\gamma)^{n+1} {E^*}^{n-2}\right]^{\frac{1}{2n-1}}, \tag{4.71}$$

$$d_c = \left(1 - \frac{2}{3} n\right) \left[\frac{9\pi\,\Delta\gamma}{2n^2 E^*} \left(\frac{1}{\kappa_n C}\right)^{1/n}\right]^{\frac{n}{2n-1}}. \tag{4.72}$$

If normalized by the magnitudes of the critical values $\tilde{F}_N := F_N/|F_c|$, $\tilde{d} := d/|d_c|$, and $\tilde{a} := a/a_c$, the equilibrium relationship exhibit an especially simple structure

$$\tilde{F}_N(\tilde{a}) = \frac{1}{|1-2n|}\left[3\tilde{a}^{n+1} - 2(n+1)\tilde{a}^{3/2}\right] \text{ and } \tilde{d}(\tilde{a}) = \frac{1}{|3-2n|}\left(3\tilde{a}^{n} - 2n\tilde{a}^{1/2}\right). \tag{4.73}$$

For $n = 1$, the results correspond to those from Problem 1, while for $n = 2$, the classical results from JKR theory are obtained. The calculation of the critical contact radius as well as the adhesion force go back to Yao and Gao [25] and were actually employed to investigate adhesion in biological structures [26]. Extended stability considerations can be found in the work by Heß [6].

Problem 4 Determine the normal force and indentation depth with respect to the contact radius for the adhesive normal contact between a sphere with the radius R and an elastic half-space. In contrast to the parabolic profile approximation in JKR theory, the exact spherical form should be considered. Simultaneously, it is assumed that only small deformations take place and the material is linearly elastic.

Solution This contact problem was already solved in Problem 8 in Chap. 3 for the case without adhesion. Referring to this exercise, we can simply take the explicitly calculated equivalent profile:

$$f(r) = R - \sqrt{R^2 - r^2} \Rightarrow g(x) = \frac{1}{2}x\ln\left(\frac{R+x}{R-x}\right). \tag{4.74}$$

By subtracting the separation length from the value of the function of the equivalent profile at the contact boundary, we obtain the indentation depth

$$d(a) = g(a) - \Delta 1_{\max}(a) = \frac{1}{2}a\ln\left(\frac{R+a}{R-a}\right) - \sqrt{\frac{2\pi a\,\Delta\gamma}{E^*}}. \tag{4.75}$$

The displacement in the one-dimensional model is then

$$u_z(x) := d - g(x) = \frac{1}{2}a\ln\left(\frac{R+a}{R-a}\right) - \sqrt{\frac{2\pi a\,\Delta\gamma}{E^*}} - \frac{1}{2}x\ln\left(\frac{R+x}{R-x}\right). \tag{4.76}$$

The calculation of the normal force requires the summation of the contributions from the individual springs and can be immediately given with the help of the solution of the contact without adhesion as

$$F_N(a) = E^*\int_{-a}^{a} u_z(x)\mathrm{d}x = E^*\frac{R^2+a^2}{2}\ln\left(\frac{R+a}{R-a}\right) - E^*Ra - \sqrt{8\pi a^3 E^*\Delta\gamma}. \tag{4.77}$$

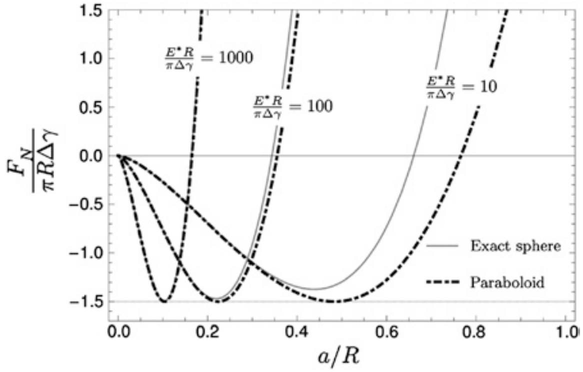

Fig. 4.10 Normal force as a function of contact radius in the normalized presentation for the adhesive contact: Comparison between the parabolic approximation and the exact spherical profile for various values of $m = E^*R/(\pi\Delta\gamma)$

By introducing the normalized values $\tilde{F}_N := \frac{F_N}{\pi R\Delta\gamma}$ and $\tilde{a} = \frac{a}{R}$ as well as the parameter $m := \frac{E^*R}{\pi\,\Delta\gamma}$, we can convert Eq. (4.77) into the dimensionless form

$$\tilde{F}_N(\tilde{a}) = \frac{1}{2}m\left(1+\tilde{a}^2\right)\ln\left(\frac{1+\tilde{a}}{1-\tilde{a}}\right) - m\tilde{a} - \sqrt{m}(2\tilde{a})^{3/2}. \tag{4.78}$$

The derived relationships agree exactly to those of the three-dimensional theory developed by Maugis [27]. For comparative purposes, let the respective normalized form of the JKR equation for a parabolic profile be noted:

$$\tilde{F}_N(\tilde{a}) = \frac{4}{3}m\tilde{a}^3 - \sqrt{m}(2\tilde{a})^{3/2}. \tag{4.79}$$

Figure 4.10 emphasizes the difference between the spherical contact and the corresponding parabolic approximation. For large values of the parameter m ($m > 1{,}000$), they agree well with one another, while for smaller values of m, significant deviations are apparent. The maximum separation force is then especially dependent on the elastic properties. The parabolic approximation appears to give acceptable results over several orders of magnitude of the parameter m up to a contact radius of $a \approx 0.2R$.

With these results, Maugis attempted to describe the contact for small spheres with that of a very soft elastic solid and in this way, proved the invalidity of the parabolic approximation if the contact radius is on the same order of magnitude as the radius of curvature. In this regime, however, the application of the theory of linear elasticity is highly questionable, which Lin and Chen [28] discovered on the basis of geometric and physical *non-linear* theory and for which Greenwood [29] suggested critical additions.

Problem 5 Determine the indentation depth and the normal force as a function of contact radius for the adhesive contact of the axially-symmetric body shown in Fig. 4.11 with an elastic half-space. The form of the body is described by a parabolic profile with a flattened tip:

$$f(r) = \begin{cases} 0 & \text{for } 0 \le r < b \\ \frac{r^2-b^2}{2R} & \text{for } b \le r \le a \end{cases}. \tag{4.80}$$

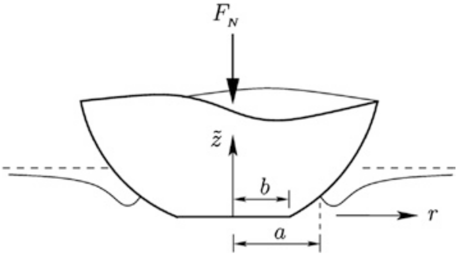

Fig. 4.11 Qualitative presentation of the adhesive contact of a parabolic profile with a flattened tip and an elastic half-space

Solution The corresponding non-adhesive contact problem was solved in Sect. 3.3. It served as an introductory example for the explicit application of the generalized formula (3.27) to determine the equivalent profile, which also composes the first step in the mapping of the contact with adhesion. By taking the derivative of the original profile into account, we obtained

$$g(x) := |x| \int_0^{|x|} \frac{f'(r)}{\sqrt{x^2-r^2}} \mathrm{d}r = \begin{cases} 0 & \text{for } 0 \le |x| < b \\ \frac{|x|}{R}\sqrt{x^2-b^2} & \text{for } b \le |x| \le a \end{cases} . \tag{4.81}$$

With the help of (4.81), the indentation depth can be directly given as

$$d(a) := g(a) - \Delta\ell_{\max}(a) = \frac{a}{R}\sqrt{a^2-b^2} - \sqrt{\frac{2\pi a\,\Delta\gamma}{E^*}}. \tag{4.82}$$

The displacements of the contact points in the linearly elastic foundation are still obtained by the difference between the indentation depth and the value of the equivalent profile and provides the change in length of the spring (with the exception of the sign). Summing the individual spring contributions, leads to the normal force

$$F_N(a) = E^* \int_{-a}^{a} u_z(x)\mathrm{d}x = \frac{2E^*}{3R}\left(2a^2+b^2\right)\sqrt{a^2-b^2} - \sqrt{8\pi a^3 E^* \Delta\gamma}. \tag{4.83}$$

The critical values (*fixed load*) in the case of $b = 0$ are those from the original theory for a parabolic body

$$a^* = \left(\frac{9\pi R^2 \Delta\gamma}{8E^*}\right)^{1/3}, \; F^* = -\frac{3}{2}\pi R\,\Delta\gamma\,, \; d^* = -\left(\frac{3\pi^2 R\,\Delta\gamma^2}{64E^{*2}}\right)^{1/3}, \tag{4.84}$$

which we took from (4.36) and renamed. By normalizing by their magnitudes, we can convert Eqs. (4.82) and (4.83) into the dimensionless forms

$$\hat{d}(\hat{a}) = 3\hat{a}^2\sqrt{1-\left(\frac{\hat{b}}{\hat{a}}\right)^2} - 4\hat{a}^{1/2}, \tag{4.85}$$

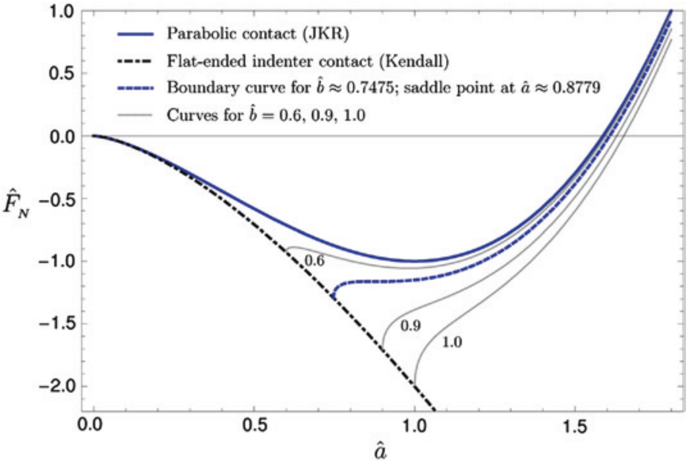

Fig. 4.12 Graphical trends of the normalized normal force as a function of the normalized contact radius for the adhesive contact between a parabolic indenter with a "worn" tip; the parameter b corresponds to the size of the flattened area of the indenter

$$\hat{F}_N(\hat{a}) = \frac{1}{2}\hat{a}^3\left[2 + \left(\frac{\hat{b}}{\hat{a}}\right)^2\right]\sqrt{1 - \left(\frac{\hat{b}}{\hat{a}}\right)^2} - 2\hat{a}^{3/2}, \tag{4.86}$$

where $\hat{F}_N := F_N/|F^*|$, $\hat{d} := d/|d^*|$, $\hat{a} := a/a^*$, and $\hat{b} := b/a^*$ were used for the normalization. In the special case of $\hat{b} = 0$, the resulting equation is (4.38) and for the case of $\hat{b} = \hat{a}$, the resulting equations are (4.61) and (4.62). These cases describe the parabolic contact and the flat indenter contact, respectively. Their graphical trends can be interpreted as extreme values for the general case, which is expressed in Fig. 4.12. Here, unstable domains are not visible. The fact that the horizontal tangents of the minimums of these curves separate the stability domains is clear. It is interesting that for $b > 0.7475\,a^*$, complete separation occurs only after $a = b$, meaning the contact radius corresponds to that of the flattened area of the indenter.

For $b < 0.7475\,a^*$, however, there exists a minimum that marks the adhesion force in a way similar to the parabolic contact. Further considerations, especially those near the boundary curves shown in Fig. 4.12, are contained in [30].

References

1. K.L. Johnson, K. Kendall, A.D. Roberts, Surface energy and the contact of elastic solids. in *Proceedings of the Royal Society of London. Series A, Mathematical and Physical Sciences,* vol. 324, no. 1558 (1971), pp. 301–313
2. B.V. Derjaguin, V.M. Muller, YuP Toporov, Effect of contact deformation on the adhesion of particles. J. Colloid Interface Sci. **55**, 314–326 (1975)
3. R.S. Bradley, The cohesive force between solid surfaces and the surface energy of solids. Philos. Mag. **13**, 853–862 (1932)

4. D. Tabor, Surface forces and surface interactions. J. Colloid Interface Sci. **58**, 2–13 (1977)
5. K.L. Johnson, J.A. Greenwood, An Adhesion Map for the Contact of Elastic Spheres. J. Colloid Interface Sci. **192**, 326–333 (1997)
6. M. Heß, *Über die exakte Abbildung ausgewählter dreidimensionaler Kontakte auf Systeme mit niedrigerer räumlicher Dimension* (Cuvillier, Berlin, 2011)
7. K. Kendall, The adhesion and surface energy of elastic solids. J. Phys. D Appl. Phys. **4**, 1186–1195 (1971)
8. A.A. Griffith, The phenomena of rupture and flow in solids. Philos. Trans. R. Soc. Lond. Ser. A **221**, 163–198 (1921)
9. A.A., Griffith, Theory of rupture. [ed.] Biezeno and Burgers. in *Proceedings of the First International Congress for Applied Mechanics,* 1925, pp. 53–64
10. D. Maugis, M. Barquins, R. Courtel, Griffith Cracks and Adhesion of Elastic Solids. Métaux, Corrosion, Industrie **605**, 1–10 (1976)
11. D. Maugis, M. Barquins, Fracture mechanics and the adherence of viscoelastic bodies. J. Phys. D Appl. Phys. **11**(14), 1989–2023 (1978)
12. G.R. Irwin, Analysis of stresses and strains near the end of a crack traversing a plate. J. Appl. Mech. **24**, 361–364 (1957)
13. Johnson, K.L. Adhesion and friction between a smooth elastic spherical asperity and a plane surface. in *Proceedings of the Royal Society of London. Series A: Mathematical, Physical and Engineering Sciences*, vol. 453, no. 1956. 1997, pp. 163–179
14. D. Maugis, M. Barquins, Adhesive contact of a conical punch on an elastic half-space. Le Journal de Physique Lettres **42**(5), 95–97 (1981)
15. M. Barquins, D. Maugis, Adhesive contact of axisymmetric punches on an elastic half-space: the modified Hertz-Huber's stress tensor for contacting spheres. J. Theor. Appl. Mech. **1**(2), 331–357 (1982)
16. I.N. Sneddon, The relation between load and penetration in the axisymmetric Boussinesq problem for a punch of arbitrary profile. Int. J. Eng. Sci. **3**, 47–57 (1965)
17. K.L. Johnson, A note on the adhesion of elastic solids. British J. Appl. Phys. **9**, 199–200 (1958)
18. D. Maugis, *Contact, adhesion and rupture of elastic solids* (Springer, Berlin, 2000), pp. 213–216
19. M. Heß, On the reduction method of dimensionality: the exact mapping of axisymmetric contact problems with and without adhesion. Phys. Mesomech. **15**(5–6), 264–269 (2012)
20. G.A.D. Briggs, B.J. Briscoe, The effect of surface topography on the adhesion of elastic solids. J. Phys. D Appl. Phys. **10**, 2453–2466 (1977)
21. K.N.G. Fuller, A.D. Roberts, Rubber rolling on rough surfaces. J. Phys. D Appl. Phys. **14**, 221–239 (1981)
22. P.R. Guduru, Detachment of a rigid solid from an elastic wavy surface: Theory. J. Mech. Phys. Solids **55**, 445–472 (2007)
23. P.R. Guduru, C. Bull, Detachment of a rigid solid from an elastic wavy surface: Experiments. J. Mech. Phys. Solids **55**, 473–488 (2007)
24. C. Jin, K. Khare, S. Vajpayee, S. Yang, A. Jagota, C.-Y. Hui, Adhesive contact between a rippled elastic surface and a rigid spherical indenter: from partial to full contact. Soft Matter **7**, 10728–10736 (2011)
25. H. Yao, H. Gao, Optimal shapes for adhesive binding between two elastic bodies. J. Colloid Interface Sci. **298**(2), 564–572 (2006)
26. H. Yao, H. Gao, Mechanical principles of robust and releasable adhesion of gecko. J. Adhes. Sci. Technol. **21**(12–13), 1185–1212 (2007)
27. D. Maugis, Extension of the Johnson-Kendall-Roberts theory of elastic contact of spheres to large contact radii. Langmuir **11**(2), 679–682 (1995)
28. Y.-Y. Lin, H.-Y. Chen, Effect of large deformation and material nonlinearity on the JKR (Johnson-Kendall-Roberts) test of soft elastic materials. J. Polym. Sci. Part B: Polym. Phys. **44**(19), 2912–2922 (2006)
29. J.A. Greenwood, Adhesion of small spheres. Philos. Mag. **89**(11), 945–965 (2009)
30. D. Maugis, M. Barquins, Adhesive contact of sectionally smooth-ended punches on elastic half-spaces: theory and experiment. J. Phys. D Appl. Phys. **16**(10), 1843–1874 (1983)

Chapter 5
Tangential Contact

Markus Heß and Valentin L. Popov

5.1 Introduction

The fundamental property that allows the reduction of three-dimensional contacts to one-dimensional ones is the proportionality of the incremental stiffness to the diameter of the contact area. This property is exhibited by both normal and tangential contacts. The idea behind dimensionality reduction can, therefore, be directly transferred to tangential contacts.

The tangential stiffness of a round contact with the diameter D between two elastic half-spaces is given by the equation [1]

$$k_x = DG^*, \tag{5.1}$$

where G^* is defined as

$$\frac{1}{G^*} = \frac{(2-\nu_1)}{4G_1} + \frac{(2-\nu_2)}{4G_2}. \tag{5.2}$$

G_1 and G_2 denote the shear moduli of the contacting bodies. Thereby, it should be noted that it is assumed that materials are "elastically similar":

$$\frac{1-2\nu_1}{G_1} = \frac{1-2\nu_2}{G_2}, \tag{5.3}$$

which allows the tangential contact problem to be decoupled from the normal contact problem [2]. This condition is identically met for the important case of a contact between a rigid body and an incompressible elastomer (both sides of Eq. (5.3) are zero in this case).

Now, we consider a linearly elastic foundation consisting of springs with the stiffness

$$\Delta k_x = G^* \Delta x, \tag{5.4}$$

V.L. Popov and M. Heß, *Method of Dimensionality Reduction in Contact Mechanics and Friction*, DOI 10.1007/978-3-642-53876-6_5

where Δx is the distance between the springs. The stiffness (5.1) is trivially reproduced with this foundation. In this chapter, we will show that the one-dimensional elastic foundation with the normal stiffness defined in Chap. 3 and the tangential stiffness (5.4) can also be used to *exactly* map tangential contacts with Coulomb friction for *arbitrarily axially-symmetric* profiles. We begin our considerations with the contact between parabolic bodies.

5.2 Tangential Contact with Friction for Parabolic Bodies

We consider a rigid three-dimensional parabolic body with the radius of curvature R that is pressed into an elastic half-space with the normal force F_N and subsequently loaded in the horizontal direction with the force F_x. We assume that the frictional forces acting in the contact can be simply described using Coulomb's law of friction with a constant coefficient of friction μ. From the theory of three-dimensional contact problems, it is known that even the application of an arbitrarily small force results in the formation of a slip domain at the boundary of the contact area, while the inner domain initially sticks [1]. With increasing tangential force, the stick domain shrinks until slip is initiated in the entire contact area. In this section, we investigate the one-dimensional mapping of the aforementioned three-dimensional contact problem (Fig. 5.1).

As before, let the indentation depth of the rigid body into the linearly elastic foundation be denoted by d. The vertical displacement of a spring at a distance x from the middle point of the contact is

$$u_z(x) = d - \frac{x^2}{2R_1}. \tag{5.5}$$

The radius R_1 must be set to $R_1 = R/2$ according to the rules of the reduction method. The elastic force of a single spring at the point x is

$$f_N(x) = E^* u_z(x) \Delta x = \left(d - \frac{x^2}{2R_1} \right) E^* \Delta x. \tag{5.6}$$

The contact radius is obtained from the condition $u_z(a) = 0$:

$$a = \sqrt{2R_1 d} = \sqrt{Rd}. \tag{5.7}$$

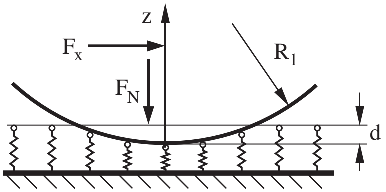

Fig. 5.1 One-dimensional mapping of contact loaded both normally and tangentially

Until now, we have only used the results known from Chap. 3. Now, we denote the horizontal displacement of the parabolic indenter with respect to the foundation with u_x. Then, the horizontal component of the force acting on a sticking spring is

$$f_x(x) = \Delta k_x u_x = G^* \Delta x \cdot u_x. \tag{5.8}$$

We determine the boundary of the sticking domain $x = \pm c$ from the condition that the tangential force achieves its maximum value:

$$f_x(c) = \mu f_N(c) \tag{5.9}$$

or

$$G^* \Delta x \cdot u_x = \mu \left(d - \frac{c^2}{2R_1} \right) E^* \Delta x. \tag{5.10}$$

From this, it follows that

$$c^2 = 2R_1 \left(d - \frac{G^*}{E^*} \frac{u_x}{\mu} \right). \tag{5.11}$$

Solving with respect to u_x results in

$$u_x = \mu \frac{E^*}{G^*} \left(d - \frac{c^2}{2R_1} \right) = \mu \frac{E^*}{G^*} \left(d - \frac{c^2}{R} \right). \tag{5.12}$$

This result agrees with the result for the three-dimensional contact problem [1].

The slip condition outside of the sticking domain means that every point here fulfills Coulomb's law of friction:

$$f_x(x) = \mu f_N(x) \quad \text{for} \quad c < |x| < a. \tag{5.13}$$

Now, we calculate the normal and tangential forces acting in the entire contact area. For the normal force, we once again obtain the Hertzian result:

$$F_N = \int_{-a}^{a} \left(d - \frac{x^2}{2R_1} \right) E^* \mathrm{d}x = \frac{4}{3} E^* (2R_1)^{1/2} d^{3/2} = \frac{2E^* a^3}{3R_1}. \tag{5.14}$$

The tangential force is calculated as

$$F_x = 2 \int_0^c G^* u_x \mathrm{d}x + 2 \int_c^a \mu \left(d - \frac{x^2}{2R_1} \right) E^* \mathrm{d}x = \frac{2E^* a^3 \mu}{3R_1} \left(1 - \left(\frac{c}{a} \right)^3 \right) = \mu F_N \left(1 - \left(\frac{c}{a} \right)^3 \right). \tag{5.15}$$

From this, the relationship between the loading and the radius of the contact area can be determined:

$$\frac{c}{a} = \left(1 - \frac{F_x}{\mu F_N} \right)^{1/3}. \tag{5.16}$$

This result also agrees exactly with that of the three-dimensional problem [1].

We obtain the displacement above which the entire contact area exhibits slip by inserting $c = 0$ into Eq. (5.12):

$$u_{x,\mathrm{max}} = u_x = \mu \frac{E^*}{G^*} d, \tag{5.17}$$

which, of course, also agrees exactly with that of the three-dimensional case.

5.3 Tangential Contact with Friction for Arbitrary Axially-Symmetric Bodies

In the last section, it was proven that the tangential contact with partial slip for two parabolic bodies can be exactly mapped using the method of dimensionality reduction. The generalization to tangential contacts of arbitrarily formed, axially-symmetric bodies is the topic of this chapter; the complete proofs including all assumptions can be found in Chap. 18.

In order to solve the classical three-dimensional contact problem, Cattaneo [3] and Mindlin [4] initially calculated the tangential displacement in the direction of the applied tangential force, which results from the state of full slip. Subsequently, they superimposed the corresponding tangential stress distribution with a second one of the same form, but with the opposite direction. In this way, constant tangential displacements were obtained for an inner circular area and the tangential stresses in the outer domain that are proportional to the normal stresses, which are the boundary conditions for the tangential contact with *partial* slip. Although the way was paved to solve tangential contact problems with the method of Cattaneo and Mindlin, its application to other geometries appeared exceedingly difficult, because they required explicit knowledge/calculation of the tangential displacements. Not until 50 years later did Truman et al. [5], using this method, successfully derive the solution to the tangential contact problem between a conical indenter and an elastic half-space. In the same year, Jäger [6] arrived at the conclusion that within the framework of Cattaneo-Mindlin theory, every axially-symmetric tangential contact problem can be completely described by the normal contact problem so that an explicit calculation of the tangential displacement is unnecessary. Thereby, we remember that elastically similar materials (5.3) are assumed everywhere in this chapter, which allows the contact problem to be decoupled. Furthermore, it is assumed that the frictional stresses point in the direction of the applied tangential force, which strictly speaking, violates a part of Coulomb's law of friction. Due to the addition of a slippage component perpendicular to the applied force, the tangential stresses and slip are not opposite each other at every point in the slip domain. In [7, 8], as well as Chap. 18, it is explained why we can neglect this deviation.

Due to the principle of superposition from Jäger [6, 9], the tangential stresses are equivalent to the difference between the actual normal stress and those that correspond to a smaller contact radius (the stick radius c) multiplied with the coefficient of friction. The same is true for the tangential force F_x and the relative tangential displacement u_x:

$$\tau_{zx}(r) = \mu\left[\sigma_{zz}(a,r) - \sigma_{zz}(c,r)\right] \tag{5.18}$$

$$F_x = \mu[F_N(a) - F_N(c)] \tag{5.19}$$

$$u_x = \mu\frac{E^*}{G^*}[d(a) - d(c)]. \tag{5.20}$$

It is proven in Chap. 18 that based on the Eqs. (5.18)–(5.20), these relationships can be obtained from the method of dimensionality reduction. Thus, the method already introduced within the framework of the tangential contact for a parabolic body is generally valid. It consists primarily of two central ansätze:

1. In the one-dimensional equivalent model, the tangential spring forces at the boundary of the stick domain must assume the maximum possible value for the static frictional force

   $$f_x(c) = \mu f_N(c) \qquad \Leftrightarrow \qquad q_x(c) = \mu\, q(c). \tag{5.21}$$

   For a given tangential displacement u_x, the radius of the stick domain c can be obtained.
2. The tangential force is given analogously to the normal force from the sum of the tangential spring forces and, therewith, the tangential distributed load

   $$F_x = \int_{-a}^{a} q_x(x)\mathrm{d}x = 2c\,G^* u_x + 2\mu\int_{c}^{a} q(x)\mathrm{d}x. \tag{5.22}$$

   On the right side, the piecewise-defined function

$$q_x(x) = \begin{cases} G^* u_x & \text{for } |x| \le c \\ \mu\, q(x) & \text{for } c < |x| \le a \\ 0 & \text{for } |x| > a \end{cases} \tag{5.23}$$

has already been inserted.

Also, based on the superposition from Jäger, the three-dimensional tangential contact with partial slip can be replaced by two three-dimensional normal contacts. This technique has already been used in various numerical simulations. It is directly evident that such a superposition also retains its validity for the equivalent one-dimensional normal contact. Nevertheless, it is preferred, and requires less effort, to directly map the three-dimensional partial slip problem to a one-dimensional partial slip problem, rather than mapping two three-dimensional normal contacts and superimposing them.

Now, we consider an axially-symmetric indenter which has a profile with a form given by a power function with a positive real exponent

$$\tilde{z}(r) = f(r) = C_n r^n \tag{5.24}$$

and is initially pressed into an elastic half-space with the normal force F_N and subsequently, maintaining the normal force, loaded with the tangential force F_x. We are now looking for the radius of the stick domain c and the relative tangential displacement u_x of both bodies. For the normal contact, one can take the solutions from Problem 2 in Chap. 3:

$$d(a) = C_n \kappa_n a^n \tag{5.25}$$

$$F_N(a) = \frac{2n}{n+1} E^* \kappa_n C_n a^{n+1}. \tag{5.26}$$

Let us remember that the relationships above arise from the indentation of the (rigid) profile

$$g(x) = \kappa_n C_n |x|^n, \tag{5.27}$$

which is vertically scaled by the factor κ_n, into a one-dimensional linearly elastic foundation.

The extension to the tangential contact requires that the spring elements be independent from one another in the tangential direction and possess the stiffness $\Delta k_x = G^* \Delta x$. As in the three-dimensional contact problem, Coulomb's law of friction is also locally valid in the one-dimensional model. By the addition of a tangential force, the tangential springs in the area near the edge of the contact area ($c < |x| \leq a$) slide because the vertical spring forces, and therefore, the maximum frictional forces, are locally too small to satisfy the condition $f_x(x) < \mu f_N(x)$. In this domain, the spring forces (normal and tangential) at every point are directly proportional to one another: $f_x(x) = \mu f_N(x)$. Within this radius ($|x| \leq c$), all of the tangential spring elements stick and, therefore, experience the same tangential displacement u_x. In summary, the distribution of the tangential spring forces can be expressed by means of the piecewise defined distributed load

$$q_x(x) = \begin{cases} G^* u_x & \text{for} \quad |x| \leq c \\ \mu E^* \kappa_n C_n (a^n - |x|^n) & \text{for} \quad c < |x| \leq a \\ 0 & \text{for} \quad |x| > a \end{cases} . \tag{5.28}$$

We determine the tangential displacement u_x as a function of the radius of the stick domain c from the condition (5.21)

$$q_x(c) = \mu q(c) \quad \Rightarrow \quad u_x(c) = \mu \frac{E^*}{G^*} \kappa_n C_n \left(a^n - c^n\right). \tag{5.29}$$

The sum of all tangential spring forces must correspond to the applied tangential force, which Eq. (5.22) provides when taking (5.29) into account:

$$F_x = \frac{2n}{n+1}\mu E^* \kappa_n C_n a^{n+1}\left[1 - \left(\frac{c}{a}\right)^{n+1}\right]. \tag{5.30}$$

Solving with respect to the characteristic ratio of the contact radii and using (5.26) leads to

$$\frac{c}{a} = \left(1 - \frac{F_x}{\mu F_N}\right)^{\frac{1}{1+n}}. \tag{5.31}$$

For $n = 2$, the result of the classical contact problem from Cattaneo and Mindlin is obtained, but also the special case of a flat, cylindrical indenter can be obtained from (5.31) if we consider $n \to \infty$. As long as the tangential force F_x is smaller than the maximum static force of friction μF_N, then the *entire* contact will stick in this case. However, if this limit is reached, then complete sliding initiates. Figure 5.2 shows Eq. (5.31) graphically for the above named geometries (paraboloid and flat indenter) as well as the conical profile ($n = 1$). The gray curve is for an exponent of $n = 6$ and signifies the family of curves for increasing n.

Using the now known radius of stick, one can also determine the tangential displacement with respect to the input values. After inserting (5.31) into (5.29) and using (5.26), it follows that

$$u_x = \frac{n+1}{2n}\frac{\mu F_N}{G^* a}\left[1 - \left(1 - \frac{F_x}{\mu F_N}\right)^{\frac{n}{n+1}}\right]. \tag{5.32}$$

Naturally, Eq. (5.32) for $n = 2$ is the result for the tangential contact of a sphere [1]. For the tangential contact between a flat, cylindrical indenter and a half-space, the limit of u_x as $n \to \infty$ must once again be found, which leads to the elementary result of

$$\lim_{n\to\infty} u_x(n) = \frac{F_x}{2G^* a}. \tag{5.33}$$

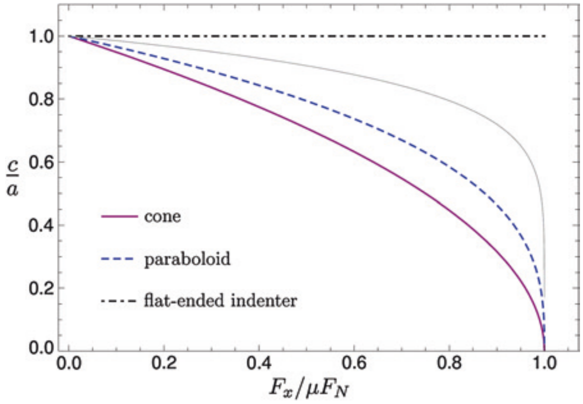

Fig. 5.2 Radius of stick c as a function of applied tangential force F_x for a conical, parabolic, and flat cylindrical indenter

Fig. 5.3 Tangential displacement u_x plotted with respect to the tangential force F_x (normalized)

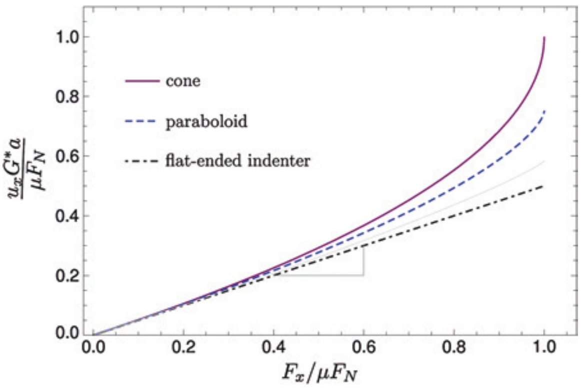

The direct proportionality between force and displacement is shown in Fig. 5.3. The slope triangle on the curve for the flat, cylindrical indenter indicates the compliance. For extremely small tangential forces, for which the slip domain is constrained to a very small ring, Eq. (5.33) is valid for all profiles, regardless of the form function exponent.

Let it once more be emphasized that the one-dimensional ansätze (5.21) and (5.22) allow for the exact mapping of tangential contacts for *arbitrary* axially-symmetric bodies. Profiles that we can describe by a *power series* as well as those that are *piecewise defined* are also included here. The latter, however, can cause difficulties, because the one-dimensional profile cannot be found simply through scaling, but must be found by integration (see Problem 3).

5.4 Mapping of Stresses in the Tangential Contact

Due to the principle of superposition from Jäger, the tangential stresses can be obtained, completely analogously to the normal stresses, from the Abel-like integral transformation of the tangential distributed load $q_x(x)$:

$$\tau_{zr}(r) = \frac{1}{\pi}\frac{1}{r}\frac{d}{dr}\int_r^a \frac{x \cdot q_x(x)}{\sqrt{x^2 - r^2}}\mathrm{d}x = \frac{1}{\pi}\int_r^a \frac{q_x'(x)}{\sqrt{x^2 - r^2}}\,\mathrm{d}x - \frac{1}{\pi}\frac{q_x(a)}{\sqrt{a^2 - r^2}}. \tag{5.34}$$

The proof for this is presented in Chap. 18. It follows from the alternate presentation of the piecewise-defined, linear force density from (5.23) as the difference between two vertical distributed loads and subsequent use of (5.18).

As an example, we want to use Eq. (5.34) on the classical tangential contact between a parabolic body and a plane. In the first step, we define the tangential linear load for the one-dimensional model, which we already implicitly drew upon for the calculation of the tangential force in (5.15):

$$q_x(x) = \begin{cases} G^* u_x & \text{for} \quad |x| \le c \\ \mu E^* \left(d - \dfrac{x^2}{R} \right) & \text{for } c < |x| \le a \\ 0 & \text{for} \quad |x| > a \end{cases} . \tag{5.35}$$

In order to keep the effort required to a minimum, we use the integral expression on the right side of (5.34),[1] which requires the derivative of the linear load:

$$q_x'(x) = \begin{cases} 0 & \text{for } |x| \le c \ \vee \ |x| > a \\ -2\mu E^* \dfrac{x}{R} & \text{for } c < |x| \le a \end{cases} . \tag{5.36}$$

By inserting (5.36) into (5.34), we must differentiate between the two cases $0 \le r < c$ and $c \le r \le a$ and, therefore, obtain

$$\tau_{zr}(r) = -\frac{2\mu E^*}{R\pi} \cdot \begin{cases} \int\limits_c^a \dfrac{x}{\sqrt{x^2 - r^2}} \, \mathrm{d}x & \text{for } 0 \le r < c \\ \int\limits_r^a \dfrac{x}{\sqrt{x^2 - r^2}} \, \mathrm{d}x & \text{for } c \le r \le a \end{cases} . \tag{5.37}$$

After simple integration, we obtain

$$\tau_{zr}(r) = -\frac{2\mu E^*}{R\pi} \left[\sqrt{a^2 - r^2} \cdot H\left(1 - \frac{r}{a}\right) - \sqrt{c^2 - r^2} \cdot H\left(1 - \frac{r}{c}\right) \right], \tag{5.38}$$

where $H(x)$ is the Heaviside step function. It is generally known that Eq. (5.38) corresponds to the exact distribution of the tangential stress in a three-dimensional contact [1].

5.5 Mapping of Local Slip

The micro-slip in the outer area of a tangential contact is generally described by the *local* slip $s_{x,3D}(r)$. This denotes the tangential relative displacement of the surface points in the slip domain of the contact area, which is required for the calculation of wear and other tribological processes. For the sake of clarity, the constant tangential displacement of all points within the sticking domain will be denoted in the section with

$$u_x(r) = \delta_x = \text{const. for } 0 \le r \le c \, . \tag{5.39}$$

---

[1] Let it be noted that in special cases of non-differentiable form functions, only the first integral expression in (5.34) may be used.

The fact that this displacement can be mapped exactly by the method of dimensional reduction has already been shown. In a similar way, the local slip in the slip domain can be reproduced as

$$s_{x,3D}(r) := u_x(r) - \delta_x \text{ for } c < r \leq a\,. \tag{5.40}$$

Once again, Jäger's principle of superposition is at the center of our considerations. Using this, the following equation for the slip of an axially-symmetric contact obtained from the slip in a one-dimensional model $s_{x,1D}(x)$ can be easily understood:

$$s_{x,3D}(r) = \frac{2}{\pi}\int_0^r \frac{s_{x,1D}(x)}{\sqrt{r^2 - x^2}}\mathrm{d}x \quad \text{with} \quad s_{x,1D}(x) = u_x(x) - \delta_x. \tag{5.41}$$

Here, $u_x(x)$ is the tangential displacement of the surface of the linearly elastic foundation.

For the classical tangential contact of a parabolic body with a plane, the application of the transformation (5.41) will be explained in the following. For this, we first introduce slip in the one-dimensional model. From the tangential distributed load according to (5.35), the tangential displacements can be directly found for the equivalent system. This is because both are proportional to each other, whereby the effective shear modulus G^* is the proportionality factor:

$$u_x(x) = \begin{cases} \delta_x & \text{for} \quad |x| \leq c \\ \mu \dfrac{E^*}{G^*} \underbrace{\left(d(a) - \dfrac{x^2}{R}\right)}_{=u_z(x)} & \text{for } c < |x| \leq a \end{cases}. \tag{5.42}$$

With this, the following is valid for the one-dimensional slip:

$$s_{x,1D}(x) := u_x(x) - \delta_x = \begin{cases} 0 & \text{for} \quad |x| \leq c \\ \mu \dfrac{E^*}{G^*}\left(d(c) - \dfrac{x^2}{R}\right) & \text{for } c < |x| \leq a \end{cases}. \tag{5.43}$$

Insertion of (5.43) into (5.41) results initially in

$$s_{x,3D}(r) = \frac{2\mu E^*}{\pi R G^*}\int_c^r \frac{c^2 - x^2}{\sqrt{r^2 - x^2}}\mathrm{d}x \text{ for } c < r \leq a \tag{5.44}$$

and after simple calculation, we find the three-dimensional slip from Johnson [7] in the domain of micro-slip:

$$s_{x,3D}(r) = \frac{\mu E^*}{\pi R G^*}\left[\left(2c^2 - r^2\right) \cdot \left(\frac{\pi}{2} - \arcsin\left(\frac{c}{r}\right)\right) - c \cdot \sqrt{r^2 - c^2}\right]. \tag{5.45}$$

5.6 Problems

Problem 1 Determine the radius of stick and the relative tangential displacement with respect to the tangential force for the tangential contact between an elastic cone and an elastic half-space. Elastically similar materials are assumed. It is also assumed that the normal contact problem for which tangential loading is investigated has already been solved (see Problem 1 in Chap. 3)

Solution The equivalent one-dimensional contact problem consists of a rigid cross-section of a conical indenter scaled vertically by a factor of $\kappa_1 = \pi/2$, which is pressed into a one-dimensional linearly elastic foundation and subsequently loaded with a tangential force. All tangential spring elements whose spring forces have not yet reached the spatially-dependent maximum static force of friction $\mu f_N(x)$ undergo the respective displacement u_x. In the outer ring, the vertical spring forces, and therefore, the force of static friction, is so small that partial sliding occurs. At the stick–slip limit, the tangential spring forces must assume the maximum force of static friction

$$G^* \Delta x \, u_x(c) = \mu \, E^* \Delta x \left[d - g(c) \right], \tag{5.46}$$

which results in *constant* tangential displacement of all points in the stick domain:

$$u_x(x) = \mu \frac{\pi}{2} \frac{E^* \tan\theta}{G^*} (a - c) \quad \text{for} \quad |x| \le c. \tag{5.47}$$

In equilibrium, the tangential force F_x must be equal to the sum of the tangential spring forces:

$$\begin{aligned} F_x &= G^* \int_{-a}^{a} u_x(x) \,\mathrm{d}x = 2G^* \int_{0}^{c} u_x(x) \,\mathrm{d}x + 2\mu E^* \int_{c}^{a} u_z(x) \,\mathrm{d}x \\ &= \frac{\pi}{2} \mu E^* \tan{(\theta)} \, a^2 \left[1 - \left(\frac{c}{a} \right)^2 \right]. \end{aligned} \tag{5.48}$$

By taking the results of the normal contact problems into account (see Problem 1 from Chap. 3), Eqs. (5.47) and (5.48) can be brought into the following form:

$$\frac{c}{a} = \sqrt{1 - \frac{F_x}{\mu F_N}} \tag{5.49}$$

$$u_x = \frac{\mu F_N}{G^* a} \left[1 - \sqrt{1 - \frac{F_x}{\mu F_N}} \right]. \tag{5.50}$$

Of course, these equations also result from (5.31) and (5.32) for $n = 1$ and correspond exactly with the three-dimensional solution from Truman et al. [5].

Problem 2 Calculate the tangential stress distribution within the contact area for the tangential contact handled in Problem 1 with the help of the Abel transformation in Eq. (5.34).

Solution The calculation of the three-dimensional tangential stress from the one-dimensional model requires setting up the equation for and subsequently differentiating the tangential linear load. The linear load was already implicitly used to find the tangential force in Eq. (5.48). Its derivative is

$$q_x'(x) = \begin{cases} 0 & \text{for } |x| \le c \quad \text{and} \quad |x| > a \\ -\mu E^* \frac{\pi}{2} \tan\theta \cdot \operatorname{sign}(x) & \text{for } c < |x| \le a \end{cases}. \tag{5.51}$$

Inserting (5.51) into Eq. (5.34) initially provides

$$\tau_{zr}(r) = -\frac{1}{2}\mu E^* \tan\theta \cdot \begin{cases} \int\limits_c^a \frac{1}{\sqrt{x^2 - r^2}} \mathrm{d}x & \text{for } 0 \le r < c \\ \int\limits_r^a \frac{1}{\sqrt{x^2 - r^2}} \mathrm{d}x & \text{for } c \le r \le a \end{cases}, \tag{5.52}$$

and after integration and simple rearrangement,

$$\tau_{zr}(r) = -\frac{1}{2}\mu E^* \tan\,\theta \left[\operatorname{arcosh}\left(\frac{a}{r}\right) \cdot H\left(1 - \frac{r}{a}\right) - \operatorname{arcosh}\left(\frac{c}{r}\right) \cdot H\left(1 - \frac{r}{c}\right)\right]. \tag{5.53}$$

The tangential stress distribution, normalized by the mean value in the case of complete sliding, is plotted in Fig. 5.4 for sizes of the stick domain. The finite value at the point $r = 0$ is

$$\lim_{r\to 0} \frac{-\tau_{zr}(r)}{\mu p_m} = \lim_{r\to 0} \left[\operatorname{arcosh}\left(\frac{a}{r}\right) - \operatorname{arcosh}\left(\frac{c}{r}\right)\right] = \lim_{r\to 0} \ln\left(\frac{a + \sqrt{a^2 - r^2}}{c + \sqrt{c^2 - r^2}}\right) = \ln\left(\frac{a}{c}\right). \tag{5.54}$$

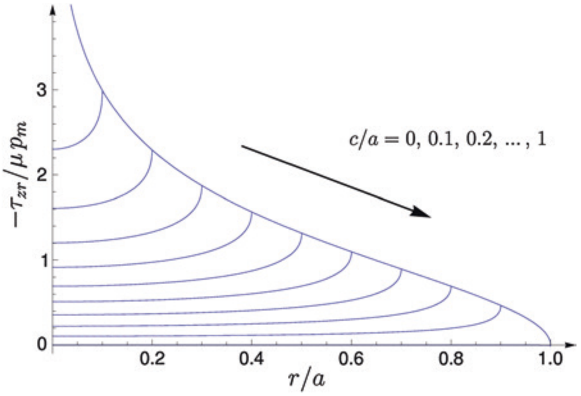

Fig. 5.4 Normalized tangential stress distribution with respect to the size of the stick domain $c/a = 0.1, 0.2, \ldots, 1$

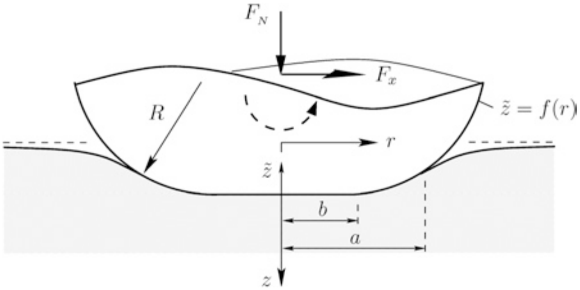

Fig. 5.5 Tangential contact of a flat indenter with rounded edges (radius R)

Problem 3 A flat, cylindrical indenter with rounded edges is initially pressed into an elastic half-space with the normal force F_N and subsequently loaded with a (presently unknown) tangential force F_x, which results in a given relative tangential displacement u_x of the two bodies. It is assumed that the bodies are composed of elastically similar materials and that the profile of the indenter is given by the following (see Fig. 5.5):

$$f(r) = \begin{cases} 0 & \text{for } 0 \le r < b \\ \frac{1}{2R}(r-b)^2 & \text{for } b \le r \le a \end{cases}. \tag{5.55}$$

Determine the indentation depth and normal force as a function of contact radius with the help of the reduction method. Furthermore, calculate the tangential displacement and tangential force as a function of the stick radius.

Solution In the first step, the one-dimensional equivalent profile must be determined. The piecewise-defined function according to (5.55) requires the application of the generalized formula (3.27)

$$g(x) = x\int_0^x \frac{f'(r)}{\sqrt{x^2-r^2}}\mathrm{d}r = \begin{cases} 0 & \text{for } 0 \le x < b \\ \frac{x}{R}\int_b^x \frac{r-b}{\sqrt{x^2-r^2}}\mathrm{d}r & \text{for } b \le x \le a \end{cases}. \tag{5.56}$$

Calculating the integral in Eq. (5.56) requires nothing more than elementary mathematics:

$$\int_b^x \frac{r-b}{\sqrt{x^2-r^2}}dr = \sqrt{x^2-b^2} - b\arccos\left(\frac{b}{x}\right). \tag{5.57}$$

Nevertheless, we must remember that (5.56) has to be extended axis-symmetrically to the domain of $-a \le x \le 0$. Then, we obtain

$$g(x) = \begin{cases} 0 & \text{for } \quad |x| < b \\ \frac{|x|}{R}\sqrt{x^2-b^2} - \frac{b|x|}{R}\arccos\left(\frac{b}{|x|}\right) & \text{for } b \le |x| \le a \end{cases}. \tag{5.58}$$

The normalized original and equivalent profiles are shown in Fig. 5.6.

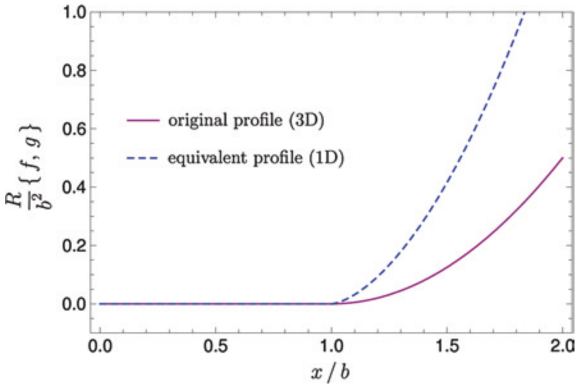

Fig. 5.6 Flat indenter with rounded edges: Comparison between the three-dimensional and one-dimensional profiles

The indentation depth as a function of the contact radius is found from the one-dimensional profile using

$$d = g(a) = \frac{a}{R}\sqrt{a^2 - b^2} - \frac{ba}{R}\arccos\left(\frac{b}{a}\right), \tag{5.59}$$

while the dependence of the normal force on the contact radius is found from the sum of all spring forces in the contact for the one-dimensional model:

$$\begin{aligned} F_N &= 2E^* \int_0^a \left[d - g(x)\right] \mathrm{d}x \\ &= 2E^* \int_0^b d\,\mathrm{d}x + 2E^* \int_b^a \left[d - \left(\frac{x}{R}\sqrt{x^2 - b^2} - \frac{bx}{R}\arccos\left(\frac{b}{x}\right)\right)\right] \mathrm{d}x. \end{aligned} \tag{5.60}$$

Integration, taking (5.59) into account, and rearranging results in

$$F_N = \frac{4}{3}E^*\frac{a^3}{R}\left[\left(1 - \frac{1}{4}\left(\frac{b}{a}\right)^2\right)\sqrt{1 - \left(\frac{b}{a}\right)^2} - \frac{3}{4}\frac{b}{a}\arccos\left(\frac{b}{a}\right)\right]. \tag{5.61}$$

The limiting case of $b = 0$ is a parabolic profile. As expected, the Eqs. (5.59) and (5.61) reproduce in this limit the Hertzian relations.

The boundary between slip and stick can be found using Eq. (5.21), in other words, requiring that the tangential spring force reaches the maximum possible force of static friction at the point $x = c$. With the help of (5.58) and (5.59), one of the relationships is found:

$$u_x = \mu\frac{E^*}{G^*}\frac{a}{R}\left[\sqrt{a^2 - b^2} - b\arccos\left(\frac{b}{a}\right) - \frac{c}{a}\left(\sqrt{c^2 - b^2} - b\arccos\left(\frac{b}{c}\right)\right)\right]. \tag{5.62}$$

Now, it is only left to find the dependence between the tangential force and the stick radius. For this, we look at a distributed load in the one-dimensional model

$$q_x(x) = \begin{cases} G^* u_x & \text{for} \quad |x| \le c \\ \mu E^* \left[d - \dfrac{|x|}{R} \left(\sqrt{x^2 - b^2} - b \arccos\left(\dfrac{b}{|x|} \right) \right) \right] & \text{for } c < |x| \le a \\ 0 & \text{for} \quad |x| > a \end{cases} \tag{5.63}$$

and integrate this over the contact width in the reduced model:

$$F_x = \int_{-a}^{a} q_x(x) \mathrm{d}x = 2cG^* u_x + 2\mu E^* \int_{c}^{a} \left[d - \frac{x}{R} \left(\sqrt{x^2 - b^2} - b \arccos\left(\frac{b}{x} \right) \right) \right] \mathrm{d}x. \tag{5.64}$$

The integral on the right-hand side already appeared in the calculation of the normal force in (5.60). After calculating the antiderivative and taking the lower limit of integration into account, we obtain

$$\begin{aligned} F_x = \mu \frac{E^*}{3R} \left[\left(4a^2 - b^2 \right) \sqrt{a^2 - b^2} - 3a^2 b \arccos\left(\frac{b}{a} \right) \right] \\ - \mu \frac{E^*}{3R} \left[\left(4c^2 - b^2 \right) \sqrt{c^2 - b^2} - 3c^2 b \arccos\left(\frac{b}{c} \right) \right]. \end{aligned} \tag{5.65}$$

We can be directly convinced of the correctness of Eq. (5.65) if we consider the principle of superposition by Jäger. According to (5.19), the tangential force is equivalent to the difference between the current normal force and one that would result in a stick radius c multiplied by the coefficient of friction. Using Eq. (5.61), this relationship can be easily verified. Figure 5.7 shows the normalized dependence of the stick radius on the tangential force for various cases. The limiting case of $b = 0$ corresponds to the classical result of Cattaneo and Mindlin. In contrast, if the contact area is only slightly larger than the flat section ($b = 0.95a$), then the curve approaches that of a flat indenter. A comparison is shown in Fig. 5.2.

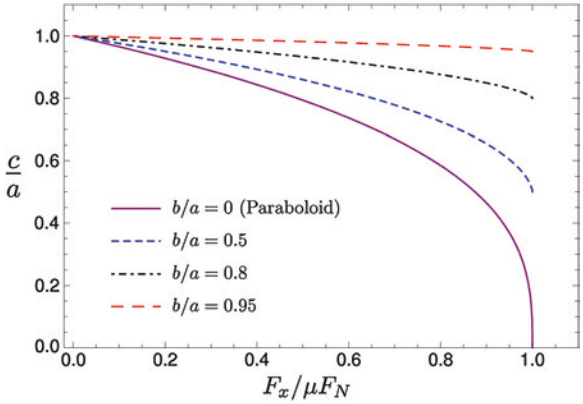

Fig. 5.7 Stick radius c as a function of applied tangential force F_x for a flat indenter with rounded edges

Although it has not yet been mentioned, it was assumed in the above calculations that $b \le c \le a$, and therefore, partial sliding within the flat section is not possible. Figure 5.7 emphasizes the validity of this assumption. As soon as the slip domain includes the rounded edges, then the transition to complete slip takes place. For the analogous planar contact problem, a corresponding behavior was analytically proven [10] and verified by finite element calculations [11].

Problem 4 Determine the integral form for the normal and tangential stress distribution for the contact between a flat indenter with rounded edges having a radius of curvature of R and a half-space (see Fig. 5.5). Assume a constant distributed loading of the one-dimensional model and visualize the numeric solutions of the integral expressions.

Solution The vertical distributed load in the one-dimensional model is directly proportional to the normal displacement of the surface and according to Eq. (5.58) is

$$q(x) = \begin{cases} d & \text{for} \quad |x| \le b \\ E^*\left[d - \frac{|x|}{R}\left(\sqrt{x^2-b^2} - b\arccos\left(\frac{b}{|x|}\right)\right)\right] & \text{for } b < |x| \le a \\ 0 & \text{for} \quad |x| > a \end{cases} . \tag{5.66}$$

The derivative is required for the calculation of the normal stress distribution. Because of axial symmetry, we only have to determine this for positive x:

$$q'(x) = \begin{cases} 0 & \text{for } 0 \le x < b \ \vee \ x > a \\ -\frac{E^*}{R}\left[2\sqrt{x^2-b^2} - b\arccos\left(\frac{b}{x}\right)\right] & \text{for} \quad b \le x \le a \end{cases} . \tag{5.67}$$

According to Eq. (3.37) from Chap. 3, the normal stress is

$$\sigma_{zz}(r) = \begin{cases} -\frac{E^*}{\pi R}\int\limits_b^a \frac{2\sqrt{x^2-b^2} - b\arccos(b/x)}{\sqrt{x^2-r^2}}\,\mathrm{d}x & \text{for } 0 \le r < b \\ -\frac{E^*}{\pi R}\int\limits_r^a \frac{2\sqrt{x^2-b^2} - b\arccos(b/x)}{\sqrt{x^2-r^2}}\,\mathrm{d}x & \text{for } b \le r \le a \end{cases} . \tag{5.68}$$

These integral relations are identical to those of the three-dimensional theory. They must be solved numerically. Figure 5.8 shows the distribution of the normal stress in normalized form, where $p_m := F_N/\pi a^2$ is the mean stress. Several ratios of the length of the flatness b and the contact radius a are shown. For $b = 0$, we understandably obtain the Hertzian results, while for $b \to a$, we obtain the singularity at the edges of the contact for a flat, cylindrical indenter (with sharp edges). The presence of rounded edges guaranties a finite maximum in stress, which decreases with b/a towards the center.

The calculation of the tangential stress follows completely analogously. The tangential distributed load of the linearly elastic foundation was already shown in Problem 3 so that we must now only focus on $0 \le x \le a$ and differentiate (5.63) with respect to x:

$$q_x'(x) = \begin{cases} 0 & \text{for } 0 \le x < c \ \vee \ x > c \\ -\frac{\mu E^*}{R}\left[2\sqrt{x^2-b^2} - b\arccos\left(\frac{b}{x}\right)\right] & \text{for} \quad c \le x \le a \end{cases} . \tag{5.69}$$

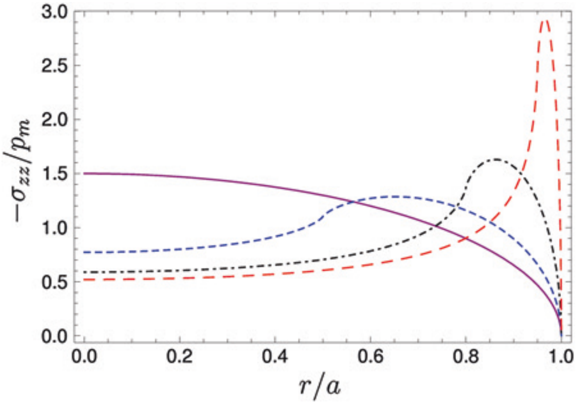

Fig. 5.8 Distribution of the normalized stress for the contact in Fig. 5.5; the cases shown are those from Problem 3: $b/a = 0$ (Hertzian pressure distribution) as well as $b/a = 0.5$, 0.8, and 0.95

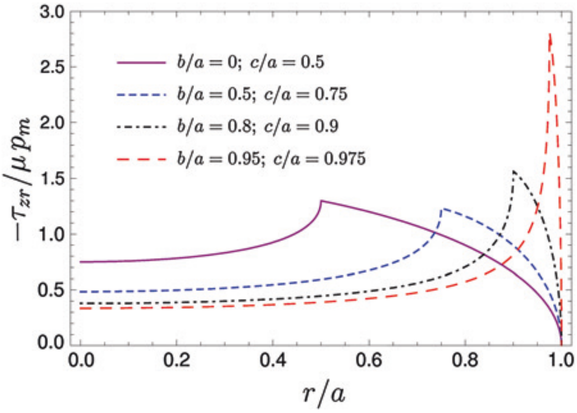

Fig. 5.9 Distribution of the tangential stress for the chosen values; the values are normalized by the average tangential stress in the case of complete sliding

Insertion of (5.69) into (5.34) results in the distribution of the tangential stress in integral form, which corresponds to (5.68) with the exception of the integral boundaries:

$$\tau_{zr}(r) = \begin{cases} -\dfrac{\mu E^*}{\pi R} \int\limits_c^a \dfrac{2\sqrt{x^2 - b^2} - b \arccos(b/x)}{\sqrt{x^2 - r^2}}\, \mathrm{d}x & \text{for } 0 \le r < c \\ -\dfrac{\mu E^*}{\pi R} \int\limits_r^a \dfrac{2\sqrt{x^2 - b^2} - b \arccos(b/x)}{\sqrt{x^2 - r^2}}\, \mathrm{d}x & \text{for } c \le r \le a \end{cases}. \tag{5.70}$$

Numerically solving (5.70) leads to the normalized trend in Fig. 5.9 for the chosen values $b \le c \le a$. A comparison with Fig. 5.8 allows the principle of superposition from Jäger to be clearly seen; especially for $b = 0$ and the arbitrarily chosen ratio of stick to contact radius $c/a = 0.5$, the classical solution from Cattaneo and Mindlin is evident.

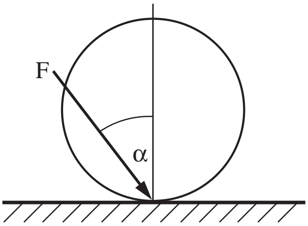

Fig. 5.10 Elastic sphere that is pressed by an inclined force onto a rigid half-space

The equations for the normal and tangential stresses according to (5.68) and (5.70) obtained from the distributed load in the one-dimensional model, occur identically in the three-dimensional theory [12].

Problem 5 An elastic sphere is pressed onto a rigid half-space, for which the direction of the indentation force always remains the same (Fig. 5.10). Determine the conditions under which the entire contact area sticks.

Solution In contrast to the three-dimensional case, the solution is trivial within the framework of the reduction method. Due to the fact that every sticking spring is loaded by the angle α, there is no sliding if the angle is smaller than the frictional angle [1]:

$$\tan\alpha < \mu. \tag{5.71}$$

The result is, as expected, exactly the same as that for the three-dimensional solution.

Problem 6 *Fretting wear*. Consider a rotationally symmetric profile which is brought into contact with a rigid surface and then oscillates in tangential direction with a given amplitude $u_x^{(0)}$. For small oscillation amplitudes, the wear occurs only in a circular slip zone at the border of the contact area. With increasing number of cycles, the wear profile tends to a limiting form, in which no further wear occurs. Under assumption of a constant coefficient of friction, the limiting form of the wear profile does not depend on the particular wear criterion. Using the method of dimensionality reduction, determine analytically this limiting form (for details see [13]).

Solution Assume that the friction can be described by a local formulation of the Amonton's law: The surfaces in contact are in the sticking state if tangential stress τ is smaller than normal pressure p multiplied with a constant coefficient of friction μ, and the tangential stress remains constant after the onset of sliding:

$$\begin{matrix} \tau < \mu p, \text{ stick} \\ \tau = \mu p, \text{ slip} \end{matrix} . \tag{5.72}$$

At the circular border of the stick region with radius c, the critical condition $\tau(c) = \mu p(c)$ is fulfilled. Inside this region, the condition $\tau < \mu p$ is valid. Due to wear outside of the sticking region, the local pressure in the sticking region will increase and outside decrease further, independently of whether the experiment is done under conditions of constant normal force or constant indentation depth d. This will lead to a progressive wear outside of the region of stick. The wear process will advance until the pressure in the sliding region becomes zero. In this limiting state, the inner parts of the contact will still remain in the sticking state, while the wear rate in the outer parts of the contact tends to zero. The final state of no wear can be considered as a sort of "shakedown" state, in which no further inelastic processes occur. The detailed kinetics of the profile depends on the wear criterion used as well as on the loading conditions (controlled force or controlled indentation). In the most cases, the Reye-Archard-Khrushchov wear criterion is used, stating that the wear volume is proportional to the dissipated energy. According to this wear criterion, the wear rate vanishes if either the relative displacement Δu_x of the bodies or tangential stress in contact is zero. In non-adhesive contacts, the latter means vanishing of the normal pressure p. The no-wear condition thus reads:

$$\text{No wear condition:} \begin{cases} \text{either} & p = 0 \\ \text{or} & \Delta u_x = 0 \end{cases}. \tag{5.73}$$

From these conditions, it follows that the pressure in the final state is non-zero only inside the stick area and vanishes outside.

Given a three-dimensional profile $z = f(r)$, we first determine the equivalent one-dimensional profile according to (3.27)

$$g(x) = |x| \int_0^{|x|} \frac{f'(r)}{\sqrt{x^2 - r^2}} \mathrm{d}r. \tag{5.74}$$

The back transformation is given by the integral

$$f(r) = \frac{2}{\pi} \int_0^{r} \frac{g(x)}{\sqrt{r^2 - x^2}} \mathrm{d}x. \tag{5.75}$$

The profile (5.74) is pressed to a given indentation depth d into an elastic foundation. The resulting vertical displacements of springs are given by

$$u_z(x) = d - g(x) \tag{5.76}$$

and the linear force density

$$q(x) = E^* u_z(x) = E^*(d - g(x)). \tag{5.77}$$

The contact radius a is given by the condition

$$g(a) = d. \tag{5.78}$$

The distribution of normal pressure $p = -\sigma_{zz}$ in the initial three-dimensional problem can be calculated using the integral transformation (3.37):

$$p(r) = -\frac{1}{\pi}\int_r^\infty \frac{q'(x)}{\sqrt{x^2 - r^2}}\mathrm{d}x = \frac{E^*}{\pi}\int_r^\infty \frac{g'(x)}{\sqrt{x^2 - r^2}}\mathrm{d}x. \tag{5.79}$$

If the profile is moved tangentially by $u_x^{(0)}$, the springs will be stressed both in the normal and tangential direction, and the radius c of the stick region will be given by the condition that the tangential force $k_x u_x^{(0)}$ is equal to the coefficient of friction μ multiplied with the normal force $k_z u_z(c)$:

$$G^* u_x^{(0)} = \mu E^*(d - g(c)). \tag{5.80}$$

Let us denote the initial three-dimensional profile as $f_0(r)$, the corresponding one-dimensional image as $g_0(x)$ and the limiting shakedown shapes as $f_\infty(r)$ and $g_\infty(x)$ correspondingly. As discussed above, the pressure outside the stick area must vanish in the limiting shakedown state: $p(r) = 0$, for $r > c$. From (5.79), it follows that

$$g'(x) = 0 \quad \text{and} \quad g(x) = const = g_0, \text{ for } c < x < a. \tag{5.81}$$

From the condition (5.76), it then follows that the one-dimensional profile in the shakedown state has the form

$$g_\infty(x) = \begin{cases} g_0(x), & \text{for } 0 < x < c \\ d, & \text{for } c < x < a \end{cases}. \tag{5.82}$$

This shape is schematically shown in Fig. 5.11. The three-dimensional limiting shape can now be calculated by the back transformation (5.75):

$$f_\infty(r) = \begin{cases} f_0(r) & \text{for } 0 < r < c \\ \dfrac{2}{\pi}\displaystyle\int_0^c \frac{g_0(x)}{\sqrt{r^2 - x^2}}\mathrm{d}x + \frac{2}{\pi} d \int_c^r \frac{1}{\sqrt{r^2 - x^2}}\mathrm{d}x, & \text{for } c < r < a \end{cases}. \tag{5.83}$$

Let us apply Eq. (5.83) to a parabolic indenter. In this case, the initial profile is $f_0(r) = r^2/(2R)$, and the corresponding one-dimensional MDR-image is $g_0(x) = x^2/R$. The radius of the stick region is given by the condition (5.80):

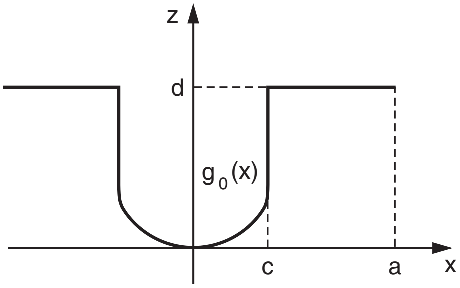

Fig. 5.11 One-dimensional MDR-image of the final "shakedown" profile

$$c = \sqrt{R\left(d - \frac{G^*}{E^*}\frac{u_x^{(0)}}{\mu}\right)}. \tag{5.84}$$

According to (5.83), the limiting three-dimensional profile has the form

$$f_\infty(r) = \begin{cases} \dfrac{r^2}{2R}, & \text{for } 0 < r < c \\ d - \dfrac{2}{\pi}\left(d - \dfrac{r^2}{2R}\right)\arcsin\dfrac{c}{r} - \dfrac{r^2}{\pi R}\left(\dfrac{c}{r}\right)\sqrt{1-\left(\dfrac{c}{r}\right)^2}, & \text{for } c < r < a \end{cases}. \tag{5.85}$$

Normalizing all vertical coordinates by the indentation depth d and horizontal coordinates by the contact radius of the initial profile, $a_0 = \sqrt{Rd}$,

$$\begin{aligned} &\tilde{f} = f/d, \quad \tilde{d} = d/d = 1 \\ &\tilde{r} = r/a_0, \quad \tilde{x} = x/a_0, \quad \tilde{c} = c/a_0, \quad \tilde{a} = a/a_0, \end{aligned} \tag{5.86}$$

we can rewrite these equations in the dimensionless form

$$\tilde{f}_\infty(\tilde{r}) = \begin{cases} \dfrac{\tilde{r}^2}{2}, & \text{for } 0 < \tilde{r} < \tilde{c} \\ 1 - \dfrac{2}{\pi}\left(1 - \dfrac{\tilde{r}^2}{2}\right)\arcsin\dfrac{\tilde{c}}{\tilde{r}} - \dfrac{\tilde{r}\tilde{c}}{\pi}\sqrt{1-\left(\dfrac{\tilde{c}}{\tilde{r}}\right)^2}, & \text{for } \tilde{c} < \tilde{r} < \tilde{a} \end{cases}. \tag{5.87}$$

The non-dimensional form of the limiting profile thus depends only on one parameter $0 < \tilde{c} < 1$. The contact radius, and thus the outer radius of the wear region, is given by the condition $\tilde{f}_\infty(\tilde{a}) = \tilde{f}_0(\tilde{a})$:

$$1 - \frac{2}{\pi}\left(1 - \frac{\tilde{a}^2}{2}\right)\arcsin\frac{\tilde{c}}{\tilde{a}} - \frac{\tilde{a}\tilde{c}}{\pi}\sqrt{1-\left(\frac{\tilde{c}}{\tilde{a}}\right)^2} = \frac{\tilde{a}^2}{2}. \tag{5.88}$$

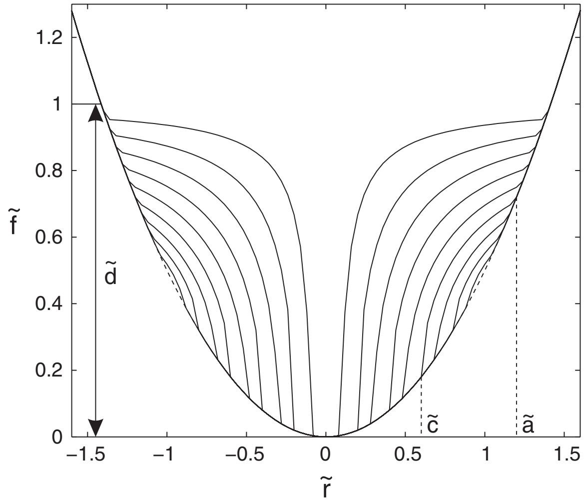

Fig. 5.12 3D profiles in the final state according to Eq. (5.87). Parameters: 9 linearly increasing $\tilde{c}$ from 0.1 to 0.9

In the limiting case $\tilde{c} = 0$, the contact radius becomes $\tilde{a} = \sqrt{2}$.

The total force can be calculated as

$$F_N = 2\int_0^a E^*(d - g(x))\mathrm{d}x = 2\int_0^c E^*\left(d - x^2\big/R\right)\mathrm{d}x = 2E^*\left(dc - \frac{c^3}{3R}\right) \tag{5.89}$$

or, under consideration of (5.84),

$$F_N = \frac{4}{3}E^*R^{1/2}\left(d - \frac{G^*}{E^*}\frac{u_x^{(0)}}{\mu}\right)^{1/2}\left(d + \frac{G^*}{2E^*}\frac{u_x^{(0)}}{\mu}\right). \tag{5.90}$$

Profiles (5.87) are shown in Fig. 5.12 for a representative set of parameters.

References

1. V.L. Popov, *Contact Mechanics and Friction. Physical Principles and Applications* (Springer, Berlin, 2010)
2. K.L. Johnson, *Contact Mechanics* (Cambridge University Press, Cambridge, 1985). (Chap. 7)
3. C. Cattaneo, Sul contatto di due corpi elastici: distribuzione locale degli sforzi. Rendiconti dell'Accademia nazionale dei Lincei. **27**, 342–348, 434–436, 474–478 (1938)
4. R.D. Mindlin, Compliance of elastic bodies in contact. J. Appl. Mech. **16**(3), 259–268 (1949)
5. C.E. Truman, A. Sackfield, D.A. Hills, Contact mechanics of wedge and cone indenters. Int. J. Mech. Sci. **37**(3), 261–275 (1995)
6. J. Jäger, Axi-symmetric bodies of equal material in contact under torsion or shift. Arch. Appl. Mech. **65**, 478–487 (1995)
7. K.L. Johnson, Surface interaction between elastically loaded bodies under tangential forces. Proc. R. Soc. **A230**, 531 (1955)
8. R.L. Munisamy, D.A. Hills, D. Nowell, Static axisymmetric hertzian contacts subject to shearing forces. ASME J. Appl. Mech. **61**, 278–283 (1994)
9. J. Jäger, A new principle in contact mechanics. J. Tribol. **120**(4), 677–684 (1998)
10. M. Ciavarella, D.A. Hills, G. Monno, The influence of rounded edges on indentation by a flat punch. J. Mech. Eng. Sci., Proc. Inst. Mech. Eng. Part C **212**(4), 319–328 (1998)
11. J. Jäger, New analytical solutions for a flat rounded punch compared with FEM. Comput. Methods Contact Mech. V, 307–316 (2001)
12. M. Ciavarella, Indentation by nominally flat or conical indenters with rounded corners. Int. J. Solids Struct. **36**, 4149–4181 (1999)
13. V.L. Popov, Analytic solution for the limiting shape of profiles due to fretting wear. Sci. Rep. **4**, 3749 (2014). doi:10.1038/srep03749

Chapter 6
Rolling Contact

Robbin Wetter, Valentin L. Popov, and Markus Heß

Rolling contacts are found in a multitude of engineering applications, such as wheel–rail or tire–street contacts, ball bearings, gears, and various transport mechanisms. In this chapter, it will be shown that the tangentially loaded, three-dimensional rolling contact can also be mapped to a one-dimensional equivalent system. In this way, the method of dimensionality reduction allows complex problems, such as the oscillating rolling contact, to be investigated.

6.1 The Mapping of Steady-State Rolling Contacts

The starting point is the Hertzian contact between an elastic half-space and a rigid sphere with the radius R. As shown in Chap. 3, this is mapped with the method of dimensionality reduction to an appropriate one-dimensional contact with a linearly elastic foundation. The foundation consists of a number of identical and independent springs with a sufficiently small separation distance Δx. The normal and tangential spring stiffness of the foundation is based on the original three-dimensional system as

$$\Delta k_z = E^* \Delta x = \frac{2G}{1-\nu}\Delta x,\ \Delta k_x = \frac{4G}{2-\nu}\Delta x. \tag{6.1}$$

Furthermore, the radius of curvature of the equivalent model is chosen as in Sect. 3.2 to be

$$R_1 = R/2. \tag{6.2}$$

This is known as the “rule of Popov”. Under these assumptions, the one-dimensional model gives the exact relations between force, contact region, and indentation depth as well as the displacement for both the normal and tangential contacts. In the following, it will be shown that a three-dimensional rolling contact also behaves in the same way.

V.L. Popov and M. Heß, *Method of Dimensionality Reduction in Contact Mechanics and Friction*, DOI 10.1007/978-3-642-53876-6_6

In this case, a rigid sphere is pressed into a linearly elastic foundation with the normal force F_N and loaded by the tangential force F_x. It is assumed that dry friction with the coefficient of friction of μ takes place between the two surfaces. Furthermore, the sphere rotates with an angular velocity of ω and its center point moves with the velocity of v in the positive x-direction (Fig. 6.1a). Thus, the model corresponds to a driven wheel.

The normal force causes an indentation with the depth d and the contact radius a:

$$a = \sqrt{2R_1 d}. \tag{6.3}$$

At the leading edge, the springs of the equivalent system are completely relaxed. As the sphere continues to roll forward, the tangential loading on an arbitrary spring f_x increases. Its normal force initially increases as well until the deepest point of the sphere rolls past it and the force once again decreases. As a result, the contact is divided into a stick region with the diameter $2c$ at the leading edge and a slip domain on the trailing edge of the sphere (Fig. 6.1b).

For further considerations, the coordinate ξ has been chosen, which moves with the sphere and has its origin exactly at the leading edge of the contact area (Fig. 6.1b). The tangential displacement $u_x(\xi)$ of a sticking spring at the position ξ relative to the leading edge of the contact area then corresponds to the distance $\Delta v_1 t$ between the sphere and substrate (attachment points of the springs) at this point. With $\xi = vt$, it follows that

$$u_x(\xi) = \Delta v_1 \cdot t = \Delta v_1 \frac{\xi}{vt} t = \frac{\Delta v_1}{v} \xi, \tag{6.4}$$

and, therewith, the tangential force of the springs in the sticking domain $0 \le \xi \le 2c$ is

$$f_x = \Delta k_x u_x = \Delta k_x \frac{\Delta v_1}{v} \xi. \tag{6.5}$$

In the rest of the contact area, from the boundary of the stick region to the trailing edge of the contact area, the springs are in a state of slip. The tangential force in the slip domain $2c \le \xi \le 2a$ is then

$$f_x = \mu f_N = \mu \Delta k_z u_z, \tag{6.6}$$

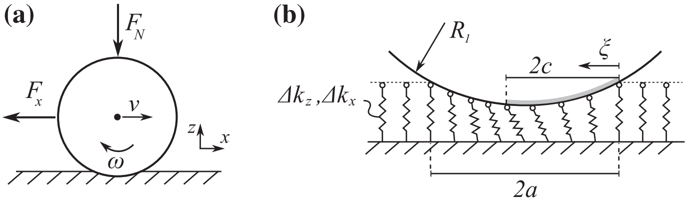

Fig. 6.1 (**a**) Rolling contact between a sphere and an elastic half-space and (**b**) the one-dimensional equivalent system with constantly moving coordinate ξ, which has its origin at the leading edge of the contact area

where the normal displacement u_z of a spring at position ξ is given by the indentation depth d and the approximate profile of the sphere

$$u_z(\xi) = d - \frac{(a-\xi)^2}{2R_1} = \frac{\left(2a\xi - \xi^2\right)}{2R_1}. \tag{6.7}$$

At the boundary of the sticking domain $\xi = 2c$, the sticking condition is exactly met:

$$f_x(2c) = \mu f_N(2c) \;\Rightarrow\; \Delta k_x \frac{\Delta v_1}{v} 2c = \mu \Delta k_z \frac{\left(4ac - 4c^2\right)}{2R_1}, \tag{6.8}$$

from which the radius of the sticking domain is obtained:

$$c = a - \frac{2R_1(1-\nu)}{\mu(2-\nu)} \frac{\Delta v_1}{v}. \tag{6.9}$$

Taking the contact radii a and c into account, the normal force F_N and the tangential force F_x can be determined by integrating over the entire contact area. Again, the normal force corresponds identically to the three-dimensional Hertzian contact problem [1]:

$$\begin{aligned} F_N &= \int_0^{2a} \frac{2G}{1-\nu} \frac{\left(2a\xi - \xi^2\right)}{2R_1} \mathrm{d}\xi = \frac{2G}{1-\nu} \frac{2a^3}{3R_1} = \frac{4}{3} E^* (2R_1)^{1/2} d^{3/2} \\ &= \frac{4}{3} E^* R^{1/2} d^{3/2}. \end{aligned} \tag{6.10}$$

By using Eqs. (6.5) to (6.9), the tangential force is obtained:

$$\begin{aligned} F_x &= \int_0^{2c} \frac{4G}{2-\nu} \frac{\Delta v_1}{v} \xi \mathrm{d}\xi + \int_{2c}^{2a} \frac{2G}{1-\nu} \mu \frac{\left(2a\xi - \xi^2\right)}{2R_1} \mathrm{d}\xi \\ &= \frac{4G}{3(1-\nu)} \frac{\mu}{R_1} \left(a^3 - c^3\right). \end{aligned} \tag{6.11}$$

Dividing Eq. (6.11) by Eq. (6.10) leads initially to

$$\frac{F_x}{F_N} = \mu \left(1 - \left(\frac{c}{a}\right)^3\right). \tag{6.12}$$

Rearranging this equation, we obtain the same expression for the radius of the stick region as in the original three-dimensional rolling contact [1]:

$$\frac{c}{a} = \left(1 - \frac{F_x}{\mu F_N}\right)^{1/3}. \tag{6.13}$$

Therefore, the results show that the modeling of steady-state rolling contacts using the method of dimensionality reduction also provides the exact relation between loading and the sizes of the stick and slip regions. Describing the foundation as being linearly elastic with the corresponding spring stiffness and taking the "rule of Popov" into account allows for these rolling contacts to be investigated.

6.2 Rules for the Exact Mapping of Rolling Contacts

The two requirements for the exact mapping of the three-dimensional rolling contact are correctly choosing the spring stiffness of the linearly elastic foundation (6.1) and following the "rule of Popov" for the one-dimensional radius (6.2). In addition to the slip and stick regions and their dependence on loading, the relative velocity between the sphere and foundation (attachment point of the springs) is a very important value for the rolling contact. The velocity difference is caused by the slip as well as the elastic deformation. By rearranging (6.9) and inserting (6.13), we obtain

$$\frac{\Delta v_1}{v} = \frac{2-\nu}{1-\nu}\frac{\mu a}{R}\left(1-\left(1-\frac{F_x}{\mu F_N}\right)^{1/3}\right). \tag{6.14}$$

Comparing this result with the slip of the original three-dimensional system [2]

$$s = \frac{\Delta v}{v} = \frac{\omega R - v}{v} = \frac{(4-3\nu)}{4(1-\nu)}\frac{\mu a}{R}\left(1-\left(1-\frac{F_x}{\mu F_N}\right)^{1/3}\right), \tag{6.15}$$

we obtain the following relation between the one-dimensional and the three-dimensional results:

$$\frac{\Delta v_1}{v} = \frac{4(2-\nu)}{(4-3\nu)}s \Rightarrow \Delta v_1 = \frac{4(2-\nu)}{(4-3\nu)}\Delta v. \tag{6.16}$$

Therefore, in addition to (6.1) and (6.2), there is another rule to be considered, according to which the one-dimensional result must be scaled in order to determine the correct relative velocity of the three-dimensional rolling contact:

$$\Delta v = \frac{(4-3\nu)}{4(2-\nu)}\Delta v_1. \tag{6.17}$$

This is due to the asymmetry in the tangential stress distribution and is valid for both the steady-state rolling as well as the oscillating rolling contact at sufficiently high amplitudes.

6.3 Shakedown and Creep in Oscillating Rolling Contacts

The results in the previous section serve as the foundation in the following for the investigation of the oscillating rolling contact. This contact is a general model for frictional contacts and allows solutions to be obtained for technical applications such as bolted connections, shrink fit assemblies, and mounts under the influence of vibrations. Examples are press-fitted hubs and bearings, joint flanges on drive shafts, and blade roots in turbines.

The tangential loading capacity of force-locked connections is essentially dependent on the normal force F_N and the coefficient of friction μ. According to Coulomb's law of friction, a connection fails if the tangential force F_x surpasses the maximum force of static friction:

$$F_x > F_{\text{max}} = \mu F_N. \tag{6.18}$$

Vibrations can cause a failure to occur in such connections at even lower values of tangential force. Partial slip with gradual frictional fatigue (fatigue fretting) and induced complete (macroscopic) slip in the contact are examples of this. The method of dimensionality reduction allows for models to be described analytically and also the microslip as well as the maximum tangential loading (as opposed to Eq. (6.18)) to be predicted.

The starting point for describing and investigating this effect is the Hertzian contact, which is composed of an elastic sphere with the radius R and a movable, rigid substrate. Using the method of dimensionality reduction, the sphere is mapped to a linearly elastic foundation with the radius R_1 and the spring stiffnesses Δk_z and Δk_x, which are given by Eqs. (6.1) and (6.2). The sphere is pressed with the normal force F_N to the indentation depth of d into the rigid substrate, which results in the contact radius a (given by Eq. (6.3)). Furthermore, dry friction is assumed to exist between the two surfaces with the coefficient of friction of μ and the movable substrate is loaded with the tangential force F_x (Fig. 6.2a). In Chap. 5, it was shown that this, in addition to the elastic properties of the sphere, causes a slip of the springs in the region $c < |x| < a$ of

$$c = a\left(1 - \frac{F_x}{\mu F_N}\right)^{1/3} \tag{6.19}$$

and a tangential displacement U_{stat} of the rigid substrate:

$$U_{stat} = \mu \frac{2-\nu}{2(1-\nu)} d \left(1 - \left(1 - \frac{F_x}{\mu F_N}\right)^{2/3}\right). \tag{6.20}$$

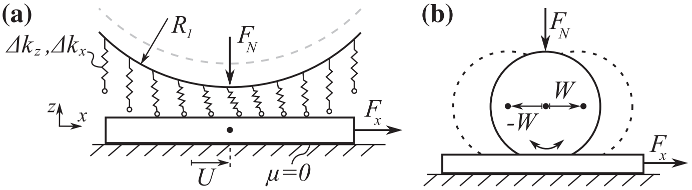

Fig. 6.2 (**a**) Rolling contact between an elastic one-dimensional sphere and a moving rigid substrate. (**b**) Oscillating rolling motion with the rolling path of the center of mass of the sphere W as the oscillation amplitude

In order to investigate the influence of the vibrations, this static tangential contact is superimposed with an oscillating rolling motion of the sphere with the period T and the oscillation amplitude W, which indicates the rolling path of the center of mass of the sphere in the tangential direction (Fig. 6.2b). Based on the properties described in Chap. 2, the influence of inertial forces may be neglected. By treating this problem in a quasi-static manner, the results can be transferred to an arbitrary cyclical loading of frictionally actuated connections of this form.

In the following, we would like to restrict ourselves to tangential forces that lie below the maximum force of static friction in Eq. (6.18) and consider only oscillation amplitudes that are smaller than the original contact area:

$$F_x \leq \mu F_N, \; W \leq a. \tag{6.21}$$

Therefore, without rolling of the sphere, there would be no complete (macroscopic) slip in the contact and in the dynamic case, the center of the contact would not move beyond the original contact area. Moreover, the pure rolling of the sphere causes no driving moment whatsoever. In this way, no additional force results and without tangential loading of the rigid foundation, no tangential displacement would result. Thus, the movement resembles that of an oscillatory rocking of the contact partners of a frictional contact for which the macroscopic loading remains constant.

In contrast, the local loading changes due to the oscillation. In the course of the back and forth movements of the elastic sphere, the normal force f_N decreases and with it, the local maximum tangential force of the springs $f_{\max} = \mu f_N$ on the current trailing edge of the rolling contact. Furthermore, the domains at the edges of the contact periodically separate from the substrate (Fig. 6.3).

Initially, this causes a small additional displacement of the rigid substrate and an increase in the size of the domain of partial slip. In the case of sufficiently small oscillation amplitudes W, the displacement of the rigid substrate ceases after a certain number of oscillation periods. At this point, the system has reached a new equilibrium state in which no partial slip occurs, regardless of whether the oscillatory rolling continues or not. One such behavior is characterized as so-called shakedown. The concept of shakedown was suggested by Melan for plastic media [3] and transferred to frictional contacts by Klarbring [4]. According to this, a system has reached a shakedown state at time t_0 after an initial slip motion, if no slip occurs for all times $t > t_0$. A necessary condition for shakedown is the existence of

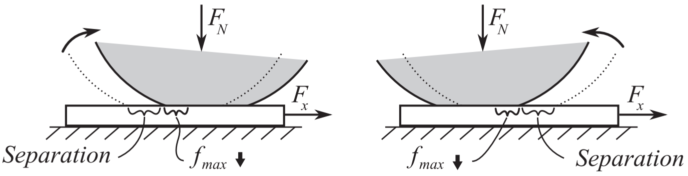

Fig. 6.3 One-dimensional model of the frictional contact. Oscillatory rolling of an elastic sphere with the alternate separation of the domains at the edges of the contact and the decrease in the local maximum force of static friction on the current trailing edge

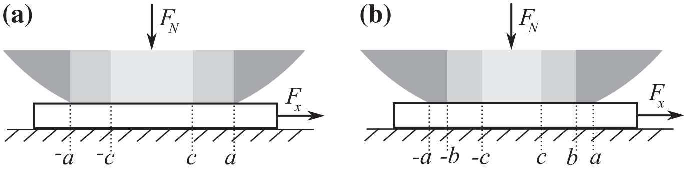

Fig. 6.4 One-dimensional model of a frictional contact. (**a**) The contact area in the original state with two contact radii before rolling. (**b**) The contact area with three contact radii in the new equilibrium state

a constant shakedown displacement for which the maximum force of static friction from Eq. (6.18) is not exceeded. There are no restrictions to the number of loading cycles until reaching the shakedown state. Therefore, it is also possible that the final displacement of the system lies below the shakedown level [5] if the oscillation ceases too early.

In the case of the oscillating frictional contact, the shakedown displacement is influenced by the oscillation amplitude and the tangential force and is increased by ΔU with respect to the static displacement U_{stat} in Eq. (6.20) [6]:

$$U = U_{stat} + \Delta U. \tag{6.22}$$

The contact area is constant after shakedown is achieved and is characterized by three characteristic radii a, b, and c (Fig. 6.4b). The radius a remains unchanged whereas the stick radius c, within which the tangential spring force is below the corresponding maximum force of static friction, decreases. Therefore, the domain $c < |x| < a$, in which partial slip occurs, is larger than that for the static case.

Now, an additional slip radius b appears, which marks the domain in which the local tangential force is equal to zero due to the periodic separation. In summary, the three individual contact radii are now
the contact radius:

$$a = \sqrt{2R_1 d}, \tag{6.23}$$

the slip radius:

$$b = a - W, \tag{6.24}$$

and the stick radius:

$$c = \sqrt{2R_1\left(d - \frac{2(1-\nu)}{\mu(2-\nu)}U\right)} - W. \tag{6.25}$$

Within the stick domain $0 < |x| < c$, the resulting tangential force of the springs is

$$f_x = \Delta k_x U. \tag{6.26}$$

In the domain of partial slip $c < |x| < b$, the tangential force is exactly equal to the force of static friction from Eq. (6.18) at the trailing edge for the maximum deflection of the sphere. This force is found using the displacement of the springs in the normal direction u_z from Eq. (6.7):

$$f_x = \mu f_N(x+W) = \mu \Delta k_z u_z(x+W) \\ = \mu \Delta k_z \left(d - \frac{(x+W)^2}{2R_1} \right). \tag{6.27}$$

By integrating over the entire symmetric contact area

$$F_x = 2\int_0^c \frac{4G}{2-\nu} U \mathrm{d}x + 2\int_c^b \mu \frac{2G}{1-\nu}\left(d - \frac{(x+W)^2}{2R_1} \right) \mathrm{d}x, \tag{6.28}$$

we obtain the analytical relationship between loading, oscillation amplitude, and displacement:

$$F_x = \mu F_N \left(1 - \left(1 - \frac{2(1-\nu)}{\mu(2-\nu)} \frac{U}{d} \right)^{3/2} \right) - \frac{8G}{(2-\nu)} UW. \tag{6.29}$$

Experiments and three-dimensional simulations yield a small correction [7]:

$$F_x = \mu F_N \left(1 - \left(1 - \frac{2(1-\nu)}{\mu(2-\nu)} \frac{U}{d} \right)^{3/2} \right) - \frac{16}{3} \frac{G}{(2-\nu)} UW. \tag{6.30}$$

Figure 6.5 illustrates Eq. (6.30) in normalized form and shows the displacement of the rigid substrate U as a function of the tangential force F_x for various oscillation amplitudes W. The maximum value of the displacement of the static tangential contact $u_{x,\max}$ from Sect. 5.2 is used to normalize the displacement U. This is increased by ΔU with respect to the static displacement U_{stat} (shown by the dashed line in Fig. 6.5), due to the rolling. The displacements for various oscillation amplitudes exhibit their own corresponding maximums (shown by the

Fig. 6.5 Normalized displacement $u = U/u_{x,\max}$ with $u_{x,\max} = \mu d(2-\nu)/2(1-\nu)$ as a function of tangential force F_x for various oscillation amplitudes W after shakedown has been achieved. The rolling causes an increase in displacement of Δu compared to static displacement u_{stat}

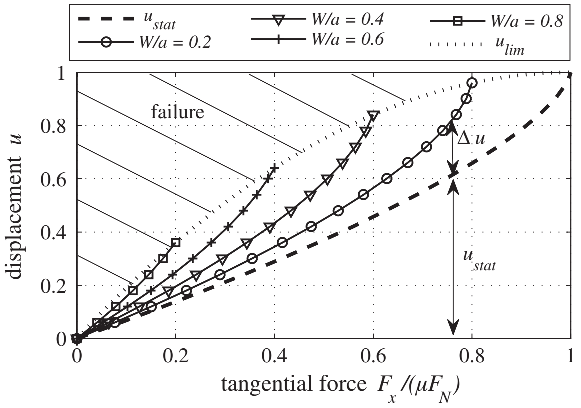

dotted line in Fig. 6.5). This shows which maximum displacements can be reached before complete slip occurs due to the rolling motion and the frictional contact fails (hatched area).

In this limiting case, the stick radius c vanishes so that from Eq. (6.25), the maximum displacement can be obtained as a function of oscillation amplitude:

$$U_{\lim} = \mu \frac{(2-\nu)}{2(1-\nu)} \left(d - \frac{W_{\lim}^2}{R} \right). \tag{6.31}$$

By inserting (6.31) into (6.30), the maximum tangential loading capacity of the oscillating rolling contact can also be obtained:

$$F_{\lim} = \mu F_N - \mu \frac{4}{3} \frac{2G}{1-\nu} d W_{\lim} = F_{\max} - \Delta F_x. \tag{6.32}$$

Equation (6.32) makes it clear that by considering only the macroscopic loading, the tangential loading capacity obtained for the case of the oscillating rolling contact is too high, because the actual loading capacity $F_{\lim}$ has been decreased by ΔF_x when compared to the maximum possible force of static friction $F_{\max}$ from Eq. (6.18).

If the tangential forces or amplitudes in Eq. (6.32) are surpassed, then the frictional contact fails. The entire contact area exhibits slip, which leads to complete sliding of the substrate. A common parameter for this so-called induced creep is the displacement per rotation amplitude ΔU_{T1}, which increases with tangential force and oscillation amplitude

$$\Delta U_{T1} = \Delta U_{T1}(F_x, W). \tag{6.33}$$

Numerical simulations show that the displacement is proportional to the supercritical component $\varDelta W = W - W_{\lim}$ of the oscillation amplitude [6]:

$$\Delta U_{T1} = \kappa \cdot (W - W_{\lim}) \tag{6.34}$$

and that the proportionality constant κ is a function of the tangential force, and with it, the static displacement U_{stat} from Eq. (6.20). Linear regression analysis allows for the function to be approximated, for which the following expression for the displacement per period can be obtained [6, 7]:

$$\Delta U_{T1} = \sqrt{\mu \frac{(2-\nu)}{(1-\nu)} \frac{U_{stat}}{R}} (W - W_{\lim}). \tag{6.35}$$

In order to determine the corresponding three-dimensional displacement, it must be remembered that the rule of (6.17) must be considered due to the proportionality to creepage:

$$\Delta U_T = \frac{(4-3\nu)}{4(2-\nu)} \Delta U_{T1} = \frac{(4-3\nu)}{4(2-\nu)} \sqrt{\mu \frac{(2-\nu)}{(1-\nu)} \frac{U_{stat}}{R}} (W - W_{\lim}). \tag{6.36}$$

The induced creep stops immediately after the end of the rolling motion. The effect explains not only why frictionally engaged contacts fail under the influence of vibrations, but also allows for the generation and control of the smallest movements.

6.4 Problems

Problem 1 Determine the minimum vibration amplitude required to free a frictionally engaged joint for a loading $F_N = 1$ kN and $F_x = 180$ N. The connection should be modeled as a Hertzian contact between a rigid substrate and an elastic steel sphere ($\nu = 0.3$, $E = 210$ GPa, $\mu = 0.3$, and $R = 10$ cm).

Solution Using (6.10), we obtain the following for the Hertzian contact: $d = 4.73$ µm and $a = 0.69$ mm. Solving Eq. (6.32) with $F_{\text{lim}} = 180$ N results in the maximum amplitude before failure

$$F_{\text{lim}} = \mu F_N - \mu \frac{4}{3} \frac{2G}{1-\nu} d W_{\text{lim}} \Rightarrow W_{\text{lim}} = 0.28 \text{ mm}. \tag{6.37}$$

With Eq. (6.31), the maximum displacement before failure can also be found:

$$U_{\text{lim}} = \mu \frac{(2-\nu)}{2(1-\nu)} \left(d - \frac{W_{\text{lim}}^2}{R} \right) = 1.45 \text{ µm}. \tag{6.38}$$

Alternatively, the maximum amplitude and maximum displacement can be simply obtained from the diagram in Fig. 6.5 with the relationship $F_x/\mu F_N \approx 0.6$:

$$W_{\text{lim}}/a \approx 0.4 \Rightarrow W_{\text{lim}} \approx 0.28 \text{ mm} \tag{6.39}$$

and

$$u_{\text{lim}} = U_{\text{lim}}/(\mu d(2-\nu)/2(1-\nu)) \approx 0.85 \Rightarrow U_{\text{lim}} \approx 1.46 \text{ µm}. \tag{6.40}$$

Problem 2 Determine the displacement and maximum loading for the frictionally engaged connection described in Problem 1 at an oscillation amplitude of $W = 0.14$ mm.

Solution Numerically solving Eq. (6.30) provides the displacement:

$$F_x = \mu F_N \left(1 - \left(1 - \frac{2(1-\nu)}{\mu(2-\nu)} \frac{U}{d} \right)^{3/2} \right) - \frac{16}{3} \frac{G}{2-\nu} UW \Rightarrow U = 0.98 \text{ µm}. \tag{6.41}$$

We obtain the maximum loading from Eq. (6.32) with $W_{\text{lim}} = 0.14$ mm:

$$F_{\text{lim}} = \mu F_N - \mu \frac{4}{3} \frac{2G}{1-\nu} d W_{\text{lim}} = 238 \text{ N}. \tag{6.42}$$

Alternatively, with the values of $F_x/\mu F_N \approx 0.6$ and $W/a \approx 0.2$ from the diagram in Fig. 6.5, we obtain

$$u = U/(\mu d(2-\nu)/2(1-\nu)) \approx 0.54 \Rightarrow U \approx 0.93\ \mu\text{m}. \tag{6.43}$$

Likewise, the maximum loading can simply be taken from the diagram. For the amplitude of $W/a \approx 0.2$, we obtain the following from the dotted line:

$$F_x/\mu F_N \approx 0.8 \ \Rightarrow \ F_{\lim} \approx 240\ \text{N}. \tag{6.44}$$

Problem 3 A micro-actuated drive is realized as an oscillating rolling contact ($\nu = 0.3$, $E = 400$ GPa, $\mu = 0.1$, and $R = 10$ mm) with a frequency of 100 Hz. Determine the necessary oscillation amplitude to produce a speed of $v = 0.3$ µm/s for a loading of $F_N = 1$ N and $F_x = 0.05$ N.

Solution For the Hertzian contact, we obtain $d = 66.3$ nm and $a = 25.74$ µm using Eq. (6.10). The static displacement is given by Eq. (6.20):

$$U_{stat} = \mu \frac{2-\nu}{2(1-\nu)} d \left(1 - \left(1 - \frac{F_x}{\mu F_N}\right)^{2/3}\right) = 2.98\ \text{nm}. \tag{6.45}$$

By solving Eq. (6.32) with $F_{\lim} = 0.05$ N, we obtain the maximum amplitude

$$F_{\lim} = \mu F_N - \mu \frac{4}{3} \frac{2G}{1-\nu} d W_{\lim} \Rightarrow W_{\lim} = 12.87\ \mu\text{m}. \tag{6.46}$$

The necessary speed at 100 Hz leads to a displacement per period of ΔU_T:

$$0.3\ \mu\text{m/s} = 100\ \text{Hz} \cdot \Delta U_T \Rightarrow \Delta U_T = 3\ \text{nm}. \tag{6.47}$$

Rearranging Eq. (6.36) and inserting the necessary values results in the amplitude in question

$$W = \Delta U_T \frac{4(2-\nu)}{(4-3\nu)} \sqrt{\frac{(1-\nu)}{\mu(2-\nu)} \frac{R}{U_{stat}}} + W_{\lim} = 37.34\ \mu\text{m}. \tag{6.48}$$

References

1. V.L. Popov, *Contact Mechanics and Friction, Physical Principles and Applications* (Springer, Berlin, 2010)
2. K.L. Johnson, *Contact Mechanics, Chapter 8* (Cambridge University Press, Cambridge, 1985)
3. E. Melan, Theorie statisch unbestimmter Systeme aus ideal-plastischem Baustoff. Sitzungsber. d.Akad. d. Wiss., Wien 2A, 145, pp. 195–218 (1936)
4. A. Klarbring, M. Ciavarella, J.R. Barber, Shakedown in elastic contact problems with Coulomb friction. Int. J. Solids Struct. **44**(11), 8355 (2007)
5. J.R. Barber, A. Klarbring, M. Ciavarella, Shakedown in frictional contact problems for the continuum. Comptes Rendus Mécanique. **336**, 34–41 (2008)
6. R. Wetter, Shakedown and induced microslip of an oscillating frictional contact. Phys. Mesomech. **15**(5), 239–299 (2012)
7. R. Wetter, V.L. Popov, Shakedown limits for an oscillating, elastic rolling contact with Coulomb friction. Int. J. Solids Struct. **51**(5), 930–935 (2013)

Chapter 7
Contacts with Elastomers

Silvio Kürschner, Valentin L. Popov, Markus Heß

7.1 Introduction

Rubber and other elastomers play a large role in many tribological applications. They are used where large frictional forces or large deformations are needed. These materials are especially used for tires, transportation rollers, shoes, seals, rubber bands, in electronic devices (e.g., contacts for keyboards) as well as applications for adhesion. When compared to purely elastic contacts, the calculation of elastomer contacts is made more difficult by the fact that they exhibit a time-dependent behavior, which is also normally characterized by a large spectrum of relaxation times. The correct mechanical description must, therefore, take several orders of magnitude in characteristic times into account. The multi-scalar properties of the surface roughness are supplemented here by the multi-scalar character of the relaxation of the material, which makes the numerical simulation of elastomers especially complicated. It is, therefore, important to develop fast simulation methods for the calculation of contact and frictional properties for this class of materials. In this chapter, we will show how the method of dimensionality reduction can be generalized to contacts of elastomers with arbitrary linear rheology.

In the first section, we remind the reader of the fundamental definitions that are necessary for the description of elastomers, for which we follow the presentation of [1]. The general process is then explained using the very simple special case of a linearly viscous material for the purposes of understanding. Only afterwards, we will continue to the treatment of general viscoelastic materials. The detailed derivations can be found in Chap. 19.

V.L. Popov and M. Heß, *Method of Dimensionality Reduction in Contact Mechanics and Friction*, DOI 10.1007/978-3-642-53876-6_7

7.2 Stress Relaxation in Elastomers

We consider a rubber block, which is loaded under shear stress (Fig. 7.1). The shear angle is denoted by ε.[1] If the block is deformed quickly by the shear angle of ε_0, then the stress increases initially to a high level $\sigma(0)$ and then relaxes slowly to a much lower level of $\sigma(\infty)$ (Fig. 7.2b). For elastomers, $\sigma(\infty)$ can be three to four orders of magnitude smaller than $\sigma(0)$. The ratio

$$G(t) = \frac{\sigma(t)}{\varepsilon_0} \tag{7.1}$$

is denoted as the *time-dependent shear modulus*. It is easy to see that this function completely describes the mechanical properties of a material, provided that the material behaves *linearly*. Let us assume that the block is deformed according to an arbitrary function in time $\varepsilon(t)$. An arbitrary dependence $\varepsilon(t)$ can always be presented as the sum of temporally shifted step functions, as shown schematically in Fig. 7.3. An elementary step function in this presentation at the time t' has the amplitude $\mathrm{d}\varepsilon(t') = \dot{\varepsilon}(t')\mathrm{d}t'$. The corresponding stress component is $\mathrm{d}\sigma = G(t-t')\dot{\varepsilon}(t')\mathrm{d}t'$, and the total stress at every point in time is, therefore, calculated as

$$\sigma(t) = \int\limits_{-\infty}^{t} G(t-t')\dot{\varepsilon}(t')\mathrm{d}t'. \tag{7.2}$$

Equation (7.2) shows that the time-dependent shear modulus can be understood as a weighted function with deformation changes in the past leading to current changes in the stress. Due to this, $G(t)$ is sometimes called the *memory function*.

If $\varepsilon(t)$ changes harmonically:

$$\varepsilon(t) = \tilde{\varepsilon}\cos(\omega t), \tag{7.3}$$

then a periodic change in the stress with the same frequency is reached after a transient period. The relationship between the changes in deformation and stress can be very easily presented if the real function $\cos(\omega t)$ is presented as the sum of two complex exponential functions:

$$\cos(\omega t) = \frac{1}{2}\left(e^{i\omega t} + e^{-i\omega t}\right). \tag{7.4}$$

Due to the superposition principle, one can first calculate the stresses that are caused by the complex oscillations

$$\varepsilon(t) = \tilde{\varepsilon}e^{i\omega t} \quad \text{and} \quad \varepsilon(t) = \tilde{\varepsilon}e^{-i\omega t}. \tag{7.5}$$

---

[1] Let it be stressed that the defined value ε is equal to *two times* the shear component of the deformation tensor.

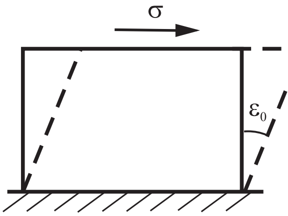

Fig. 7.1 Shear deformation of a rubber block. ε_0 is the shear angle

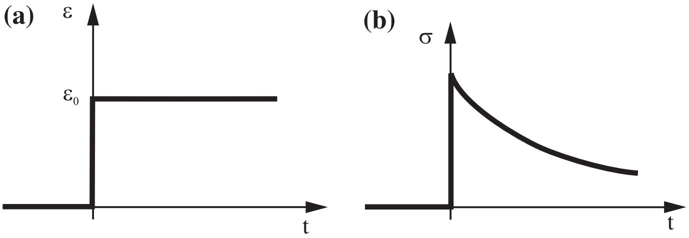

Fig. 7.2 If a rubber block is quickly deformed at time $t = 0$ by ε_0, then the stress increases initially to a high level and then relaxes with time to a much lower stress

Fig. 7.3 Presentation of a time-dependent function as a superposition of multiple temporally displaced step functions

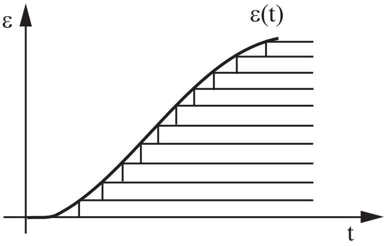

Subsequently, these may be summed. If we insert $\varepsilon(t) = \tilde{\varepsilon} e^{i\omega t}$ into (7.2), then we obtain a stress of

$$\sigma(t) = \int_{-\infty}^{t} G(t - t') i\omega\tilde{\varepsilon} e^{i\omega t'} dt'. \tag{7.6}$$

By substituting $\xi = t - t'$, we bring the integral into the following form:

$$\sigma(t) = i\omega\tilde{\varepsilon} e^{i\omega t} \int_{0}^{\infty} G(\xi) e^{-i\omega\xi} d\xi \tag{7.7}$$

or

$$\sigma(t) = \hat{G}(\omega)\tilde{\varepsilon}e^{i\omega t} = \hat{G}(\omega)\varepsilon(t). \tag{7.8}$$

For a harmonic excitation in the form of a complex exponential function $e^{i\omega t}$, the stress is proportional to the deformation. The proportionality coefficient

$$\hat{G}(\omega) = i\omega \int_0^\infty G(\xi)e^{-i\omega\xi}d\xi \tag{7.9}$$

is generally a complex value and is called the *complex shear modulus*. Its real component $G'(\omega) = \operatorname{Re}\hat{G}(\omega)$ is called the *storage modulus*, and its imaginary component $G''(\omega) = \operatorname{Im}\hat{G}(\omega)$ is called the *loss modulus*. Further details as to the definition and measurement methods of the time-dependent shear modulus and the complex shear modulus can be found in the book [1].

7.3 Application of the Method of Dimensionality Reduction in Viscoelastic Media: The Basic Idea

If the indentation or slip speed for the dynamic loading of an elastomer is lower than the lowest speed of sound (which is related to the smallest relevant modulus of elasticity), then the contact can be considered to be quasi-static. If this condition is met and an area of the elastomer is excited with an angular frequency of ω, then the material exhibits a linear relationship between stress and deformation, and therefore, between force and displacement. Thereby, the medium can be considered to be an elastic body with the effective shear modulus of $G(\omega)$. All theorems that are valid for elastic bodies must also be valid for harmonically excited viscoelastic media. More importantly, the incremental stiffness is proportional to the diameter of the contact area, which forms the mathematical basis for the applicability of the method of dimensionality reduction. Because of this, an elastomer can be mapped to a one-dimensional system, for which the individual springs can be chosen according to (3.5):

$$\Delta k_z = E^* \Delta x. \tag{7.10}$$

The only difference to the elastic contact is the fact that the effective modulus of elasticity is now a function of frequency. Elastomers can be often considered to be incompressible media. In this case, $\nu = 1/2$ and

$$\Delta k_z = E^*(\omega)\Delta x = \frac{E(\omega)}{1-\nu^2}\Delta x = \frac{2G(\omega)}{1-\nu}\Delta x \approx 4G(\omega)\Delta x. \tag{7.11}$$

In the case of rubber, the stiffness of the individual "springs" of the linearly elastic foundation is equal to four-fold the shear modulus multiplied by the discretization step size. In the one-dimensional equivalent system, we obtain the following spring force for a harmonic excitation:

$$f_N(x,\omega) = E^*(\omega)\Delta x \cdot u_z(x,\omega) \approx 4G(\omega)\Delta x \cdot u_z(x,\omega). \tag{7.12}$$

The reverse transformation into the time domain results in the force law

$$f_N(x,t) = 4\Delta x \int_{-\infty}^{t} G(t-t')\dot{u}_z(x,t')\mathrm{d}t'. \tag{7.13}$$

In the next section, we will explain this general, but somewhat formally described, idea by using the simplest example of the linearly viscous medium. We discuss how the viscoelastic contact problem can be reduced to the elastic contact problem and, subsequently, how this can be mapped to a one-dimensional system.

7.4 Radok's Method of the Functional Equations

In 1955, Lee [2] published a method for solving viscoelastic contact problems by reducing them to elastic problems. This procedure is advantageous because contacts between elastic bodies are comparatively simpler to solve and the solution to many problems can already be found in many textbooks. The procedure was later generalized by Radok [3] and entered the literature as the *principle of the functional equations*.

The basic idea of the method is conceivably simple. Beginning with a given viscoelastic problem, the material properties are replaced by those of an elastic body. However, all other influences, such as geometric configuration, remain unchanged. Subsequently, the elastic problem is solved. One obtains the solution to the viscoelastic problem by once again replacing the elastic properties in the elastic solution by the viscoelastic properties. This substitution takes place in the Laplace domain and takes the most effort. The entire algorithm is presented schematically in Fig. 7.4.

We will explain the procedure by using a concrete example. Let us consider a linearly viscous, incompressible body with the viscosity η, which is also large

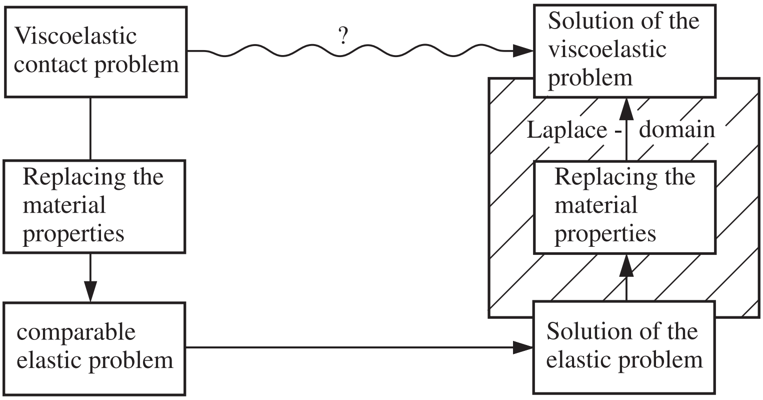

Fig. 7.4 Principle of the functional equations (schematic presentation)

enough that the half-space approximation is valid. The body is loaded on the surface by a constant point-loaded normal force. How will the surface of the body be deformed? The comparable elastic problem is simply the loading of a linearly elastic, incompressible half-space by a constant normal force. The solution to the problem can be found in many textbooks on elasticity theory or contact mechanics (e.g., [4] or [1]). If G is the shear modulus, F_N is the normal force, and r is the distance to the point of force application, then the normal displacement of the surface can be given by the expression[2]

$$u(r) = \frac{F_N}{4\pi G r}. \tag{7.14}$$

This equation is the solution to the comparable elastic problem. The solution now undergoes a Laplace transformation. For the description of the viscoelastic problem, contrary to elastic problems, it is necessary to specify the history of the normal force. We assume that the force begins loading at the time $t = 0$ and is then constant with the magnitude F_N:

$$F(t) = F_N H(t), \tag{7.15}$$

where

$$H(t) = \begin{cases} 1, & t > 0 \\ 0, & t < 0 \end{cases} \tag{7.16}$$

is the Heaviside function. The application of the Laplace transformation, the replacement of the material properties, and the reverse transformation are carried out in Chap. 19. We obtain the following surface deformation as the solution to the viscous contact problem:

$$u(r,t) = \frac{F_N t}{4\pi \eta r}. \tag{7.17}$$

If one differentiates (7.17) with respect to time, the velocity is obtained with which the surface is deformed in response to the external force:

$$\dot{u}(r) = \frac{F_N}{4\pi \eta r}. \tag{7.18}$$

If we consider (7.18) as a solution and compare this with that of the elastic problem, then it is easy to recognize how the two equations are related. Apparently, the elastic solution (7.14) switches to the viscous solution (7.18) when the shear modulus G is replaced by the shear viscosity η and the deformation u, by the deformation velocity $\dot{u}$. We would like to stress that the transition to this form is only valid for linearly viscous materials using the force law (7.15). Figure 7.5 presents this process schematically.

---

[2] Let us once again remember that we are dealing with an incompressible, viscous medium; therefore, the corresponding elastic medium is also incompressible and it is assumed that $\nu = 1/2$.

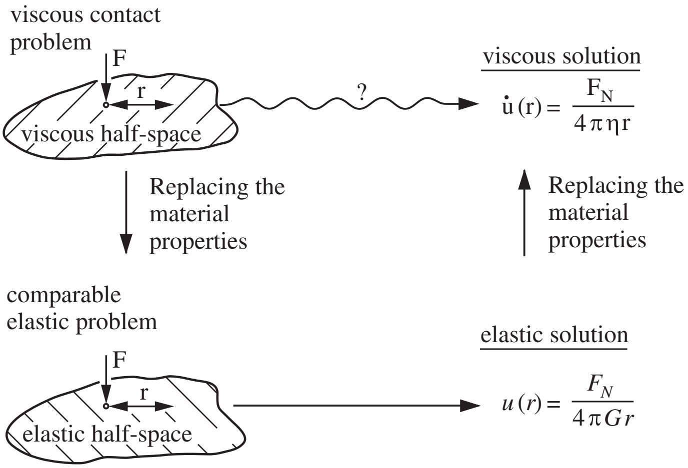

Fig. 7.5 Solution of the viscous contact problem with Radok's principle of the functional equations

One could also derive Eq. (7.18) without the Laplace transformation directly from the following analogy. The deformation of the surface of an elastic body is uniquely determined due to the equilibrium equation

$$G\Delta\vec{u} + (\lambda + G)\nabla(\nabla \cdot \vec{u}) = 0 \tag{7.19}$$

as well as the stress distribution on the surface. In this equation, the first Lamé coefficient is $\lambda = 2\nu G/(1 - 2\nu)$ [4]. The corresponding "equilibrium equation" for the creeping flow of a linearly viscous fluid (Navier-Stokes equation without the inertial term) is [5]

$$\eta\Delta\dot{\vec{u}} + (\xi + \eta)\nabla(\nabla \cdot \dot{\vec{u}}) = 0. \tag{7.20}$$

By integrating this equation once with respect to time and assuming that the medium is in a non-deformed state at time $t = 0$, we obtain

$$\eta\Delta\vec{u} + (\xi + \eta)\nabla(\nabla \cdot \vec{u}) = 0. \tag{7.21}$$

With the exception of the constants, this equation corresponds identically with Eq. (7.19) for an elastic continuum. If a displacement now occurs in a particular contact area, then the displacement fields in the elastic and viscous case will be *identical*.[3] This implication is exact and is not only valid for a linearly viscous fluid, but also for a medium with an arbitrary linear rheology. It was Lee and Radok that first came to this conclusion and based upon this, developed the study of contact mechanics of viscoelastic media [2].

---

[3] We stress, thereby, that we use the "non-penetration" boundary conditions and gravitation and capillary effects are completely neglected.

If we are additionally looking for the relationship between the forces and displacements, then we must take into account the fact that the stress in an elastic continuum is a linear function of the gradient of the displacement field $\vec{u}$, while in a fluid, it is a linear function of the gradient of the velocity field $\dot{\vec{u}}$. The fact that the equilibrium equations and the expressions for stress have the same form means that all relations that are valid for the relationship between force and displacement for a given stress distribution in the case of an elastic body are also valid for force and velocity in the case of a fluid. From this, it directly follows that the solution (7.18) for the velocity field in a fluid is obtained from the solution (7.14) for the displacement in an elastic continuum by replacing $u \to \dot{u}$ and $G \to \eta$.

7.5 Formulation of the Reduction Method for Linearly Viscous Elastomers

In this section, the results thus far will be used to demonstrate the application of the reduction method on elastomers. As in the previous section, the procedure will be first shown using a concrete example, the indentation of a rigid indenter into a linearly viscous incompressible half-space. The comparable elastic problem was closely examined in the previous chapter using the reduction method for an elastic half-space. The elastic half-space is mapped to a chain of independent linear spring elements, whose stiffness is

$$\Delta k_z = 4G\Delta x, \tag{7.22}$$

where incompressibility has already been taken into account. The corresponding force law for the ith element of the linearly elastic foundation is

$$f_{N,i} = 4G\Delta x \cdot u_{z,i}. \tag{7.23}$$

This equation can be seen as the solution of the comparable elastic problem. It must now be transferred to the viscous solution by replacing the material properties. The detour by way of the Laplace transformation is not necessary here. We can, as in the previous section, simply conduct the substitution $u \to \dot{u}$, $G \to \eta$ in Eq. (7.23) and obtain the solution

$$f_{N,i} = 4\eta\Delta x \cdot \dot{u}_{z,i}. \tag{7.24}$$

Obviously, this describes the force law of a linear damper with a damping coefficient of

$$\Delta d_z = 4\eta\Delta x. \tag{7.25}$$

The geometry of the indenter must be scaled as in the elastic case [6].

With this, the following may be summarized. The formulation of the reduction method for a linearly viscous material is obtained from that of the elastic material by replacing the springs by dampers with a damping coefficient of Δd_z. In Fig. 7.6, the procedure is schematically presented.

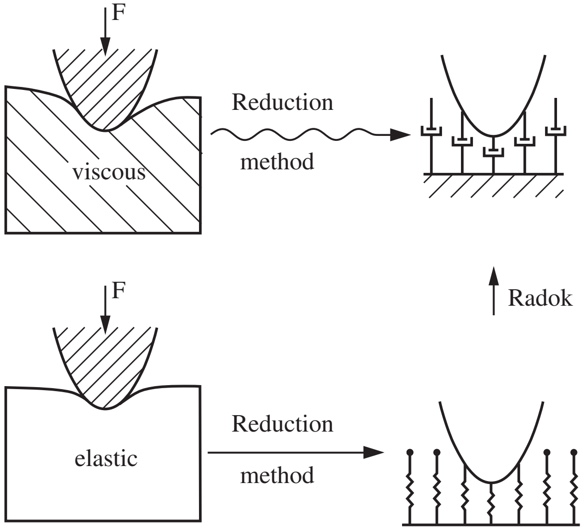

Fig. 7.6 Formulation of the reduction method for a linearly viscous incompressible material

Transferring this to a real viscoelastic material model (i.e., with viscous and elastic components) is done completely analogously and will be shortly explained in the next section and in detail in Chap. 19. In this case, the springs in the elastic formulation are replaced by spring–damper combinations, whose mathematical description can be obtained by replacing the material parameters in the Laplace domain.

7.6 The General Viscoelastic Material Law

In the previous sections, we have referred to the very simple special case of a linearly viscous material. The reason for this is the simplicity of the procedure and the clarity of the results. In this section, we show the results for the general case of an isotropic viscoelastic material. The exact derivations can be found in Chap. 19. The behavior of elastomers can be described by the relationships between deformation and stress with respect to compression

$$\sigma_{ii}(t) = \int_0^t K(t-t')\dot{\varepsilon}_{ii}(t')\mathrm{d}t' \tag{7.26}$$

and shear

$$s_{ik}(t) = 2\int_0^t G(t-t')\dot{e}_{ik}(t')\mathrm{d}t', \tag{7.27}$$

whereby we have denoted the shear component of the stress tensor with e_{ik}, in order to differentiate it from the previously introduced shear angle ε. The functions $K(t)$ and $G(t)$ are the corresponding relaxation functions. In Chap. 19, it will be shown how contacts with materials having this behavior can be solved using the reduction method. The springs in the linearly elastic foundation are replaced with elements having the characteristic

$$f_N(t) = 4\Delta x \int\limits_0^t V(t-t')\dot{u}_z(t')\mathrm{d}t', \, V(t) := \mathcal{L}^{-1}\left\{ \frac{G^*(s)(K^*(s)+G^*(s))}{K^*(s)+4G^*(s)} \right\}, \tag{7.28}$$

for which $\mathcal{L}^{-1}$ is the inverse Laplace transformation.[4] If the problem is limited to incompressible viscoelastic media (the compression modulus K is set to infinity), then the expression simplifies to

$$f_N(t) = 4\Delta x \int\limits_0^t G(t-t')\dot{u}_z(t')\mathrm{d}t', \tag{7.29}$$

which agrees with Eq. (7.13).

7.7 Problems

Problem 1 The face (radius a) of a rigid, smooth cylindrical indenter is pressed into a linearly viscous half-space (viscosity η) with a constant force F_N (Fig. 7.7). Determine the indentation velocity and the indentation depth δ as a function of time with the help of the reduction method.

Solution The equivalent one-dimensional indenter is a rectangle with a width of $2a$ pressed into a chain of independent dampers. The distance between the dampers is Δx and the damping coefficient is $\Delta d_z = 4\eta\Delta x$. The external force is evenly distributed over the dampers so that every damper experiences a force of

$$f = \frac{\Delta x}{2a} F_N. \tag{7.30}$$

With this, all dampers are compressed with the velocity

$$\dot{\delta} = \frac{f}{\Delta d_z} = \frac{F_N}{8a\eta}. \tag{7.31}$$

The indentation depth is obtained by integrating with respect to time and is equal to

---

[4] The details of the notation are explained in detail in Chap.19.

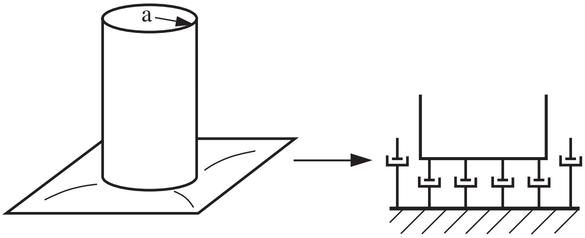

Fig. 7.7 Indentation of a cylindrical indenter into a viscous half-space

$$\delta(t) = \frac{F_N t}{8a\eta}. \tag{7.32}$$

Equation (7.31) can be obtained directly from the comparable elastic problem

$$F_N = 8Ga\delta \tag{7.33}$$

if the indentation depth and shear modulus are replaced by the velocity and shear viscosity in the result for the comparable elastic problem [1] (compare Chap. 17, Eq. 17.28):

$$F_N = 8\eta a\dot{\delta}. \tag{7.34}$$

It is easy to see that the equation is valid for an arbitrary-axially symmetric indenter as well a is considered to be the instantaneous value for the contact radius:

$$F_N(t) = 8\eta a(t)\dot{\delta}(t). \tag{7.35}$$

Problem 2 A rigid cone is pressed into a linearly viscous half-space (viscosity η) with a constant force F_N (Fig. 7.8). Determine the indentation depth as a function of time with the help of the reduction method.

Solution The surface of the cone can be described by the equation

$$f(r) = \tan\theta \cdot |r|. \tag{7.36}$$

The equivalent one-dimensional system (as described in Sect. 3.2) is

$$g(x) = \frac{\pi}{2}\tan\theta \cdot |x|. \tag{7.37}$$

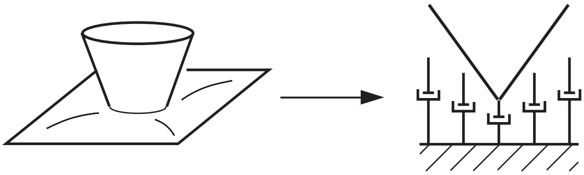

Fig. 7.8 Indentation of a cone into a viscous half-space

If the indenter is pressed to a depth of δ, then the vertical displacement of the foundation at point x is given by $u_z(x) = \delta - (\pi/2)\tan\theta \cdot |x|$. The contact radius is calculated by requiring that $u_z(a) = 0$, resulting in

$$a = \frac{2}{\pi}\frac{\delta}{\tan\theta}. \tag{7.38}$$

Equation (7.35) is also valid in this case. By inserting (7.38) into this equation, we obtain

$$F_N = \frac{16\eta}{\pi\tan\theta}\delta\dot{\delta}. \tag{7.39}$$

Separating the variables and integrating with the initial condition $\delta(0) = 0$ results in

$$F_N t = \frac{8\eta}{\pi\tan\theta}\delta^2. \tag{7.40}$$

The indentation depth as a function of time is then described by the equation

$$\delta(t) = \sqrt{\frac{\pi\tan\theta}{8}\frac{F_N}{\eta}t}. \tag{7.41}$$

Problem 3 A rigid axially-symmetric paraboloid is pressed into a half-space (viscosity η) with a constant force F_N (Fig. 7.9). Determine the indentation speed and indentation depth with the help of the reduction method.

Solution The surface of the paraboloid is described by the equation

$$f(r) = \frac{r^2}{2R}. \tag{7.42}$$

The one-dimensional indenter is a parabola that (according to Sect. 3.2) is scaled by a factor of 2:

$$g(x) = \frac{x^2}{R}. \tag{7.43}$$

If the indenter is now pressed to a depth of δ, then the contact radius is

$$a = \sqrt{R\delta}. \tag{7.44}$$

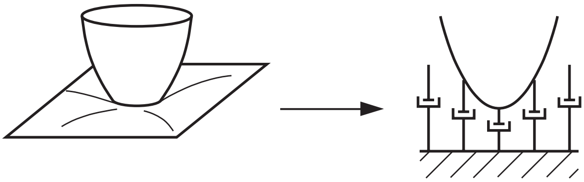

Fig. 7.9 Indentation of an axially-symmetric paraboloid into a viscous half-space

In this case, the force is also found using Eq. (7.35). Inserting (7.44) into (7.35) results in

$$F_N = 8\eta R^{1/2}\delta^{1/2}\dot{\delta}. \tag{7.45}$$

Integration with the initial condition $\delta(0) = 0$ results in

$$F_N t = \frac{16}{3}\eta R^{1/2}\delta^{3/2}. \tag{7.46}$$

The indentation depth as a function of time is then

$$\delta = \left(\frac{3F_N t}{16\eta R^{1/2}}\right)^{2/3}. \tag{7.47}$$

Differentiating with respect to time results in the indentation speed as a function of time:

$$\dot{\delta} = \frac{2}{3}\left(\frac{3F_N}{16\eta R^{1/2}}\right)^{2/3} t^{-1/3}. \tag{7.48}$$

This result is the exact solution to the corresponding three-dimensional problem and is also able to be derived without using the reduction method [7].

Problem 4 A rigid conical indenter is pressed into a viscoelastic (Kelvin body with the shear modulus G and the viscosity η) half-space with a constant force F_N. Find the dependence of the indentation depth on time.

Solution The equivalent one-dimensional indenter is given by Eq. (7.37) and the contact radius by Eq. (7.38) (it is not dependent on the rheological properties of the medium). To determine the force, we must now use the superposition of the elastic component (Eq. 3.44)

$$F_{N,el} = \frac{8G}{\pi}\frac{\delta^2}{\tan\theta} \tag{7.49}$$

and the viscous component (Eq. 7.39):

$$F_N = \frac{8G}{\pi}\frac{\delta^2}{\tan\theta} + \frac{16\eta}{\pi\tan\theta}\delta\dot{\delta}. \tag{7.50}$$

This equation can be written in the form

$$\frac{\pi\tan\theta\cdot F_N}{8G} = \delta^2 + 2\tau\delta\dot{\delta} = \delta^2 + \tau\frac{\mathrm{d}\left(\delta^2\right)}{\mathrm{d}t}, \tag{7.51}$$

where $\tau = \eta/G$ is the relaxation time of the medium. Integration with the initial condition $\delta(0) = 0$ results in

$$\delta^2(t) = \frac{\pi\tan\theta\cdot F_N}{8G}\left(1 - e^{-t/\tau}\right). \tag{7.52}$$

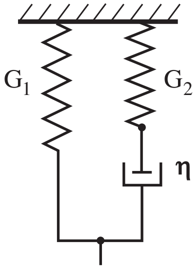

Fig. 7.10 Standard model for an elastomer consisting of a spring and a parallely attached Maxwell element

Problem 5 A rigid cylindrical indenter is pressed into an elastomer, which is described by the "standard model" [1] (Fig. 7.10). Find the dependence of the indentation depth on time.

Solution The standard model for an elastomer is shown in Fig. 7.10. It consists of a Maxwell element (a stiffness G_2 and damper η in series) and a stiffness G_1 attached in parallel.

The one-dimensional opposing side is a foundation of elements with a separation distance of Δx, the individual components of which can be characterized by the parameters $4G_1\Delta x$, $4G_2\Delta x$, and $4\eta\Delta x$. The equivalent one-dimensional indenter is a rectangle with the width $2a$. The normal force is

$$F_N = 8G_1 a u_z + 8G_2 a(u_z - u_1), \tag{7.53}$$

where u_1 satisfies the following equation:

$$u_z = u_1 + \tau \dot{u}_1 \tag{7.54}$$

and $\tau = \eta/G_2$. Solving the equation with the initial conditions $u_z(0) = 0$ and $u_1(0) = 0$ results in

$$u_1(t) = \frac{F_N}{8G_1 a}\left(1 - \exp\left(-\frac{G_1 t}{\tau(G_1 + G_2)}\right)\right), \tag{7.55}$$

$$u_z(t) = \frac{F_N}{8G_1 a}\left(1 - \frac{G_2}{G_1 + G_2}\exp\left(-\frac{G_1 t}{\tau(G_1 + G_2)}\right)\right). \tag{7.56}$$

In the special case of $G_2 \gg G_1$, we obtain the result for the Kelvin body:

$$u_z(t) = \frac{F_N}{8G_1 a}\left(1 - \exp\left(-\frac{G_1 t}{\eta}\right)\right). \tag{7.57}$$

References

1. V.L. Popov, *Kontaktmechanik und Reibung*, 2nd edn. (Springer, Berlin, 2010)
2. E.H. Lee, Quart. Appl. Math. **13**(183), 1 (1955)
3. J.R.M. Radok, Quart. Appl. Math. **15**, 198 (1957)
4. L.D. Landau, E.M. Lifschitz, Lehrbuch der Theoretischen Physik, Band VII Elastizitätstheorie, 1st edn. (Akademie, Berlin, 1965)

5. L.D. Landau, E.M.Lifschitz, Lehrbuch der Theoretischen Physik, Band 6: Hydrodynamik, Akademie-Verlag, Berlin, 5. Auflage, 1991
6. S. Kürschner, A.E. Filippov, Phys. Mesomech. **15**, 270–274 (2012)
7. S. Kürschner, V.L. Popov, A.E. Filippov, in 53. Tribologie-Fachtagung (Gesellschaft für Tribologie e.V., Göttingen, 2012), pp. 3/1–3/11

Chapter 8
Heat Transfer and Heat Generation

Markus Heß and Valentin L. Popov

8.1 Thermal Conductivity and Resistance

Thermal conductivity is a decisive parameter for the sizing of heat sinks for semiconductors or for other elements in electronic circuits. It is defined as

$$\Lambda_W = \frac{Q}{\delta T}, \tag{8.1}$$

where Q is the heat flux through the element and δT is the difference in temperature between both ends. Alternately, the thermal resistance R_W is used, which is simply the inverse of the thermal conductivity:

$$R_W = \frac{1}{\Lambda_W} = \frac{\delta T}{Q}. \tag{8.2}$$

The *heat flux density* $\vec{q}$ in an isotropic continuum is proportional to the temperature gradient:

$$\vec{q} = -\lambda \nabla T, \tag{8.3}$$

where λ is the specific thermal conductivity.

The change in temperature in a homogenous medium is described by the heat equation

$$\rho c \frac{\partial T}{\partial t} = -\operatorname{div} \vec{q} = \lambda \Delta T, \tag{8.4}$$

in which ρ is the density and c is the specific heat capacity of the medium. Using the thermal diffusivity $\alpha = \lambda / \rho c$, Eq. (8.4) can also be written in the form

$$\frac{\partial T}{\partial t} = \alpha \Delta T. \tag{8.5}$$

V.L. Popov and M. Heß, *Method of Dimensionality Reduction in Contact Mechanics and Friction*, DOI 10.1007/978-3-642-53876-6_8

In the steady-state case, the temperature distribution must satisfy the Laplace equation

$$\Delta T = 0, \tag{8.6}$$

the solution of which is the next topic of discussion for various boundary conditions. The results will directly show that also heat conductivity problems can be exactly solved within the framework of the method of dimensionality reduction. The mappability is not only limited to the thermal conductivity or resistance, but rather includes also local parameters, such as the temperature distribution on the surface.

8.2 Temperature Distribution for a Point Heat Source on a Conductive Half-Space

We consider a point heat source Q on an isotropic half-space, as shown in Fig. 8.1. With the exception of the location of the point source, let the entire surface be ideally insolated (adiabatic) and at an infinite distance, the temperature T_0 is reached. With these thermal boundary conditions, the solution to the steady-state conduction problem (see, for example [1]) is

$$\delta T(R) := T(R) - T_0 = \frac{Q}{2\pi\lambda R} \quad \text{with } R := \sqrt{x^2 + y^2 + z^2}. \tag{8.7}$$

On the surface of the half-space ($z = 0$), the resulting temperature distribution is

$$\delta T(r) := T(r) - T_0 = \frac{Q}{2\pi\lambda r} \quad \text{with } r := \sqrt{x^2 + y^2}. \tag{8.8}$$

A relationship equivalent to (8.8) appears also in the *elastic* problem, which was shown by Francis [2], among others. The normal surface displacement of an elastic half-space caused by a normal force at the origin is [3]

$$\bar{u}_z(r) = \frac{1-\nu^2}{\pi E}\frac{F_N}{r}. \tag{8.9}$$

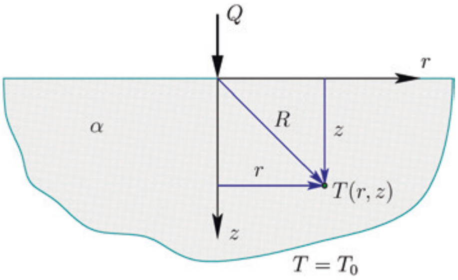

Fig. 8.1 Point heat source Q on a homogeneous half-space with the thermal diffusivity α

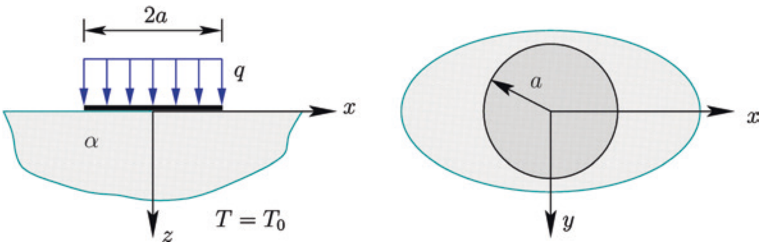

Fig. 8.2 Constant heat flux density from a *circular area* of radius a into the half-space; *cross-sectional view* in the x–z plane (*left*), *top view* (*right*)

Following this analogy and the interpretation of (8.8) and (8.9) as Green's functions of the corresponding problem, arbitrary heat flux density distributions $q(x, y)$ on the surface of the half-space present no difficulties. In place of the explicit calculation of the integral

$$\delta T(x, y) = \frac{1}{2\pi\lambda} \iint\limits_{A} \frac{q(\tilde{x}, \tilde{y})}{\sqrt{(x - \tilde{x})^2 + (y - \tilde{y})^2}} \mathrm{d}\tilde{x}\,\mathrm{d}\tilde{y}, \tag{8.10}$$

we can call on the solution of the (equivalent) elastic problem and transfer this directly to the heat transfer problem. For this, we need only undertake the following reassignments:

$$p(x, y) \mapsto q(x, y), \quad \bar{u}_z(x, y) \mapsto \delta T(x, y), \quad \text{and } E/\left(1 - \nu^2\right) \mapsto 2\lambda, \tag{8.11}$$

where $q(x, y)$ is the component of the heat flux density that is normal to the surface. Figure 8.2 shows an example of a constant heat flux density (isoflux) on a circular area with the radius a. Determining the corresponding temperature distribution on the surface is the goal of Problem 5.

Let it be mentioned that the equivalence is limited to the surface and is not valid for the field within the media. This does not, however, affect the heat flux Q through the surface, which is calculated by integrating the heat flux density over the surface:

$$Q := \int\limits_{A} q(x, y) dA. \tag{8.12}$$

In the elastic problem, this is the role of the normal force, which is similarly defined as the integral of the normal stress.

It is known from Chap. 3 that every axially-symmetric elastic contact problem can be mapped exactly to a one-dimensional model. Due to the existing equivalence between the heat transfer and the elastic contact, characterized by the reassignments in (8.11), the dimensionality reduction must also be valid for these problems.

8.3 The Universal Dependence of Thermal Conductivity and Contact Stiffness

If two half-spaces are in an ideal thermal contact by means of a circular area with the radius a and the temperature difference between the two is δT at an infinite distance, then the entire steady-state heat flux through the contact area is

$$Q = 4a\lambda^{*}\delta T \tag{8.13}$$

and the conductivity of the contact is [1]

$$\Lambda_W := \frac{Q}{\delta T} = 4a\lambda^{*} \quad \text{with} \; \frac{1}{\lambda^{*}} = \frac{1}{\lambda_1} + \frac{1}{\lambda_2}. \tag{8.14}$$

Here, λ_1 and λ_2 denote the specific thermal conductivity of the two half-spaces and we can summarize λ^{*} as a type of *effective* specific thermal conductivity. Comparing this to the contact stiffness of a circular contact with the radius a,

$$k_z := \frac{\mathrm{d}F_N}{\mathrm{d}\delta} = 2aE^{*}, \tag{8.15}$$

shows that there exists the following relationship between the thermal conductivity and contact stiffness:

$$\Lambda_W = \frac{2\lambda^{*}}{E^{*}} k_z. \tag{8.16}$$

Both properties are proportional to the characteristic *length* of the contact. Interestingly, the validity of Eq. (8.16) goes much beyond the circular contact. It is, likewise, valid for individual contacts with arbitrarily formed isothermal contact areas and even remains unchanged for the contact between rough surfaces (Sevostianov and Kachanov [4], Barber [5]). This universal relation has a very important meaning, because with its help, one must not investigate both the thermal and elastic behavior of a contact separately. Contact stiffness and thermal conductivity are connected in a simple way.

It is generally known that thermal conduction and electrical conduction are equivalent problems. If a constant electric potential difference U is applied at a sufficiently large separation distance over the contact between two half-spaces, then a steady-state electric current flows through the contact area. If we once again assume a circular ideal contact (without impurities), then the entire current must flow through this *constriction,* which is characterized by the so-called constriction resistance R_E and can be interpreted as the contact resistance. The entire electrical current I through the equipotential contact area is

$$I = \frac{4a}{\rho_1 + \rho_2} U \tag{8.17}$$

and the corresponding constriction resistance is

$$R_E := \frac{U}{I} = \frac{\rho_1 + \rho_2}{4a}, \tag{8.18}$$

where ρ_1 and ρ_2 are the specific resistances of the two bodies. If instead of the resistances in Eq. (8.18), we use the inverse of the (specific) electrical conductivities, this leads to the electrical contact conductivity

$$\Lambda_E := \frac{I}{\delta V} = 4a\lambda_E^* \quad \text{with } \frac{1}{\lambda_E^*} = \frac{1}{\lambda_{E1}} + \frac{1}{\lambda_{E2}}. \tag{8.19}$$

Completely identically to the thermal contact, the electrical conductivity is proportional to the *contact length*. Except for the form factor, the proportionality is also valid for contact areas of other forms as well as multiple micro-contacts sufficiently far from one another. For the latter, the contact length is the sum of the characteristic diameters for the so-called *a-spots* [6].

Of course, the conductivity for arbitrary contacts can also be determined from the incremental contact stiffness, because Eq. (8.16) remains absolutely valid when replacing the thermal properties by the analogous electrical properties.

8.4 The Implementation of the Steady-State Current Flow Within the Framework of the Reduction Method

The contact stiffness of arbitrary axially-symmetric bodies and rough contact is correctly mapped using the method of dimensionality reduction. A simple way for calculating the thermal and electrical conductivity of a (rough) contact consists of first determining the contact stiffness using the method of dimensionality reduction and subsequently calculating the conductivity using Eq. (8.16). Alternatively, we can look at every element of the linearly elastic foundation as having a (specific) conductivity of

$$\varDelta\varLambda = 2\lambda^* \cdot \Delta x. \tag{8.20}$$

The latter is imperative, when mapping contacts with arbitrary thermal or electrical boundary conditions.[1] Due to the analogy with the elastic problem in the form of the reassignments in Eq. (8.11), both the global relations and the local parameters on the surface can be correctly mapped. According to Eq. (8.11), the thermal flow density $q(r)$ takes over the role of the normal stress σ_{zz} and temperature, the role of the normal surface displacement.

As an example, we want to investigate the thermal contact between two half-spaces. At an infinite distance, there exists a temperature difference of δT. The non-contacting surface is adiabatic and the contact area has a radius of a. We would like to determine the heat flux Q, the thermal resistance R_W, and the distribution of the heat flux density q within the contact area. In the three-dimensional

---

[1] In the following, we constrict ourselves to the mapping of thermal contacts, because these can be directly transferred to electrical contacts.

problem, there is a so-called isothermal contact area. This means that every point on the contact area has the same temperature. The equivalent elastic problem is the indentation of a flat cylinder, the equivalent profile of which remains the same. This leads to the fact that the temperature in all of the elements of the foundation is the same and also that the heat flux through every element ΔQ is independent of the coordinate:

$$\Delta Q(x) = \Delta \Lambda \cdot \delta T(x) = 2\lambda^* \cdot \Delta x \cdot \delta T. \tag{8.21}$$

The flux density j (*per unit length in the one-dimensional system*) is equal to

$$j(x) = \frac{\Delta Q(x)}{\Delta x} = 2\lambda^* \cdot \delta T \tag{8.22}$$

and the entire flux is found by integration of the one-dimensional flux density over the contact area:

$$Q := \int_{-a}^{a} j(x)\mathrm{d}x = 2\int_{0}^{a} 2\lambda^* \delta T \,\mathrm{d}x = 4a\lambda^* \delta T, \tag{8.23}$$

which corresponds to the three-dimensional result (8.13). The same is true for the thermal resistance

$$R_W := \frac{\delta T}{Q} = \frac{1}{4a\lambda^*}. \tag{8.24}$$

Analogously to the elastic contact, we can calculate the three-dimensional heat flux density $q(r)$ by using the Abel transformation (3.37) of the one-dimensional flux density $j(x)$:

$$q(r) := -\frac{1}{\pi}\frac{1}{r}\frac{d}{dr}\int_{r}^{a} \frac{x \cdot j(x)}{\sqrt{x^2 - r^2}}\mathrm{d}x = -\frac{1}{\pi}\int_{r}^{a} \frac{j'(x)}{\sqrt{x^2 - r^2}}\,\mathrm{d}x + \frac{1}{\pi}\frac{j(a)}{\sqrt{a^2 - r^2}}. \tag{8.25}$$

In the present case of a constant, one-dimensional flux density according to (8.22), the integral on the right-hand side of (8.25) disappears so that only the three-dimensional flux density remains:

$$q(r) = \frac{1}{\pi}\frac{2\lambda^* \delta T}{\sqrt{a^2 - r^2}}. \tag{8.26}$$

Also this result corresponds exactly to the three-dimensional distribution. In the thermal contact considered, we assume an *isothermal* contact surface. In the case of an axially-symmetric, spatial temperature distribution, we must transfer the three-dimensional to a one-dimensional temperature distribution. The respective transformation takes place in the familiar way (3.27):

$$\delta T_{1D}(x) = \delta T_{3D}(0) + |x| \int_{0}^{|x|} \frac{\delta T'_{3D}(r)}{\sqrt{x^2 - r^2}}\mathrm{d}r. \tag{8.27}$$

The constant term on the right-hand side disappeared in the equivalent elastic problem by choosing the appropriate coordinates,[2] the second term expresses the same relationship as that in Eq. (3.27). As it will be seen in the next section, the inverse question is also interesting: How can we determine the three-dimensional temperature distribution from the one-dimensional distribution? Referring to [7], the inverse transformation is

$$\delta T_{3D}(r) = \frac{2}{\pi} \int\limits_0^r \frac{\delta T_{1D}(x)}{\sqrt{r^2 - x^2}}\,\mathrm{d}x. \tag{8.28}$$

In the mentioned literature, the transformation is given as well as the physical interpretation that allows for the calculation of the one-dimensional flux density distribution from the three-dimensional distribution:

$$j(x) = 2 \int\limits_x^a \frac{r \cdot q(r)}{\sqrt{r^2 - x^2}}\,\mathrm{d}r. \tag{8.29}$$

We would like to clarify its application using a simple example. In this example, we assume that a stable constant thermal flux density is given on the surface of the half-space within a circle of radius a (see Fig. 8.2) of

$$q(r) = q_0 \quad \text{for} \quad 0 < r < a, \tag{8.30}$$

and the rest of the surface is adiabatic. We want to find the one-dimensional flux density and the one-dimensional and three-dimensional temperature distribution. When taking Eq. (8.30) into account, Eq. (8.29) provides the one-dimensional flux density

$$j(x) = 2 \int\limits_x^a \frac{r q_0}{\sqrt{r^2 - x^2}}\,\mathrm{d}r = 2 q_0 \sqrt{a^2 - x^2}, \tag{8.31}$$

which of course leads to the entire flux of the original contact after integrating over the contact length:

$$Q = \int\limits_{-a}^{a} j(x)\mathrm{d}x = 4 q_0 \int\limits_0^a \sqrt{a^2 - x^2}\,\mathrm{d}x = 4 q_0 a^2 \int\limits_0^{\pi/2} \cos^2 \varphi\,\mathrm{d}\varphi = q_0 \pi a^2. \tag{8.32}$$

In the one-dimensional model, the temperature of the element is proportional to the flux density at that point (Eq. 8.22). For this example, it is

$$\delta T_{1D}(x) = \frac{1}{2\lambda^*} j(x) = \frac{q_0}{\lambda^*} \sqrt{a^2 - x^2}. \tag{8.33}$$

---

[2] The point of the indenter is the origin of the coordinate system used for the indenter profile.

With the help of Eq. (8.28), it follows that

$$\delta T_{3D}(r) = \frac{2q_0}{\pi\lambda^*}\int_0^r \frac{\sqrt{a^2-x^2}}{\sqrt{r^2-x^2}}\,\mathrm{d}x = \frac{2q_0 a}{\pi\lambda^*}\int_0^{\pi/2}\sqrt{1-(r/a)^2\sin^2\varphi}\,\mathrm{d}\varphi = \frac{2q_0 a}{\pi\lambda^*}\mathrm{E}\left(\frac{r}{a}\right), \tag{8.34}$$

for which the complete elliptical integral of the second kind is shortened to E. Comparing this to the expressions found in literature [8] verifies it to be correct. Further applications of the transformation formulas are handled in the problems at the end of this chapter.

8.5 Heat Generation and Temperature in the Contact of Elastic Bodies

Until now, we have only investigated cases with no relative motion between the bodies. Furthermore, steady-state thermal states have been assumed. We would like to continue to respect the latter, but now allow for relative motion between the bodies. For this, we consider a stationary point source Q under which a half-space moves with a constant speed of v in the x-direction; this is sketched in Fig. 8.3.

While the x, y, z coordinate system is stationary, the $\tilde{x}$, $\tilde{y}$, $\tilde{z}$ system moves with the body. To describe the temperature distribution (measured in the stationary system), the Laplace Eq. (8.6) must be supplemented by a convective term:

$$\Delta T = \frac{v}{\alpha}\frac{\partial T}{\partial x}, \tag{8.35}$$

the steady-state solution of which is [1]

$$\delta T(x,y,z) = T(x,y,z) - T_0 = \frac{Q}{2\pi\lambda R}e^{\frac{-v(R-x)}{2\alpha}} \quad \text{with } R := \sqrt{x^2+y^2+z^2}. \tag{8.36}$$

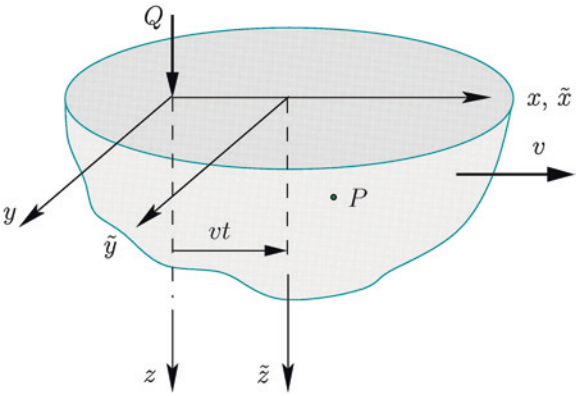

Fig. 8.3 Stationary point source under which a half-space moves at a constant speed of v in the x-direction

In order to calculate the temperature distribution for a distributed thermal flux density of the surface, Eq. (8.36) must be used as Green's function. This is especially essential for the investigation of frictional contacts, for which the (entire) frictional energy is transformed into heat. However, this is only necessary for one part of the solution. For the body on which the stationary frictional position is located, we can simply use the solution for the stationary case (8.7). Only in the special case of very low speeds or very small *Péclet* numbers

$$Pe := \frac{va}{2\alpha} \ll 1, \tag{8.37}$$

can we add the approximation for the other body and, therefore, take advantage of all equivalencies for the entirety of both surfaces (a is the contact radius). We will constrict ourselves in the following to such cases.

We will now consider a frictional contact with the frictional coefficient μ, for which the contact partners move with a relative speed of v with respect to one another. For the heat generated on the contact surface, the following is valid:

$$q(x,y) = \mu v p(x,y) \Rightarrow Q = \mu v F_N \,, \tag{8.38}$$

for which $p(x,y)$ denotes the normal stress distribution and F_N, the normal force distribution. The heat flows into both half-spaces respectively according to

$$q_1(x,y) = \beta \cdot \mu v p(x,y) \quad \text{and} \quad q_2(x,y) = (1-\beta) \cdot \mu v p(x,y). \tag{8.39}$$

The distribution between the two sometimes causes difficulties, because the weighted function β is generally dependent on x and y in order not to violate the continuity of the temperature within the contact area [9]. We circumvent the problem by assuming that one of the contacts is non-conductive, so that the entire heat flows into the other body. We would now like to determine the temperature distribution on the surface of this body by using the reduction method; its specific thermal conductivity is λ. We consider an element of the linearly elastic foundation with the coordinate x that is indented by $u_z(x)$. The known force acting on this element is then $f_N = E^* \Delta x \cdot u_z(x)$. The frictional power of the element is $\Delta Q(x) = \mu v f_N(x) = \mu v E^* \Delta x \cdot u_z(x)$, for which the resulting temperature difference of the element is

$$\delta T_{1D}(x) = \frac{\Delta Q(x)}{2\lambda \cdot \Delta x} = \frac{E^*}{2\lambda} \mu \cdot v \cdot u_z(x). \tag{8.40}$$

The temperature difference for the three-dimensional model at the point r on the surface within the contact area can be obtained using Eq. (8.28). The temperature can be calculated even outside of the contact surface. For this, we must simply change the upper boundary of the integral in Eq. (8.28):

$$\delta T_{3D}(r) = \frac{2}{\pi} \int\limits_0^a \frac{\delta T_{1D}(x)}{\sqrt{r^2 - x^2}} \, \mathrm{d}x \quad \text{for } r > a. \tag{8.41}$$

Applying this classical transformation to the classical example of a parabolic frictional contact is the topic of Problem 1. It is possible that the reader may not see the benefits of the method of dimensionality reduction compared to other methods because of the complicated transformations. Therefore, we would like to emphasize the fact that the reduction method maps *global* parameters such as normal force, indentation depth, contact area/length, total heat flow rate, and maximum surface temperature as well the contact stiffness and resistance seemingly effortlessly and exactly. These relationships are at the forefront of the investigation of rough contacts. If only information about *local* parameters is of interest, then this can also be reconstructed using the transformation rules from the one-dimensional model.

8.6 Heat Generation and Temperature in the Contact of Viscoelastic Bodies

Heat can not only be generated on the surface, but also directly in the material of the contacting bodies, assuming that they exhibit viscoelastic properties. One can qualitatively approximate the temperature distribution as follows. Let us consider an element in a viscoelastic foundation at the point x and assume that it is deformed in the vertical direction with the speed $\dot{u}_z(x,t)$. Thereby, the force produced is given by

$$f_N(x,t) = 4\Delta x \int_0^t G(t-t')\dot{u}_z(x,t')\mathrm{d}t', \tag{8.42}$$

for which an incompressible material is assumed (see Chap. 7).

The heat generation in the element is

$$\Delta Q(x,t) = f_N(x,t)\cdot\dot{u}_z(x,t) = \dot{u}_z(x,t)\cdot 4\Delta x \int_0^t G(t-t')\dot{u}_z(x,t')\mathrm{d}t'. \tag{8.43}$$

If we interpret this heat generation as that produced in the frictional contact, then we obtain the temperature in the element according to (8.40):

$$\delta T_{1D}(x,t) = \frac{\Delta Q(x,t)}{2\lambda^*\cdot\Delta x} = \frac{2}{\lambda^*}\dot{u}_z(x,t)\int_0^t G(t-t')\dot{u}_z(x,t')\mathrm{d}t'. \tag{8.44}$$

As an example, we consider a simple viscoelastic medium (Kelvin body). In this case, the normal force is given by

$$f_N(x,t) = (4Gu_z(x,t) + 4\eta\dot{u}_z(x,t))\Delta x \tag{8.45}$$

and the temperature by

$$\delta T_{1D}(x,t) = \frac{2}{\lambda^*}(Gu_z(x,t) + \eta\dot{u}_z(x,t))\dot{u}_z(x,t). \tag{8.46}$$

The temperature is, therefore, dependent on the time and can generally either increase or decrease (adiabatic cooling).

8.7 Problems

Problem 1 A non-conducting, rigid body with a smooth surface slides over an elastic half-space with a parabolically curved surface of radius R with a speed of v_0. The modulus of elasticity E, Poisson's ratio ν, and the thermal conductivity λ of the half-space are given. Determine the temperature distribution of the surface of the half-space using the reduction method and assuming steady-state conditions.

Solution We have already solved the purely elastic problem multiple times and carry over several intermediate results. After converting the three-dimensional profile to a one-dimensional equivalent profile using the *rule of Popov* and calculating the indentation depth into a linearly elastic foundation, we obtain the displacement in the one-dimensional system:

$$u_z(x) = d - \frac{x^2}{R} \quad \text{with } d = \frac{a^2}{R}, \tag{8.47}$$

for which the relationship between the indentation depth d and the normal force F_N is given by the Hertzian relation $F_N = \frac{4}{3}E^* R^{1/2} d^{3/2}$. According to (8.40), this leads to the one-dimensional temperature difference

$$\delta T_{1D}(x) = \frac{E^*}{2\lambda}\mu \cdot v_o \cdot u_z(x) = \frac{E^*}{2\lambda}\mu \cdot v_o \cdot \left(d - \frac{x^2}{R}\right) \quad \text{with } E^* = \frac{E}{1-\nu^2}. \tag{8.48}$$

Insertion of (8.48) into (8.28) results in the three-dimensional distribution of the surface temperature within the contact area:

$$\begin{aligned}
\delta T_{3D}(r) &= \frac{2}{\pi}\int_0^r \frac{\delta T_{1D}(x)}{\sqrt{r^2-x^2}}\,\mathrm{d}x = \frac{\mu v_o E^*}{\pi\lambda R}\int_0^r \frac{a^2-x^2}{\sqrt{r^2-x^2}}\,\mathrm{d}x \\
&= \frac{\mu v_o E^*}{\pi\lambda R}\left[a^2 \arcsin\left(\frac{x}{r}\right)\Big|_0^r + x\sqrt{r^2-x^2}\Big|_0^r - r^2\int_0^{\pi/2}\cos^2\varphi\,\mathrm{d}\varphi\right]. \\
&= \frac{\mu v_o E^*}{4\lambda R}\left(2a^2 - r^2\right)
\end{aligned} \tag{8.49}$$

By using the Hertzian relationship between normal force and contact radius and taking (8.38) into account, we obtain

$$\delta T_{3D}(r) = \frac{3Q}{16\lambda a^3}\left(2a^2 - r^2\right) \quad \text{for } 0 < r < a. \tag{8.50}$$

We obtain the distribution outside of the contact area from (8.41). Because the formula differs from that valid in the contact area only by the upper bound of the integral, we can simply carry over the antiderivative in (8.49). After rearrangement, we obtain

$$\delta T_{3D}(r) = \frac{3Q}{8\pi\lambda a^3}\left[\left(2a^2 - r^2\right)\arcsin\left(\frac{a}{r}\right) + a\sqrt{r^2 - a^2}\right] \quad \text{for } r > a. \tag{8.51}$$

The reader may be convinced of the validity of the results by the usage of equivalency [2].

Problem 2 Determine the thermal resistance of the contact from Problem 1. Assume a one-dimensional model.

Solution The thermal resistance, as defined in (8.2), presumes an isothermal contact that is not present here. Therefore, we refer here to the *maximum* surface temperature that is present in the middle of the contact. This takes the role of the indentation depth in the elastic contact, where the indentation depth is the same for both the one-dimensional and three-dimensional models. Therefore, the maximum temperature in the middle of the contact is also the same in both models. From (8.48), we obtain

$$\delta T_{\max} = \delta T_{1D}(0) = \frac{E^*\mu v_o a^2}{2\lambda R} = \frac{3Q}{8\lambda a} \tag{8.52}$$

and with it, the thermal resistance

$$R_W := \frac{\delta T_{\max}}{Q} = \frac{3}{8\lambda a}. \tag{8.53}$$

This result initially appears to conflict with the universal formula (8.16), because this would result in

$$R_W := \frac{E^*}{2\lambda \cdot k_z} = \frac{E^*}{2\lambda \cdot 2E^* a} = \frac{1}{4\lambda a}. \tag{8.54}$$

This is indeed the thermal resistance for a round contact, however, this relationship is only (!) valid for isothermal contact areas. Even redefining the thermal resistance with respect to the average temperature instead of the maximum temperature does not help. In this case, the thermal resistance is

$$\frac{\overline{\delta T_{3D}}}{Q} = \frac{9}{32\lambda a}, \tag{8.55}$$

although the deviation is not very large. The proportionality to the contact length is of course always present.

Problem 3 A half-space with a parabolically curved surface having a radius of curvature of R is pressed into a second half-space with a flat surface. Before

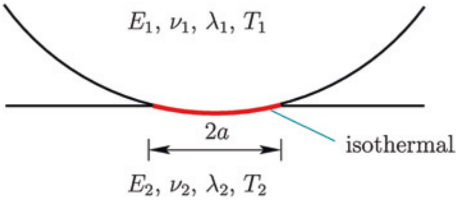

Fig. 8.4 Qualitative presentation of a Hertzian contact with steady-state heat conduction

contact, the bodies exhibit the temperatures T_1 and T_2. Upon bringing the bodies together, a heat flux flows through the contact area. If the temperatures far from the contact surface are held constant, then a steady-state flow will occur after some time. Let it be mentioned that the contact area is isothermal and temperature related deformations are neglected. Calculate the dependence of the thermal resistance on the normal force in the case of an *elastic* contact, which is qualitatively shown in Fig. 8.4.

Solution We can solve the elastic problem and heat conduction problem *separately* with the help of the method of dimensionality reduction. The solution of the elastic problem can be found in Chap. 3. The dependence of the normal force on the contact radius was

$$F_N(a) = \frac{4}{3}E^*\frac{a^3}{R} \quad \text{with } \frac{1}{E^*} = \frac{1-\nu_1^2}{E_1} + \frac{1-\nu_2^2}{E_2}. \tag{8.56}$$

For a round contact with an isothermal contact area Eq. (8.14) is valid with which we further express the conductivity by means of the resistance:

$$R_W = \frac{1}{4a\lambda^*} \quad \text{with } \frac{1}{\lambda^*} = \frac{1}{\lambda_1} + \frac{1}{\lambda_2}. \tag{8.57}$$

We have also already derived this relationship with the reduction method. By solving (8.56) with respect to the contact radius and inserting this into (8.57), we obtain the desired dependence:

$$R_W = \frac{(E^*)^{1/3}}{\lambda^*(48RF_N)^{1/3}} \sim F_N^{-1/3}. \tag{8.58}$$

In conclusion, let it be noted that for the complete plastic contact, the result is

$$F_N \sim a^2 \Rightarrow R_W \sim F_N^{-1/2}. \tag{8.59}$$

Problem 4 Determine the total current, the constriction resistance, and the current density distribution for the electrical contact between two half-spaces with the specific resistances ρ_1 and ρ_2 within a circular area (radius a). It should be assumed that far from the contact, there exist equipotential surfaces within the half-spaces having a difference in potential of U. Furthermore, determine the radius b of the partial contact area through which half of the total current flows.

Solution We have already discussed the equivalent heat conduction problem in Sect. 8.4. First, we reduce the electrical contact between two bodies to the steady-state flow through one body whose effective specific conductivity is

$$\lambda^* = \frac{1}{\rho_1 + \rho_2}. \tag{8.60}$$

Between the circular equipotential surface, and another at infinity (or at a sufficiently large distance), there exists the potential difference U. Because a *constant* three-dimensional potential difference exists, no modification whatsoever is needed and it can be carried over to the one-dimensional system. Every element in the linearly elastic foundation obtains the specific conductivity $\Delta\Lambda = 2\lambda^* \cdot \Delta x$ and the following partial current flows through each:

$$\Delta I(x) = \Delta\Lambda \cdot \delta V(x) = 2\lambda^* \cdot \Delta x \cdot U. \tag{8.61}$$

By summation of the partial currents through all of the elements in the foundation, we obtain the total current:

$$I = \int_{-a}^{a} 2\lambda^* \delta V(x)\,\mathrm{d}x = 4a\lambda^* U \tag{8.62}$$

and from this, the constriction resistance

$$R_E := \frac{U}{I} = \frac{1}{4a\lambda^*} = \frac{\rho_1 + \rho_2}{4a}. \tag{8.63}$$

The three-dimensional distribution of the flux density within the contact area is calculated using (8.25), which is trivial due to the *constant* one-dimensional current density:

$$q(r) = \frac{1}{\pi}\frac{2\lambda^* U}{\sqrt{a^2 - r^2}} = \frac{I}{2\pi a}\frac{1}{\sqrt{a^2 - r^2}}. \tag{8.64}$$

Of course, all results correspond to those in the three-dimensional problem. For this solution of the supplemental problem, we may not assume a one-dimensional current density, but must use the determined three-dimensional current density. For this, we integrate (8.64) over the three-dimensional contact area with the upper radial boundary b and require that the result corresponds to half of the current:

$$\frac{I}{2\pi a}\int_0^b \frac{r}{\sqrt{a^2 - r^2}} 2\pi\,\mathrm{d}r \overset{!}{=} \frac{I}{2}. \tag{8.65}$$

Elementary integration and a few rearrangements lead to

$$b = \frac{1}{2}\sqrt{3}\,a \approx 0.866\,a. \tag{8.66}$$

Although the radius b divides the surface by the ratio 3:1, meaning that the outer ring is only a quarter of the total area, half of the total current flows through it.

Problem 5 Determine the temperature distribution on the surface as well as the thermal resistance for the conduction problem (*isoflux*) shown in Fig. 8.2. Use the analogy to the elastic problem, the solution of which is considered to be known. According to this, the loading of an elastic half-space by a constant stress p over a circular area with the radius a leads to the following normal surface displacements (see, for example [3]):

$$\bar{u}_z(r) = \begin{cases} \frac{4(1-\nu^2)pa}{\pi E}\mathrm{E}(r/a) & \text{for } r < a \\ \frac{4(1-\nu^2)pr}{\pi E}\left[\mathrm{E}(r/a) - \left(1 - \frac{a^2}{r^2}\right)\mathrm{K}(a/r)\right] & \text{for } r > a \end{cases}, \tag{8.67}$$

where K and E are the complete elliptical integrals of the second kind:

$$\mathrm{K}(k) := \int_0^{\pi/2} \frac{1}{\sqrt{1 - k^2 \sin^2 \varphi}} \mathrm{d}\varphi \quad \text{and } \mathrm{E}(k) := \int_0^{\pi/2} \sqrt{1 - k^2 \sin^2 \varphi}\, \mathrm{d}\varphi. \tag{8.68}$$

Solution According to Eq. (8.11), we must only replace the displacement with the temperature, the normal stress with the heat flux density, and the effective modulus of elasticity with double the conductivity:

$$\delta T(r) = \begin{cases} \frac{2qa}{\pi\lambda}\mathrm{E}(r/a) & \text{for } r < a \\ \frac{2qr}{\pi\lambda}\left[\mathrm{E}(r/a) - \left(1 - \frac{a^2}{r^2}\right)\mathrm{K}(a/r)\right] & \text{for } r > a \end{cases}. \tag{8.69}$$

In order to calculate the thermal resistance, we need the maximum surface temperature. This is given in the center and has a value of

$$\delta T_{\max} = \delta T(0) = \frac{qa}{\lambda}, \tag{8.70}$$

where we have taken $\mathrm{E}(0) = \pi/2$ into account. The resulting thermal resistance is then

$$R_W := \frac{\delta T_{\max}}{Q} = \frac{qa}{\lambda\pi qa^2} = \frac{1}{\pi\lambda a}. \tag{8.71}$$

References

1. H.S. Carslaw, J.S. Jaeger, *Conduction of Heat in Solids*, 2nd edn. (Oxford University Press, London, 1954)
2. H.A. Francis, Interfacial temperature distribution within a sliding Hertzian contact. ASLE Trans. **14**(1), 41–54 (1971)
3. K.L. Johnson, *Contact Mechanics*. (Cambridge University Press, Oxford, 1987)
4. I. Sevostianov, M. Kachanov, Incremental compliance and resistance of contacts and contact clusters: Implications of the cross-property connection. Int. J. Eng. Sci. **47**, 974–989 (2009)

5. J.R. Barber, Bounds on the electrical resistance between contacting elastic rough bodies, in *Proceedings of the Royal Society of London. Series A: Mathematical, Physical and Engineering Sciences*, vol. 459, no. 2029 (2003), pp. 53–66
6. R. Holm, *Die technische Physik der elektrischen Kontakte*, Band 4, Edwards Bros. (1944)
7. M. Heß, *Über die exakte Abbildung ausgewählter dreidimensionaler Kontakte auf Systeme mit niedrigerer räumlicher Dimension* (Cuvillier , Berlin, 2011), Kap. 2
8. M.M. Yovanovich, E.E. Marotta, Thermal spreading and contact resistances. *Heat Transfer Handbook*, chap. 4 (2003), pp. 261–394
9. H. Blok, Theoretical study of temperature rise at surfaces of actual contact under oiliness lubricating conditions, in *General Discussion on Lubrication*, vol. 2 (Institution of Mechanical Engineers, 1937) , pp. 222–235

Chapter 9
Adhesion with Elastomers

Valentin L. Popov and Markus Heß

9.1 Introduction

The application of the method of dimensionality reduction to adhesive contacts between *elastic* bodies is given by the *rule of Heß* (Eq. 4.1). However, this rule cannot be directly generalized to include contacts between viscoelastic bodies. This can already be seen in the fact that the "separation criterion" from Heß contains the modulus of elasticity. The effective modulus of elasticity of elastomers, however, is dependent on the deformation speed or frequency. Therefore, to be able to transfer the results of Heß [1] to those of viscoelastic media, a better physical understanding of the phenomenon of adhesion is necessary. For this, it is helpful to consider a microscopic picture of an adhesive contact. The fundamentals of this were already described in Chap. 4. At this point, we will generalize these ideas for their application to viscoelastic media.

9.2 Stress Concentration Near the Boundary of an Adhesive Contact

We consider an adhesive contact between a rigid flat indenter and an elastic body (Fig. 9.1). When the indenter is pulled with an upwards-oriented force F, the following stress distribution develops in the contact area [2]:

$$\sigma = \sigma_0 \left(1 - \left(\frac{r}{a} \right)^2 \right)^{-1/2} \tag{9.1}$$

with

$$\sigma_0 = \frac{F}{2\pi a^2}. \tag{9.2}$$

V.L. Popov and M. Heß, *Method of Dimensionality Reduction in Contact Mechanics and Friction*, DOI 10.1007/978-3-642-53876-6_9

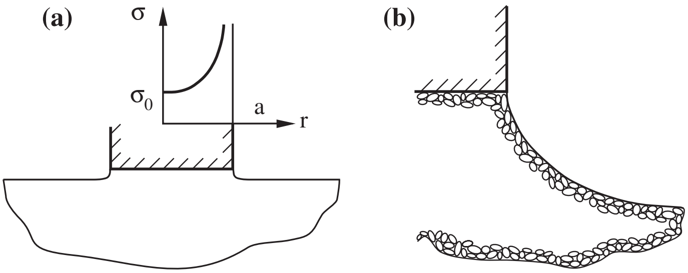

Fig. 9.1 **a** Adhesive contact of an elastic body with a flat indenter; **b** Enlarged view of the "tip of the crack" (the area in immediate vicinity to the edge of the contact)

At the edge near the tip of the crack, for $r = a - \Delta r$, the distribution has a singularity of the form

$$\sigma = \sigma_0 \sqrt{\frac{a}{2\Delta r}}. \tag{9.3}$$

As discussed in Chap. 4 and can be seen in the classical works of Griffith [3] and Prandtl [4], this singularity is essentially the physical cause for the rupture of the adhesive connection between the two bodies. Because the rupture process takes place in a very narrow "process zone" near the tip of the crack, only the form of the singularity is important for the global equilibrium. The stress distribution far from the tip does not play a role. Noteworthy is that the relationship (9.3) does not contain the elastic properties of the medium. Therefore, it is also valid for *arbitrary* media with a linear rheology.

In the most simple microscopic examination of an adhesive contact, we can think of the bodies as being made of molecules of the characteristic length b. Because of the molecular structure, the singularity (9.3) would not exist in reality, because the distance to the tip cannot be smaller than the size of the molecules. The stress then reaches a high, but finite, maximum on the order of magnitude of

$$\sigma_{\max} \approx \sigma_0 \sqrt{\frac{a}{2b}}. \tag{9.4}$$

The length b can be interpreted as the size of the "process zone" [5].

The breaking of molecular bonds near the edge of an adhesive contact occurs when certain critical values are exceeded. In the elastic case, it does not matter if we exceed a critical strain, stress, or work, because all three are distinctly related to one another. For the case of elastomers, this is no longer true: For an elastomer, the stress is no longer only a function of strain, but also of the strain rate. Depending on which independent value (stress or strain) assumes a critical value, we obtain different separation criteria. In this chapter, we discuss two criteria, whereby also many other criteria are conceivable. We begin with the case of elastic bodies and later go on to the investigation of viscoelastic bodies.

9.3 Deformation Criterion

Both the stress and the strain obtain their maximum values in the immediate vicinity of the crack tip—roughly put—within one molecular diameter from the crack tip. Thereby, the maximum stress (9.4) leads to a deformation of the material on the order of magnitude of

$$\varepsilon_{\max} \approx \frac{\sigma_{\max}}{E^*} = \frac{\sigma_0}{E^*}\sqrt{\frac{a}{2b}}. \tag{9.5}$$

Let us assume that the molecular contact is lost, when the relative displacement of the "contacting molecules" in the vertical direction reaches a critical value b_c. We can then rewrite the approximation (9.5) in the following form:

$$\varepsilon_{\max} \approx \frac{b_c}{b} \approx \frac{\sigma_0}{E^*}\sqrt{\frac{a}{2b}}. \tag{9.6}$$

From this, we obtain the critical value of σ_0:

$$\sigma_0 \approx \sqrt{2}E^* \frac{b_c}{\sqrt{ab}}. \tag{9.7}$$

For the adhesion force, we obtain

$$F_A = 2\pi a^2 \sigma_0 \approx 2^{3/2}\pi E^* b_c b^{-1/2} a^{3/2}. \tag{9.8}$$

The maximum vertical displacement of the indenter before separation is given by the equation

$$u_A = \frac{F_A}{2aE^*} = 2^{1/2}\pi b_c b^{-1/2} a^{1/2}. \tag{9.9}$$

By defining

$$b^* = 2\pi^2 b_c^2 / b \tag{9.10}$$

(b^* is the characteristic length on the order of magnitude of the length of a polymer molecule) we bring (9.9) into the form

$$u_A = \sqrt{b^* a}. \tag{9.11}$$

Note that this equation does not contain the modulus of elasticity; therefore, it also valid in the same form for arbitrary media with a linear rheology, as long as the assumed deformation criterion for the crack retains its validity. For elastomers in the case of the "deformation criterion," the fracture criterion from Heß (4.1) must be replaced by

$$\Delta\ell_{\max}(a) = \sqrt{b^* a}. \tag{9.12}$$

9.4 Stress Criterion

Other criteria are also conceivable. For instance, the contact may be lost when the tip stress (9.4) reaches a critical value σ_c:

$$\sigma_{\max} \approx \sigma_0 \sqrt{\frac{a}{2b}} = \sigma_c. \tag{9.13}$$

Because the relationship (9.4) is universally valid for all media with a linear rheology, we obtain the adhesion force

$$F_A = 2\pi a^2 \sigma_0 = 2^{3/2} \pi a^{3/2} b^{1/2} \sigma_c. \tag{9.14}$$

For this criterion, the adhesion force is not dependent on the separation speed. The Heß criterion (4.1) must be replaced in this case with the requirement that the force in the individual springs reaches the critical value

$$\Delta f_{z,\max} = \pi \sigma_c \sqrt{2ab} \cdot \Delta x. \tag{9.15}$$

9.5 Adhesive Contacts Without Initial Stress

In this section, we consider a rigid cylindrical indenter with the diameter L, which is brought into contact with an elastomer without a normal force in a way that the contacting surfaces adhere. Subsequently, a separation force $F(t)$ is applied. In the one-dimensional system, a flat profile of the length L is brought into contact with an array of viscoelastic elements, defined according to the rules in Chap. 7. In the *elastic* case, the normal force F and the vertical displacement u are related by the equation

$$F = LE^* u. \tag{9.16}$$

For incompressible *elastomers,* as explained in Chap. 7, this relationship must be replaced by the integral relationship

$$F(t) = 4L \int_{-\infty}^{t} G\left(t - t'\right) \frac{\mathrm{d}u}{\mathrm{d}t'} \mathrm{d}t'. \tag{9.17}$$

With the help of this equation, we will now discuss the separation process using the deformation criterion. If the deformation criterion is valid, the separation will always occur upon reaching the critical vertical displacement given by (9.12). It is easy to calculate the force exhibited in this state. Let us assume that the speed $\mathrm{d}u/\mathrm{d}t$ is zero until the time $t = 0$ and at this time, it jumps to v_0 and remains constant. The force is then given by the equation

$$F(t) = 4Lv_0 \int_{0}^{t} G\left(t - t'\right) \mathrm{d}t' = 4Lv_0 \int_{0}^{t} G(\xi) \mathrm{d}\xi \tag{9.18}$$

and reaches its maximum value at $t = u_A/v_0$:

$$F_A = 4Lv_0 \int_0^{u_A/v_0} G(\xi)\mathrm{d}\xi, \tag{9.19}$$

where u_A is taken from Eq. (9.11).

We constrict ourselves at this point to the simplest rheology imaginable—that of a linearly viscous fluid. The adhesive contact between media that exhibit a more complicated rheology will be handled in the problems at the end of this chapter. For a linearly viscous medium, Eq. (9.17) can be directly written in the form

$$F(t) = 4L\eta \frac{\mathrm{d}u}{\mathrm{d}t}. \tag{9.20}$$

For a constant velocity, it is not dependent on time as long as the displacement has not reached its critical value (9.11). Therefore, the adhesion force is

$$F_A = 4L\eta \frac{\mathrm{d}u}{\mathrm{d}t}. \tag{9.21}$$

It is proportional to the diameter of the contact and to the separation speed. This equation is also applicable to pure liquids as long as the capillary effect is neglected. Furthermore, cavitation is not taken into account.

9.6 Problems

Problem 1 Determine the force of separation (without initial stress) of a rigid cylindrical indenter with the diameter L from a medium that is described by the "standard model" (Fig. 9.2). Use the stress and deformation criteria.

Solution

(a) *Stress criterion*. If the stress criterion is applicable, the adhesion force is given by Eq. (9.14):

$$F_A = \pi L^{3/2} b^{1/2} \sigma_c. \tag{9.22}$$

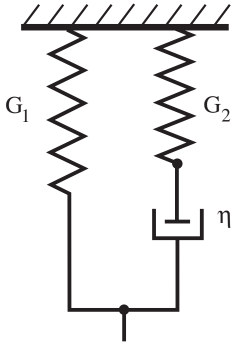

Fig. 9.2 A simple model for an elastomer ("standard model")

It is proportional to $L^{3/2}$ and is dependent on the critical stress and the size of the process zone, but not on the separation speed. The dependence of the adhesion force on the separation speed is, therefore, an indication that the stress criterion is not valid for a flat indenter.

(b) *Deformation criterion.* The time-dependent shear modulus for this model is [2]

$$G(t) = G_1 + G_2 e^{-t/\tau}, \tag{9.23}$$

with $\tau = \eta/G_2$. Insertion into (9.19) results in the adhesion force:

$$\begin{aligned} F_A &= 4Lv_0 \int\limits_0^{u_A/v_0} \left(G_1 + G_2 e^{-\xi/\tau}\right)\mathrm{d}\xi = 4Lv_0\left[\frac{G_1 u_A}{v_0} + \tau G_2\left(1 - e^{-\frac{u_A}{v_0\tau}}\right)\right] \\ &= 4G_1 L u_A + 4Lv_0\eta\left(1 - e^{-\frac{u_A}{v_0\tau}}\right). \end{aligned} \tag{9.24}$$

By taking Eq. (9.11) into account, one can write this equation in the following explicit form:

$$F_A \approx 2^{3/2} L G_1 \sqrt{b^* L} + 4Lv_0\tau G_2\left(1 - e^{-\frac{\sqrt{b^* L}}{2^{1/2} v_0 \tau}}\right). \tag{9.25}$$

By introducing

$$\zeta = \frac{2^{1/2} v_0 \tau}{\sqrt{b^* L}}, \tag{9.26}$$

we can write (9.25) in the form

$$F_A \approx 2^{3/2} L^{3/2} b^{*1/2}\left(G_1 + G_2\zeta\left(1 - e^{-\frac{1}{\zeta}}\right)\right). \tag{9.27}$$

From this, it is obvious that the separation force is only dependent on the combination of parameters in (9.26). The dependence of the dimensionless force $f_A = F_A/\left(2^{3/2} L^{3/2} b^{*1/2} G_1\right)$ on ζ is presented in Fig. 9.3.

In the curve of the adhesion force function, three domains can be recognized:

I. $\zeta \ll \frac{G_1}{G_2}$. In this case,

$$F_A \approx 2^{3/2} L^{3/2} b^{*1/2} G_1 \tag{9.28}$$

is valid. This is the classical result for the adhesion between a rigid cylinder and an elastic medium with the shear modulus G_1.

II. $\frac{G_1}{G_2} \leq \zeta \leq 1$. In this interval,

$$F_A \approx 4L\eta v_0 \tag{9.29}$$

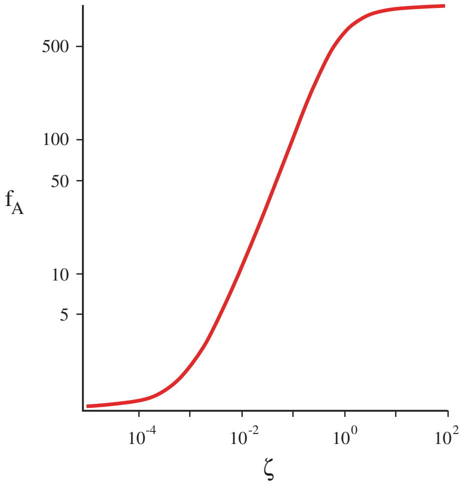

Fig. 9.3 Dependence of the dimensionless force $f_A = F_A/\left(2^{3/2}L^{3/2}b^{*1/2}G_1\right)$ on the dimensionless separation speed ζ for the case of an elastomer, which is described by the standard model, where $G_2/G_1 = 1{,}000$ is chosen

is valid, which may be expected, as the system behaves like a linearly viscous fluid here and satisfies Eq. (9.21).

III. $1 \ll \zeta$. In this domain,

$$F_A \approx 2^{3/2}L^{3/2}b^{*1/2}(G_1 + G_2) \tag{9.30}$$

is valid. This is the same relation as (9.28), but with a different shear modulus.

Let it be noted that in interval II, the adhesion force is not dependent on the exact microscopic fracture criterion, but only on the viscosity of the medium. The limiting case of a simple viscoelastic body (Kelvin body) is obtained from the general expression (9.25) by inserting $G_2 \to \infty$. The result is

$$F_A \approx 2^{3/2}L^{3/2}b^{*1/2}G_1 + 4L\eta v_0. \tag{9.31}$$

Because the viscosity exhibits a strong temperature dependence, one may expect that in the intermediate interval of separation speeds, the adhesion force increases with a decrease in temperature.

Problem 2 A rigid cylinder with the diameter L is pressed into a viscoelastic medium described by the "standard model" (Fig. 9.2) with the normal force F_N and, after a long settling time, pulled away with the speed v_0. Determine the adhesion force by using the stress and deformation criteria.

Solution

(a) *Stress criterion*. In using the stress criterion, Eq. (9.22) remains valid: The adhesion force is the same as the case without initial stress.

(b) *Deformation criterion*. During the indentation phase, the material reacts completely elastic after a long settling time, with the shear modulus G_1. The indenter presses into the material to a depth of

$$d_1 = \frac{F_N}{4LG_1}. \tag{9.32}$$

Instead of Eq. (9.18), a modified equation must be used:

$$F(t) = -F_N + 4Lv_0 \int_0^t G(t-t')\mathrm{d}t' = -F_N + 4Lv_0 \int_0^t G(\xi)\mathrm{d}\xi. \tag{9.33}$$

$F(t)$ is a monotonically increasing function in time: The force increases until the fracture criterion (9.12) is reached:

$$u = -d_1 + v_0 t = u_A = \sqrt{b^* L/2}. \tag{9.34}$$

From this, the separation time $\tilde{t}$ can be determined:

$$\tilde{t} = \frac{d_1 + u_A}{v_0} = \frac{d_1 + \sqrt{b^* L/2}}{v_0}. \tag{9.35}$$

Consequently, the adhesion force in the general case is

$$F_A = -F_N + 4Lv_0 \int_0^{\frac{d_1+\sqrt{b^*L/2}}{v_0}} G(\xi)\mathrm{d}\xi. \tag{9.36}$$

Substitution of the time-dependent shear modulus for the standard model (9.23) results in

I. If $v_0\tau \ll d_1 + \sqrt{b^*L/2}$, then

$$\begin{aligned} F_A &= -F_N + 4Lv_0 \int_0^{\frac{d_1+\sqrt{b^*L/2}}{v_0}} \left(G_1 + G_2 e^{-\xi/\tau}\right)\mathrm{d}\xi \\ &= 4LG_1\sqrt{b^*L/2} + 4Lv_0\tau G_{02}\left(1 - e^{-\frac{d_1+\sqrt{b^*L/2}}{v_0\tau}}\right). \end{aligned} \tag{9.37}$$

$$F_A \approx 4LG_1\sqrt{b^*L/2} + 4Lv_0\eta \tag{9.38}$$

and the adhesion force is independent from the indentation force.

II. If $v_0\tau \gg d_1 + \sqrt{b^*L/2}$, then

$$F_A \approx F_N\frac{G_2}{G_1} + 4L\sqrt{b^*L/2}(G_1 + G_2). \tag{9.39}$$

In this interval, the adhesion force increases linearly with the indentation force. Let it be noted that the boundaries of this interval are dependent on the indentation force itself.

Equation (9.37) can be written in the form

$$f_A \approx 1 + \frac{G_2}{G_1}\zeta\left(1 - e^{-\frac{1+f}{\zeta}}\right), \tag{9.40}$$

where, in addition to the relation (9.26), we have inserted the dimensionless force f_A:

$$f_A = \frac{F_A}{2^{3/2} b^{*1/2} L^{3/2} G_1} \tag{9.41}$$

and the dimensionless initial force f:

$$f = \frac{F_N}{2^{3/2} b^{*1/2} L^{3/2} G_1}. \tag{9.42}$$

The dependence of (9.40) is presented in Fig. 9.4. While the adhesion force for small separation speeds is not dependent on the indentation force, it can be increased significantly by the indentation force for sufficiently large separation speeds.

Problem 3 A conical indenter (Fig. 9.5) is pressed into a linearly viscous elastomer to a depth of d_0 and subsequently pulled up. Using the deformation criterion for the crack, determine the dependence of the contact radius on the indentation depth d.

Solution The form of the cone is described by the equation $f(r) = \tan\theta \cdot r$. The corresponding scaling factor is $\kappa_1 = \pi/2$, so that the resulting equivalent one-dimensional profile is $g(x) = (\pi/2)\tan\theta \cdot |x|$. If the indenter is pressed to a depth

Fig. 9.4 Dependence of the dimensionless adhesion force on the dimensionless speed for four values of the dimensionless indentation force $f = 0; 0.1; 1; 10$ and $G_2/G_1 = 1{,}000$

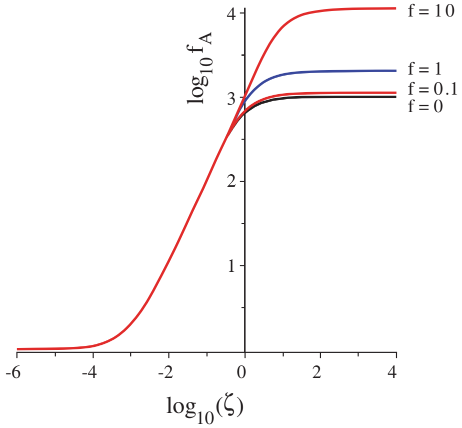

Fig. 9.5 Conical indenter that is pressed into a linearly viscous medium

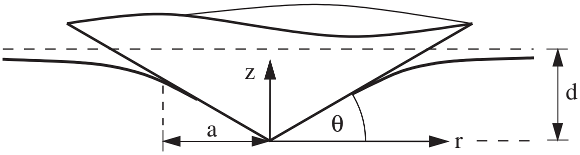

of d_0 and then pulled out to a depth of d, then the vertical displacement of the foundation at point x is given by

$$u_z(x) = d - (\pi/2)\tan\theta \cdot |x|. \tag{9.43}$$

Using the deformation criterion (9.11), we calculate the contact radius a by requiring that $u_z(a) = -u_A$:

$$d - (\pi/2)\tan\theta \cdot a = -\sqrt{b^* a}. \tag{9.44}$$

Introducing

$$\tilde{d} = \frac{d}{(\pi/2)\tan\theta} \tag{9.45}$$

and

$$\tilde{b} = \frac{b^*}{(\pi/2)^2 \tan^2\theta}, \tag{9.46}$$

we rewrite Eq. (9.44) in the form

$$\tilde{d} - a = -\sqrt{\tilde{b}a}. \tag{9.47}$$

From this, we obtain the contact radius

$$a = \left(\tilde{d} + \frac{\tilde{b}}{2}\right) + \sqrt{\tilde{d}\tilde{b} + \left(\frac{\tilde{b}}{2}\right)^2}. \tag{9.48}$$

Separation occurs at $\tilde{d} = -\tilde{b}/4$. Thereby, the contact radius is $a = \tilde{b}/4$. Let it be noted that this result is independent from the elastic (or rheological) properties and is valid for a medium of arbitrary rheology (as long as the deformation criterion is valid for the crack).

Problem 4 Discuss the influence of roughness in the case of the contact with a linearly viscous medium (Kelvin body).

Solution Assume that the spectrum of the roughness exhibits a cut-off at $q_{\min} \gg 2\pi/L$ (see more in Problem 2 in Chap. 10). We denote the root mean square of the roughness as h. In this case, the contact length is approximately proportional to the normal force

$$L_{\text{cont}} \approx \frac{F_N}{Gh}, \tag{9.49}$$

as long as it remains smaller than the system size L, at which point it remains constant:

$$L_{\text{cont}} = L. \tag{9.50}$$

If the indenter is now pulled off quickly, then the force is given predominantly by the viscous term (9.29):

$$F_A = 4v_0\eta L_{\text{cont}}. \tag{9.51}$$

For subcritical normal forces, the adhesion force is then

$$F_A = F_N \frac{4v_0\eta}{Gh} = F_N \frac{4v_0\tau}{h}, \tag{9.52}$$

with $\tau = \eta/G$. For supercritical forces, it is

$$F_A = 4v_0\eta L, \tag{9.53}$$

independently from the indentation force and the roughness. This coincides with the adhesion force of a smooth indenter.

References

1. M. Heß, On the reduction method of dimensionality: the exact mapping of axisymmetric contact problems with and without adhesion. Phys. Mesomech. **15**, 264–269 (2012)
2. V.L. Popov, *Contact Mechanics and Friction. Physical Principles and Applications* (Springer, Berlin, 2010), 362 p
3. A.A. Griffith, The phenomena of rupture and flow in solids. Philos. Trans. R. Soc. London A **221**, 163–198 (1921)
4. L. Prandtl, ZAMM J. Appl. Math. Mech. **13**, 129–133 (1933)
5. D. Maugis, *Contact, Adhesion, and Rupture of Elastic Solids* (Springer, Berlin, 2000)

Chapter 10
Normal Contact of Rough Surfaces

Roman Pohrt, Valentin L. Popov and Markus Heß

10.1 Introduction

In addition to the strict geometrically defined cases that were mapped in Chap. 3 with the method of dimensionality reduction, we would now like to devote ourselves to the question of whether rough surfaces can also be handled with a reduction method. The importance of surface roughness for tribological processes was already emphasized by Bowden and Tabor [1] in the 1940s and since that time has become generally accepted. The most important fundamental work dealing with the contact mechanics of rough surfaces was conducted in the 1950s by Archard [2] and in the 1960s by Greenwood and Williamson [3]. However, the contact mechanics of rough surfaces remains even today a current and to some extent a controversial topic. In this chapter, we will show that there exist theoretical as well as empirical reasons for why the method of dimensionality reduction is also able to be applied to randomly rough surfaces. In this way, the method presents itself as a practical tool for the fast calculation of contact problems. While we could always call on the known analytical solutions in the previous chapters for comparison, we will carry out the validation in this chapter using a standard numerical method. The missing analytical framework highlights, thereby, exactly the application potential for the reduction method for unsolved problems, especially those for which the solutions push the boundaries of being feasible with the current level of computing power. The main reason for the unavailable possibility of simulating realistic contact mechanics is, as mentioned in Chap. 1, the multi-scalar character of contact problems due to the roughness of the contacting bodies. For instance, if the contact mechanics of a 1 cm × 1 cm large component are completely described with FEM and we have the requirement that all scales down to the order of magnitude of 1 nm must be discretized, then we would have to solve a system with roughly 10^{14} elements and in the process of doing so, we would have merely mapped the surface. Using the reduction method, we would only have 10^{7} degrees of freedom. Additionally, the problem to be solved in three dimensions is

V.L. Popov and M. Heß, *Method of Dimensionality Reduction in Contact Mechanics and Friction*, DOI 10.1007/978-3-642-53876-6_10

an integral equation, while the one-dimensional case collapses to independent linear algebraic equations. This chapter is on the one hand, dedicated to an explanation of the functionality of the method of dimensionality reduction in the case of contacts between two rough bodies. On the other hand, the verification of the method is undertaken by comparison with three-dimensional results.

10.2 Randomly Rough, Statistically Isotropic Surfaces

The type of roughness can range from regular profiles to so-called "randomly rough" surfaces. The most exact way to characterize the roughness of a surface is to specify a particular surface profile. An equally valid alternative is to specify the complete Fourier spectrum of the surface. In doing so, the individual Fourier components are characterized by their amplitude and phase. However, if we assume that the phases are *random*, then the type of surface topography, in a statistical sense, is explicitly defined by the magnitude of the Fourier components. Such surfaces are called "randomly rough." Of course, randomly rough surfaces form only a subclass of all possible types of roughness. In this chapter, however, we will assume for the sake of simplicity that we are only dealing with this type of surfaces. One may show that the magnitude of the Fourier components for randomly rough surfaces is correlated to the so-called *power spectrum of the surface topography* $C_{\mathrm{2D}}(\vec{q})$. This is defined according to

$$C_{\mathrm{2D}}(\vec{q}) = \frac{1}{(2\pi)^2} \int \left\langle z(\vec{x}) z\left(\vec{0}\right) \right\rangle e^{-i\vec{\mathbf{q}}\cdot\vec{\mathbf{x}}} \mathrm{d}^2 x, \tag{10.1}$$

where $z(\vec{x})$ is the height profile (measured from the mean, so that $\langle z \rangle = 0$). Here, $\langle \cdot \rangle$ means the average over a statistical ensemble. Furthermore, we assume that the surface topography is statistically homogeneous and isotropic. Under these conditions, the power spectrum $C_{\mathrm{2D}}(\vec{q})$ is only dependent on the magnitude q of the wave vector $\vec{q}$. At this point, we would like to emphasize that the method of dimensionality reduction can, in principle, also be applied to anisotropic surface topographies.

In a similar way, the power spectrum $C_{\mathrm{1D}}(q)$ of a one-dimensional rough line is introduced:

$$C_{\mathrm{1D}}(q) = \frac{1}{2\pi} \int \langle z(x) z(0) \rangle e^{-iqx} \mathrm{d}x. \tag{10.2}$$

The surface topography for the two-dimensional case is reconstructed with the help of the power spectrum according to

$$z(\vec{x}) = \sum_{\vec{q}} B_{2D}(\vec{q}) \exp\left(i(\vec{q} \cdot \vec{x} + \phi(\vec{q}))\right), \tag{10.3}$$

with

$$B_{2D}(\vec{q}) = \frac{2\pi}{L} \sqrt{C_{2D}(\vec{q})} = \bar{B}_{2D}\left(-\vec{q}\right) \tag{10.4}$$

and the phases $\phi(\vec{q}) = -\phi(-\vec{q})$ randomly distributed over the interval $[0, 2\pi)$.

In the one-dimensional case,

$$z(x) = \sum_q B_{1D}(q) \exp(i(qx + \phi(q))) \tag{10.5}$$

with

$$B_{1D}(q) = \sqrt{\frac{2\pi}{L} C_{1D}(q)} = \bar{B}_{1D}(-q) \tag{10.6}$$

and randomly distributed phases $\phi(q) = -\phi(-q)$ over the interval $[0, 2\pi)$. Fast numerical strategies are based on the *fast Fourier transform* (FFT) instead of the direct calculation of the summations (10.3) or (10.5).

10.3 Fractal, Self-Affine Surfaces

Many natural or man-made surfaces exhibit on certain spatial scales a property, which is called *fractality*, the presence of roughness on *all* spatial scales. A fractal surface $z(x, y)$ is called *self-affine* if it "looks the same" after proper magnification. Mathematically, this means that the surface obtained by a proper scaling of in-plane and out-of-plane coordinates cannot be distinguished from the original surface:

$$z'(x, y) = \psi^H z(x/\psi, y/\psi). \tag{10.7}$$

Here, ψ is an arbitrary magnification and H is the so-called Hurst exponent. In the special case of $H = 1$, the surface is known as being self-similar. In the case of $0 < H < 1$, the power spectrum is [4]

$$C_{2D}(q) = C_0 (Lq)^{-2H-2}. \tag{10.8}$$

Here, C_0 is a constant and L is the length of the system.[1]

One parameter equivalent to the Hurst exponent is the fractal dimension D_f [4], where

$$D_f = 3 - H. \tag{10.9}$$

The fractal description of a surface is only then complete if one defines the boundaries $q_{\min}$ and $q_{\max}$ of the interval of wavenumbers for which Eq. (10.8) is valid. In other words, the domain of the spatial scales is defined (from $2\pi/q_{\max}$ to $2\pi/q_{\min}$) as that where the property of self-affinity (10.7) is present. In Fig. 10.1 the power

---

[1] As can be seen in the further considerations, this relationship between the Hurst exponent and the form of the power spectrum is valid over an even larger interval: $0 < H < 2$.

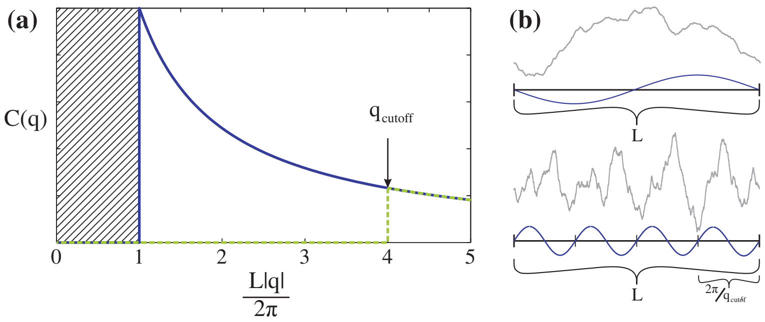

Fig. 10.1 (**a**) Power spectrum of a fractally rough surface. The spectrum decays at higher frequencies according to the power function (10.8). It can be limited by a cut-off wave vector (*green*). (**b**) Cross-section through an arbitrarily generated realization of a fractally rough surface with (*below*) and without (*above*) a characteristic cut-off wave vector

spectrum of a fractal, self-affine surface is schematically presented as a function of the “dimensionless wavenumber” $Lq/(2\pi)$.

The minimum wavenumber in the power spectrum—independent of the type of spectrum—is fundamentally determined by the size L of the system and is equal to $2\pi/L$ (Fig. 10.1a, blue, solid line). Smaller wavenumbers are excluded, because the wavelength of the roughness cannot exceed the size of the system. The property of self-affinity may also end at a smaller scale than that of the system (or at a wavenumber $q_{\min} = q_{\mathrm{cutoff}}$, larger than $L/(2\pi)$). This is shown with the green line in Fig. 10.1 . The surfaces with and without cut-off for the long wavelengths have a different macroscopic appearance, as is illustrated in Fig. 10.1b. The surfaces without cut-off show the unevenness up to the largest scale of the system as a whole (Fig. 10.1b, upper image). The macroscopic unevenness is superimposed with roughness of ever smaller scales. This surface topography shows the property of self-affinity on all existing scales (limited only by the size of the system as a whole and by discretization). A surface with a long wavelength cut-off, on the contrary, contains no long wavelength components and is, therefore, “nominally flat.” It exhibits roughness beginning only below a certain wavelength (Fig. 10.1b, lower image). Contact mechanical properties of these two types of surface topographies can be very different from one another. In this chapter, we will focus our attention on “real fractal” surfaces without long wavelength cut-off.

10.4 Generating the Equivalent One-Dimensional System

Now, how can a given three-dimensional system with a randomly rough surface be transformed into a one-dimensional line so that the essential contact mechanical properties are not lost? In the motivation of this conversion, we use several ideas from the model of Greenwood and Williamson [3]. The results and quality of the equivalent system, however, prove to be much better than the Greenwood–Williamson model itself.

In the model from Greenwood and Williamson individual micro-contacts are considered independently from one another. Under these conditions, only the distribution of the height of the asperities and their radii of curvature play a role. We obtain a first rough idea of the conversion rule if we demand that the one-dimensional equivalent system has the same statistical distribution of heights and radii of curvature as the three-dimensional original counterpart.[2] Let the starting point be an isotropic, three-dimensional surface and its power spectrum C_{2D}. The root mean square of the roughness for such a surface is

$$h_{2D}^2 = \left\langle z^2 \right\rangle_{2D} = \int_{-\infty}^{\infty} \int_{-\infty}^{\infty} C_{2D}(\vec{q}) \mathrm{d}^2 q = 2\pi \int_{0}^{\infty} q C_{2D}(|\vec{q}|) \mathrm{d}q, \tag{10.10}$$

while that for a rough line is

$$h_{1D}^2 = \left\langle z^2 \right\rangle_{1D} = \int_{-\infty}^{\infty} C_{1D}(q) \mathrm{d}q = 2 \int_{0}^{\infty} C_{1D}(q) \mathrm{d}q. \tag{10.11}$$

It is easy to see that these are the same if

$$C_{1D}(q) = \pi q C_{2D}(q). \tag{10.12}$$

This is known as the *rule of Geike* [5]. With this, the power spectrum for a fractal line with a Hurst exponent of H is calculated as

$$C_{1D}(q) = \frac{\pi C_0}{L} (L \cdot q)^{-2H-1}. \tag{10.13}$$

This new power spectrum in one dimension fulfills further interesting equivalencies. The root mean square slopes and profile curvatures are also the same in both cases. Furthermore, a line having a power spectrum according to (10.13) also retains the property of self-affinity with the same Hurst exponent:

$$z'(x) = \psi^H z\big(x/\psi\big). \tag{10.14}$$

As was described in Sect. 10.6, this is the key property that makes it possible to map a three-dimensional system exactly to a one-dimensional system.

We will see empirically that the conversion rule (10.12), initially motivated by geometry, leads to the same results in both one and three dimensions in the

---

[2] We will later see that the interactions between the asperities play no role in the method of dimensionality reduction: The only property that is required is the self-affinity of the surface, regardless of whether the profile is regular or randomly rough.

case of a fractal surface, where the correct conversion coefficient in (10.12) is not necessarily "π" and can depend on the Hurst exponent:

$$C_{1D}(q) = \lambda(H) q C_{2D}(q). \tag{10.15}$$

The reasons for this are of various natures. One is purely formal and has to do with the discrete numerical implementation of the rule mentioned above. We will explain this problem below. The deeper physical reasons will be touched upon in Sect. 10.5.

In the discrete realization of rough surfaces with a discrete mesh distance Δx according to (10.3) and (10.5), the RMS-roughness is determined as follows:

$$\left\langle z_{2D}^2(\vec{x}) \right\rangle = \sum_{\vec{q}} |B_{2D}(q)|^2 = \frac{4\pi^2}{L^2} \sum_{\vec{q}} C_{2D}(\vec{q}), \tag{10.16}$$

$$\left\langle z_{1D}^2(x) \right\rangle = \sum_{q} |B_{1D}(q)|^2 = \frac{2\pi}{L} \sum_{q} C_{1D}(q). \tag{10.17}$$

If the summation in (10.16) is taken over a quadratic mesh with a step size of $\Delta q = 2\pi/L$ from $q_{\min} = 2\pi/L$ to $q_{\max} = \pi/\Delta x$ and the spectral density is able to be presented in the form (10.8), then

$$\left\langle z_{2D}^2(\vec{x}) \right\rangle = \frac{4\pi^2 C_0}{L^2 (2\pi)^{2H+2}} \sum_{\substack{n=-N, m=-N \\ \text{not } n=m=0}}^{N} \frac{1}{\left(n^2+m^2\right)^{H+1}}, \tag{10.18}$$

$$\left\langle z_{1D}^2(x) \right\rangle = \lambda(H) \frac{8\pi^2 C_0}{L^2 (2\pi)^{2H+2}} \sum_{n=1}^{N} \frac{1}{n^{2H+1}}, \tag{10.19}$$

with the number of points $N = L/(2 \cdot \Delta x)$, for which we have used the general rule of conversion (10.15).

The two RMS-roughnesses are the same on average if $\lambda(H)$ is chosen as follows:

$$\lambda(H) = \frac{1}{2} \frac{\sum_{\substack{n=-N, m=-N \\ \text{not } n=m=0}}^{N} \frac{1}{\left(n^2+m^2\right)^{H+1}}}{\sum_{n=-N}^{N} \frac{1}{|n|^{2H+1}}}. \tag{10.20}$$

The dependence of the factor $\lambda(H)$ on the exponent H is presented in Fig. 10.2.

The conversion factor $\lambda(H)$ presented in Fig. 10.2 only guarantees the invariance of the RMS-roughness. The correct conversion factor that is necessary for the invariance of the contact mechanical properties can, at this time, only be determined empirically by comparison with direct three-dimensional simulations. This will be conducted in the next section.

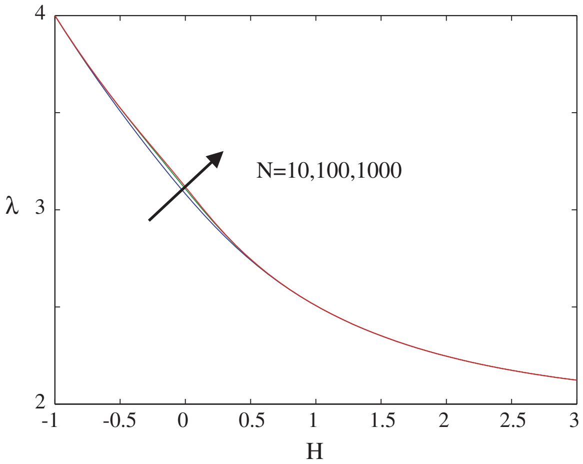

Fig. 10.2 Multiplicator $\lambda(H)$ in Eq. (10.15) as a function of the exponent H for various values of N: $N = 10$, $N = 100$, $N = 1{,}000$ according to Eq. (10.20). The conversion factor $\lambda(H)$ presented here guarantees only the invariance of the RMS-roughness. With this, the contact mechanical properties are not yet given

10.5 Numerical Results of the Boundary Element Method and the Method of Dimensionality Reduction

In this section, the three-dimensional problem of an elastic half-space and a rigid indenter with a self-affine, fractal surface will be initially solved numerically. These results will then be subsequently compared to those of a one-dimensional calculation based on the procedure of the method of dimensionality reduction. It will be confirmed that the conversion formula for the spectral density has the form (10.15) and the conversion coefficient $\lambda(H)$ will be determined empirically.

The three-dimensional reference to be compared with the one-dimensional solution is presented in Fig. 10.3. A rigid indenter is brought into contact with an elastic half-space. Let the roughness of surface of the indenter be self-affine and

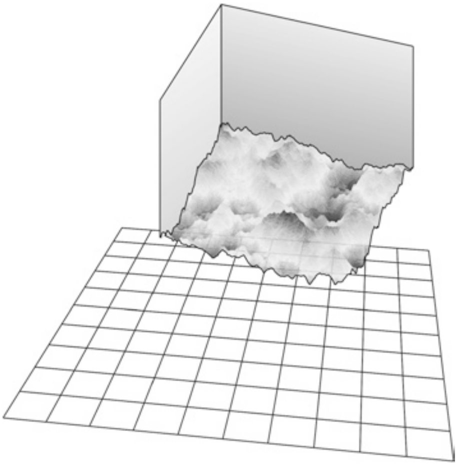

Fig. 10.3 Three-dimensional problem: a fractally rough indenter is pressed into an elastic half-space

fractal on all scales from the discretization step Δx up to the size L of the system. Then,

$$q_{\min} = \frac{2\pi}{L}, \quad q_{\max} = \frac{\pi}{\Delta x}. \tag{10.21}$$

Now, if the indenter is pressed into the elastic half-space with a normal force F_N, then the highest points come into contact first, while at a sufficiently high normal force, approximately the entire area is in contact. At complete contact, the stiffness reaches the saturation value $1.1419E^*L$. It is, therefore, logical to normalize the incremental stiffness

$$k_z = \frac{\partial F_N}{\partial d} \tag{10.22}$$

using this value:

$$\bar{k}_z = \frac{k_z}{1.1419E^*L}. \tag{10.23}$$

Here, d is the indentation depth (measured from the first point of contact).

For a better orientation in this multi-parameter problem, we will first show that for the sake of having the correct units, there are certain limitations for the form of the dependencies between the normal force and normal stiffness. Numerical simulations always show that for small forces, the stiffness is a power function of the normal force. We take this empirical fact as our working thesis and assume that the stiffness–force relation is dependent only on the effective modulus of elasticity E^* and the RMS-roughness. Under these assumptions, it is easy to show that the problem only contains the following independent dimensionless variables: The dimensionless stiffness $\bar{k}_z = k_z/(1.1419E^*L)$, dimensionless force $F_N/\left(E^*L^2\right)$, and dimensionless roughness h/L. The general form of a power function that connects these three variables is

$$\frac{k_z}{1.1419E^*L} = \zeta \left(\frac{F_N}{E^*L^2}\right)^{\alpha} \left(\frac{h}{L}\right)^{\delta}, \tag{10.24}$$

where ζ is a dimensionless constant and α and δ, exponents; all constants can now only depend on the Hurst exponent. A further scaling property determines the relationship between the exponents α and δ: If the "vertical" scale of the roughness is multiplied with an arbitrary factor, then the contact configuration does *not* change if the force and the indentation depth are simultaneously multiplied by the same factor. This means, however, that the stiffness remains unchanged in the process. Consequently, the following relationship must be met: $\alpha + \delta = 0$, meaning $\delta = -\alpha$. Therefore, the possible form of the stiffness–force relation is reduced to

$$\frac{k_z}{1.1419E^*L} = \zeta \left(\frac{F_N}{E^*Lh}\right)^{\alpha}. \tag{10.25}$$

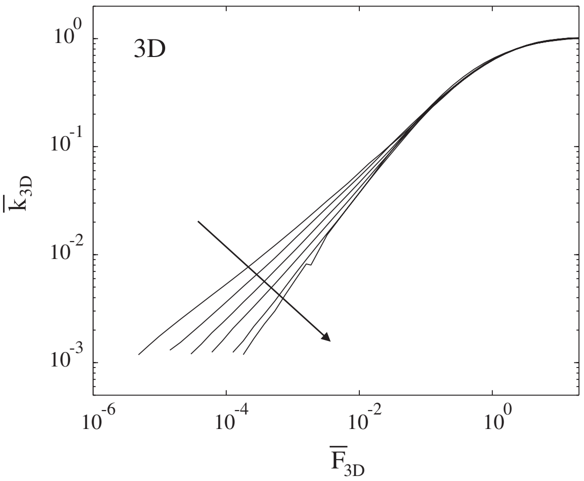

Fig. 10.4 Normal stiffness with respect to normal force for the three-dimensional contact problem from Fig. 10.3. Results are from [6]. The curves correspond to Hurst exponents $\{1,\ 0.8,\ 0.6,\ 0.4,\ 0.2,\ 0\}$ in the direction of the arrow

If we define the dimensionless force according to

$$\overline{F_{3D}} = \frac{F_N}{E^* L h}, \tag{10.26}$$

then we come to the following dimensionless form of the stiffness–force relation:

$$\bar{k}_z = \zeta \overline{F_{3D}}^{\alpha}. \tag{10.27}$$

We will now verify this relation in three dimensions using a numerical solution and subsequently compare this to the one-dimensional solution obtained using the method of dimensionality reduction.

The authors produced the numerical solution of this indentation problem in 2012 in [6]. It is presented in Fig. 10.4 and will serve in the following as a reference. The stiffness does not increase any further as soon as a sufficiently large portion of the surface comes into contact (Fig. 10.5d, e). In these cases, the rough indenter behaves

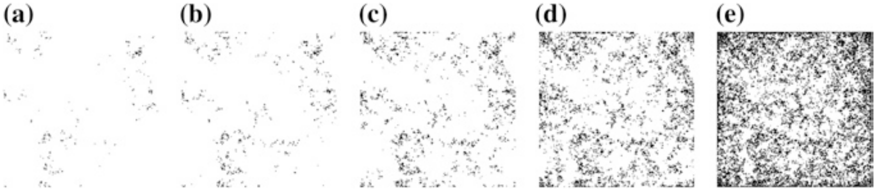

Fig. 10.5 Resulting real contact areas in the contact problem in Fig. 10.3 ($H = 0.4$). With increasing normal force (from left to right), new areas come into contact. For very large forces, the effective contact configuration is that of the entire system (here, a *square*) so that the stiffness is saturated. Thereby, the real contact surface may still be much smaller that the apparent contact area

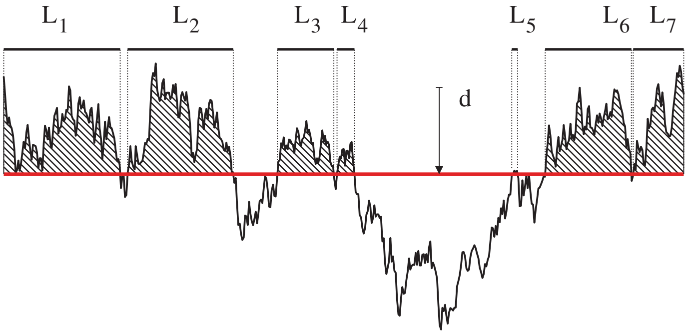

Fig. 10.6 Indentation of a one-dimensional rough line. In the one-dimensional system, all degrees of freedom are independent from one another and the stiffness is simply proportional to the entire "contact length."

effectively as a flat square indenter (see Sect. 7.3 in [7]), even before complete material contact has been reached. For smaller forces, the relationship between force and stiffness transitions to a power law dependence of the form in (10.27).

The asymptotic behavior for smaller stiffnesses is determined by the discretization and is, therefore, not shown in Fig. 10.4.

We now continue to the same problem in one dimension. A rough line is produced according to Eq. (10.13) and analyzed for various indentation depths, as shown in Fig. 10.6.

In the one-dimensional case, the stiffness and normal force may be directly taken or added together. When all of the springs come into contact, then the total stiffness is equal to LE^*. Also in one dimension, we normalize the stiffness by the saturation value:

$$\overline{k_{1D}} = \frac{\partial F_N}{\partial d} \frac{1}{E^* L}. \tag{10.28}$$

In doing so, it is guaranteed that the saturation value of the stiffness corresponds exactly to the three-dimensional contact. We define the normalized force anagoulously to Eq. (10.26)

$$\overline{F_{1D}} = \frac{F_N}{E^* L h_{1D}}. \tag{10.29}$$

The result from the one-dimensional indentation process is presented in Fig. 10.7. The saturation of the stiffness at large normal forces is easy to see. For intermediately large down to small forces, a power law dependence can be seen.

In the one-dimensional system, the computation time is so extremely low that systems of much higher resolution may be mapped, with a much higher $q_{\max}$ and correspondingly small normal forces and stiffnesses. One can see a very good

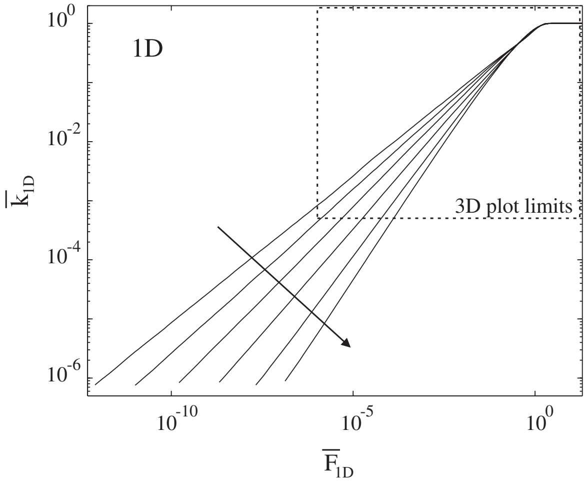

Fig. 10.7 Normal force–stiffness curves for the one-dimensional contact problem in Fig. 10.6. The results are from Pohrt/Popov/Filippov [8]. The values of the Hurst exponents H are the same as those in Fig. 10.4

agreement for the forces that can be calculated in both one and three dimensions. The reduction method extends the force domain that can be investigated to much smaller forces. These results suggest that the power law dependence would continue asymptotically for arbitrarily small forces. In actuality, geometric and physical arguments can be found with which this dependence can not only be confirmed, but also allow for an analytical expression $\alpha = (H+1)^{-1}$ to be found for the exponent in (10.25) that is valid in the physically relevant domain $H > 0.5$ (see Sect. 10.6). The prefactor $\zeta(H)$ in Eq. (10.27) must be obtained from numerical data and is approximated as $1.7\big/(H+1)$. With this, we obtain

$$\bar{k} \approx \frac{1.7}{H+1} \bar{F}^{\frac{1}{H+1}}. \tag{10.30}$$

10.6 Self-Affinity and the Method of Dimensionality Reduction

In Chap. 3, we have seen that the possibility of mapping a three-dimensional contact problem to a one-dimensional problem in the case of axially-symmetric profiles of the form $z \propto r^n$ is only due to the self-similarity of the profile. The arguments used there can be easily generalized. It can be shown that similar arguments are valid for all self-affine surfaces, whether the surfaces are isotropic, regularly rough, or random. Here, we will explain these arguments once more especially for the application to randomly rough, fractal, self-affine surfaces.

Fractal surfaces without a long wavelength cut-off have distinctive roughness features on all scales, including that of the entire system. Therefore, for small contact forces, the entire contact area (which may exhibit an arbitrarily complicated, fractal inner structure) is localized to the area around a single point within the apparent contact area. Now, we conduct the following transformation of the surface:

$$\begin{aligned} L' &= \psi L \\ z' &= \psi^H z. \\ d' &= d \end{aligned} \tag{10.31}$$

In accordance with the definition of self-affinity, this transformation produces the same surface (or at least one with the same statistical properties). This means that this transformation leaves the "contact state," including contact force and stiffness $\partial F/\partial d$, unchanged:

$$\begin{aligned} F' &= F \\ k' &= k. \end{aligned} \tag{10.32}$$

Insertion of (10.31) and (10.32) into (10.25) results in

$$\alpha = \frac{1}{1+H}. \tag{10.33}$$

This relationship was found by Pohrt and Popov and was published in [8].[3] These scaling arguments are not dependent on the dimensionality of the system and are equally valid for both the original three-dimensional case as well as the mapped one-dimensional case. The constant ζ can, of course, be different in both cases. Exactly as in the case of the axially-symmetric body, equivalence can be obtained by means of a conversion factor $\lambda(H)$ in (10.15).

So, we see that the method of dimensionality reduction produces *exact* results in both asymptotically limiting cases of very small and very large forces.

10.7 Contact Mechanics for Self-Affine Surfaces for $-1 < H < 3$

Self-affine surfaces are often investigated over the interval of Hurst exponents of $0 < H < 1$. Equation (10.8), however, can formally be used also over a larger interval. In doing so, the parameter H loses the general meaning of the "Hurst exponent," which is a parameter that describes the property of self-affinity [Eq. (10.7)]. However, investigations of surfaces generated using (10.16) show that surfaces generated in this way posess the property of self-affinity with the Hurst exponent H in the larger interval $0 < H < 2$ as is typically assumed. In the following, we want to go beyond this interval and investigate contacts between surfaces with power spectra according to Eq. (10.8) with the parameter H in the interval $-1 < H < 3$.

---

[3] It was only after the appearance of paper [8] and of the German edition of this book, the authors were called attention to the fact that dependencies (10.27) an (10.33) have been derived already in 1993 in [9] using almost the same arguments.

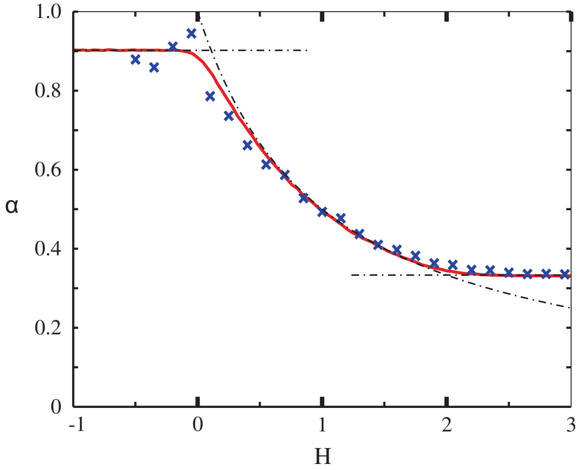

Fig. 10.8 Exponent α from (10.25) as a function of the Hurst exponent for a rough surface. The crosses are the results from a three-dimensional BEM study. The solid line was produced using the reduction method

To note is the fact that the value $H = -1$ corresponds to a constant power spectrum that is independent of wavelength. Many surfaces have this property beginning at a certain "roll-off" wave vector. Thus, $H = -1$ corresponds to a rough surface with a pure "roll-off." At $H > 2$, the spectral density decreases so fast that practically only the components with the largest wavelengths remain: We are dealing with a single smooth asperity. In this limiting case, the Hertzian contact theory should be valid. Thus, the chosen interval $-1 < H < 3$ covers practically all thinkable types of rough surfaces beginning with spectrums described by white noise down to smooth surfaces.

Numerical simulations show that for all values of H over the said interval, the contact stiffness is a power function (10.25) of the normal force. The values of the exponent α that are obtained from the directly simulated three-dimensional cases are presented in Fig. 10.8 as crosses. The solid line shows the exponents α that result from the corresponding one-dimensional simulations. For $H < 0$, α is practically constant and lies near

$$\alpha \approx 0.9. \tag{10.34}$$

For such surfaces, the stiffness is approximately proportional to the normal force, a result that is predicted by many contact theories of rough surfaces [2–4].

Over the interval $0 < H < 2$, the exponent α can be described very well with the "Pohrt–Popov" law (10.33) [8]. In this interval, the surface exhibits the property of self-affinity.

For $H > 2$, we are dealing with a Hertzian contact and the exponent is that of the Hertzian contact:

$$\alpha = \frac{1}{3}. \tag{10.35}$$

Because three-dimensional and one-dimensional calculations provide the same exponent α, it is always possible to choose a conversion factor $\lambda(H)$ in (10.15) so that the one-dimensional and the three-dimensional relationships correspond

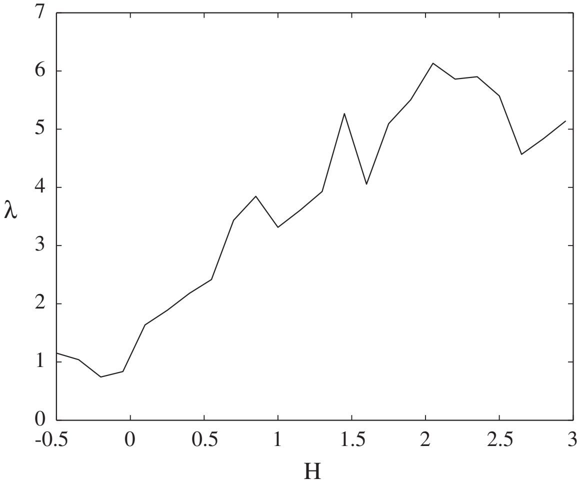

Fig. 10.9 The best results at present for the value of the conversion factor $\lambda(H)$ in (10.15) that lead to agreement in the contact stiffness for both the three-dimensional and one-dimensional cases

exactly. Due to the fact that the saturation value of the stiffness for a complete contact is not dependent on the conversion process, it is always "automatically" correct. The value of the conversion factor $\lambda(H)$ which guarantees the identical contact properties in both the three-dimensional and one-dimensional cases can, until now, only be determined by a comparison with three-dimensional, numerical results. The best results (at this time) are presented in Fig. 10.9.

The calculated stiffnesses for these values of $\lambda(H)$ for Hurst exponents over the interval $0 < H < 2$ are presented in Fig. 10.10. In the transitional domain from power

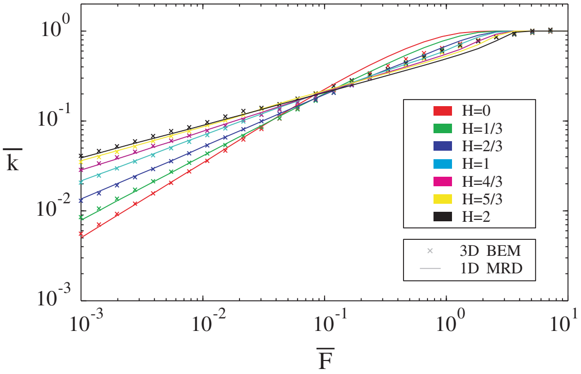

Fig. 10.10 The dependencies of the stiffness on the normal force calculated with the factor $\lambda(H)$ from Fig. 10.9 for Hurst exponents over the interval $0 < H < 2$ show that the exact agreement between one-dimensional and three-dimensional results is valid for small forces and in the saturation domain. The three-dimensional calculations were conducted on a square mesh with 513×513 discretization points

law to saturation, the results for the three-dimensional and one-dimensional calculations correspond almost identically in the proximity of $H = 2/3$, while there are deviations for very small ($H \approx 0$) and very large ($H \approx 2$) values of the Hurst exponent. In contrast to the axially-symmetric case, the method of dimensionality reduction is not exact in the application to randomly rough surfaces, but presents a very good approximation.

The conversion factor $\lambda(H)$ is dependent on the Hurst exponent. This dependence means that it must be possible to formulate a general rule for the conversion of arbitrary power spectra that are not necessarily self-affine. This conversion must have the form of an integral transformation:

$$C_{1D}(q) = \int_{q}^{q_{\max}} C_{2D}(q')K(q,q')\mathrm{d}q', \tag{10.36}$$

where $K\left(q,q'\right)$ is a homogeneous zero order function of q and q'. The exact form of the transformation is not yet known.

10.8 Equivalence Between Rough Self-Affine and Axially-Symmetric Contacts with the Same Hurst Exponent

In Chap. 3 and the current chapter, it was shown that both axially-symmetric and randomly rough, fractal surfaces may be described using the reduction method. This provides another possibility to drastically reduce the computational costs of the numerical simulation of rough contacts by replacing the rough surface by a single asperity. In the following, this idea will be shortly explained.

Let us consider a three-dimensional, pointed, axially-symmetric indenter of the form

$$z(r) = Q_{3D} \cdot r^n, \tag{10.37}$$

with $0 < n \leq 1$, as can be seen in Fig. 10.11. It is easy to recognize that this form is also “self-affine,” because the key property (10.7) is also met here. Indeed, if we investigate such an indenter near $r = 0$ and zoom in or out, then it appears unchanged and the following is valid:

$$z'(r) = \psi^n z\left(r/\psi\right). \tag{10.38}$$

Such form can also be understood as being a self-affine surface, however, without the property of being randomly rough. The Hurst exponent in this somewhat abstract self-affine roughness is

$$H = n. \tag{10.39}$$

Furthermore, we want to assume that the indentation behavior can be sufficiently described within the framework of half-space theory also with this pointed

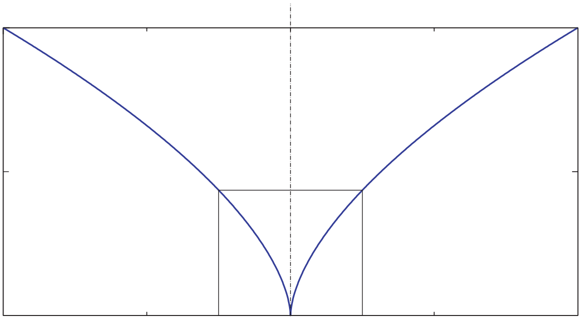

Fig. 10.11 Cross-section of an axially-symmetric indenter having the form (10.37) with $n = 0.6$

indenter. We know the following relationship between the acting normal force and contact stiffness for three-dimensional, axially-symmetric bodies from Chap. 3:

$$\frac{\partial F}{\partial d} = k = 2E^* \left(\frac{(n+1)F}{2Q_{3D}E^* n\kappa(n)} \right)^{\frac{1}{n+1}} \propto F^{\frac{1}{n+1}}. \tag{10.40}$$

This can be rearranged into the form from Eq. (10.25):

$$\frac{k}{E^*L} = \frac{2}{L} \left(\frac{(H+1)F}{2Q_{3D}E^* H\kappa(H)} \right)^{\frac{1}{H+1}} = \frac{2}{L} \left(\frac{(H+1)Lh}{2Q_{3D}H\kappa(H)} \right)^{\frac{1}{H+1}} \left(\frac{F}{E^*hL} \right)^{\frac{1}{H+1}}. \tag{10.41}$$

After setting this equal to Eq. (10.30), it results that the axially-symmetric, three-dimensional indenter behaves exactly like a fractal surface if the prefactor Q_{3D} in Eq. (10.37) is chosen to be

$$Q_{3D} = \left(\frac{2(H+1)}{1.9412L} \right)^{H+1} \frac{(H+1)L}{2H\kappa(H)} h. \tag{10.42}$$

By applying the rule of Heß, we directly obtain the corresponding prefactor for the equivalent one-dimensional indenter through multiplication with $\kappa(H)$:

$$Q_{1D} = \left(\frac{2(H+1)}{1.9412L} \right)^{H+1} \frac{(H+1)L}{2H} h. \tag{10.43}$$

Table 10.1 summarizes the equivalencies once more. The three-dimensional, axially-symmetric case was solved in the 1950s and 60s by Galin and Sneddon [10]. By using the rule of Heß, we arrive at the one-dimensional system. For the randomly rough surfaces in one and three dimensions, there exist power law dependencies whose prefactors can be approximated using Eq. (10.30) so that the conversion to the analytically solved axially-symmetric cases can be undertaken using Eqs. (10.42) or (10.43), respectively.

Table 10.1 Relationships and equivalencies for the fractal contact problem

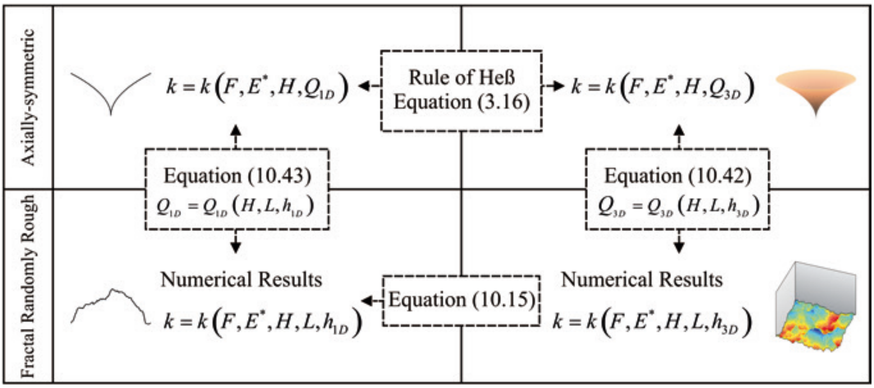

The equivalency of the axially-symmetric indenter to a fractally rough surface is, of course, only valid for the average of several realizations. The fact that fractal surfaces are randomly rough (in other words, exhibit different phases), results in the reality that two realizations with the same Hurst exponent may differ in stiffness behavior. In the cited investigations, standard deviations on the order of 30 % were observed, both in one and three dimensions (see Fig. 14.1). The equivalent system of an axially-symmetric indenter, on the other hand, is deterministic and exhibits no deviations.

10.9 Problems

Problem 1 In electric cars, aluminum cables are becoming more frequently used in the place of copper cables. Let us imagine such a massive conductor that has been fractured by careless mounting and is pressed back together slightly offset from the original configuration. How large is the additional electrical resistance that is now exhibited by the cable? (Fig. 10.12).

Solution Through the offset, the contacting surfaces do not match one another and the current can only flow through the contact areas. According to the analogy from Barber ([11], also see Sect. 8.3), the electrical resistance can be obtained from the contact stiffness using

$$\frac{k}{E^*} = \frac{(\rho_1 + \rho_2)}{2R}, \tag{10.44}$$

where R is the electrical contact resistance (or constriction resistance) and ρ_1 and ρ_2 are the specific resistances of the contacting bodies. For identical materials, we obtain

$$\frac{1}{R} = \frac{k}{E^* \rho}. \tag{10.45}$$

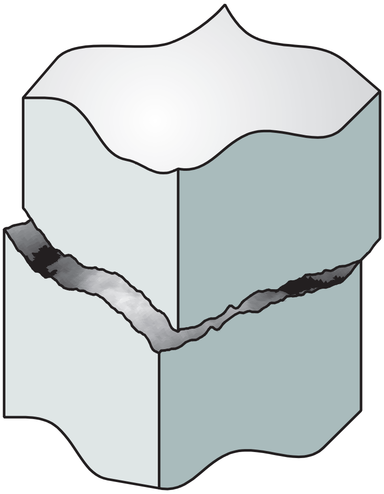

Fig. 10.12 A solid electrical conductor, which was fractured and pressed back together slightly offset

With k according to Eq. (10.30):

$$k = \frac{1.9412}{H+1} E^* L \left(\frac{F_N}{E^* L h_{rms}} \right)^{\frac{1}{H+1}}, \tag{10.46}$$

we obtain the additional constriction resistance:

$$R = \frac{(H+1)\rho}{1.9412 L} \left(\frac{F_N}{E^* L h_{rms}} \right)^{\frac{-1}{H+1}}. \tag{10.47}$$

Fractured surfaces typically exhibit a Hurst exponent of 0.8.

Problem 2 Approximate the stiffness of a "fractal" surface that exhibits a distinct long wavelength cut-off. There are no roughnesses having a wavelength $\lambda > \lambda_{\text{cutoff}}$, where $\lambda_{\text{cutoff}} \ll L$. How does the contact stiffness $k(F_N)$ behave for such a surface at small forces?

Solution A surface with a cut-off wavelength λ_{cutoff} exhibits many local maximums or asperities that come into contact first (see Fig. 10.1b, bottom). The various maximums are separated by a characteristic distance λ_{cutoff}. For the indentation with small forces, we want to assume that no elastic coupling takes place between the asperities. This assumption is supported by the fact that the few highest asperities are not necessarily near one another. Furthermore, we want to assume that the height distribution of the asperities is exponential. The existing contact configuration corresponds to connecting the stiffnesses of all asperities in parallel that have come into contact at the current indentation depth. The approach to this problem is analogous to the model of Greenwood and Williamson [3] with the difference that the behavior of the contact of the indenting asperities is not

Hertzian, but rather the behavior of a fractal indenter *without* long wavelength cut-off. Therefore, we have

$$F(d) = \Omega d^{\frac{H+1}{H}} \tag{10.48}$$

for the individual tips of the roughness, where

$$\Omega = E^* h^{-\frac{1}{H}} L \left(1.1419 \frac{H}{H+1} \zeta \right)^{\frac{H+1}{H}}. \tag{10.49}$$

The combined surface now consists of a large number of such individual systems, the maximums of which are distributed exponentially, with the probability density

$$\phi(z) = \begin{cases} \lambda e^{-\lambda z}, & z > 0 \\ 0, & else. \end{cases} \tag{10.50}$$

At a given indentation depth, we obtain the total force as the integral of the height distribution multiplied by the individual force per asperity, where N_0 is the total number of asperities:

$$F_G = N_0 \Omega \int_h^\infty \phi(z)(z-h)^{\frac{H+1}{H}} dz, \tag{10.51}$$

$$F_G = \underbrace{N_0 \Omega \lambda^{-1-\frac{1}{H}} \Gamma\left(2 + \frac{1}{H}\right)}_{S(H)} e^{-\lambda h}, \tag{10.52}$$

$$F_G = S(H) e^{-\lambda h}. \tag{10.53}$$

The derivative with respect to $d = -h$ finally results in the total stiffness

$$k_G = \frac{\partial F_G}{\partial d} = -\frac{\partial F_G}{\partial h} = S(H)\lambda e^{-\lambda h}, \tag{10.54}$$

and we obtain

$$k_G(F_G) = \lambda F_G \tag{10.55}$$

for the total stiffness with respect to the total force.

So, there is a linear relationship between normal force and contact stiffness for systems with long wavelength cut-off. The prefactor of this relationship is dependent only on the type of distribution of the highest asperities. It is noteworthy that all dependencies on the Hurst exponent are eliminated in Eq. (10.55). The linear dependence (10.55) is valid also if Hertzian behavior is assumed instead of fractal asperities. This relationship has been confirmed by numerical studies by other

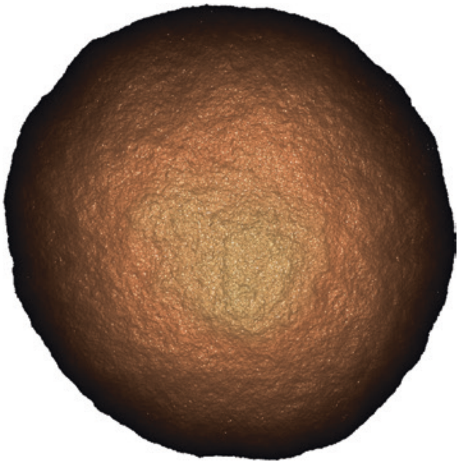

Fig. 10.13 A numerically generated sphere having a surface roughness, $H = 0.7$

authors and becomes even more valid the larger the system is in comparison to the chosen cut-off wavelength, meaning the more asperities being accounted for in the spatial average.

Problem 3 Given is a sphere with radius R, the surface of which is covered with a roughness (Hurst exponent H, RMS-height h). Determine the contact stiffness as a function of normal force (Fig. 10.13).

Solution This problem may be solved analytically in one dimension by taking the equivalency between random roughness and an axially-symmetric indenter into account and by using the generalized rule of Heß. The original system of the sphere with the superimposed roughness is first replaced by an equivalent three-dimensional system in the form of an axially-symmetric indenter of the form

$$z(r) = \frac{r^2}{2R} + Q_{3D} r^H, \tag{10.56}$$

where Q_{3D} is determined by (10.42). This three-dimensional indenter can be converted to an axisymmetric one-dimensional system according to the rule of Heß as

$$z(x) = \underbrace{\frac{\kappa(2)}{2R}}_{\tau_2} x^2 + \underbrace{\left(\frac{2(H+1)}{1.9412L}\right)^{H+1} \frac{(H+1)L}{2H} h}_{\tau_H} |x|^H. \tag{10.57}$$

The force as a function of contact radius a is

$$F(a) = 2E^* \left(a \cdot z(a) - \int_0^a z(a) \mathrm{d}a \right) = 2E^* \left[\frac{2}{3} \tau_2 a^3 + \tau_H \left(\frac{H}{H+1} \right) a^{H+1} \right]. \tag{10.58}$$

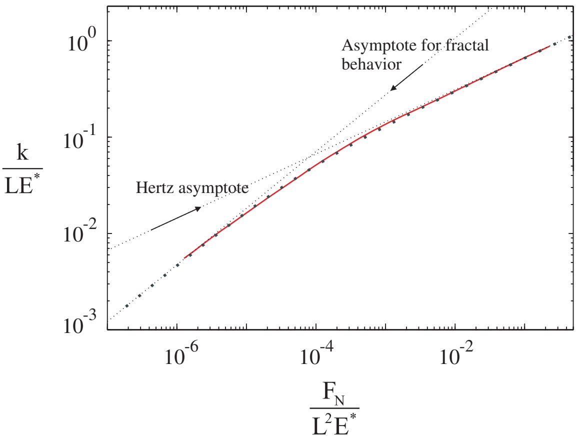

Fig. 10.14 Normal force and stiffness for a spherical indenter that is superimposed with a fractal roughness $\left(R = 0.5\,, H = 0.7\,, L = 1\,, h_{rms} = 9 \times 10^{-3}\right)$. The red line shows the results of a three-dimensional BEM simulation. The dotted line corresponds to the one-dimensional analytical solution from Eq. (10.59). Additionally, the asymptotic behavior according to Hertz and Eq. (10.30) are shown

With $k = 2aE^*$ and (10.57), we obtain

$$F(k) = E^* \left[\frac{4}{3} \tau_2 \left(\frac{k}{2E^*} \right)^3 + Lh \left(\frac{(H+1)}{1.9412} \frac{k}{E^* L} \right)^{H+1} \right]. \qquad (10.59)$$

In Fig. 10.14, this dependence is presented together with the complete three-dimensional numerical solution. For very small forces, the system behavior is expectedly dominated by the roughness. For larger forces, the influence of the roughness vanishes and the combined system behaves like a smooth Hertzian contact. A more detailed discussion can be found in [12].

References

1. F.P. Bowden, D. Tabor, *The Friction and Lubrication of Solids* (Clarendon Press, Oxford, 1986)
2. J.F. Archard, Elastic deformation and the laws of friction. Proc. R. Soc. A **243**, 190 (1957)
3. J. Greenwood, J. Williamson, Contact of nominally flat surfaces. Proc. R. Soc. Bd. A**295**, 300 (1966)
4. B.N.J. Persson, Contact mechanics for randomly rough surfaces. Surf. Sci. Rep. **61**, 201 (2006)
5. T. Geike, *Theoretische Grundlagen eines schnellen Berechnungsverfahrens für den Kontakt rauer Oberflächen* (Techn. Univ., Diss, Berlin, 2007)
6. R. Pohrt, V.L. Popov, Normal contact stiffness of elastic solids with fractal rough surfaces. Phys. Rev. Lett. **108**(4), 104301 (2012)

7. V.L. Popov, Kontaktmechanik und Reibung, Von der Nanotribologie bis zur Erdbebendynamik. 2., überarbeitete Auflage (Springer, Berlin, 2010)
8. R. Pohrt, V.L. Popov, A.E. Filippov, Normal contact stiffness of elastic solids with fractal rough surfaces for one- and three-dimensional systems. Phys. Rev. E. **86**, 026710 (2012)
9. S. Roux, J. Schmittbuhl, J.-P. Vilotte, A. Hansen, Some physical properties of self-affine rough surfaces. Europhys. Lett. **23**(4), 277–282 (1993)
10. I.N. Sneddon, The relation between load and penetration in the axisymmetric boussinesq problem for a punch of arbitrary profile. Int. J. Eng. Sci. **3**, 47–57 (1965)
11. J. Barber, Bounds on the electrical resistance between contacting elastic rough bodies. Proc. R. Soc. London **A495**, 53–60 (2003)
12. R. Pohrt, V.L. Popov, Contact mechanics of rough spheres: crossover from fractal to hertzian behavior. Adv. Tribol. **2013**, 974178 (2013)

Chapter 11
Frictional Force

Valentin L. Popov, Silvio Kürschner and Markus Heß

11.1 Introduction

The frictional force can be determined in one of two ways: Either by a direct calculation of the tangential force components and determining their mean or by calculating the energy dissipation that is caused by material deformation. If the average power $\langle \dot{W} \rangle$ is dissipated during a macroscopic steady-state motion, then the entirety of the power dissipation can be attributed to the frictional force (from the macroscopic point of view). Therefore,

$$\langle \dot{W} \rangle = F_R v. \tag{11.1}$$

The frictional force is determined from the ratio of the power dissipation to the velocity:

$$F_R = \frac{\langle \dot{W} \rangle}{v}. \tag{11.2}$$

In the previous chapters, we have seen that within the framework of the method of dimensionality reduction, the relationships between force and displacement can be correctly determined in both the normal and tangential directions. This means that also the energy dissipation, and with it the frictional force, must be mappable. In this chapter, we discuss in detail how the frictional forces between an elastomer and a rigid surface (smooth or rough) can be modeled.

Throughout the entire chapter, we will assume that the elastomer can be described as an incompressible medium with a general linear rheology:

$$\sigma(t) = \int_{-\infty}^{t} G(t - t')\dot{\varepsilon}(t')\mathrm{d}t', \tag{11.3}$$

V.L. Popov and M. Heß, *Method of Dimensionality Reduction in Contact Mechanics and Friction*, DOI 10.1007/978-3-642-53876-6_11

where $\sigma(t)$ is the shear stress, $\varepsilon(t)$ is the shear angle, and $G(t)$ is the time-dependent shear modulus ([1], Chap. 15). Using the reduction method, this medium is replaced by a one-dimensional foundation, for which the forces in the individual elements are defined according to Eq. (7.13):

$$f_N(t) = 4\Delta x \int_{-\infty}^{t} G(t-t')\dot{u}_z(t')\mathrm{d}t'. \tag{11.4}$$

We begin our considerations with a qualitative discussion of energy dissipation and the frictional forces in the contact between simple axially-symmetric profiles (or their one-dimensional equivalents).

11.2 Energy Dissipation in an Elastomer with Linear Rheology

We consider the contact between a rigid cylindrical indenter with the diameter D and a viscoelastic half-space, the rheology of which is characterized by a complex, frequency-dependent shear modulus $\hat{G}(\omega)$ (see Eq. (7.9)). We assume that the indenter moves periodically according to $d = d_0(t + \cos\omega t)/2$. The oscillating component of the movement is equal to

$$\Delta d(t) = \frac{d_0}{2}\cos\omega t = \frac{d_0}{4}\left(e^{i\omega t} + e^{-i\omega t}\right). \tag{11.5}$$

The force acting on the indenter is calculated as

$$\Delta F(t) = \frac{d_0}{4}\left(DE^*(\omega)e^{i\omega t} + DE^*(-\omega)e^{-i\omega t}\right), \tag{11.6}$$

where

$$E^*(\omega) = \frac{2}{1-\nu}G(\omega) = 4G(\omega). \tag{11.7}$$

On the right side of Eq. (11.7), we have substituted $\nu = 1/2$, therefore, requiring incompressibility. The average power dissipation is calculated as the time-averaged product between the force and the velocity:

$$\begin{aligned}\left\langle \dot{W} \right\rangle = \left\langle \Delta F(t) \cdot \frac{\mathrm{d}(\Delta d(t))}{\mathrm{d}t} \right\rangle = \frac{Dd_0^2}{4}\Big\langle \left(G(\omega)e^{i\omega t} + G(-\omega)e^{-i\omega t}\right) \\ \left(i\omega e^{i\omega t} - i\omega e^{-i\omega t}\right)\Big\rangle.\end{aligned} \tag{11.8}$$

The angled brackets denote a temporal average. After insertion of $\hat{G}(\omega) = G'(\omega) + iG''(\omega)$, we obtain

$$\left\langle \dot{W} \right\rangle = \frac{1}{2}Dd_0^2\omega G''(\omega). \tag{11.9}$$

The force–displacement relations used for the derivation of this equation are identical to those in the one-dimensional case. Thus, the result (11.9) is also valid in the one-dimensional equivalent model.

11.3 Frictional Force Between a Rigid Axially-Symmetric Indenter and an Elastomer

11.3.1 Parabolic Indenter

We will illustrate the basic idea of the calculation of the frictional force using the example of an axially-symmetric parabolic profile

$$\tilde{z}(r) = \frac{r^2}{2R}. \tag{11.10}$$

If this profile is pressed into a viscoelastic half-space to a depth of d and then tangentially moved with the velocity v, then a contact area is formed with the characteristic radius

$$a = \sqrt{Rd}. \tag{11.11}$$

The size of the contact area (for the given indentation depth) is not dependent on the elastic properties of the medium. Equation (11.11) is valid for the normal indentation into an arbitrary linearly viscous medium. As a qualitative approximation, it is also valid for tangential motion, independent of the rheological properties of the viscoelastic medium and the tangential velocity.

For a tangential motion with the velocity v, the material near the contact area is loaded with the characteristic frequency

$$\omega \approx \frac{2\pi}{\lambda} v \approx \frac{\pi}{a} v. \tag{11.12}$$

The approximation for the normal force is

$$F_N \approx \frac{4}{3} \left| E^*(\omega) \right| R^{1/2} d^{3/2} = \frac{16}{3} |G(\omega)| R^{1/2} d^{3/2}. \tag{11.13}$$

The dissipation power can be approximated using Eq. (11.9):

$$\left\langle \dot{W} \right\rangle \approx \frac{1}{2} D d^2 \omega G''(\omega) \approx a d^2 \omega G''(\omega) \approx \pi v d^2 G''(\omega). \tag{11.14}$$

Therefore, the following approximation results for the tangential force:

$$F_x = \frac{\langle \dot{W} \rangle}{v} \approx \pi d^2 G''(\omega). \tag{11.15}$$

Even if the tangential force is not proportional to the normal force, we can formally define the coefficient of friction as

$$\mu = \frac{F_x}{F_N} \approx \frac{3\pi}{16}\frac{G''(\omega)}{|G(\omega)|}\left(\frac{d}{R}\right)^{1/2} = \frac{3\pi}{16}\frac{G''(\omega)}{|G(\omega)|}\left(\frac{a}{R}\right). \tag{11.16}$$

Equations (11.11)–(11.16) are equally valid in both the three-dimensional system and its equivalent one-dimensional system. At the same time, it must be stressed that we are not dealing with a rigorous derivation, but rather a qualitative approximation that will be more precisely refined in the following, more exact, treatment.

We now introduce the average gradient of the profile:

$$|\nabla z|_{3D} = \frac{\int\limits_0^a \frac{r}{R} 2\pi r dr}{\int\limits_0^a 2\pi r dr} = \frac{2}{3}\frac{a}{R}. \tag{11.17}$$

By introducing the average gradient, Eq. (11.16) can be written in the form

$$\mu = \frac{9\pi}{32}\frac{G''(\omega)}{|G(\omega)|}|\nabla z|_{3D}, \tag{11.18}$$

which is a very universal qualitative approximation, except for the fact that the coefficient may change.

11.3.2 Axially-Symmetric Indenter with an Arbitrary Form

As a second example, we consider an arbitrary axially-symmetric profile having the form

$$\tilde{z}(r) = c_n r^n. \tag{11.19}$$

The contact radius as a function of indentation depth d is given by the following general equation:

$$a = \left(\frac{d}{k_n c_n}\right)^{1/n}, \quad \tilde{c}_n = \kappa_n c_n, \tag{11.20}$$

where κ_n is defined according to (3.16). The normal force is given by Eq. (3.24):

$$F_N = \frac{2n}{n+1}E^* \tilde{c}_n^{-1/n} d^{\frac{n+1}{n}} = \frac{8n}{n+1}|G(\omega)|\tilde{c}_n^{-1/n} d^{\frac{n+1}{n}}. \tag{11.21}$$

As before, the tangential force is calculated using (11.15). The resulting coefficient of friction is

$$\mu = \frac{F_x}{F_N} \approx \frac{\pi(n+1)}{8n}\tilde{c}_n^{1/n} d^{\frac{n-1}{n}} \frac{G''(\omega)}{|G(\omega)|} = \frac{\pi(n+1)^2\kappa_n}{16n^2}\frac{G''(\omega)}{|G(\omega)|}|\nabla z|_{3D}, \tag{11.22}$$

where we have once again introduced the average gradient $|\nabla z|_{3D} = \frac{2n}{n+1}c_n a^{n-1}$. For the interesting case of the conical indenter ($n = 1$, $\kappa_n = \pi/2$), we obtain

$$\mu = \frac{\pi^2}{8}\frac{G''(\omega)}{|G(\omega)|}|\nabla z|_{3D}. \tag{11.23}$$

11.4 The Half-Space Approximation

Everywhere in this book, we assume that the surface deformation is small. Especially, the slope of the surface is assumed to be small at all points. Only under this condition is the linear relationship between the surface stresses and displacements of the medium valid (and with them the classical solutions to the contact problems). This assumption also has direct implications to the application of the reduction method, which we would like to explain at this point.

We now consider a rigid line with the inclination angle θ in contact with an element of a linearly elastic foundation, as shown in Fig. 11.1. The force components in the x-direction and z-direction are given by the equations

$$\Delta F_x = k_x u_x + \gamma_x \dot{u}_x = \Delta F_N \sin\theta, \tag{11.24}$$

$$\Delta F_z = k_z u_z + \gamma_z \dot{u}_z = \Delta F_N \cos\theta. \tag{11.25}$$

From this, it follows that

$$\Delta F_x = \Delta F_z \tan\theta. \tag{11.26}$$

For small inclination angles, it follows from Eqs. (11.24) and (11.25) that the order of magnitude of the horizontal and vertical displacements are related as

$$|u_x| \approx |u_z|\tan\theta \ll |u_z|. \tag{11.27}$$

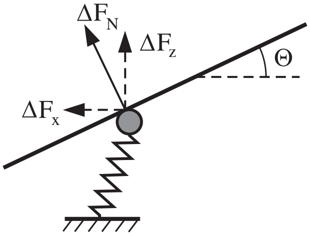

Fig. 11.1 Frictional contact between a viscoelastic element and an inclined rigid plane

In the same approximation, one can assume that $\Delta F_z \approx \Delta F_N$. We come to the conclusion that we can restrict ourselves in the half-space approximation to considering the vertical displacement. From this, the vertical force is calculated next. The horizontal force component is subsequently obtained by multiplying the result with the local slope of the rigid surface.

11.5 Calculation of the Frictional Force with a Conical Indenter Within the Framework of the Method of Dimensionality Reduction

For contacts with a one-dimensional foundation, the calculations can be carried out completely analytically for the simplest cases. As an example, we consider a rigid wedge-shaped indenter of the form

$$\tilde{z} = g(x) = c|x|, \tag{11.28}$$

which is pressed into a viscoelastic foundation to a depth of d and moved tangentially with the velocity v (Fig. 11.2a) so that its form is described at time t by the equation

$$\tilde{z} = g(x + vt) = g(\tilde{x}). \tag{11.29}$$

For convenience, we have introduced the coordinate $\tilde{x}$ in the frame of reference that moves with the rigid indenter.

To simplify our task, we assume that the elastomer is a simple viscoelastic material (Kelvin body), which can be modeled as parallelly connected springs and dampers (Fig. 11.2b). If the three-dimensional medium is characterized by the shear modulus G and the viscosity η, then the the single elements of the viscoelastic foundation must be chosen according to the rule (11.4) as parallelly connected springs with a stiffness Δk_z and dampers with the damping coefficient $\Delta\gamma$, where

$$\Delta k_z = 4G\Delta x, \quad \Delta\gamma = 4\eta\Delta x. \tag{11.30}$$

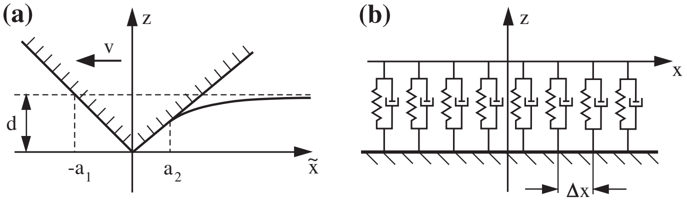

Fig. 11.2 (**a**) Contact between an elastomer and rigid conical indenter, which is moved tangentially with the velocity v. (**b**) Rheological model for a viscoelastic medium

We denote the coordinates of the boundary of the contact area as $\tilde{x} = -a_1$ and $\tilde{x} = a_2$ (Fig. 11.2a). Vertical displacements u_z in the entire contact area are determined by the purely geometric condition

$$u_z(x,t) = d - g(x+vt) = d - g(\tilde{x}). \tag{11.31}$$

The vertical velocities are

$$\frac{\partial u_z(x,t)}{\partial t} = -\frac{\partial g(x+vt)}{\partial t} = -vg'(\tilde{x}) \tag{11.32}$$

and the force acting on one element is

$$f_N(\tilde{x}) = \Delta k_z \cdot u_z + \Delta\gamma \cdot \dot{u}_z = 4\left[G \cdot (d - g(\tilde{x})) - \eta v g'(\tilde{x})\right]\Delta x. \tag{11.33}$$

The left boundary of the contact area is determined by the condition $u_z(-a_1) = 0$ and the right boundary, from the condition $f_N(a_2) = 0$. From this, it follows that

$$a_1 = d/c, \quad a_2 = d/c - v\tau, \tag{11.34}$$

where we have introduced the relaxation time

$$\tau = \eta/G. \tag{11.35}$$

We can consider two velocity domains:

$$\text{I:} \quad v < \frac{d}{c\tau}, \tag{11.36}$$

$$\text{II:} \quad v > \frac{d}{c\tau}. \tag{11.37}$$

In the first, the right contact point lies to the right of the tip of the cone. In the second, it coincides with the tip.

Velocity domain I: The total normal force is

$$\begin{aligned} F_N &= 4\int_{-a_1}^{a_2} \left[G(d - g(\tilde{x})) - \eta v g'(\tilde{x})\right] \mathrm{d}\tilde{x} \\ &= 4\int_{-a_1}^{0} \left[G(d + c\tilde{x}) + \eta v c\right] \mathrm{d}\tilde{x} + 4\int_{0}^{a_2} \left[G(d - c\tilde{x}) - \eta v c\right] \mathrm{d}\tilde{x} \\ &= 4G\left\{d(a_1 + a_2) + \tau v c(a_1 - a_2) - \frac{c}{2}\left(a_1^2 + a_2^2\right)\right\} \\ &= \frac{4G}{c}\left[d^2 + \frac{1}{2}(cv\tau)^2\right]. \end{aligned} \tag{11.38}$$

The tangential force is calculated as

$$\begin{aligned} F_x &= -4\int_{-a_1}^{a_2} g'(\tilde{x})\left[G(d-g(\tilde{x}))-\eta v g'(\tilde{x})\right]\mathrm{d}\tilde{x} \\ &= 4c\int_{-a_1}^{0}\left[G(d+c\tilde{x})+\eta v c\right]\mathrm{d}\tilde{x}-4c\int_{0}^{a_2}\left[G(d-c\tilde{x})-\eta v c\right]\mathrm{d}\tilde{x} \\ &= 4Gc\left\{d(a_1-a_2)+\tau v c(a_1+a_2)-\frac{c}{2}\left(a_1^2-a_2^2\right)\right\} \\ &= 4Gc\left[2d(v\tau)-\frac{c}{2}(v\tau)^2\right]. \end{aligned} \tag{11.39}$$

The resulting coefficient of friction is

$$\mu=\frac{F_x}{F_N}=c\frac{\left[2\left(\frac{cv\tau}{d}\right)-\frac{1}{2}\left(\frac{cv\tau}{d}\right)^2\right]}{\left[1+\frac{1}{2}\left(\frac{cv\tau}{d}\right)^2\right]}. \tag{11.40}$$

By taking into account that $c=|\nabla z|$ and $(cv\tau)/d\approx v\tau/a\approx\omega\tau$, this result corresponds qualitatively with the approximation (11.23), however, there are minor deviations from the simple approximation.

Velocity domain II: The normal force is

$$\begin{aligned} F_N &= 4\int_{-a_1}^{0}\left[G(d-g(\tilde{x}))-\eta v g'(\tilde{x})\right]\mathrm{d}\tilde{x}=4\int_{-a_1}^{0}\left[G(d+c\tilde{x})+\eta v c\right]\mathrm{d}\tilde{x} \\ &= 4G\left\{da_1+\tau v c a_1-\frac{c}{2}a_1^2\right\}=\frac{4G}{c}\left[\frac{d^2}{2}+cdv\tau\right] \end{aligned} \tag{11.41}$$

and the coefficient of friction is

$$\mu=c=const. \tag{11.42}$$

This limiting case is also valid for the case of a contact with a linear fluid ($G=0$). In this case, $F_N=4d\eta v$ and the coefficient of friction is constant.

If we express the indentation depth as a function of normal force in Eq. (11.38) and set it equal to Eq. (11.40), then we obtain a coefficient of friction of

$$\mu=\frac{F_x}{F_N}=\begin{cases} c\left[2^{3/2}\psi\sqrt{1-\psi^2}-\psi^2\right], & \psi^2<1/3 \\ c, & \psi^2>1/3 \end{cases}, \tag{11.43}$$

with

$$\psi^2=\frac{2cGv^2\tau^2}{F_N}. \tag{11.44}$$

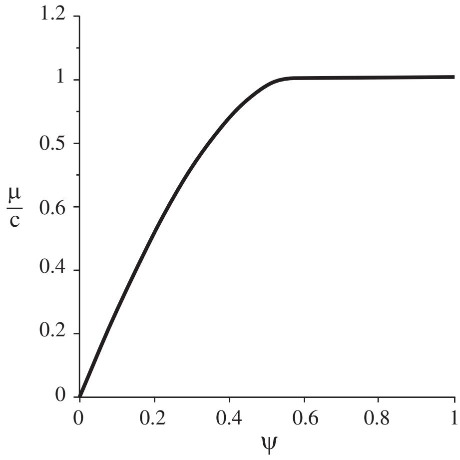

Fig. 11.3 The coefficient of friction (normalized by the surface gradients) for a conical indenter as a function of the variable $\psi = v\tau\sqrt{2cG/F_N}$

According to this, the coefficient of friction is a universal function of the parameter combination ψ and is dependent on the viscosity, shear modulus, velocity, normal force, and average surface gradient. For values of ψ larger than a critical value, the coefficient of friction remains constant (Fig. 11.3).

11.6 Correction Coefficient for the Conversion from Three-Dimensional to One-Dimensional Profiles

In Sect. 11.3, we have shown that the frictional force for axially-symmetric, three-dimensional profiles must agree with the corresponding one-dimensional profiles, based on a qualitative approximation. With such qualitative arguments, however, the equivalence can only be shown up to a constant coefficient; the constant must be obtained either through a comparison between exact one-dimensional and three-dimensional solutions or through a comparison with numerical solutions. In this section, we carry out such a comparison between exact one-dimensional and numerically obtained three-dimensional solutions in the simplest case of a linearly viscous medium.

In the first example, we consider a three-dimensional, conical indenter, the surface of which we once again define as $f(r) = \tan\theta \cdot |r|$. This cone is pressed into a viscous half-space with a constant external force and tangentially moved with a constant velocity. Initially, the cone sinks further into the viscous medium. At a certain depth, however, the external force is compensated for by the vertical component of the reaction force between the indenter and the viscous medium. A steady-state process is achieved for which we determine the coefficient of friction. We have simulated this process using the boundary element method for various velocities. The result for a cone with $\tan\theta = 0.1$ is drawn in Fig. 11.4 as a blue curve.

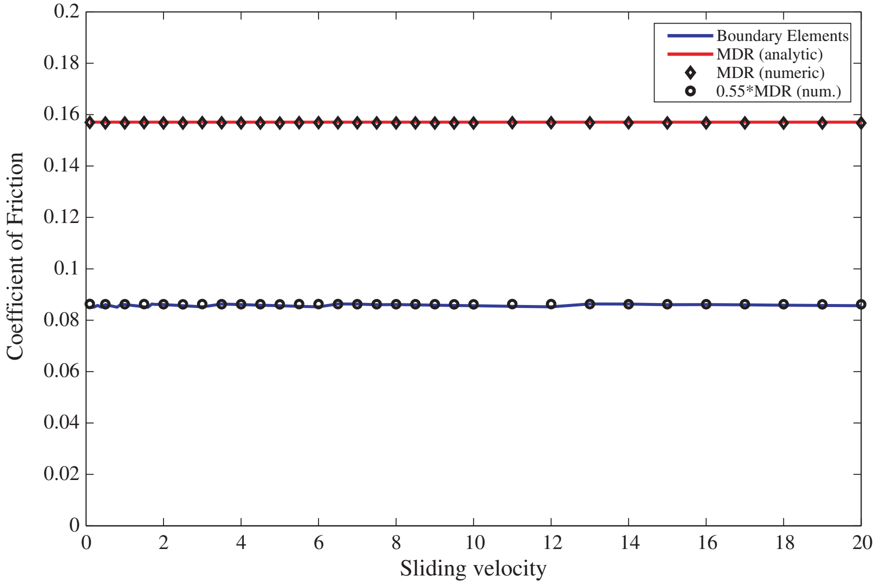

Fig. 11.4 The coefficient of friction for tangential displacements of an imbedded cone with the slope $\tan\theta = 0.1$

In the previous section, we already found an analytical solution for a one-dimensional consideration. We must simply adapt this to the simplified material model by taking the missing elastic properties as $G \to 0$ into account. According to (11.42), we obtain a very simple result for the (one-dimensional) coefficient of friction $\mu_{1,D}$: It is identical to the slope of the one-dimensional profile. However, this is a factor of $\pi/2$ larger than that in the original three-dimensional system. Therefore,

$$\mu_{1D} = \frac{\pi}{2}\tan\theta. \tag{11.45}$$

This result is shown in Fig. 11.4 as the red curve. To check this, the analytical result was verified using numerical simulations with the reduction method. Both results correspond exactly. In Fig. 11.4, the numerically determined results from the reduction method are identified as black diamonds. By comparing the one-dimensional results with those of the boundary element method, we obtain the correction factor for a conical indenter:

$$\frac{\mu_{3D}}{\mu_{1D}} = 0.55. \tag{11.46}$$

In a second example, we consider an indenter having the form of a rotated paraboloid, the surface of which is defined according to Eq. (11.10). A boundary element calculation was also carried out for this indenter for various tangential velocities. The results are presented in Fig. 11.5 as a blue curve.

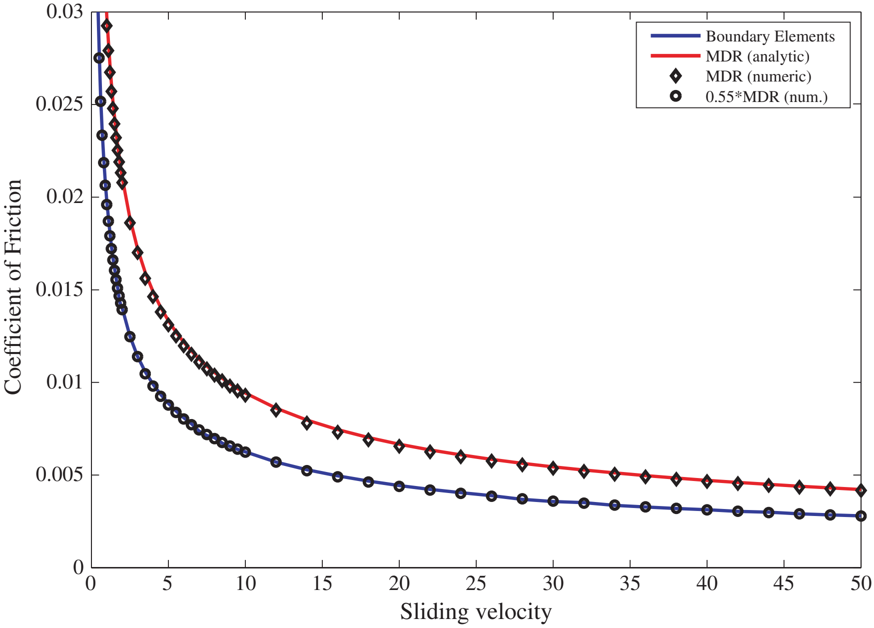

Fig. 11.5 The coefficient of friction for tangential displacement of an imbedded rotated paraboloid with the radius of curvature of $c = 0.1\ \mathrm{m}^{-1}$

Now, we take the results from the problems at the end of this chapter for the corresponding one-dimensional consideration. In the first example problem, we adapt the material model by setting $G \to 0$. Additionally, we replace $1/(2R) = c$ and obtain the analytical solution from Eq. (11.67):

$$\mu_{1D} = \frac{2^{3/2}}{3}\sqrt{\frac{cF}{\eta v}}. \tag{11.47}$$

In Fig. 11.5, this is shown as a red curve. Also in this case, we have verified the results by conducting a corresponding simulation using the reduction method. These are shown in Fig. 11.5 as black diamonds.

By comparing the one-dimensional results with those of the boundary element method, we obtain the correction factor for the parabolic indenter:

$$\frac{\mu_{3D}}{\mu_{1D}} = 0.67. \tag{11.48}$$

The results of the reduction method scaled with this factor are shown as black circles.

We see that the coefficient of friction calculated using the equivalent one-dimensional model is larger than that in the three-dimensional original system. To obtain the correct coefficient of friction for the original system, the

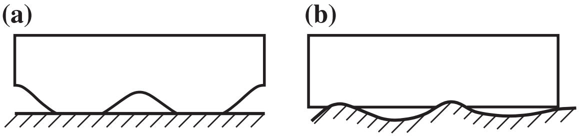

Fig. 11.6 (**a**) A rough rubber block on a smooth rigid plane and (**b**) a smooth rubber block on a rough, rigid plane

one-dimensional result must be multiplied by a correction factor which is dependent on the exponent n in the case of the axially-symmetric profile and on the Hurst exponent H in the case of a rough surface. For Hurst exponents near 1, one may expect (in support of the results for the conical profile) that the conversion factor is approximately equal to 0.5. A more detailed discussion can be found in [2].

11.7 Contacts Between Rough Surfaces

In a contact between a rigid surface and an elastomer, energy can only be dissipated through deformation of the elastomer. For this reason, the roughness of the rigid surface and that of the surface of the elastomer play completely different roles. This is illustrated in Fig. 11.6. If the elastomer slides over a smooth, rigid plane (Fig. 11.6a), then there is no time-dependent change in the deformation state of the elastomer, and therefore, no energy dissipation: There is no friction. In contrast, if the elastomer is slid over a rough surface (Fig. 11.6b), then the local deformation state of individual areas of the elastomer is time-dependent and energy is dissipated. From this, it follows that the roughness of the elastomer surface plays no direct role in this case: The friction is primarily determined by the roughness of the rigid surface. We will see, however, that for a certain interval of indentation force, the elastomer friction is dependent on the real contact length. This is, in turn, dependent on the roughness of the elastomer. In considering the elastomer friction between two rough surfaces, we begin with the contact between a rigid, rough surface and an elastomer, the surface of which we assume to be flat.

11.8 Contact of a Flat, Smooth Elastomer with a Nominally Flat, Rough Body

We now discuss the friction with a nominally flat, but rough, profile and initially assume that the normal force is so large that complete contact is obtained with the elastomer. For the force, we have the equations

$$F_N = 4\int_0^L \left[G\left(d - g(\tilde{x})\right) - \eta v g'(\tilde{x})\right] d\tilde{x}, \tag{11.49}$$

$$F_x = -4\int_0^L g'(\tilde{x})\left[G\left(d - g(\tilde{x})\right) - \eta v g'(\tilde{x})\right] d\tilde{x}. \tag{11.50}$$

The integral extends over the entire length L of the system. Due to the macroscopic homogeneity of the profile, the integrals $\int_0^L \eta v g'(\tilde{x}) \mathrm{d}\tilde{x}$ and $\int_0^L g'(\tilde{x}) G(d - g(\tilde{x})) \mathrm{d}\tilde{x}$ vanish. The integral $\int_0^L G g(\tilde{x}) \mathrm{d}\tilde{x}$ also vanishes, because we define the profile so that its mean is equal to zero. Therefore,

$$F_N = 4Gdl, \tag{11.51}$$

$$F_x = 4\eta v \int_0^L \left[g'(\tilde{x})\right]^2 \mathrm{d}\tilde{x} = 4\eta v \left\langle \nabla z^2 \right\rangle L. \tag{11.52}$$

According to this, the coefficient of friction is

$$\mu = \frac{\eta v \langle \nabla z^2 \rangle}{Gd} = \frac{v\tau \langle \nabla z^2 \rangle}{d} = \frac{4GLv\tau}{F_N} \left\langle \nabla z^2 \right\rangle. \tag{11.53}$$

For a complete contact, it is proportional to the velocity and the RMS-surface gradient. If the indentation depth is much larger than the roughness of the profile, then one can gather from Eq. (11.33) that contact separation occurs at the trailing edge of microcontacts when the condition

$$d/(\tau v \nabla z) \approx 1 \tag{11.54}$$

is met, where ∇z is the characteristic value of the surface gradient. At this point, the coefficient of friction achieves an approximately constant value of $\mu \approx \nabla z$. By taking Eq. (11.51) into account, this condition can be written as

$$\frac{4G\tau v L \nabla z}{F_N} = \frac{4\eta v L \nabla z}{F_N} \approx 1. \tag{11.55}$$

11.9 Contact Between a Rough Elastomer and a Rigid, Rough Surface

The general case of a contact between two rough surfaces can be analyzed numerically. Therefore, we restrict ourselves in this chapter to a qualitative discussion of an elastomer with a large enough roughness. If the roughness of the elastomer is so large that in the relevant force interval, complete contact is not achieved, then the indentation depth in Eq. (11.54) is dependent on the normal force. This dependence can be derived from Eq. (10.30) (for $0.4 < H < 1$):

$$d \approx h \frac{(H+1)^2}{1{,}9412H} \left(\frac{F_N}{4GLh} \right)^{\frac{H}{H+1}}. \tag{11.56}$$

Inserting this into the criterion (11.54) results in

$$\frac{19{,}412H}{(H+1)^2} \frac{\tau v \nabla z}{h^{\frac{1}{H+1}}} \left(\frac{4GL}{F_N} \right)^{\frac{H}{H+1}} \approx 1. \tag{11.57}$$

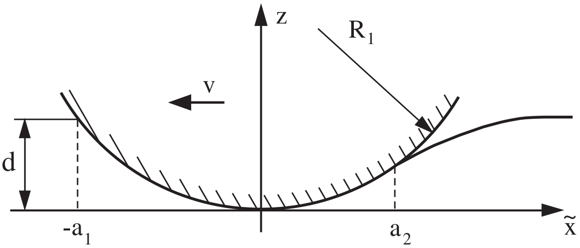

Fig. 11.7 Contact between an elastomer and a rigid, parabolic indenter that is moved tangentially at a velocity v

We note that even if the length of the system L explicitly appears in this equation, the criterion is independent from this length, as $h \propto L^H$ is valid for fractal surfaces and the length is canceled out. This equation determines the order of magnitude of the velocity at which a saturation value is achieved for the coefficient of friction.

11.10 Problems

Problem 1 Determine the coefficient of friction between a parabolic profile and a viscoelastic half-space (Kelvin body) within the framework of the reduction method.

Solution The derivation in Sect. 11.5 is independent of the specific form of the indenter, up to and including Eq. (11.33), and it is also valid in the case of a parabolic indenter. Only the exact form of the profile must be inserted, in this case $\tilde{z} = \tilde{x}^2/(2R_1)$. For the coordinates of the boundary points (Fig. 11.7), we obtain

$$a_1 = \sqrt{2R_1 d}, \quad a_2 = \sqrt{2R_1 d + (v\tau)^2} - v\tau. \tag{11.58}$$

The total normal force is calculated as

$$\begin{aligned} F_N &= 4 \int\limits_{-a_1}^{a_2} \left[G(d - g(\tilde{x})) - \eta v g'(\tilde{x})\right] \mathrm{d}\tilde{x} \\ &= 4 \int\limits_{-a_1}^{a_2} \left[G\left(d - \frac{\tilde{x}^2}{2R_1}\right) - \eta v \frac{\tilde{x}}{R^1}\right] \mathrm{d}\tilde{x} \\ &= \frac{4G}{2R_1} \int\limits_{-a_1}^{a_2} \left[\left(a_1^2 - \tilde{x}^2\right) - 2\tau v \tilde{x}\right] \mathrm{d}\tilde{x} \\ &= \frac{4G}{3R_1} \int\limits_{-a_1}^{a_2} \left[(2R_1 d)^{3/2} - (\tau v)^3 \left(2R_1 d + (\tau v)^2\right)^{3/2}\right] \\ &= \frac{4G(v\tau)^3}{3R_1} \xi \left[1 - \xi^3 + \left(1 + \xi^2\right)^{3/2}\right] \end{aligned} \tag{11.59}$$

with

$$\xi = \frac{\nu\tau}{(2R_1 d)^{1/2}}. \tag{11.60}$$

For the tangential force, we obtain

$$\begin{aligned}
F_x &= -4\int_{-a_1}^{a_2} g'(\tilde{x})\left[G(d-g(\tilde{x})) - \eta\nu g'(\tilde{x})\right]d\tilde{x}\\
&= -\frac{2G}{R_1^2}\int_{-a_1}^{a_2}\tilde{x}\left[\left(a_1^2-\tilde{x}^2\right) - 2\tau\nu\tilde{x}\right]d\tilde{x}\\
&= \frac{2G\nu\tau}{3R_1^2}\left[2(2R_1 d)^{3/2} - 3(2R_1 d)\nu\tau - 2(\nu\tau)^3 + 2\left(2R_1 d + (\nu\tau)^2\right)^{3/2}\right]\\
&= \frac{8G}{3}d^2\xi\left[2 - 3\xi - 2\xi^3 + 2\left(1+\xi^2\right)^{3/2}\right]\\
&= \frac{2G(\nu\tau)^4}{3R_1^2}\xi^{-3}\left[2 - 3\xi - 2\xi^3 + 2\left(1+\xi^2\right)^{3/2}\right].
\end{aligned} \tag{11.61}$$

The resulting coefficient of friction is

$$\begin{aligned}
\mu &= \frac{F_x}{F_N}\\
&= \left(\frac{d}{2R_1}\right)^{1/2}\frac{\frac{\nu\tau}{(2R_1 d)^{1/2}}\left[2(2R_1 d)^{3/2} - 3(2R_1 d)\nu\tau - 2(\nu\tau)^3 + 2\left(2R_1 d + (\nu\tau)^2\right)^{3/2}\right]}{\left[(2R_1 d)^{3/2} - (\nu\tau)^3 + \left(2R_1 d + (\nu\tau)^2\right)^{3/2}\right]}\\
&= \left(\frac{d}{2R_1}\right)^{3/2}\frac{\xi\left[2 - 3\xi - 2\xi^3 + 2\left(1+\xi^2\right)^{3/2}\right]}{\left[1-\xi^3+\left(1+\xi^2\right)^{3/2}\right]}.\\
&= |\nabla z|_{1D}\frac{\xi\left[2 - 3\xi - 2\xi^3 + 2\left(1+\xi^2\right)^{3/2}\right]}{\left[1-\xi^3+\left(1+\xi^2\right)^{3/2}\right]}\\
&= \left(\frac{\nu\tau}{2R_1}\right)\frac{\xi\left[2 - 3\xi - 2\xi^3 + 2\left(1+\xi^2\right)^{3/2}\right]}{\left[1-\xi^3+\left(1+\xi^2\right)^{3/2}\right]}.
\end{aligned} \tag{11.62}$$

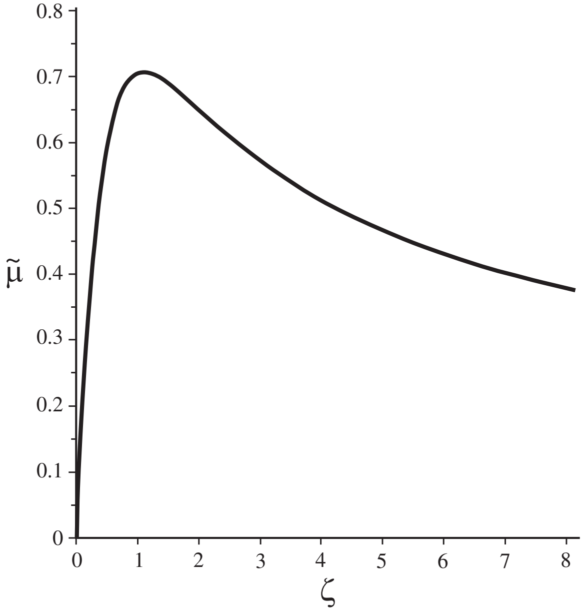

Fig. 11.8 The normalized frictional coefficient between a viscoelastic medium and a parabolic indenter as a function of the dimensionless velocity

Equation (11.59) can be written in the form

$$\zeta = \frac{\xi}{\left[1 - \xi^3 + \left(1+\xi^2\right)^{3/2}\right]^{1/3}}, \tag{11.63}$$

where

$$\zeta = v\tau \left(\frac{4G}{3F_N R_1}\right)^{1/3}; \tag{11.64}$$

and the coefficient of friction (11.62) can be written in the form

$$\tilde{\mu} = \frac{\xi\left[2 - 3\xi - 2\xi^3 + 2\left(1+\xi^2\right)^{3/2}\right]}{\left[1 - \xi^3 + \left(1+\xi^2\right)^{3/2}\right]^{4/3}}, \tag{11.65}$$

where we have introduced the normalized coefficient of friction $\tilde{\mu}$:

$$\tilde{\mu} = \mu \left(\frac{32R_1^2 G}{3F_N}\right)^{1/3}. \tag{11.66}$$

Equations (11.63) and (11.65), in parametric form, determine the dependence of the dimensionless coefficient of friction (11.66) on the dimensionless velocity (11.64). This “master curve” is plotted in Fig. 11.8. It reaches a maximum of 0.703 at $\zeta = 1.11$ and then decreases once again. This decrease, however, is not due to the

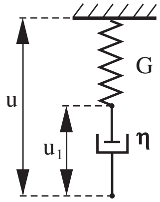

Fig. 11.9 The Maxwell element

frequency dependence of the shear modulus, but rather is a result of the decrease of the effective surface gradient. The asymptotic behavior at very small and very large velocities is described by the following equations:

$$\mu \approx \begin{cases} \frac{v\tau}{R_1}, & \zeta \ll 1, \\ \frac{2^{3/2}}{3}\left(\frac{F_N}{4GR_1 v\tau}\right)^{1/2}, & \zeta \gg 1. \end{cases} \tag{11.67}$$

Problem 2 Calculate the frictional force between a conical indenter and an elastomer, the rheology of which is described by the Maxwell element (spring and damper attached in parallel, Fig. 11.9).

Solution The geometry of the problem is shown is Fig. 11.2a. We denote the "outer coordinate" of the Maxwell element as u and the coordinate of the connection between G and η as u_1. The dynamics of the element and the force relationships are described by two equations:

$$f_N = 4Gu_1\Delta x, \tag{11.68}$$

$$4Gu_1 = 4\eta(\dot{u} - \dot{u}_1), \quad \text{or} \quad \dot{u}_1 + \frac{1}{\tau}u_1 = \dot{u}, \tag{11.69}$$

with $\tau = \eta/G$. In the entire contact area, the displacement u is given by the Eq. (11.31):

$$u(x,t) = d - g(x + vt) = d - g(\tilde{x}) \tag{11.70}$$

and with this, the vertical velocity is given by Eq. (11.32):

$$\frac{\partial u(x,t)}{\partial t} = -vg'(x + vt) = -vg'(\tilde{x}). \tag{11.71}$$

Left of the first contact point, the springs are in the non-stressed state with $u = 0$ and $u_1 = 0$. At the initial contact at $\tilde{x} = -a_1 = -d/c$, the change in the coordinate $\tilde{x}$ of a given element begins according to $\tilde{x} = -a_1 + vt$. The solution to Eq. (11.69) with said initial conditions is

$$u_1 = e^{-\frac{t}{\tau}} \int_0^t \dot{u}(\tilde{t}) e^{\frac{\tilde{t}}{\tau}} \mathrm{d}\tilde{t}. \tag{11.72}$$

Through the substitution $\hat{x} = -a_1 + v\tilde{t}$, it can be brought into the form

$$u_1 = -e^{-\frac{\tilde{x}}{v\tau}} \int\limits_{-a_1}^{\tilde{x}} g'\left(\hat{x}\right) e^{\frac{\tilde{x}}{v\tau}} \mathrm{d}\hat{x}. \tag{11.73}$$

The force acting on the element is

$$f_N = 4Gu_1\Delta x = -4G\Delta x e^{\frac{\tilde{x}}{v\tau}} \int\limits_{-a_1}^{\tilde{x}} g'\left(\hat{x}\right) e^{\frac{\tilde{x}}{v\tau}} \mathrm{d}\hat{x}. \tag{11.74}$$

The right contact point is determined from the condition $f_N = 0$, or in explicit form,

$$\int\limits_{-a_1}^{0} (-c) e^{\frac{\hat{x}}{v\tau}} \mathrm{d}\hat{x} + \int\limits_{0}^{a_2} c e^{\frac{\hat{x}}{v\tau}} \mathrm{d}\hat{x} = 0. \tag{11.75}$$

After a simple calculation, it follows that

$$a_2 = v\tau \ln\left(2 - e^{-\frac{d}{cv\tau}}\right). \tag{11.76}$$

We obtain the following for the force in individual springs:

$$f_N = 4G\Delta x \begin{cases} e^{-\frac{\tilde{x}}{v\tau}} \int\limits_{-a_1}^{\tilde{x}} c e^{\frac{\hat{x}}{v\tau}} \mathrm{d}\hat{x}, & \tilde{x} < 0 \\ e^{-\frac{\tilde{x}}{v\tau}} \left(\int\limits_{-a_1}^{0} c e^{-\frac{\hat{x}}{v\tau}} \mathrm{d}\hat{x} - \int\limits_{0}^{\tilde{x}} c e^{\frac{\hat{x}}{v\tau}} \mathrm{d}\hat{x} \right), & \tilde{x} > 0 \end{cases}. \tag{11.77}$$

Calculating the integral results in

$$f_N = 4Gcv\tau\Delta x \begin{cases} 1 - e^{-\frac{d}{cv\tau}} e^{-\frac{\tilde{x}}{v\tau}}, & \tilde{x} < 0 \\ e^{-\frac{\tilde{x}}{v\tau}} \left(2 - e^{-\frac{d}{cv\tau}}\right) - 1, & \tilde{x} > 0 \end{cases}. \tag{11.78}$$

The entire normal and tangential forces are now

$$F_N = 4Gcv\tau\Delta x \left(\int\limits_{-a_1}^{0} \left(1 - e^{-\frac{d}{cv\tau}} e^{-\frac{\tilde{x}}{v\tau}}\right) \mathrm{d}\tilde{x} + \int\limits_{0}^{a_2} \left(e^{-\frac{\tilde{x}}{v\tau}} \left(2 - e^{-\frac{d}{cv\tau}}\right) - 1 \right) \mathrm{d}\tilde{x} \right), \tag{11.79}$$

$$F_x = 4Gcv\tau\Delta x \left(c \int\limits_{-a_1}^{0} \left(1 - e^{-\frac{d}{cv\tau}} e^{-\frac{\tilde{x}}{v\tau}}\right) \mathrm{d}\tilde{x} - c \int\limits_{0}^{a_2} \left(e^{-\frac{\tilde{x}}{v\tau}} \left(2 - e^{-\frac{d}{cv\tau}}\right) - 1 \right) \mathrm{d}\tilde{x} \right). \tag{11.80}$$

Calculating these integrals finally provides

$$F_N = 4Gv\tau\,\Delta x\left[d - cv\tau\ \ln\left(2 - e^{-\frac{d}{cv\tau}}\right)\right], \tag{11.81}$$

$$F_x = 4Gcv\tau\,\Delta x\left(d - 2cv\tau\left(1 - e^{-\frac{d}{cv\tau}}\right) + cv\tau\ \ln\left(2 - e^{-\frac{d}{cv\tau}}\right)\right), \tag{11.82}$$

and we obtain a coefficient of friction of

$$\mu = c\frac{\frac{d}{cv\tau} - 2\left(1 - e^{-\frac{d}{cv\tau}}\right) + \ln\left(2 - e^{-\frac{d}{cv\tau}}\right)}{\frac{d}{cv\tau} - \ln\left(2 - e^{-\frac{d}{cv\tau}}\right)}. \tag{11.83}$$

This dependence is presented in Fig. 11.10.

We note that for a Maxwell element, the relations $G'' = G\frac{\omega\tau}{1+(\omega\tau)^2}$ and $|G| = G\frac{\omega\tau}{\sqrt{1+(\omega\tau)^2}}$ are valid so that the "rheological factor" in Eq. (11.23) decreases with the frequency:

$$\frac{G''(\omega)}{|G(\omega)|} = \frac{1}{\sqrt{1 + (\omega\tau)^2}}, \tag{11.84}$$

which corresponds qualitatively with the obtained solution.

Problem 3 Determine the frictional force between a rigid, rough surface and an elastomer in complete contact.

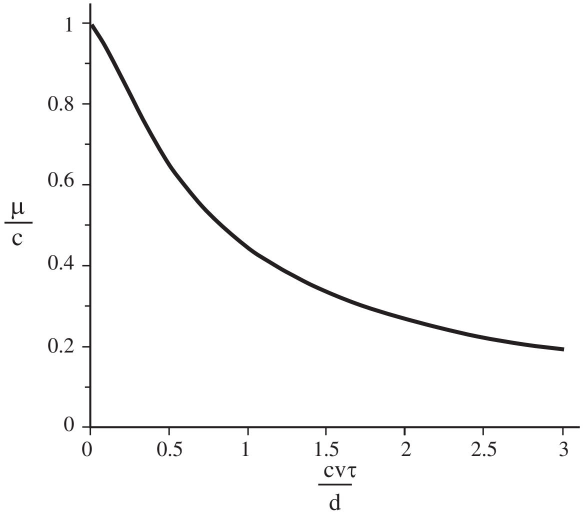

Fig. 11.10 Dependence of the normalized coefficient of friction with respect to the variable *cvτ/d* for a conical indenter in contact with the Maxwell medium

Solution If the normal force is so large that the surface of the elastomer is in contact at all points with the rough surface, then the coefficient of friction can be calculated using the following equation [3]:

$$\mu = \frac{L^2}{2F_N} \int \mathrm{d}q q^3 C_{2D}(q) \int_0^{2\pi} \mathrm{d}\varphi \cos\varphi \, \mathrm{Im}\left[4G(qv\cos(\varphi))\right]. \tag{11.85}$$

For a viscoelastic elastomer, the following is valid:

$$\mu = \eta v \frac{L^2}{F_N} \int 2\pi C_{2D}(q) q^4 \mathrm{d}q. \tag{11.86}$$

Problem 4 Friction between elastomers and differently shaped rough bodies. Determine the frictional force between a rigid, rough curved surface (rough sphere or rough cone) and an elastomer (Kelvin body).

Solution Let us consider a rigid indenter having the form

$$z = g(x) = g_0(x) + h(x) \tag{11.87}$$

consisting of the macroscopic power-shaped profile

$$g_0(x) = c_n |x|^n \tag{11.88}$$

and a superimposed roughness *h(x)*, as shown in Fig. 11.11. $n = 1$ corresponds to a conical and $n = 2$ to a parabolic indenter. Coordinates x and z are measured from the minimum of the macroscopic form, so that $g_0(0) = 0$. The ensemble average of

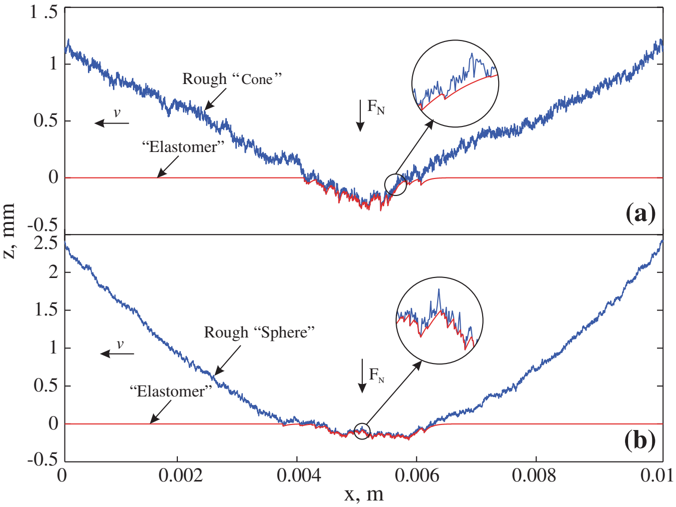

Fig. 11.11 One-dimensional contact between a visco-elastic body and (**a**) a rough '*cone*'; (**b**) a rough '*sphere*'

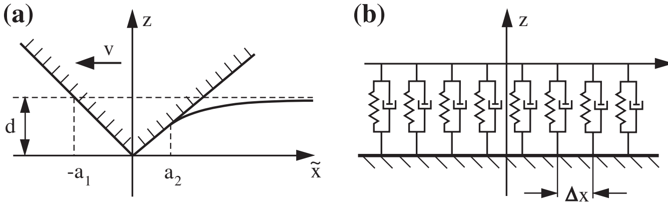

Fig. 11.12 (**a**) A "large scale picture" of a contact of an elastomer and a rigid conical indenter which is moving with velocity v. (**b**) Rheological model for a viscoelastic medium

the rough profile is assumed to be zero: $\langle h(x)\rangle = 0$. The roughness is assumed to be a self-affine fractal having the power spectral density $C_{1D} \propto q^{-2H-1}$, where q is the wave vector and H, the Hurst exponent. This one-dimensional power density corresponds to the two-dimensional power density of the form $C_{2D} \propto q^{-2H-2}$. The spectral density is assumed to be defined in the interval from $q_{\min} = 2\pi/L$, where L is some reference length, to the upper cut-off wave vector $q_{\max} = \pi/\Delta x$. The spacing Δx determines the upper cut-off wave vector.

Surface topography can be characterized by the rms roughness h_0, which is dominated by the long wavelength components of the power spectrum and the rms gradient of the surface ∇z, dominated by the short wavelength part of the spectrum. Throughout this book, we will assume that the indentation depth of the indenter, d, is much larger than the rms value of the roughness, $h_0 \ll d$. This means that the large-scale configuration of the contact is primarily determined by the macroscopic form of the indenter and does not depend on the roughness.

According to the method of dimensionality reduction, the Kelvin body can be modeled as a series of parallel springs with stiffness Δk_z and dash pots with damping constant $\Delta\gamma$ (Fig. 11.12b), where

$$\Delta k_z = 4G\Delta x, \;\; \Delta\gamma = 4\eta\Delta x. \tag{11.89}$$

The rigid indenter is pressed into a viscoelastic foundation to the depth d and is moved in the tangential direction with velocity v (Fig. 11.12a), so that at time t it is described by the equation

$$z = g(x + vt) - d = g(\tilde{x}) - d. \tag{11.90}$$

For convenience, we introduced the coordinate $\tilde{x} = x + vt$ in the coordinate system moving together with the rigid indenter. The normal force in each particular element of the viscoelastic foundation is given by

$$f = -4\Delta x[Gu(x) + \eta\dot{u}(x,t)], \tag{11.91}$$

where u is the vertical displacement of the element of the viscoelastic foundation. For elements in contact with the rigid surface, this means that

$$f = 4\Delta x\big[G(d - g(\tilde{x})) - \eta v g'(\tilde{x})\big]. \tag{11.92}$$

The normal and the tangential forces are determined by the equations

$$F_N = 4 \int_{-a_1}^{a_2} \left[G(d - g(\tilde{x})) - \eta v g'(\tilde{x})\right] d\tilde{x}, \tag{11.93}$$

$$F_x = -4 \int_{-a_1}^{a_2} g'(\tilde{x}) \left[G(d - g(\tilde{x})) - \eta v g'(\tilde{x})\right] d\tilde{x}. \tag{11.94}$$

We first consider the force of friction at very low velocities. The contact configuration is then approximately equal to the static contact. The uppermost left and uppermost right points $-a_1$ and a_2 of the contact (see Fig. 11.12a) are then both determined by the condition $g(-a_1) - d \approx g(a_2) - d = 0$. Because of the relation $g(-a_1) = g(a_2)$, the integrals $4 \int_{-a_1}^{a_2} \eta v g'(\tilde{x}) \mathrm{d}\tilde{x}$ and $\int_{-a_1}^{a_2} g'(\tilde{x}) G(d - g(\tilde{x})) \mathrm{d}\tilde{x}$ in (11.93) and (11.94) vanish. Therefore,

$$F_N = 4 \int_{-a_1}^{a_2} G(d - g(\tilde{x})) \mathrm{d}\tilde{x} \approx 4 \int_{-a_1}^{a_2} G(d - g_0(\tilde{x})) \mathrm{d}\tilde{x}, \tag{11.95}$$

$$F_x = 4\eta v \int_{-a_1}^{a_2} \left[g'(\tilde{x})\right]^2 \mathrm{d}\tilde{x} \approx 4\eta v \int_{-a_1}^{a_2} \left[g_0'(\tilde{x})^2 + h'(\tilde{x})^2\right] \mathrm{d}\tilde{x}. \tag{11.96}$$

We assume that the gradient of the macroscopic shape of the indenter is much smaller than that of the roughness, $\left\langle g_0'(x)^2 \right\rangle \ll \left\langle h'(x)^2 \right\rangle$, so that

$$F_x \approx 4\eta v \int_{-a_1}^{a_2} h'(x)^2 \mathrm{d}\tilde{x} \approx 4\eta v \nabla z^2 L_{\mathrm{cont}}, \tag{11.97}$$

where ∇z is the rms value of the surface gradient and $L_{\mathrm{cont}} = a_1 + a_2$, the contact length. For the coefficient of friction, we get

$$\mu \approx \frac{4 L_{\mathrm{cont}} v \eta}{F_N} \nabla z^2 = \frac{4 G L_{\mathrm{cont}} v \tau}{F_N} \nabla z^2, \tag{11.98}$$

where $\tau = \eta / G$ is the relaxation time. This equation shows that both the macroscopic shape of the indenter and the microscopic properties of surface topography determine the coefficient of friction: The contact length is primarily determined by the macroscopic properties (shape of the body and the normal force) while the rms gradient is primarily determined by the roughness at the smallest scale.

Consider the opposite case of *high* sliding velocities. The detachment of elastomer from the indenter occurs when the normal force (which is the sum of elastic and viscous force, Eq. (11.92)) vanishes. If the rms value of elastic force and viscous force become of the same order of magnitude, the detachment will occur in almost all points with a negative surface gradient, thus, a one-sided detachment of the elastomer from the indenter will take place. Characteristic rms values of three terms in Eq. (11.92) are proportional to Gd, Gh, and $\eta v \nabla z$. If the indentation depth is much larger than the roughness of the profile, $d \gg h$, then the condition for one-sided detachment of the elastomer from the indenter reads $Gd \approx \eta v \nabla z$ or

$$d \big/ (\tau v \nabla z) \approx 1. \tag{11.99}$$

In that case, the friction coefficient achieves an approximately constant value of

$$\mu \approx \sqrt{2} \nabla z. \tag{11.100}$$

Details of a derivation of this result can be found in [4].

For the macroscopic power law shape (11.88), the indentation depth and contact radius are given by

$$a = \left(\frac{F_N (n+1)}{8 G c_n n} \right)^{\frac{1}{n+1}}, \; d = \left(\frac{F_N (n+1) c_n^{1/n}}{8 G n} \right)^{\frac{1}{n+1}}, \tag{11.101}$$

which follows from (Eq. (3.20) and (3.24)). Substituting the contact length $L_{\text{cont}} = 2a$ into Eq. (11.98), we obtain the coefficient of friction at low velocities:

$$\tilde{\mu} = \xi, \tag{11.102}$$

where we introduced dimensionless variables

$$\tilde{\mu} = \frac{\mu}{\sqrt{2} \nabla z}, \; \xi = \frac{v \tau \nabla z}{\sqrt{2}} \left(\frac{8G}{F_N} \right)^{\frac{n}{n+1}} \left(\frac{n+1}{c_n n} \right)^{\frac{n}{n+1}}. \tag{11.103}$$

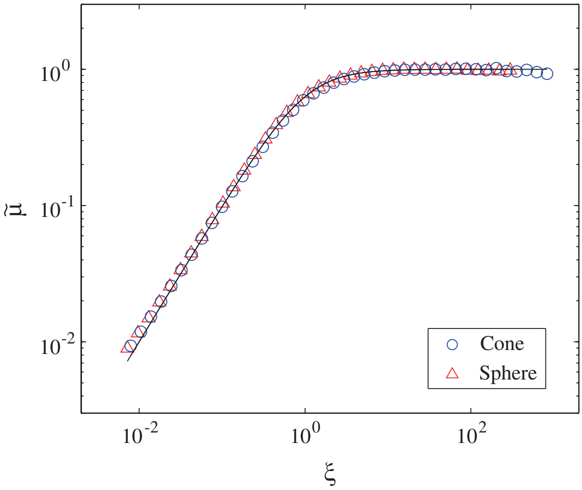

Fig. 11.13 Dependence of $\tilde{\mu}$ on ξ for conical indenter and parabolic indenter. The solid line corresponds to the analytical approximation (11.104) with $\alpha = 1.5$. *Source* [5]

It is easily seen that we can get both limits (11.102) and (11.100) by writing

$$\frac{\mu}{\sqrt{2}\nabla z} = \left(1 + \xi^{-\alpha}\right)^{-1/\alpha}, \tag{11.104}$$

where α is a dimensionless fitting parameter. Numerical simulations carried out in [5] show that the best fit is achieved with $\alpha = 1.5$ independently on the macroscopic shape of the indenter (see Fig. 11.13). This generalized law of friction describes dependence of the frictional force on velocity, normal force, and material parameters.

References

1. V.L. Popov, *Contact Mechanics and Friction, Physical Principles and Applications* (Springer, Berlin, 2010), p. 362
2. S. Kürschner, Friction between a rigid body and a model elastomer having a linear viscous rheology. ZAMM—Z. Angew. Math. Mech, 1–9 (2014) doi:10.1002/zamm.201300300
3. B.N.J. Persson, Theory of rubber friction and contact mechanics. J. Chem. Phys. **115**, 3840–3861 (2001)
4. Q. Li, M. Popov, A. Dimaki, A.E. Filippov, S. Kürschner, V.L. Popov, Friction between a viscoelastic body and a rigid surface with random self-affine roughness. Phys. Rev. Lett. **111**(5), 034301 (2013)
5. V.L. Popov, L. Voll, Q. Li, Y.S. Chai, M. Popov, Generalized law of friction between elastomers and differently shaped rough bodies. Sci. Rep. **4**, 3750 (2014). doi:10.1038/srep03750

Chapter 12
Frictional Damping

Elena Teidelt, Valentin L. Popov and Markus Heß

12.1 Introduction

Friction is a dissipative process, in which mechanical energy is transformed into heat. This can be both unwanted as well as purposefully taken advantage of. Even at very small amplitudes of tangential oscillations, the small slip displacements at the border of the contact area always lead to energy dissipation. This effect is the physical mechanism of damping in periodically forced frictionally engaged joints, for example, in leaf springs for commercial and transportation vehicles. Similar effects are generally exhibited in all frictionally engaged joints and are, therefore, of great interest. For the investigation of damping caused by dry friction, a dynamic tangential contact is of interest. The exact coincidence of the frictional damping in a true three-dimensional contact and its one-dimensional representation in the framework of the method of dimensionality reduction follows from general theorems concerning tangential contacts. This chapter is an illustration how the use of the MDR makes dynamic tangential problems simple without loss of exactness.

12.2 Damping by Dry Friction

In the following, a dynamic tangential contact is considered, the movement of which is damped by Coulomb friction. An elastic parabolic indenter is loaded with the normal force F_N and oscillates subsequently in the tangential direction. As discussed in Chap. 5, this problem can be mapped to an equivalent one-dimensional problem. In this equivalent problem, all elements are considered independently of one another. We can, therefore, begin with the energy dissipation of a single element, as illustrated in Fig. 12.1. Afterwards, the results will be generalized to the entire system.

V.L. Popov and M. Heß, *Method of Dimensionality Reduction in Contact Mechanics and Friction*, DOI 10.1007/978-3-642-53876-6_12

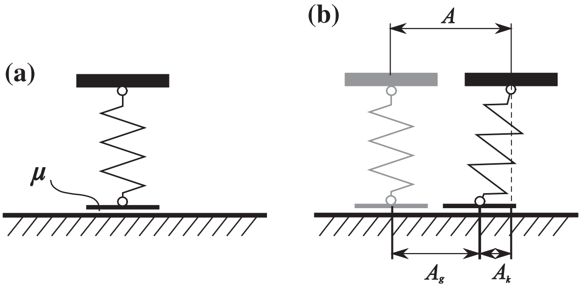

Fig. 12.1 (**a**) Contact of a spring with a rigid substrate. (**b**) The top of the spring is moved from the original position to the right by a distance of A

Let the spring be compressed in the vertical direction by u_z. It possesses a normal spring stiffness of $k_z = E^* \Delta x$ (see Eq. (3.5)) and a tangential spring stiffness of $k_x = G^* \Delta x$ (see Eq. (5.4)). If the top of the spring is moved to the side by A, then the bottom of the spring remains in a state of stick as long as the spring force in the tangential direction is smaller than the maximum force of static friction:

$$F_x = k_x A < \mu F_N = \mu k_z u_z. \tag{12.1}$$

The critical value of the displacement is

$$A_k = \mu \frac{k_z}{k_x} u_z = \mu \kappa u_z, \tag{12.2}$$

where we have introduced the constant κ:

$$\kappa := \frac{k_z}{k_x} = \frac{E^*}{G^*} = \frac{2-\nu}{2(1-\nu)}. \tag{12.3}$$

If A is larger than the critical value $A > A_k$, then the bottom of the spring remains in a state of stick until the critical displacement is achieved and slips for the remainder of the distance $A_g = A - A_k$. The work done by the frictional force is then

$$W = (A - A_k)\mu k_z u_z. \tag{12.4}$$

Now, we consider an oscillating spring having a peak-to-peak amplitude of $2A$. If the top of the spring is brought back by this amplitude, then the bottom of the spring sticks until the top has moved by a distance of $2A_k$ and then slips a distance of $2A - 2A_k$ (see Fig. 12.2).

In further oscillations, this distance always remains the same and is traversed two times per period. Therefore, the frictional work done per period for a cyclical movement is

$$W_{cycle} = 4(A - A_k)\mu k_z u_z. \tag{12.5}$$

Now, we consider a system of independent springs. The critical amplitude for a spring with the coordinate x is given by

$$A_k(x) = \mu u_z(x)\kappa. \tag{12.6}$$

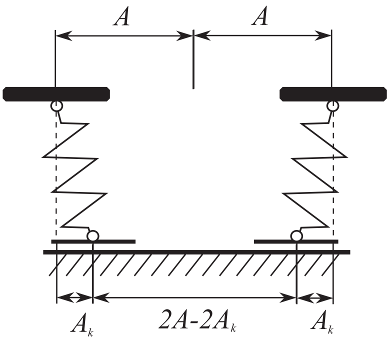

Fig. 12.2 The slip movement of a periodically oscillating frictional contact

The work of the frictional contact during one period for a cyclical movement with the amplitude $2A$ is

$$\Delta W(x) = 4(A - A_k(x))\mu u_z(x) \cdot k_z = 4\mu E^*(A - \mu\kappa u_z(x))u_z(x)\Delta x. \quad (12.7)$$

Within the framework of the method of dimensionality reduction, a parabolic indenter with the profile $\tilde{z} = r^2/(2R)$ is replaced with the profile $\tilde{z} = x^2/R$. If the indentation depth of the indenter is equal to d, then the spring with the coordinate x is indented by

$$u_z(x) = d - \frac{x^2}{R}. \quad (12.8)$$

Therefore, the work of the frictional contact of one spring is

$$\Delta W(x) = 4\mu E^*\left(A - \mu\kappa\left(d - \frac{x^2}{R}\right)\right)\left(d - \frac{x^2}{R}\right)\Delta x. \quad (12.9)$$

The entire energy dissipated during one period is then the integral over the slip domain in the contact:

$$W = 2\int_c^a 4\mu E^*\left(A - \mu\kappa\left(d - \frac{x^2}{R}\right)\right)\left(d - \frac{x^2}{R}\right)\mathrm{d}x. \quad (12.10)$$

The geometric relation $a = \sqrt{Rd}$ is valid for the outer radius of the contact. The lower boundary of the integral is determined by the springs that are in the stick state exactly at their maximum displacement: $\mu k_z u_z(c) = Ak_x$. Therefore, by using Eq. (12.8), we obtain $c = \sqrt{Rd - AR/(\mu\kappa)}$. The entire work done is then calculated as

$$W = 8E^*R^{1/2}\kappa^{-3/2}\mu^{-1/2}\begin{pmatrix} A_{k0}(A - A_{k0})\left((A_{k0})^{1/2} - (A_{k0} - A)^{1/2}\right) \\ +\frac{1}{3}(2A_{k0} - A)\left((A_{k0})^{3/2} - (A_{k0} - A)^{3/2}\right) \\ -\frac{1}{5}\left((A_{k0})^{5/2} - (A_{k0} - A)^{5/2}\right) \end{pmatrix}, \quad (12.11)$$

with $A_{k0} = \mu\kappa d$. If the oscillation amplitudes are small, then the equation can be converted to a Taylor series:

$$W = 8E^* R^{1/2} \kappa^{-3/2} \mu^{-1/2} A_{k0}^{5/2} \left(\frac{1}{12} \left(\frac{A}{A_{k0}} \right)^3 + \frac{1}{48} \left(\frac{A}{A_{k0}} \right)^4 + \frac{3}{320} \left(\frac{A}{A_{k0}} \right)^5 \right). \tag{12.12}$$

The leading term of this series is

$$W \approx \frac{2}{3} \kappa^{-2} E^* R^{1/2} \mu^{-1} d^{-1/2} A^3, \tag{12.13}$$

which corresponds *exactly* to the results from Mindlin et al. [1].

12.3 Damping of Elastomers for Normal Oscillations

In elastomers, energy is also dissipated for the vertical oscillation of contact partners. We consider an axially-symmetric indenter that is pressed into an elastomer to a depth of d by an average normal force of F_N so that the (static) contact radius a is formed. If the indenter is now moved according to a harmonic law

$$d = d_0 + A \cos \omega t = d_0 + \frac{A}{2} \left(e^{i\omega t} + e^{-i\omega t} \right) \tag{12.14}$$

with a small amplitude A, then this movement leads to energy dissipation. Within the framework of the reduction method, a contact with a diameter of $2a$ is replaced by a contact with a viscoelastic foundation having a length of $L = 2a$ using Eq. (7.29):

$$f_N(t) = 4\Delta x \int_0^t G(t - t') \dot{u}_z(t') \mathrm{d}t'. \tag{12.15}$$

The oscillation of an element of the form $u_1 = (A/2)e^{i\omega t}$ leads to the force $f_1 = 4G(\omega) \cdot \Delta x \cdot u_1$ and an oscillation of the form $u_2 = (A/2)e^{-i\omega t}$ leads to the force $f_2 = 4G(-\omega) \cdot \Delta x \cdot u_2$. Due to linearity, an oscillation of

$$\Delta d(t) = \frac{A}{2} \left(e^{i\omega t} + e^{-i\omega t} \right) = u_1 + u_2 \tag{12.16}$$

leads to the force

$$f_N = f_1 + f_2 = 2A \cdot \Delta x \cdot \left(G(\omega) e^{i\omega t} + G(-\omega) e^{-i\omega t} \right). \tag{12.17}$$

The average power of this force averaged over one period is equal to

$$\Delta P = \langle f_N \cdot \Delta \dot{d} \rangle = \left\langle 2A \cdot \Delta x \cdot \left(G(\omega) e^{i\omega t} + G(-\omega) e^{-i\omega t} \right) \frac{A}{2} \left(i\omega e^{i\omega t} - i\omega e^{-i\omega t} \right) \right\rangle, \tag{12.18}$$

and yields

$$\Delta P = i\omega A^2 \cdot \Delta x \cdot (-G(\omega) + G(-\omega)). \tag{12.19}$$

By writing the complex shear modulus in the form

$$G(\omega) = G'(\omega) + iG''(\omega) \tag{12.20}$$

and taking into account that $G'(-\omega) = G'(\omega)$ and $G''(-\omega) = -G''(\omega)$, we obtain the average energy dissipation power of one spring:

$$\Delta P = 2\omega A^2 G''(\omega) \cdot \Delta x. \tag{12.21}$$

The dissipation power in the entire contact area is then

$$P = 2\omega A^2 G''(\omega) L = 4\omega A^2 G''(\omega) a. \tag{12.22}$$

12.4 Problems

Problem 1 Determine the attenuation behavior of the horizontal oscillation of a mass, the movement of which is impeded by a frictionally engaged joint with a sphere (see Fig. 12.3). The initial displacement of the mass is $A(0) = A_0$.

Solution In principle, we are dealing with an oscillator with frictional damping. For a harmonic oscillation, the total energy is equal to the maximum potential energy:

$$U = \frac{k_x A^2}{2}, \tag{12.23}$$

where A is the amplitude of the oscillation. The change in this energy during one period $T = 2\pi/\omega$ is equal to the work done by the frictional dissipation (see Eq. (12.13)):

$$\Delta U = -\frac{2}{3}\kappa^{-2} E^* R^{1/2} \mu^{-1} d^{-1/2} A^3. \tag{12.24}$$

Fig. 12.3 Spherical contact between an elastic sphere and a rigid mass *m*

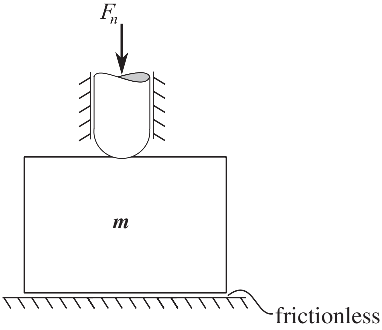

Fig. 12.4 The dependence of amplitude with respect to time

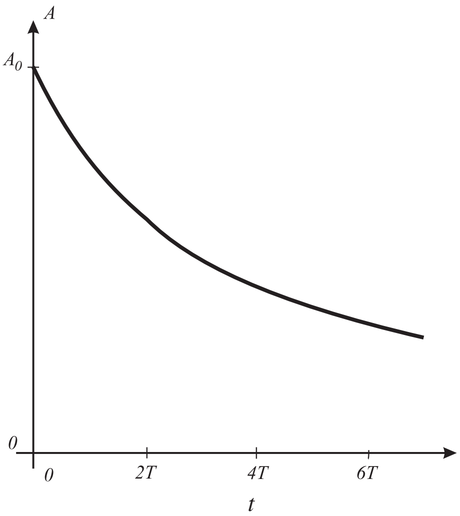

The change in potential energy per unit time is then

$$\frac{dU}{dt} = \frac{\Delta U}{T} = -\frac{1}{T}\frac{2}{3}\kappa^{-2} \cdot E^* R^{1/2} \mu^{-1} d^{-1/2} A^3. \tag{12.25}$$

Rearranged with respect to the amplitude and assuming that $k_x = G^* 2\sqrt{Rd}$ (see Eq. (5.1)), the differential equation reads

$$\frac{dA}{dt} = -\frac{1}{3}\frac{A^2}{\kappa T \mu d}. \tag{12.26}$$

The solution to this differential equation with the initial condition $A(0) = A_0$ is

$$A = \frac{A_0}{1 + \frac{1}{3}\frac{A_0}{\kappa T \mu d} t}. \tag{12.27}$$

For an amplitude at which complete slip is first exhibited ($A_0 \approx A_{k0} = \mu \kappa d$), the following is valid:

$$A = \frac{A_0}{1 + \frac{1}{3T} t}. \tag{12.28}$$

The attenuation behavior of the amplitude per period is presented schematically in Fig. 12.4. It is clear that the oscillations are only slowly (according to a power law) damped by dry friction. This means that it is recommended to integrate a further damping mechanism into vibration sensitive systems.

Reference

1. R.D. Mindlin, W.P. Mason, J.F. Osmer, H. Deresiewicz, Effects of an oscillation tangential force on the contact surfaces of elastic spheres, in *Prof. 1st US National Congress of Applied Mechanics*, vol. 227 (ASME, New York, 1952), pp. 203–208

Chapter 13
The Coupling to Macroscopic Dynamics

Elena Teidelt, Valentin L. Popov and Markus Heß

13.1 Introduction

In practical applications, mechanical models are frequently considered in which macroscopic frictional contacts are present. The typical procedure used to describe frictional contacts is to formulate a suitable law of friction, which is then subsequently applied in a macroscopic simulation of the system dynamics. However, it is often difficult to formulate a useable law of friction, as the frictional force is not only a function of the instantaneous state of motion of the system, but is also dependent on the previous history of the system motion. Here, the method of dimensionality reduction opens up a new path: The simulations using the reduction method are carried out so quickly that one can completely forego the previous formulation of the frictional law. The calculation of the contact and frictional forces is then carried out directly within the framework of the macroscopic simulation of the system dynamics. Models that combine both the macrosimulations and microsimulations into one are termed hybrid models in the following. In this chapter, it will be explained how the method of dimensionality reduction is used for formulation of hybrid models.

13.2 Hybrid Models: Foregoing the Formulation of an Explicit Law of Friction

Existing laws of friction are as different and numerous as the various applications of frictional processes. The most well-known, and also the most universal, law of friction is Coulomb's lawof dry friction, which says that the frictional force is linearly proportional to the normal force by a prefactor known as thecoefficient of friction μ. However, even Coulomb was aware of the fact that the coefficient of

V.L. Popov and M. Heß, *Method of Dimensionality Reduction in Contact Mechanics and Friction*, DOI 10.1007/978-3-642-53876-6_13

friction is in no way constant, but rather increases with contact time and is also dependent on the sliding velocity. Many other factors, such as the roughness, temperature, and Stribeck effects must be taken into account in a more exact model. Especially in dynamic processes, where one or more of the above named factors may change with respect to time, it has been essential until now to formulate an explicit law of friction and implement this law in the dynamic (numerical) modeling. For instance, frequently used frictional relationships are the Dieterichlaw of friction [1, 2], often used to describe tectonic friction, or the so-called elasto–plastic model [3, 4], used to describe the friction in stick-slip micro-drives, just to name a few. Moreover, the Prandtl–Tomlinson model (orginal publication see [5] and its English translation [6]) is also worth mentioning. It is used, among other things, to describe the friction on the tip of an atomic force microscope. Most of these models required several empirical or material-dependent parameters and, nevertheless, do not lead to the desired results for dynamic simulations.

Characteristic properties, such as "preliminary slip" (a displacement before complete slip begins) as well as velocity and state dependence of the frictional force may be described by the above friction laws. According to these laws, this behavior is a product of surface roughness and the resulting micro-slip areas. This microscopic picture of the contact, however, is almost always used only in a "conceptual sense": The exact contact mechanics is not considered, which has not been possible until now, as no effective simulation methods exist for the calculation of the contacts between rough surfaces. However, the consideration of real microscopic contacts is essential and results in the correct description of frictional forces and the formulation of a realistic law of friction without the countless adjustment parameters for every special case. The reduction method offers the tool with which this can be accomplished. In this chapter, we will show that using this method, relatively complicated dynamic behavior can be described without adjustment parameters of any kind.

The general procedure for developing a hybrid model is described in the following. First, a dynamic model is developed that describes the considered system. Contact and frictional forces, which are dependent on contact area as well as time, are part of the equations of motion. The macroscopic model is now coupled to the microscopic contact model. The microscopic part of the model describes the frictional force using the reduction method, which is obtained from the time-dependent spring forces. Due to the one-dimensionality and the independence of the degrees of freedom in the reduction method, the calculation of the contact and frictional forces is carried out so fast that it can be conducted for every time step in the macroscopic simulation of the system dynamics.

Now, we consider a single macroscopic contact (either smooth or rough). Let N be the number of springs in the contact. Every spring exhibits an individual deformation in both the vertical $u_{z,i}$ and horizontal $u_{x,i}$ directions at every point in time t, with $\mathrm{i} = 1, \ldots, \mathrm{N}$. With this, each spring is subjected to a force component in both the horizontal and vertical direction according to Eqs. (3.9) and (5.8):

$$\begin{aligned} f_{z,i} &= \Delta k_z u_{z,i} \\ f_{x,i} &= \Delta k_x u_{x,i}. \end{aligned} \tag{13.1}$$

Noteworthy is the fact that even if Coulomb's law of friction with a constant coefficient of friction is assumed on the microscale, the macroscopic behavior can be much more complicated. In this chapter, we constrict ourselves to the consideration of the simplest law from Coulomb *on the microscale*: Movement of a spring occurs only after the tangential force $f_{x,i} = \Delta k_x u_{x,i}$ surpasses a threshold

$$f_{x,i} = \mu f_{z,i}. \tag{13.2}$$

Afterwards, the spring slips and sticks again in a new state in which

$$u_{x,i} = \mu \frac{f_{z,i}}{\Delta k_x} = \mu \frac{E^*}{G^*} u_{z,i}. \tag{13.3}$$

The total frictional force in every time step can be determined with

$$F_r = \sum_{i=1}^{N} f_{x,i}. \tag{13.4}$$

A link between this calculation and the macroscopic simulation is shown schematically in Fig. 13.1.

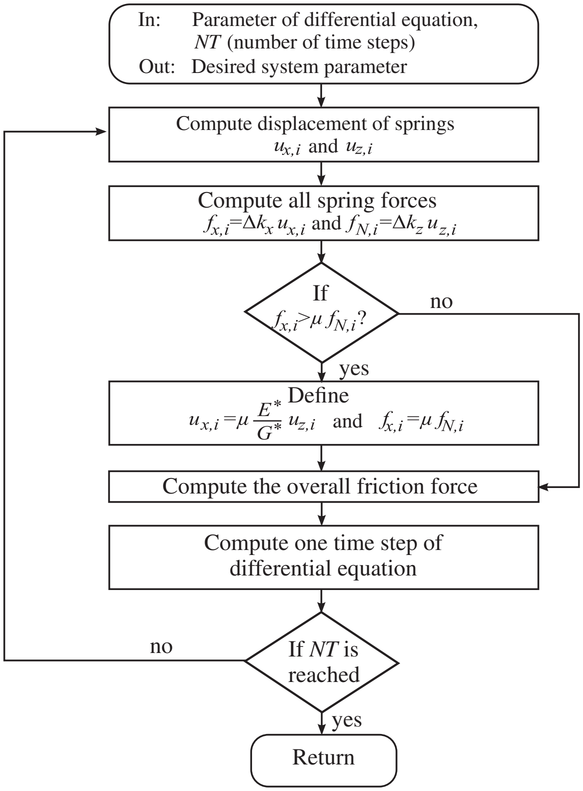

Fig. 13.1 A possible algorithm for implementing the reduction method in a dynamic contact without an explicit law of friction

Let it be once again noted that the macroscopic law of friction that results from the dynamic simulation is *not* Coulomb's simple law of friction, even if this law is assumed on the microscale. In particular, it will exhibit a "preliminary slip" and energy dissipation before the onset of macroscopic sliding. In the following section, the procedure described here will be explained using the simulation of an existing stick–slip micro-drive that has already been experimentally investigated.

13.3 Simulation of a Micro-Drive

Stick–slip micro-drives serve to move objects using an asymmetric, periodic excitation. In Fig. 13.2a and b, one such conveyor is presented schematically. The main part of the setup is a steel runner with a mass of m mounted between six actuators in the form of ruby hemispheres. These ruby hemispheres, mounted onto piezoelectric elements, oscillate as shown in Fig. 13.2c synchronously with an amplitude following a saw-tooth curve. In the slow forwards motion, the actuator sticks to the runner; in the quick backwards motion, the actuator slips (partially). In this way, a motion is achieved in the x-direction. For the micro-drive described here, the runner is pressed into the force sensor during the forward motion. This micro-drive has been investigated in detail experimentally and numerically with the explicitly formulated empirical law of friction in [7, 8]. In the following, however, the actuator contacts are simulated using the reduction method and the general motion of the runner is determined using a simple Euler method.

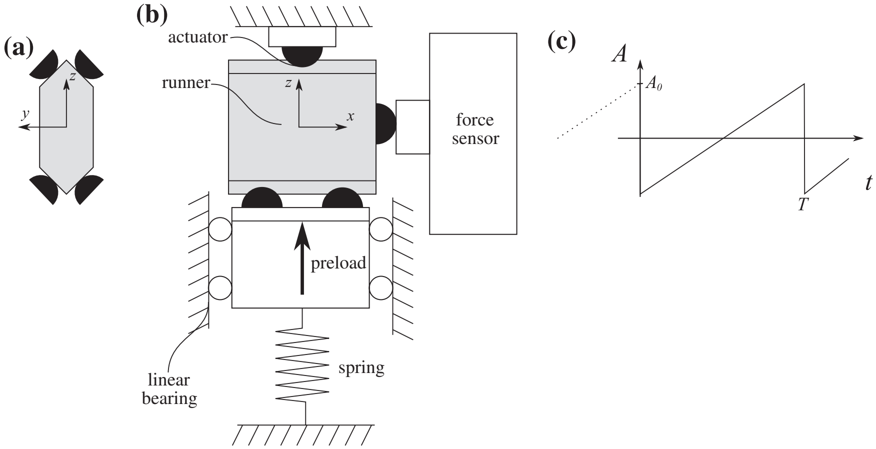

Fig. 13.2 (**a**) Top view of the cross-section of the runner with the actuators. (**b**) Side view of the runner. (**c**) Saw-toothed excitation signal for the actuators

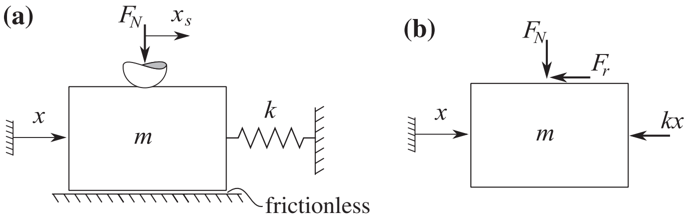

Fig. 13.3 (**a**) Stick–slip micro-drive with only one actuator. (**b**) Free-body diagram of the runner

13.3.1 Creating a Macroscopic Model

For a better understanding, let it be initially assumed that we are dealing with a runner being excited by only one actuator (see Fig. 13.3).

Using Newton's second law and assuming that the runner can only move in the x-direction, we obtain

$$m\ddot{x} = -kx + F_r(t). \tag{13.5}$$

The force sensor is shown as a linear spring with the stiffness k. The frictional force is brought about by the actuator and changes with respect to its displacement.

13.3.2 Creating a Microscopic Model

The actuator is described as being a tangential contact with a parabolic body according to Sect. 5.2. The frictional force found in Eq. (13.5) is then the sum of the individual spring forces. The linearly elastic foundation contains N individual springs. Then, we obtain

$$F_r(t) = \sum_{i=1}^{N} f_{x,i}(t). \tag{13.6}$$

First, the deformations of the springs, must be determined at an arbitrary time t. This deformation is the difference between the displacement of the runner and the movement of the actuator based on the saw-tooth function $x_s\,(t)$:

$$u_{x,i}(t) = x(t) - x_s(t). \tag{13.7}$$

The individual springs can be in either a state of stick or one of slip, depending on whether or not the stick criterion $\mu f_z > f_x$ is met. The springs in a state of slip will stick in a new equilibrium position. The displacements of the springs are calculated as

$$u_{x,i}(t) = \begin{cases} x - x_s & \text{stick} \\ \frac{\mu f_{z,i}}{\Delta k_x} & \text{slip} \end{cases}. \tag{13.8}$$

Table 13.1 Material and geometric data used for the numerical simulation

Young's modulus of steel E_1	200 GPa
Young's modulus of ruby E_2	370 GPa
Poisson's ratio ν_1, ν_2	0.3
Coefficient of friction μ	0.3
Radius of ruby hemisphere	0.5 mm
Mass of the runner m	3 g

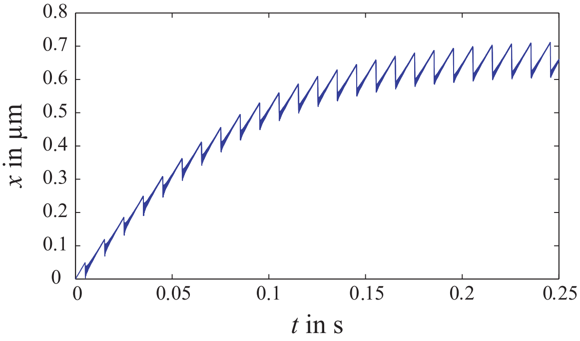

Fig. 13.4 Motion of the runner with respect to time

With Eqs. (13.1) and (13.7), the frictional force can now be determined. If an iterative technique is used to solve the differential equation, such as the Euler method or Runge–Kutta method, then the frictional force must be determined anew for every time step. By direct modeling of the contact, the continuously changing properties can now be simulated. In particular, both the effect of damping by the dry friction and the appearance of the so-called 0-amplitude result in a natural way from the dynamic simulation. The 0-amplitude is the maximum amplitude of the saw-tooth function at which the runner does not move despite the excitation. The extensive details to the implementation and the results of the simulation can be found in [9]. Here, only example results will be demonstrated. The material parameters used are shown in Table 13.1.

In Fig. 13.4, the traveled distance is shown as a function of time for one actuator with a preloading force of $F_N = 0.1$ N and an amplitude for the saw-tooth function of $A_0 = 100$ nm.

Two effects may be seen: First, the step-wise forward movement of the runner. In the slip phase, the quick backwards movement of the actuator also causes the runner to reverse its course. The following stick phase is superimposed with an oscillation around the overall displacement. The damping of this vibration is described very well by Coulomb's damping (Problem 1 in Chap. 12). Furthermore, it is able to be seen that the runner reaches a saturation position. This can be explained by the fact that the displacement of the runner by the actuator is in equilibrium with the opposing force of the spring of the force sensor. The force produced, corresponding to the average maximum displacement, is denoted as F_{gen}.

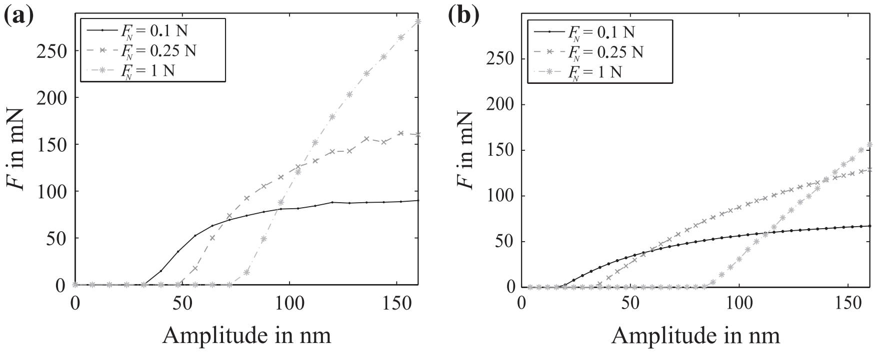

Fig. 13.5 (**a**) Experimental dependence of the force generated with respect to the amplitude. (**b**) Numerical dependence of the force generated with respect to the amplitude

For the purpose of comparison, experimental data for the force F_{gen} as a function of the saw-tooth amplitude for three different normal forces are shown in Fig. 13.5a. The numerical data are produced using a model with six actuators. Once again, two effects are seen: on the one hand, the 0-amplitude can be easily seen as the amplitude for which no generated force can be detected. This amplitude of the saw-tooth function is roughly interpreted as the displacement of a classical tangential contact for which slip is not yet exhibited, $u_{x,\max}$ according to Eq. (5.17). Of course, the 0-amplitude increases with increasing normal force. Secondly, it can be noticed that for large amplitudes, a saturated force level develops.

Let it be noted that in the comparison between the numerical and experimental values, *no adjustment parameter* was used. A discrepancy can be seen in the 0-amplitude. Although, the general forms are similar, the numerically calculated amplitudes are smaller than those experimentally measured. This is due to the fact that only simplified smooth excitation spheres were simulated. Taking the roughness into account, however, is not a problem when using the method of dimensionality reduction and the discrepancies are eliminated. In summary, let it be stressed that the reduction method offers an efficient and simple way to describe dynamic systems without an explicit law of friction.

13.4 Problems

Problem 1 Develop an algorithm to implement the equation of motion of the mass m for the model in Fig. 13.6, consisting of a body with a spherical profile of radius R, Young's modulus E, and Poison's ratio ν. Keep in mind that the normal force changes with respect to time: $F_N(t) = F_{N,0} + \Delta F_N \cos \omega t$. Furthermore,

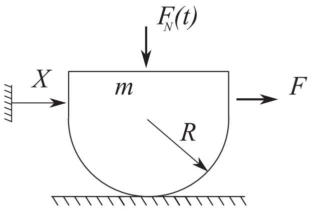

Fig. 13.6 Model for a point mass with a circular contact surface

the coefficient of friction μ is valid on the microscale. Proceed analogously to the hybrid model presented above.

Solution The *macroscopic model* is obtained from Newton's second law. It reads

$$m\ddot{X} = F - F_r. \tag{13.9}$$

Due to the fact that the normal force varies with respect to time, this is implicitly valid also for the frictional force F_r. *Microscopically*, the frictional force and the contact area can be described by the reduction method as follows: From the normal force $F_N(t) = F_{N,0} + \Delta F_N \cos \omega t$, the indentation depth of the sphere can be determined, and from this, the individual spring deformations in the horizontal and vertical directions $u_{x,i}$ and $u_{z,i}$ can be found. For these, we obtain

$$\begin{aligned} d &= \left(\frac{3}{4}\frac{FN(t)}{E^*\sqrt{R}}\right)^{\frac{2}{3}} \\ u_{x,i}(t+\Delta t) &= u_{x,i}(t) + \mathrm{d}X \\ u_{z,i} &= d - \frac{x_i^2}{R}. \end{aligned} \tag{13.10}$$

Here, dX is the distance that the mass travels forward during one time step and x_i are the coordinates of the individual springs with respect to the middle of the contact. The radius in the one-dimensional model is divided by two according to the procedure of the reduction method. The normal force in every individual spring is then $f_{z,i} = \Delta k_z u_{z,i}$. Whether a particular spring is currently in stick or slip state is determined from the stick condition $f_{z,i} = \mu f_{z,i}$. If the frictional force $f_{x,i} = \Delta k_x u_{x,i}$ is larger than that from the stick condition, a new spring deformation must be calculated $u_{x,i} = \mu f_{z,i}/\Delta k_x$. The total frictional force is the sum of the spring forces:

$$F_r = \sum_{i=1}^{N} f_{x,i}, \tag{13.11}$$

Fig. 13.7 Algorithm for calculating the differential Eq. (13.9)

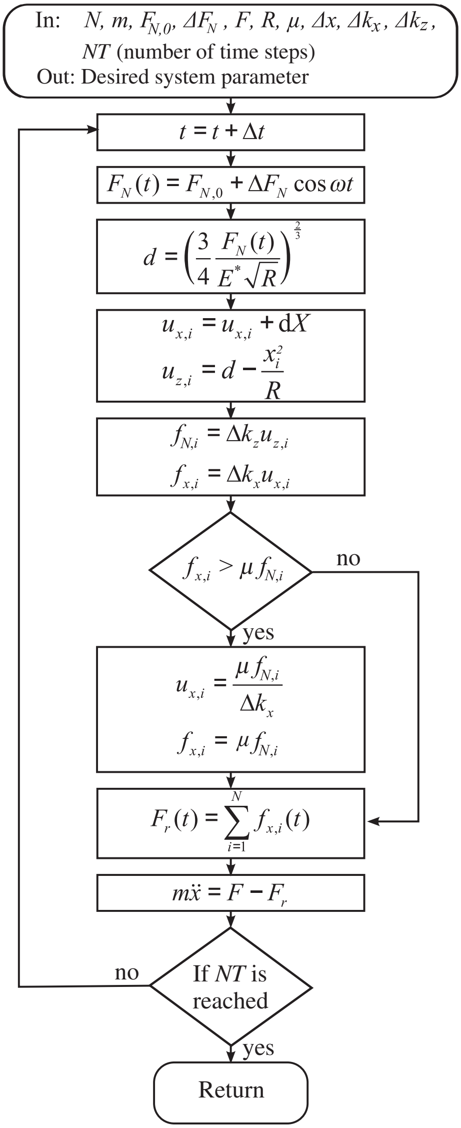

where N is the total number of springs. The adapted algorithm from Fig. 13.1, would then be as Fig. 13.7.

References

1. J.H. Dieterich, Modeling of rock friction: 1. Experimental results and constitutive equations. J. Geophys. Res. **84**, 2161 (1979)
2. A. Ruina, Slip instability and state variable friction laws. J. Geophys. Res. **88**, 10359 (1983)
3. P. Dupont, V. Hayward, B. Armstrong, F. Altpeter, Single state elastoplastic friction models. IEEE Trans. Autom. Control **47**, 787–792 (2002)
4. P. Dupont, B. Armstrong, V. Hayward, Elasto-plastic friction model: contact compliance and stiction, in *Proceedings of the American control conference*, vol. 2, pp. 1072–1077 (2000)
5. L. Prandtl, Ein Gedankenmodell zur kinetischen Theorie der festen Körper. ZAMM—Zeitschrift für Angewandte Mathematik und Mechanik **8**, 85–106 (1928)
6. V.L. Popov, J.A.T. Gray, Prandtl-Tomlinson Model: History and applications in friction, plasticity, and nanotechnologies. ZAMM—Zeitschrift für Angewandte Mathematik und Mechanik **92**, 683–708 (2012)
7. C. Edeler, Modellierung und Validierung der Krafterzeugung mit Stick-Slip-Antrieben für nanorobotische Anwendungen (2011)
8. C. Edeler, I. Meyer, S. Fatikow, Modeling of stick-slip micro-drives. J. Micro-Nano Mechatron. (2011). doi:10.1007/s12213-011-0034-9
9. E. Teidelt, E. Willert, A.E. Filippov, V.L. Popov, Modeling of the dynamic contact in stick-slip microdrives using the method of reduction of dimensionality. Phys. Mesomech. **15**(5–6), 287–292 (2012)

Chapter 14
Acoustic Emission in Rolling Contacts

Mikhail Popov, Justus Benad, Valentin L. Popov and Markus Heß

14.1 Introduction

Technical surfaces typically have roughness ranging from the size of the system to the nanometer scale. During sliding or rolling on rough surfaces, vibration occurs that results in audible and inaudible acoustic emission. In 2006 Ford und Thompson [1] used a one-dimensional model for the analysis of the acoustic emission of a rolling wheel. This model was identical to the method of dimensionality reduction, although Ford and Thompson chose to call it two-dimensional. They compared the results obtained with the one-dimensional model with results of boundary element simulations and found very good agreement in the entire spectral range. They came to the conclusion that the 1D-model "might have an unexpectedly wide range of applicability."

The method of dimensionality reduction can be applied not only for analysis of mean values of forces but also of their fluctuations. This is confirmed by the results shown in Fig. 14.1. This figure shows the results of simulations in which a rigid indenter with random self-affine roughness (with Hurst exponents ranging from $H = 0.4$ to $H = 1$) was pressed into an elastic half-space. The three-dimensional calculations were performed with the boundary element method. 60 random surfaces were generated and the mean values as well as the standard deviation of the contact stiffness were computed for each normal force. The same calculation was performed with the equivalent one-dimensional model for 500 random realizations. The comparison of the results shows very similar behavior of the standard deviation in both the three-dimensional and one-dimensional model. Because the rolling or sliding motion continuously brings new parts of the surfaces into contact, this can be interpreted as contacts with different random realizations of the roughness. This suggests that the one-dimensional model can describe the dynamic behavior of rolling contacts.

V.L. Popov and M. Heß, *Method of Dimensionality Reduction in Contact Mechanics and Friction*, DOI 10.1007/978-3-642-53876-6_14

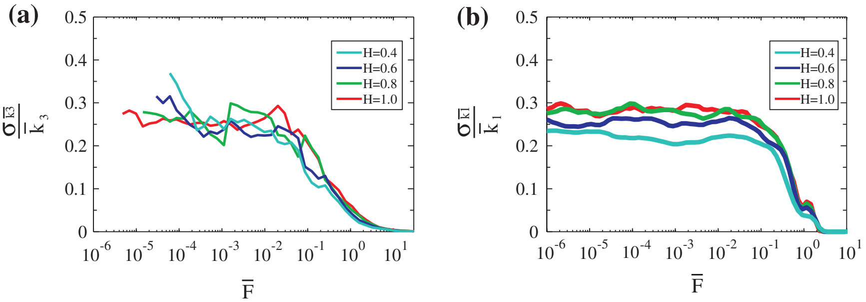

Fig. 14.1 (**a**) Relative standard deviation of the stiffness as a function of normal force for 60 realizations of three-dimensional boundary element simulations, as presented in [2]. (**b**) Relative standard deviation in the one-dimensional case, computed with 500 realizations. Data provided by R. Pohrt

In this chapter, the force fluctuations due to surface roughness of the contacting bodies will be investigated using the method of dimensionality reduction.

14.2 Acoustic Emission Resulting from the Rolling of a Wheel—An Analytical Solution

The system under consideration is a cylindrical steel wheel with a radius R and mass m that is loaded with a constant normal force F_N and is rolling on a steel rail with a velocity v_0. The rail is assumed to have the same transverse radius of curvature such that the entire problem can be reduced to the rolling of a sphere with a radius R on a half-space. The wheel and the rail both have surface roughness that can be characterized by an isotropic power spectrum. The dynamics of the wheel assembly and car structure is not considered here and is only represented through the constant normal force. Thus, we obtain our model which will be studied numerically and analytically in the following: An elastic, rough sphere rolls on a rigid, flat surface. The roughness-induced normal acceleration of the sphere is determined. This three-dimensional, dynamic contact problem is difficult to solve with traditional methods (e.g., finite elements or boundary elements) due to the extremely large computational cost. In the framework of the reduction method, however, an almost complete analytical solution is possible.

Let us consider the one-dimensional representation of the rolling wheel on a rough surface (Fig. 14.2). The form of the wheel is given by the macroscopic substitute profile

$$z = Z_0(x - \tilde{x}) \tag{14.1}$$

with

$$Z_0(x) = \frac{x^2}{R}, \tag{14.2}$$

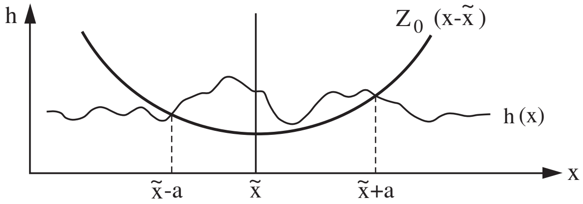

Fig. 14.2 One-dimensional representation of the rolling wheel on a rough surface

where $\tilde{x}$ is the coordinate of the wheel center. The profile of the rough surface is given by

$$z = h(x). \tag{14.3}$$

The numerical analysis of this system can proceed without additional assumptions. For the analytical solution, however, we will make some additional simplifications. First we assume that the indentation depth d is much larger than the rms value of the roughness. Under this assumption, the coordinates of the left and right boundaries of the contact depend only weakly on $\tilde{x}$ and we will assume that

$$\begin{aligned} x_1 &= \tilde{x} - a, \\ x_2 &= \tilde{x} + a, \end{aligned} \tag{14.4}$$

where a is the Hertzian contact radius for the contact of a sphere with a smooth plane. We also assume that the indentation depth remains approximately constant and experiences only small deviations from its mean value. This corresponds to a constant contact radius a. The normal force is then calculated according to the rules of the reduction method as

$$F_N(\tilde{x}) = E^* \int\limits_{\tilde{x}-a}^{\tilde{x}+a} (h(x) - Z_0(x - \tilde{x}))\mathrm{d}x = E^* \int\limits_{\tilde{x}-a}^{\tilde{x}+a} h(x)\mathrm{d}x - E^* \int\limits_{\tilde{x}-a}^{\tilde{x}+a} Z_0(x - \tilde{x})\mathrm{d}x. \tag{14.5}$$

The second part of this equation does not depend on $\tilde{x}$. It follows that

$$\frac{\mathrm{d}F_N(\tilde{x})}{\mathrm{d}\tilde{x}} = E^* \left[h(\tilde{x} + a) - h(\tilde{x} - a)\right], \tag{14.6}$$

which results in

$$F_N(\tilde{x}) = E^* \int \left[h(\tilde{x} + a) - h(\tilde{x} - a)\right] d\tilde{x}. \tag{14.7}$$

Let us now assume that the rough profile is given by the customary Eq. (10.5)

$$h(x) = \sum_{q=-\pi/\Delta x}^{\pi/\Delta x} B_{1D}(q)\exp(i(qx + \phi(q))), \tag{14.8}$$

where

$$B_{1D}(q) = \sqrt{\frac{2\pi}{L} C_{1D}(q)} = \bar{B}_{1D}\,(-q), \tag{14.9}$$

the discretization step is given by $\Delta q = 2\pi/L$, and the random phases $\phi(\vec{q}) = -\phi(-\vec{q})$ are equally distributed on the interval $[0, 2\pi)$. It follows that

$$\begin{aligned} h(\tilde{x}+a) - h(\tilde{x}-a) &= \sum_{q=-\pi/\Delta x}^{\pi/\Delta x} B_{1D}(q) \exp(i(q\tilde{x} + \phi(q))) \left[\exp(iqa) - \exp(-iqa)\right] \\ &= \sum_{q=-\pi/\Delta x}^{\pi/\Delta x} 2iB_{1D}(q) \exp(i(q\tilde{x} + \phi(q))) \sin(qa) \end{aligned} \tag{14.10}$$

and

$$F_N(\tilde{x}) = E^* \sum_{q=-\pi/\Delta x}^{\pi/\Delta x} \frac{2}{q} B_{1D}(q) \sin(qa) \exp\left(i(q\tilde{x} + \phi(q))\right). \tag{14.11}$$

From this equation, we see immediately that the spectral density $C_{1D}(q)$ of the roughness and the spectral density $C_F(q)$ of the normal force are connected by the following relationship:

$$C_F(q) = \frac{4E^{*2}}{q^2} C_{1D}(q) \sin^2(qa). \tag{14.12}$$

In the case of a randomly self-affine rough surface with the spectral density $C_{2D}(q) = Aq^{-2H-2}$, the equivalent one-dimensional spectral density is given by the rule of Geike [Eq. (10.12)] as $C_{1D}(q) = \pi q C_{2D}(q) = \pi A q^{-2H-1}$. The spectral density of the force is then given by

$$C_F(q) \approx \frac{4E^{*2}}{q^2} A\pi q^{-2H-1} \sin^2(qa). \tag{14.13}$$

This dependence is shown for $H = 0.7$ in Fig. 14.3. Under the assumption that $qa \gg 1$, $\sin^2(qa)$ is a quickly oscillating function with the mean value $1/2$. Averaging over these oscillations gives

$$\langle C_F(q) \rangle = \frac{2E^{*2}}{q^2} C_{1D}(q). \tag{14.14}$$

This relation makes it possible to deduce the spectral density of the contact force from the spectral density of the roughness, and vice versa.

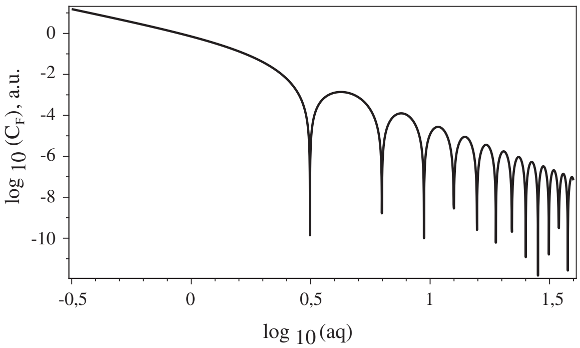

Fig. 14.3 Dependence of the power spectrum of the normal force on the wave number

14.3 Acoustic Emission Resulting from Rolling of a Wheel—A Dynamic Simulation

With the reduction method, we can easily perform full dynamic simulations of the rolling motion. In this section, we present the results of such simulations. They are also an example of the hybrid models as described in the previous chapter. The rolling of the wheel with the velocity v_0 is modelled by shifting the "spherical profile" in the positive x-direction with the velocity v_0, while the roughness profile remains stationary:

$$z(x,t) = \frac{(x - v_0 t)^2}{R} + h(x). \tag{14.15}$$

This profile is explicitly time-dependent and results in variations of the contact force F_{cont}, which in turn causes vertical motion. The equation of motion of the wheel

$$m\ddot{z}(t) = F_{cont} - F_N \tag{14.16}$$

is solved numerically, with re-computation of F_{cont} (using the reduction method) in every integration step. The time step of the dynamic simulation is set to $\Delta t = \Delta x / v_0$, so that the system moves by one spatial discretization unit during every time step. The immediate result of the dynamic simulation is the time dependence of the vertical coordinate of the wheel $z(t)$. The second derivative of the coordinate produces the normal acceleration $a(t)$. Since the acceleration is, like the roughness, a statistical quantity, we will characterize it through its spectral density, which is computed as follows:

$$A = |\mathrm{FFT}(a)|^2 \frac{\Delta t^2}{T}. \tag{14.17}$$

Here, $\mathrm{FFT}(a)$ denotes the fast Fourier transform of the acceleration, and T is the total simulation time.

Table 14.1 Parameters of the simulation

$E = 210\,\text{GPa}$	Elastic modulus of steel
$\nu = 1/3$	Poisson's number of steel
$R = 0.5\,\text{m}$	Radius of wheel
$M = 500\,\text{kg}$	Mass of wheel
$h_0 = 0.5\,\mu\text{m}$	Roughness

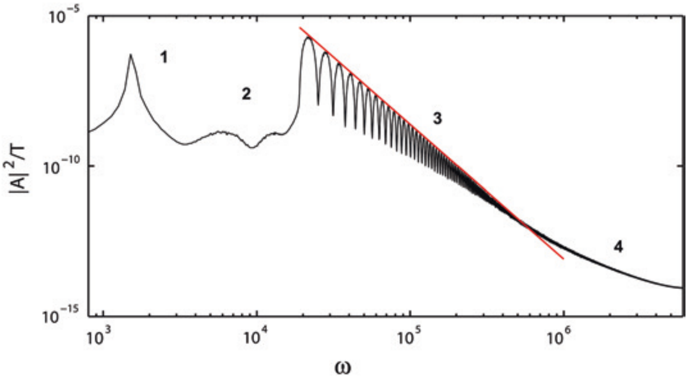

Fig. 14.4 A typical dependence of the spectral density of the acceleration on the frequency

The parameters that were used for the simulation are summarized in Table 14.1. The roughness was randomly self-affine and had the power spectrum

$$C_{1D} = const \cdot q^{-2H-1} \tag{14.18}$$

with wave numbers in the interval

$$q_{\min} < |q| < q_{\max}. \tag{14.19}$$

The constant in (14.18) was chosen such that the average roughness of the profile, defined as $h = \sqrt{\langle h(x)^2 \rangle}$, was exactly equal to h_0.

The simulation was run 300 times with different realizations of the rough profiles. The averaged result of the spectral density of the acceleration as a function of frequency is shown in Fig. 14.4.

The spectrum of the acceleration can be divided in four regions:

1. In the first region there is a sharp, quickly decaying maximum.
2. Then follows a "plateau" with an oscillating substructure.
3. There is a sharp rise at the beginning of the third region, which falls linearly in double-logarithmic coordinates. This region also shows an oscillating substructure.
4. The last region with a different slope than region 3 continues to the maximum frequency $\omega_{\max} = q_{\max} v_0$.

The third region has an oscillating substructure with a constant period of $\Delta\omega_3$ (in the frequency domain!). The origin of this region and its substructure was already explained by the above analytical treatment. The oscillation results from the factor $\sin^2(qa)$ in (14.12), where $\Delta\omega_3 = \pi/a$. The slope (in double-logarithmic axes) in region 3 is equal to $\alpha = -2H - 3$, which follows directly from Eq. (14.13).

The other regions were not predicted by the analytical treatment; they arise due to non-linearity of the system dynamics of the contact, which was neglected for the analytical calculation. Only in the direct numerical simulation do these effects become apparent.

In the following, we discuss the physical nature of the above four regions.

1. The first peak of the spectral density coincides exactly with the resonance frequency of the wheel $\omega_{eigen} = \sqrt{2aE^*/m}$. Parameter studies show that this frequency does not depend on any of $q_{\min}$, $q_{\max}$, v_0 or H. This confirms that the peak is in fact the eigen frequency of the wheel.
2. The "plateau" after the resonance peak may or may not have a substructure, depending on the parameters.
3. Power-law region.

The third region begins with a sharp rise in the power spectrum. It seems plausible to suppose that this rise is linked to the cutoff (i.e., the value of $q_{\min}$) in the assumed roughness spectrum. It turns out that the rise, and therefore the start of the third region, is indeed found at the frequency

$$\omega_{jump} = q_{\min} v_0, \tag{14.20}$$

which is directly dependent on the smallest wave number in the roughness spectrum. This relationship was confirmed by variation of both the velocity and

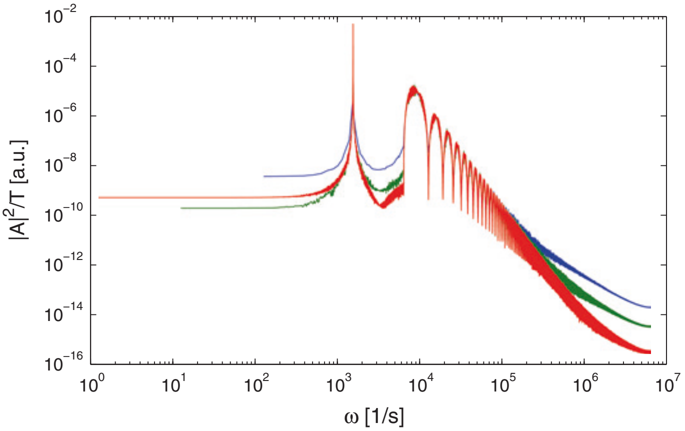

Fig. 14.5 Results of simulations with identical roughness parameters but different rolling distances, and therefore, more elements (*blue*—smallest distance, *red*—longest distance)

the cut-off wave number. At small velocities, the jump moves closer to the resonance peak, and the plateau “2” may disappear entirely.

4. “Break” in the spectral density

The third and fourth regions are separated by a “break.” The fourth region is related to the finite simulation. If the rolling of the wheel is simulated over a very long distance, the frequency of the “break” moves further to the right, and will probably disappear entirely with sufficiently long distances. This can be seen in Fig. 14.5, where the results of simulations with different rolling distances are shown. A possible explanation is that the last region is due to the spectrum of the finite “window function,” which decreases very slowly at high frequencies. In any case, region 4 seems to be an artifact of the simulation that can be reduced by using more elements.

References

1. R.A.J. Ford, D.J. Thompson, Simplified contact filters in wheel/rail noise prediction. J. Sound Vibr. **293**, 807–818 (2006)
2. R. Pohrt, V.L. Popov, A.E. Filippov, Normal contact stiffness of elastic solids with fractal rough surfaces for one- and three-dimensional systems. Phys. Rev. E **86**, 026710 (2012)

Chapter 15
Coupling to the Microscale

Valentin L. Popov, Roman Pohrt and Markus Heß

15.1 Introduction

The application of the method of dimensionality reduction is, of course, limited to the spatial scales for which continuum mechanics can be used. Every practical application using the method will lose its validity even earlier, due to the finite spatial resolution of the surface topography. Therefore, it begs the question of whether the interactions on even smaller scales can be summarized into a microscopic "contact law" or "law of friction," so that also the properties of the smallest possible scale can be taken into account in the simulation. A complete method can only exist after the coupling to the macroscale as well as to the microscale has been accomplished. In this chapter, we explain how the limitations of the finite spatial resolution can be eliminated by the introduction of a "microscopic" non-linear stiffness.

15.2 Non-Linear Stiffness on the "Microscale"

Let us consider the classical Hertzian problem: a rigid sphere with the radius R is pressed into an elastic half-space with the effective modulus of elasticity of E^*. This problem can be expressed by an equivalent one-dimensional contact between a rigid sphere with the radius $R_1 = R/2$ and the linearly elastic foundation with the stiffness per unit length E^*. The dependence of the force on the indentation depth is given by the Hertzian Eq. (3.13). However, this is only valid if the contact radius is much larger than the discretization step size Δx of the linearly elastic foundation. As soon as only one spring is in contact, the stiffness is constant and the result deviates from that of the Hertzian equation. In order for the force-indentation depth relation to remain correct also at

V.L. Popov and M. Heß, *Method of Dimensionality Reduction in Contact Mechanics and Friction*, DOI 10.1007/978-3-642-53876-6_15

smaller forces, the discretization step size can always be chosen to be smaller. An alternative solution is based on the idea that the single spring is assigned a non-linear stiffness. The introduction of non-linear stiffness for the simulation of processes on the microscale is not a new idea. For example, this idea was used in [1] and [2] and is the foundation of the concept of "interfacial stiffness," which is currently being used actively by many experts in the field of contact mechanics [3–5].

As explained in Sect. 10.8, a completely fractal surface can be replaced (in the sense of an average contact stiffness) by a single non-linear spring. This idea does not have to be applied to the entire system, but can also be used beginning at a certain scale. We illustrate this idea using two examples: The Hertzian contact and the contact with a randomly rough, fractal surface.

15.3 Coupling with the Microscale Using the Example of the Hertzian Contact

Here, we consider the case of the Hertzian contact, meaning the indentation of a paraboloid. As seen in Chap. 3, the original radius R is replaced in the one-dimensional model by $R_1 = R/2$. In this way, we obtain the form of the indenter:

$$g(x) = \frac{x^2}{R}. \tag{15.1}$$

As soon as the indentation depth decreases beyond a critical value $u_z^{(0)} = g(\Delta x)$, only a single spring is in contact. Here, the dependence of the stiffness on the indenter form loses its validity and assumes the behavior of a single spring. If we now change the linear force law of a single spring to that effect so that each of them reproduces the asymptotic Hertzian behavior, then this problem can be avoided. So, we replace the local linear spring behavior with the following non-linear law for the spring force:

$$f_i = E^* \begin{cases} \frac{4}{3} R^{1/2} u_{z,i}^{3/2}, & \text{if} \quad u_{z,i} < u_{z,i}^{(0)} = \frac{\Delta x^2}{R} \\ \left(\frac{\Delta x^3}{3R} + \Delta x \cdot u_{z,i} \right), & \text{if} \quad u_{z,i} \geq \frac{\Delta x^2}{R} \end{cases}. \tag{15.2}$$

For large values of $u_{z,i}$, the limiting case of the standard linearly elastic foundation results. Figure 15.1 shows the force–indentation depth relationship in the transitional domain of the standard model of linear springs in blue and with the spring behavior from Eq. (15.2) in green. The force with respect to the indentation depth is now correctly given for both very large and very small forces, regardless of the size of the discretization step Δx. In the domain where only one spring is in contact, there is a small irregularity that cannot be avoided. As we will see in the next section, this procedure works much better for randomly rough surfaces, because small irregularities due to statistical scatter are "averaged out."

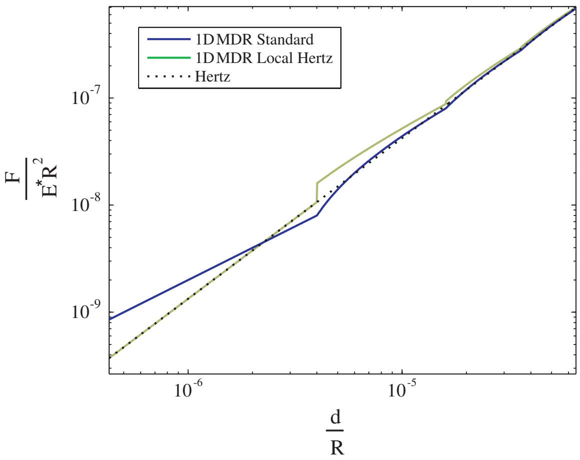

Fig. 15.1 Dependence of the force on the indentation depth plotted logarithmically: the exact solution of the Hertzian problem, results of the classical one-dimensional equivalent system with a discretization step size of Δx, and the results for the one-dimensional equivalent model with a stiffness according to (15.2)

15.4 Coupling with the Microscale for the Case of a Randomly Rough, Fractal Surface

In Chap. 10, we have investigated fractal surfaces and seen that they follow a power law for asymptotically small forces (or indentation depths). For a fractal surface with a length L and a roughness h, the force as a function of indentation depth is determined according to Eq. (10.48):

$$F(d) = E^* h^{-\frac{1}{H}} L \left(1.9412 \frac{H}{(H+1)^2} \right)^{\frac{H+1}{H}} d^{\frac{H+1}{H}}. \tag{15.3}$$

We obtain the critical indentation depth when the stiffness corresponds exactly to that of a single linear spring. According to this, the following results from (10.30):

$$k_{krit} = \Delta x E^* = \overline{k_{krit}} 1.1419 E^* L = \frac{1.9412 E^* L}{H+1} \left(\frac{F_{krit}}{E^* h L} \right)^{\frac{1}{H+1}}. \tag{15.4}$$

From this, it follows that

$$F_{krit} = E^* h L \left(\frac{H+1}{1.9412 L} \Delta x \right)^{H+1}. \tag{15.5}$$

Insertion into (15.3) results in the critical indentation depth

$$u_{z,j}^{(0)} = \frac{(H+1)^2}{1.9412 H} \left(\frac{H+1}{1.9412} \frac{\Delta x}{L} \right)^{H} h. \tag{15.6}$$

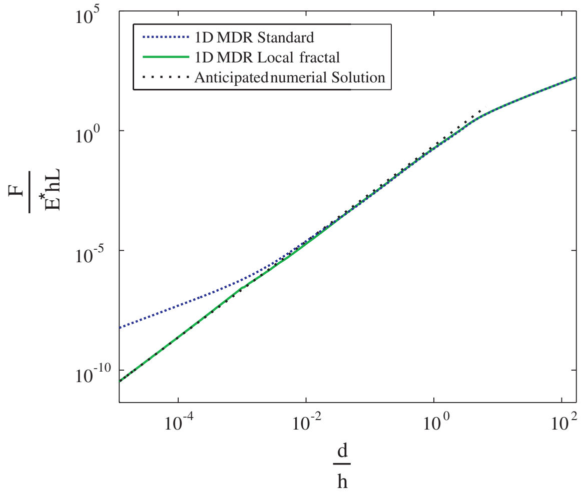

Fig. 15.2 Dependence of the force on the indentation depth plotted logarithmically for fractally rough lines. Approximate numerical solution for the average of many surface realizations according to Eq. (15.3), numerical results using the reduction method and the reduction method with a non-linear spring behavior according to Eq. (15.7). The bend in the blue curve for small indentation depths can be corrected using the non-linear spring behavior. Data from the plot are $N = 2{,}049$, $H = 1$

In order to correctly map the asymptotic behavior, the force of a single spring, for small indentation depths, has to be defined accordingly to (15.3) while for larger indentation depths, a linear behavior should be valid. Accordingly, we define

$$f_i = E^* \begin{cases} h^{-\frac{1}{H}} L \left(\frac{1.9412H}{(H+1)^2} \right)^{\frac{H+1}{H}} u_{z,i}^{\frac{H+1}{H}}, & \text{if} \quad u_{z,i} < u_{z,i}^{(0)} \\ -\left[\frac{H+1}{H} \right] \left(\frac{H+1}{1.9412} \frac{\Delta x}{L} \right)^H \frac{\Delta x h}{1.9412} + \Delta x u_{z,i}, & \text{if} \quad u_{z,i} \geq u_{z,i}^{(0)} \end{cases} . \tag{15.7}$$

Figure 15.2 shows, analogously to Fig. 15.1, the curve of the normal force with respect to the indentation depth for the linear standard model (dotted blue line) and with the definition of the single spring according to (15.7). The expected approximation in the domain of asymptotically small indentations (10.48) is shown as a dotted line.

We have seen that the behavior on the microscales can be “coupled” to the reduction method by allowing a single spring to behave non-linearly in the domain of small indentations. In addition to the possibility of reducing the discretisation step to account for known problems, this procedure can also be used to integrate models below the scales of continuum mechanics, or to represent a cut-off domain of shorter wavelengths. Surface spectra that exhibit such a cut-off are microscopically smooth below this wavelength. This means that they form effectively the smallest possible asperities with a characteristic radius of curvature so that the Hertzian behavior can be used, as in Eq. (15.2).

References

1. M. Ciavarella, S. Dibello, G. Demelio, Conductance of rough random profiles. Int. J. Solids Struct. **45**, 879–893 (2007)
2. K. Willner, *Kontinuums- und Kontaktmechanik: Synthetische und analytische Darstellung* (Springer, Berlin, 2003), p. 560
3. C. Campana, M.H. Müser, Phys. Rev. B **74**, 075 420 (2006)
4. S. Akarapu, T. Sharp, M.O. Robbins, Phys. Rev. Lett. **106**, 204301 (2011)
5. C. Campana, B.N.J. Persson, M.H. Müser, Transverse and normal interfacial stiffness of solids with randomly rough surfaces. J. Phys.: Condens. Matter **23**, 085001 (2011)

Chapter 16
And Now What?

Valentin L. Popov and M. Heß

16.1 Introduction

The most valuable aspect of the method of dimensionality reduction is the fact that it is a practical tool for many engineering applications. In several applications, such as the contact mechanics of axially-symmetric bodies, it provides exact results. In this field, it summarizes not only the multitude of exact three-dimensional solutions in a simple, compact way, but at the same time, is also distinguished by its extremely simple numerical implementation. This trait is also true for other types of problems, such as the contact of randomly rough surfaces. Here, the method provides asymptotically exact results (for very small and very large forces). In the transitional domain, the results are not exact, but offer a very good approximation, the accuracy of which exceeds that of the typically available values for material and surface parameters.

In this chapter, we would like to discuss several ideas that are also only valid to "engineering accuracy," but expand the possibilities of the reduction method and can further simplify its application. At no point in this chapter, a claim to a final and ultimate truth will be made. Our goal is much more to make the simulation of good approximations possible for instances in which simulations have not yet been possible.

16.2 Linear Scans for Direct Application in the One-Dimensional Model

In order to apply the method of dimensionality reduction to contacts between rough surfaces, it is necessary to convert the two-dimensional topography into the effective one-dimensional topography. The conversion rule for self-affine surfaces is

V.L. Popov and M. Heß, *Method of Dimensionality Reduction in Contact Mechanics and Friction*, DOI 10.1007/978-3-642-53876-6_16

given by Eq. (10.15) with the factor $\lambda(H)$, which has been determined empirically until now and is presented in Fig. 10.9. The factor $\lambda(H)$ for typical Hurst exponents in the interval $H = 0.3$ to $H = 0.7$ varies only slightly around a value of 2. Every practitioner that has once measured a rough surface and attempted to determine its fractal dimension would know that the scatter for such measurements normally far exceeds the possible variation of the coefficient $\lambda(H)$. Using an exact coefficient, such as 2, would be purely pedantic and simply an exaggeration of the actual accuracy of the surface data available to engineers. For practical purposes, therefore, we can recommend the simple conversion formula

$$C_{1D}(q) = 2qC_{2D}(q). \tag{16.1}$$

On the other hand, it will be shown in Chap. 20 Eq. (20.23) that the one-dimensional power spectrum of a linear cross-section is approximately given by a two-dimensional surface by using Eq. (16.1). This means that the one-dimensional spectrum used in the method of dimensionality reduction corresponds to the spectrum of a one-dimensional cross-section of the original, as a first order approximation. In this approximation, the entire procedure is simplified extremely: First, the determination of the two-dimensional topography is no longer necessary, because the one-dimensional cross-section is sufficient. Second, the chain of transformations is also no longer necessary: (a) Determining the two-dimensional power spectrum, (b) the conversion to the one-dimensional power spectrum, and (c) the generation of the one-dimensional profile. Now, the one-dimensional cross-section can directly be used.

16.3 Anisotropy: Linear Scans in the Direction of Motion?

Until now, we have only investigated isotropic surfaces, either axially-symmetric or statistically isotropic. However, tribological surfaces are frequently non-isotropic. Even if the surfaces are manufactured to be isotropic, they become non-isotropic during the tribological process itself, because the sliding direction causes a certain directionality in the material. As we have seen in Chaps. 3 and 10, the correct reproducibility of force-displacement relationship of a three-dimensional contact using a one-dimensional equivalent system is based solely on the scaling properties of the self-affine surface. These are not only limited to isotropic surfaces but are applicable to all self-affine surfaces, regardless of whether we are dealing with single non-isotropic “peaks” or rough surfaces. However, this is only valid for the normal contact problem. For tangential contact problems, and especially for friction, anisotropy is of crucial importance. It then begs the question of whether or not it is possible to produce a one-dimensional system in such a way that it maps the anisotropy of a two-dimensional surface. For this, a separate rough line must be generated for every sliding direction. However, each line must still exhibit the same normal stiffness. This requirement is met easily, because the stiffness is only dependent on the RMS-roughness, as seen in Eq. (10.25), and not on the RMS-surface gradients. If, for example, the linear cross-section is considered to be self-affine but non-isotropic, then all of them will exhibit the same RMS-roughness and Hurst exponent, and therefore, the same dependence of the normal stiffness on force. Simultaneously, they will exhibit different RMS-surface gradients and different frictional forces. The exact conversion method for non-isotropic surfaces is not yet known and is the topic of current research. A simple rough rule, however, can already be formulated.

On the basis of the previous paragraphs, we can here form the following hypotheses, which can be used as an initial approximation for the production of a one-dimensional replacement system for a non-isotropic two-dimensional surface. In the case of isotropic surfaces, it has been shown that the one-dimensional cross-section is directly suited to be used as the one-dimensional equivalent profile. We have seen that this is essentially due to the fact that the cross-sections have the same RMS-roughness and RMS-surface gradient as the two-dimensional original and, furthermore, exhibit the same Hurst exponent. Based on this, it is guaranteed that the normal stiffness can be correctly reproduced. For elastomers, it is then also assured that the characteristic value of the coefficient of friction (in the middle velocity domain, in which the loss modulus is larger than the storage modulus) can be reproduced correctly. In this domain, it obviously depends on the RMS-surface gradient *in the direction of motion* [1]. This is, however, exactly the RMS-surface gradient of a section in the direction of motion! The linear cross-section, therefore, exhibits the correct normal stiffness *and* the correct characteristic value of the coefficient of friction, and this for an arbitrary direction of motion. If this hypothesis (perhaps in a somewhat modified form) can be substantiated, we would have a very simple and effective tool for the simulation of non-isotropic rough surfaces.

16.4 Can the Method of Dimensionality Reduction also be Applied to Non-Randomly Rough Surfaces?

In all previous chapters, we have assumed randomly rough surfaces, which present only a subclass of possible rough surface profiles. The simple method shown in Sect. 16.2 for the generation of a one-dimensional equivalent profile begs the question of whether the one-dimensional cross-sections of *non-randomly rough* surfaces are also suited to be used as one-dimensional equivalent profiles. The fact that this can by all means be a good approximation has already been made clear in an example of an axially-symmetric profile. In Sect. 3.3, a flattened sphere was considered and the exact equivalent profile was determined using the generalized conversion formula. However, it differs from the simple linear cross-section of the three-dimensional profile, stretched vertically by a factor of two, only slightly (Fig. 16.1). Our hypothesis consists of the consideration that the one-dimensional cross-section through a rough surface is also a good approximation for a representative one-dimensional profile for non-randomly rough surfaces. If this hypothesis is confirmed, then it will open up wide applications for the treatment of correlated (e.g., worn) profiles.

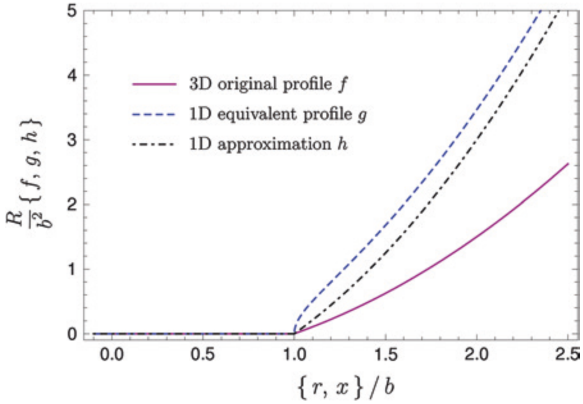

Fig. 16.1 The three-dimensional profile of a flattened sphere f, its exact one-dimensional equivalent profile g and the two-fold scaled profile of a linear cross-section through the center of the sphere h in a normalized presentation

16.5 Heterogeneous Systems

Many real tribological systems are heterogeneous systems, such as a brake pad. The current version of the method of dimensionality reduction can only by applied to homogeneous systems. A heterogeneous system must first be homogenized before it can be treated with the methods described in this book. It is of interest to obtain an exact, explicit description of the heterogeneity. The main ideas of how this could be done are discussed in [2].

16.6 Fracture and Plastic Deformation in the Method of Dimensionality Reduction

The simple feature indicating that a physical quantity can be simulated very easily using a one-dimensional mapping, is the proportionality of this quantity to the diameter of the contact. This property can be trivially "one-dimensionalized." Therefore, parameters such as stiffness and electrical/thermal conductivity are easily mappable to one-dimensional systems. Also the dependence of the total force on the macroscopic displacement falls into this category and is given excellently by the reduction method. Parameters that do not have this property, such as contact area, cannot be mapped (at least not without limiting assumptions). Plastic and fracture behavior do not appear at first glance to belong to the properties to which the reduction method can be directly applied. In reality, there is a set of systems for which also plastic deformation and fracture processes can be included (at least half quantitatively) to solvable problems for the method of dimensionality reduction. This will always be the case when the critical forces for plastic deformation or fracture are linearly dependent on the contact radius. In the work [3], for instance, the strength of microcontacts for Au–Au and Au–Pt in tension and Au–Au in shear were investigated. The fracture force was proportional to the contact radius for contacts with a radius of 10–100 nm:

$$F = 2a\Psi, \tag{16.2}$$

where Ψ is a constant. This property can be directly mapped using the method of dimensionality reduction by defining the fracture criterion for individual springs in the linearly elastic foundation as follows:

$$f_c = \Psi \cdot \Delta x. \tag{16.3}$$

The strong dependence of the fracture strength on the size of the contact on the nanoscale appears to be more the rule than the exception.

Incidentally, this is not only valid for the fracture force, but also for the force at which plastic deformation initiates. The authors of the work [4], for example, have investigated the indentation of polydimethylsiloxane (PDMS) and determined that the hardness was inversely proportional to the contact radius for a wide interval of indentation depths (which corresponded to three orders of magnitude). In other words, the force scaled practically linearly with respect to the size of the contact. Similar results were found for the nanoindentation of gold [5]. For such materials, the condition for plastic deformation of the surface can be implemented similarly to (16.3). A more detailed discussion of description of plastic deformation and fracture in the framework of MDR can be found in [6].

References

1. G. Carbone, B. Lorenz, B.N.J. Persson, A. Wohlers, Contact mechanics and rubber friction for randomly rough surfaces with anisotropic statistical properties. Eur. Phys. J., E. **29**, 275–284 (2009)
2. V.L. Popov, Method of dimensionality reduction. Heterogeneous media. Phys. Mesomech. **17**(1), 50–57 (2014)
3. R. Budakian, S.J. Putterman, Time scales for cold welding and the origins of stick-slip friction. Phys. Rev. B **65**, 235429 (2002)
4. A.J. Wrucke, C.-S. Han, P. Majumdar, Indentation size effects of multiple orders of magnitude in Polydimethylsiloxane. J. Appl. Polym. Sci. **128**, 258–264 (2013)
5. S.G. Corcoran, J. Colton, Anomalous plastic deformation at surfaces: nanoindentation of gold single crystals. Phys. Rev. B **55**, R16057 (1997)
6. V.L. Popov, Dimension reduction in multiscale simulation of impact on composite structures. Scoltech J.: Educ., Sci., Technol. **N.1**, 63–68 (2013)

Chapter 17
Appendix 1: Exact Solutions in Three Dimensions for the Normal Contact of Axially-Symmetric Bodies

Markus Heß and Valentin L. Popov

17.1 Introduction

In this chapter, the complete proofs will be shown that allow for the *exact* mapping of frictionless, axially-symmetric contact problems with and without adhesion to one-dimensional contacts. The starting point is the three-dimensional theory for the calculation of axially-symmetric contacts, which we will change step-by-step in a way that the one-dimensional properties may be clearly seen. We assume simply connected, and therefore, circular contact areas. Let us first consider the indentation of a rigid, axially-symmetric indenter into an elastic half-space according to Fig. 17.1a. Here, the profile of the indenter is defined as $\tilde{z} = f(r)$, where the $\tilde{z}$-axis is positive in the upwards direction starting at the tip of the indenter. The indentation depth d denotes the maximum surface displacement that is always present at the tip of the indenter in the case of a convex profile. In addition to the indentation depth d, the contact depth d_c may be seen in the figure. The contact depth is

$$d_c = f(a). \tag{17.1}$$

The mixed boundary conditions are

$$\begin{array}{lll} u_z(r,0) = d - f(r), & 0 \le r \le a & \\ \sigma_{zz}(r,0) = 0, & r > a & , \\ \tau_{rz}(r,0) = 0 & & \end{array} \tag{17.2}$$

where u_z, σ_{zz}, and τ_{rz} correspond to the components of the displacement and stress tensors at the surface. Galin [1] and Sneddon [2] solved this classical elasticity problem using integral transformations, obtaining the following equations, which are only dependent on the form of the indenter:

$$d = a \int_0^a \frac{f'(r)}{\sqrt{a^2 - r^2}} \mathrm{d}r + \frac{\pi}{2} \chi(a) \tag{17.3}$$

V.L. Popov and M. Heß, *Method of Dimensionality Reduction in Contact Mechanics and Friction*, DOI 10.1007/978-3-642-53876-6_17

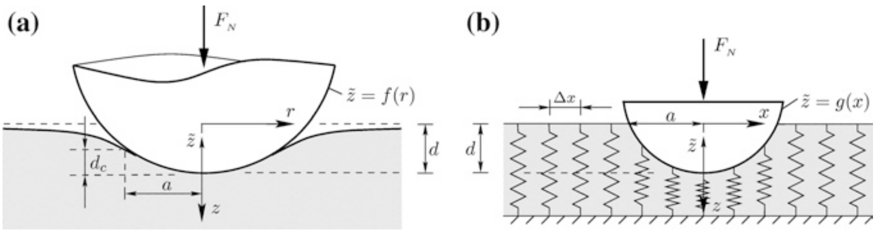

Fig. 17.1 (**a**) Contact between a rigid, axially-symmetric indenter and an elastic half-space. (**b**) The equivalent one-dimensional system

$$F_N = \pi E^* \int_0^a \chi(x)\,\mathrm{d}x \tag{17.4}$$

$$\sigma_{zz}(r,0) = \frac{E^*}{2}\frac{1}{r}\frac{\mathrm{d}}{\mathrm{d}r}\int_r^a \frac{\chi(x)x}{\sqrt{x^2-r^2}}\mathrm{d}x = \frac{E^*}{2}\left[\int_r^a \frac{\chi'(x)}{\sqrt{x^2-r^2}}\mathrm{d}x - \frac{\chi(a)}{\sqrt{a^2-r^2}}\right], \quad 0 < r < a \tag{17.5}$$

$$u_z(r,0) = \int_0^a \frac{\chi(x)}{\sqrt{r^2-x^2}}\mathrm{d}x, \quad r > a. \tag{17.6}$$

The function $\chi(x)$ is calculated from the form function $f(r)$ according to

$$\chi(x) = \frac{2}{\pi}\frac{\mathrm{d}}{\mathrm{d}x}\int_0^x \frac{r(d-f(r))}{\sqrt{x^2-r^2}}\mathrm{d}r = \frac{2}{\pi}\left(d - x\int_0^x \frac{f'(r)}{\sqrt{x^2-r^2}}\mathrm{d}r\right). \tag{17.7}$$

With the exception of the profile of a *flat*, cylindrical indenter, the contact radius a is not known in the equations above; its calculation requires an additional condition, which we will discuss later.

By expressing the indentation depth d in right-hand side of Eq. (17.7) using Eq. (17.3), we obtain a relationship that is important for the application of the reduction method:

$$\chi(x) = \chi(a) + \frac{2}{\pi}\left[g(a) - g(x)\right], \tag{17.8}$$

with

$$g(x) = x\int_0^x \frac{f'(r)}{\sqrt{x^2-r^2}}\mathrm{d}r \;\text{ for }\; x > 0. \tag{17.9}$$

By taking Eq. (17.8) into account, the conditional equation for the normal force (17.4) can be formulated in the following syntax:

$$F_N = 2E^* \int_0^a \left[g(a) + \frac{\pi}{2}\chi(a) - g(x) \right] \mathrm{d}x = 2E^* \int_0^a \left[d - g(x) \right] \mathrm{d}x. \tag{17.10}$$

We can physically redefine this equation if we interpret the integrand as the displacement within an equivalent system:

$$u_{z,1D}(x) := \frac{\pi}{2}\chi(x) = g(a) + \frac{\pi}{2}\chi(a) - g(x) = d - g(x), \tag{17.11}$$

which is sketched in Fig. 17.1b. It consists of a series of equally-spaced longitudinal springs having the stiffness $\Delta k_z = E^* \Delta x$, into which a rigid profile is indented, which is described by Eq. (17.9) and its mirrored image about the y-axis:

$$g(x) = |x| \int_0^{|x|} \frac{f'(r)}{\sqrt{x^2 - r^2}} \mathrm{d}r \;\; \text{for} \;\; x \in \mathbb{R}, \tag{17.12}$$

which we have additionally supplemented by $g(0) := \lim\limits_{x \to 0} g(x) = 0$.

The contribution of a single spring to the normal force at the point x_i is

$$f_N(x_i) = E^* \Delta x \cdot u_{z,1D}(x_i). \tag{17.13}$$

Summing the force components in the loaded springs and subsequently taking the limit $\Delta x \to 0$ then leads to Eq. (17.10):

$$F_N = E^* \int_{-a}^{a} u_{z,1D}(x) \mathrm{d}x = E^* \int_{-a}^{a} \left[d - g(x) \right] \mathrm{d}x. \tag{17.14}$$

From Eq. (17.11) with the help of Eq. (17.3), the following equation results:

$$u_{z,1D}(a) = d - g(a) = \frac{\pi}{2}\chi(a), \tag{17.15}$$

from which we can calculate the indentation depth for both the contacts with and without adhesion by taking the conditions into account which will be discussed in the next section. The dependencies between the indentation depth, contact radius, and normal force resulting from the presented reduced contact are all exactly those that would result in a three-dimensional, axially-symmetric contact.

In the three-dimensional problem, the indentation depth is equal to the displacement at the point $r = 0$. The same is valid for the equivalent one-dimensional:

$$u_{z,3D}(r)\big|_{r=0} = d = u_{z,1D}(x)\big|_{x=0}. \tag{17.16}$$

Nevertheless, there exists a fundamental difference, because in the one-dimensional case the indentation depth and the contact depth are identical, which allows for a much simpler calculation.

Let it be noted here that, generally, also contacts with concave profiles may be mapped if we require, as mentioned above, that the contact area is simply connected and in the place of the indentation depth at the contact boundary, continue to use the displacement at the center of the contact as the characteristic value (see Problem 6 in Chap. 3).

17.2 Normal Contacts Without Adhesion

First, only contacts without adhesion will be considered. Later, we will see that using the method of dimensionality reduction for non-adhesive contacts lays at the same time the foundation for mapping adhesive contacts. Boussinesq [3] already indicated that the normal stresses at the edge of the contact between a half-space and a convexly formed indenter must vanish. Sneddon [2] showed that this property leads to

$$\chi(a) = 0 \tag{17.17}$$

if the stresses at the edge of the contact are observed using Eq. (17.5). With this, the missing equation for the calculation of the contact radius is found for contacts without adhesion. This is equally valid for the one-dimensional model, due to the fact that after insertion of (17.17) into (17.15), only a trivial condition remains for the determination of the indentation depth within the framework of the reduction method:

$$u_{z,\,1D}(a) = 0 \Rightarrow d = g(a). \tag{17.18}$$

With this relation, the equation for calculating the normal force can be further simplified:

$$F_N = E^* \int_{-a}^{a} u_{z,\,1D}(x)\mathrm{d}x = E^* \int_{-a}^{a} \left[g(a) - g(x)\right]\mathrm{d}x = 2E^* \int_{0}^{a} \left[g(a) - g(x)\right]\mathrm{d}x. \tag{17.19}$$

The calculation of the equivalent profile from the original, according to Eq. (17.12) and subsequent evaluation of Eqs. (17.18) and (17.19) form the central premise for calculating the exact solution to three-dimensional contact problems using the method of dimensionality reduction.[1] In Chap. 3, the procedure is explained using many examples. If at all, the only difficulty lies in calculating the equivalent profile from the original according to (17.9) and (17.12), respectively. Depending on the type of profile function, even this step may be further simplified, which we would like to explain in the following.

---

[1] Assuming convex profiles.

17.2.1 Single-Term Profiles—Power Function

We first assume an indenter with the form

$$\tilde{z} = f(r) = c_n r^n, \tag{17.20}$$

where the exponent n is an arbitrary *positive real* number. Insertion of (17.20) into (17.12) and subsequent integration results in

$$g(x) = nc_n|x| \int_0^{|x|} \frac{r^{n-1}}{\sqrt{x^2 - r^2}} dr = \kappa_n c_n |x|^n = \kappa_n f(|x|). \tag{17.21}$$

For the introduced exponent n of the power function, the coefficient κ_n is

$$\kappa_n := n \int_0^{\pi/2} (\sin u)^{n-1} \mathrm{d}u = \frac{\sqrt{\pi}}{2} \frac{n\Gamma(\frac{n}{2})}{\Gamma(\frac{n+1}{2})}, \tag{17.22}$$

where $\Gamma(n)$ denotes the gamma function. According to (17.21), the function g, and with it the equivalent profile, arises from a simple vertical scaling of the original profile by the factor κ_n. We can physically interpret the scaling factor, if we calculate the indentation depth from the condition (17.18):

$$d = \kappa_n f(a) = \kappa_n c_n a^n = \kappa_n d_c. \tag{17.23}$$

According to Eq. (17.23), the scaling factor specifies the relation between the indentation depth d and the contact depth d_c. With this, we can write the normal surface displacement in the one-dimensional model according to (17.11) as follows:

$$u_{z,\,1D}(x) := d - g(x) = \kappa_n(f(a) - f(x)) = \kappa_n(d_c - f(x)). \tag{17.24}$$

We can see from the parentheses that the one-dimensional displacement is determined from the corresponding scaling of the three-dimensional *relative* displacement with respect to the contact boundary, which is graphically supported by comparing the subfigures in Fig. 17.1. The geometry of the equivalent model, therefore, requires only a simple modification of the original profile (rule of Heß [4]):

$$f(r) = c_n r^n \;\mapsto\; g(x) = \tilde{c}_n |x|^n \text{ with } \tilde{c}_n = \kappa_n c_n \text{ and } \kappa_n = \frac{\sqrt{\pi}}{2} \frac{n\Gamma(\frac{n}{2})}{\Gamma(\frac{n+1}{2})}. \tag{17.25}$$

Figure 3.3 from Chap. 3 shows the graphical trend of the change in the scaling factor κ_n with respect to the exponent n.

17.2.2 The Special Case of the Flat, Cylindrical Indenter

In the case of a flat, cylindrical indenter being pressed into an elastic half-space, the normal displacement at the edge of the contact is *not* differentiable. Because of this, the Boussinesq condition (17.17) is violated and we may not use Eqs. (17.18) or (17.19). However, the contact radius a is already known. The profile is then

$$\tilde{z} = f(r) = 0, \tag{17.26}$$

which after insertion of Eq. (17.12), leads to

$$\tilde{z} = g(x) = 0. \tag{17.27}$$

For the normal force, we turn back to Eq. (17.14):

$$F_N = 2E^* \int_0^a d \,\mathrm{d}x = E^* \int_{-a}^a d \,\mathrm{d}x = 2E^* a d, \tag{17.28}$$

for which we intentionally show the intermediate step in order to make it clear that this equation corresponds to the contact between a one-dimensional profile and a linearly elastic foundation.

17.2.3 Superposition Principle for Multi-Termed Profiles

For profiles in the form of power functions (with arbitrary positive real exponents), using the general transformation formula (17.12), leads to a constant scaling relationship. Due to the superposition principle, we can use the especially simple mapping rules also for multi-termed profiles. In the following, we will consider a multi-termed profile function in the form of a power series according to

$$\tilde{z} = f(r) = \underbrace{c_1 r^1}_{f_1(r)} + \underbrace{c_2 r^2}_{f_2(r)} + \cdots + \underbrace{c_k r^k}_{f_k(r)} + \cdots = \sum_{n=1}^{\infty} c_n r^n. \tag{17.29}$$

One such profile, for example, was used by Segedin [5] for investigating the contact radius of a spherical indenter with an elastic half-space. In contrast to the Hertzian approximation, he defined the spherical profile as a Taylor series. Insertion of (17.29) into (17.11) and taking (17.12) into account leads to the normal displacement in the equivalent model

$$u_{z,\,1D}(x) = d - |x| \int_0^{|x|} \sum_{n=1}^{\infty} \frac{n c_n r^{n-1}}{\sqrt{x^2 - r^2}} \,\mathrm{d}r = d - \sum_{n=1}^{\infty} \kappa_n f_n(|x|). \tag{17.30}$$

In doing so, we have switched the integral and the summation in the first step and, subsequently, conducted the integration analogously to Eq. (17.21). According to Eq. (17.18), the displacement in the equivalent model at the point $x = \pm a$ must vanish for non-adhesive contacts, for which the indentation depth may be found:

$$d = \sum_{n=1}^{\infty} \kappa_n f_n(a) = \sum_{n=1}^{\infty} d_n(a) = \sum_{n=1}^{\infty} g_n(a). \tag{17.31}$$

This presents nothing other than the superposition of the indentation depths d_n which every single term in the profile would produce. As already described in Chap. 3, the application of the superposition principle requires *identical contact areas*, which is the case here (circular area with the radius a). Because the reduction method is valid for each one of these single profiles, it must automatically be valid for the sum of these, which is shown on the right-hand side of Eq. (17.31). This is, of course, also true for the mapping of the normal force as a function of the contact radius. If we first insert (17.31) into (17.30) and then use the result in the conditional Eq. (17.19) for the normal force, we obtain

$$F_N = \sum_{n=1}^{\infty} E^* \int_{-a}^{a} \left[g_n(a) - g_n(x)\right] \mathrm{d}x = \sum_{n=1}^{\infty} F_n(a). \tag{17.32}$$

Mapping profiles in the form of power series is valuable also for a complete other reason. If there is no closed solution for the integral in the generalized transformation formula (17.12), but the original profile can be defined as a series, then we can always determine the equivalent profile in this way. Only piecewise-defined profiles require that the transformation formula be explicitly applied.

17.3 Normal Contacts with Adhesion According to the Generalized JKR Theory

In the following, the proofs of the ansätze used in Chap. 4 will be shown for the exact mapping of the adhesion theory by Johnson et al. [6] as well as their generalizations to arbitrary axially-symmetric contacts. Thereby, we make use of the method from Maugis and Barquins [7], which exploits the analogy to linearly elastic fracture mechanics. We begin by using Eqs. (17.5) and (17.6) from Sneddon, which were defined in the immediate proximity to the contact area:

$$\sigma_{zz}(r = a - \varepsilon a) \approx -\frac{E^*}{2a} \frac{\chi(a)}{\sqrt{2\varepsilon}} \tag{17.33}$$

$$\Delta u_z(r = a + \varepsilon a) \approx -\chi(a)\sqrt{2\varepsilon}, \tag{17.34}$$

where $\Delta u_z(r) := f(r) - d + u_z(r)$ is the difference between the normal displacement of the indenter and that of the half-space surface outside of the contact area and, as usual, $\varepsilon \ll 1$ is valid. This relationship corresponds exactly to that for the near field in the proximity of a mode I crack, the intensity of which is only expressed by the so-called stress intensity factor K_I. The latter realization prompted Irwin [8] to define a fracture criterion. According to this, propagation of the fracture occurs only after K_I, which is generally dependent on material, geometry, length, and loading of the crack, reaches the so-called fracture toughness, which is able to be experimentally determined from standardized fracture tests. The relationship between $K_I(a)$ and the yet unknown modified rigid body translation $\chi(a)$ is

$$K_I(a) = \lim_{\varepsilon \to 0} \sqrt{2\pi a \varepsilon} \cdot \sigma_{zz}(a - \varepsilon a) = -\frac{\sqrt{\pi} E^* \chi(a)}{2\sqrt{a}} = -\frac{E^*}{\sqrt{\pi a}} u_{z,1D}(a), \tag{17.35}$$

the right side of which arises from (17.15).

Irwin not only recognized that the description of a singular stress field using the intensity factor is the same for all fundamental fracture modes, but also discovered the connection to the energetic ansatz from Griffith [9]. Thus, the elastic energy release rate $\mathcal{G}$ and the stress intensity factor for a mode I crack in a state of plane strain are related according to

$$\mathcal{G} = \frac{K_I^2(a)}{2E^*}. \tag{17.36}$$

This form results in

$$\mathcal{G} = \frac{E^*}{2\pi a} u_{z,1D}^2(a) \tag{17.37}$$

after insertion of (17.35).

In a state of equilibrium, the elastic energy release rate must be equal to the Dupré energy of adhesion $\Delta\gamma$:

$$\mathcal{G} = \Delta\gamma. \tag{17.38}$$

The latter presents a *relative* surface energy, which is dependent on the surface energies γ_1 and γ_2 of the two bodies as well as the interface energy γ_{12}, according to

$$\Delta\gamma := \gamma_1 + \gamma_2 - \gamma_{12}. \tag{17.39}$$

After insertion of (17.37) into (17.38), we obtain

$$u_{z,1D}(a) = -\Delta\ell_{\max}(a) \text{ with } \Delta\ell_{\max}(a) := \sqrt{\frac{2\pi a\,\Delta\gamma}{E^*}}. \tag{17.40}$$

This relationship takes the place of the Boussinesq condition (17.17) for contacts with adhesion. With its help, the (equilibrium) displacement can be given in the one-dimensional model according to Eq. (17.11) in the form

$$u_{z,1D}(x) = g(a) - g(x) - \Delta\ell_{\max}(a). \tag{17.41}$$

In contrast to the non-adhesive case, the equilibrium of all contacting springs is lengthened by an additional $\Delta\ell_{\max}(a)$, which we can simply see from the springs at the boundary (see Fig. 17.2b). The indentation depth is the displacement at the point $x = 0$, for which we obtain a central requirement for the one-dimensional model by taking (17.41) into account:

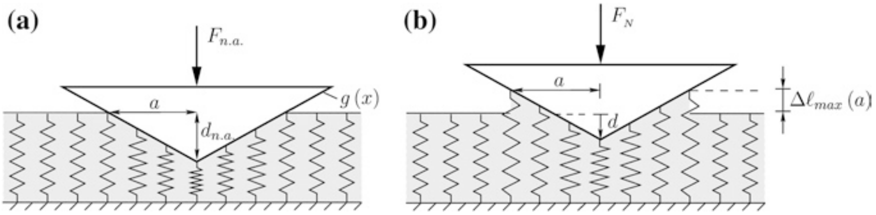

Fig. 17.2 Qualitative presentation of the indentation (**a**) and separation (**b**) processes using the reduction method for the example of a conical contact

$$d := u_{z,1D}(0) = g(a) - \Delta\ell_{\max}(a). \tag{17.42}$$

The normal force still results from the sum of the individual spring forces according to (17.14):

$$F_N := E^* \int_{-a}^{a} u_{z,1D}(x)\mathrm{d}x = E^* \int_{-a}^{a} \left[d - g(x)\right]\mathrm{d}x.$$

Due to this "new" definition of the indentation depth (17.42), which is supplemented by an additional rigid body translation, the normal force contains (in contrast to the contact without adhesion) an "unloading" component, as exhibited by the movement of a flat, cylindrical indenter. If we denote the apparent values with "n.a." that would lead to the same contact radius a in a non-adhesive contact, as that resulting in an adhesive contact, we can alternately formulate (17.42) and (17.14) as

$$d(a) = d_{n.a.}(a) - \Delta\ell_{\max}(a) \tag{17.43}$$

$$F_N(a) = F_{n.a.}(a) - 2E^* a\,\Delta\ell_{\max}(a). \tag{17.44}$$

These two equations lead to the fundamental relationship

$$\Delta F := F_{n.a.} - F_N = 2E^* a(d_{n.a.} - d) = 2E^* a\,\Delta d, \tag{17.45}$$

which, as mentioned above, exhibits the same structure which characterizes a flat indenter contact (see Sect. 17.2.2, especially Eq. (17.28)). With the help of the "apparent values," the procedure for exactly mapping the contact with adhesion is explained very quickly. In the first step, the equivalent profile must be determined according to (17.12) and subsequently indented into the uniaxial layer of springs. The loading phase resulting in a contact radius of a is exactly the same as in the contact without adhesion. We denote the corresponding normal force and indentation depth with $F_{n.a.}$ and $d_{n.a.}$, respectively. In the second step, we now assume that all springs in contact adhere to the indenter and we successively reduce the normal force. Then, more springs will be loaded in tension starting from the edge of the contact and continuing towards the center, during which the contact radius remains unchanged. As soon as the springs at the edge of the contact reach the critical elongation of $\Delta\ell_{\max}(a)$, the state between adherence and separation is achieved. This equilibrium state, defined by the triplet F_N,d-a corresponds exactly with that of the three-dimensional contact with adhesion. Figure 17.2 shows the indentation and separation process for the example of a conical contact. Let it be emphasized that the critical displacement at the contact boundary for the critical state is dependent on the contact half-width a (according to Eq. (17.40)). Equation (17.40) is known as the *rule of Heß for adhesive contacts* [4].

The implementation of adhesion within the framework of the method of dimensionality reduction requires only the investigation of the edge of the contact, according to the procedure above. Due to the dependence of the separation criterion on the contact radius, the stability of the contact should be correctly given by a numerical investigation. Nevertheless, we would like to derive a further criterion, which appears to be helpful for the explicit calculation of *critical values* and differentiates between the typical *fixed-load* and *fixed-grips* conditions, depending on which value is controlled. The starting point of the consideration is the elastic energy release rate in the form (17.37). The stability of the equilibrium state requires that the change in the energy release rate with respect to the contact area is larger than zero [10]:

$$\left.\frac{\partial \mathcal{G}}{\partial A}\right|_{F_N} > 0 \text{ or } \left.\frac{\partial \mathcal{G}}{\partial A}\right|_{d} > 0\,. \tag{17.46}$$

In this case, the crack will always reclose after a variation or perturbation. Applying (17.46) to (17.37) results in

$$\frac{u_{z,1D}(a)}{a} > 2\left.\frac{\partial u_{z,1D}(a)}{\partial a}\right|_{F_N} \text{ or } \frac{u_{z,1D}(a)}{a} > 2\left.\frac{\partial u_{z,1D}(a)}{\partial a}\right|_{d}. \tag{17.47}$$

We can obtain the derivatives in (17.47) from Eqs. (17.14) and (17.15). For the calculation at a *constant normal force*, we first rearrange Eq. (17.14):

$$F_N(a) = 2E^* \int\limits_0^a \left[g(a) - g(x)\right] dx + 2E^* a\, u_{z,1D}(a) \tag{17.48}$$

and then differentiate both sides with respect to a. Then, the left side becomes zero and we can rearrange with respect to the desired derivative. For the various boundary conditions, we obtain

$$\left.\frac{\partial u_{z,1D}(a)}{\partial a}\right|_{F_N} = -\frac{u_{z,1D}(a)}{a} - \frac{\partial g(a)}{\partial a} \text{ or } \left.\frac{\partial u_{z,1D}(a)}{\partial a}\right|_{d} = -\frac{\partial g(a)}{\partial a}. \tag{17.49}$$

Reinserting this back into Eq. (17.47) leads first to the inequality

$$\frac{u_{z,1D}(a)}{a} > -k\frac{\partial g(a)}{\partial a} \quad \text{with } k = \begin{cases} 2/3 & \text{for } F_N = const \\ 2 & \text{for } d = const \end{cases}, \tag{17.50}$$

which, after using the rule of Heß (17.40), leads to a stability criterion for equilibrium:

$$\frac{\Delta\ell_{\max}(a)}{a} < k\frac{\partial g(a)}{\partial a} \quad \text{with } k = \begin{cases} 2/3 & \text{for } F_N = const \\ 2 & \text{for } d = const \end{cases}. \tag{17.51}$$

The critical contact radii, for which the maximum separation force and minimum indentation depth result, correspond to the marginally stable state. By replacing "<" by "=" in Eq. (17.51), the conditional equations may be found for the critical contact radii:

$$\frac{\Delta\ell\mathrm{max}(a)}{a} = k\frac{\partial g(a)}{\partial a} \qquad \text{with } k = \begin{cases} 2/3 & \text{for } F_N = cons \\ 2 & \text{for } \ \ d = const \end{cases} \tag{17.52}$$

According to this, the (weighted) slope of the equivalent profile at the edge of the contact is compared to the quotient of the fracture length to the contact radius, which can be carried out without any difficulty.

17.4 The Mapping of Stresses

While in the three-dimensional contact, the normal displacement of a point on the contact surface is dependent on the stress distribution within the entire contact area, the one-dimensional contact with the linearly elastic foundation exhibits a direct proportionality between the spring force and the displacement at point x. If we take the "linear character" of the foundation into account, then the distributed load in the equivalent model may be defined as

$$q(x) = E^* u_{z,\,1D}(x) = E^* \big[d - g(x)\big]. \tag{17.53}$$

The normal stress distribution $\sigma_{zz}(r)$ of the initial three-dimensional contact does not appear in the equivalent one-dimensional model. Nevertheless, the exact stress distribution may be obtained from the "spring forces" using Eq. (17.5). We can also write Eq. (17.7) as

$$\chi(x) = \frac{2}{\pi}\big[d - g(x)\big]. \tag{17.54}$$

After the insertion of (17.54) into (17.5) and taking (17.53) into account, the conditional equation is found for the normal stress distribution, which requires only the knowledge of the distributed load in the equivalent system:

$$\sigma_{zz}(r) = \frac{1}{\pi}\frac{1}{r}\frac{\mathrm{d}}{\mathrm{d}r}\int_r^a \frac{x \cdot q(x)}{\sqrt{x^2 - r^2}}\mathrm{d}x. \tag{17.55}$$

This formula is valid for both contacts with and without adhesion, because Eq. (17.54) may contain an additional rigid body displacement component. After partial integration and subsequent differentiation with respect to r, we obtain a formulation equivalent to (17.55), which has been used the most in this book.[2]

$$\sigma_{zz}(r) = \frac{1}{\pi}\int_r^a \frac{q'(x)}{\sqrt{x^2 - r^2}}\,\mathrm{d}x - \frac{1}{\pi}\frac{q(a)}{\sqrt{a^2 - r^2}}. \tag{17.56}$$

---

[2] For piecewise-defined profile functions, it may be necessary to modify the equation.

The first term in Eq. (17.56) provides the Abel transformation (of the second kind) of $q'(x)$. The second term, on the other hand, describes the influence of the superimposed rigid body displacement. This leads to a discontinuity in the distributed load at the edge of the contact, and therefore, to a stress distribution as that under a flat, cylindrical indenter.

References

1. L.A. Galin, Contact problems in the theory of elasticity, 1961, North Carolina State College. This book is an Englisch translation of the Russian original of 1953: Л.А. Галин, Контактные задачи теории упругости. М. (1953)
2. I.N. Sneddon, The relation between load and penetration in the axisymmetric Boussinesq problem for a punch of arbitrary profile. Int. J. Eng. Sci. **3**, 47–57 (1965)
3. J. Boussinesq, Application des Potentiels a L'etude de L'equilibre et du Mouvement des Solides Elastiques (1885)
4. M. Heß, *Über die exakte Abbildung ausgewählter dreidimensionaler Kontakte auf Systeme mit niedrigerer räumlicher Dimension* (Cuvillier, Berlin, 2011)
5. C.M. Segedin, The relation between load and penetration for a spherical punch. Mathematika **4**(2), 156–161 (1957)
6. K.L. Johnson, K. Kendall, A.D. Roberts, *Surface energy and the contact of elastic solids*, in Proceedings of the Royal Society of London. Series A, Mathematical and Physical Sciences, vol. 324, 1558 (1971) pp. 301–313
7. M. Barquins, D. Maugis, Adhesive contact of axisymmetric punches on an elastic half-space: the modified Hertz-Huber's stress tensor for contacting spheres. J. Theor. Appl. Mech. **1**(2), 331–357 (1982)
8. G.R. Irwin, Analysis of stresses and strains near the end of a crack traversing a plate. J. Appl. Mech. **24**, 361–364 (1957)
9. A.A. Griffith, The phenomena of rupture and flow in solids. Philos. Trans. R. Soc. Lond. Ser. A **221**, 163–198 (1921)
10. D. Maugis, M. Barquins, Fracture mechanics and the adherence of viscoelastic bodies. J. Phys. D Appl. Phys. **11**(14), 1989–2023 (1978)

Chapter 18
Appendix 2: Exact Solutions in Three Dimensions for the Tangential Contact of Axially-Symmetric Bodies

Markus Heß and Valentin L. Popov

The derivation for the exact mapping of the tangential contact of axially-symmetric bodies requires only the knowledge of one of Jäger's superposition principles. Before we go into this in more detail, let us mention the usual restrictions. According to these, the influence of the tangential stress on the normal displacement as well as the influence of the normal stress on the tangential displacement of the surface should be neglected. It is well known that such a decoupling of the contact problem is only able to be undertaken when Dundurs' second constant β_D is as follows:

$$\beta_D := \frac{(1-2\nu_1)G_2 - (1-2\nu_2)G_1}{2(1-\nu_1)G_2 + 2(1-\nu_2)G_1} \ll 1. \tag{18.1}$$

According to this, either elastically similar materials must be assumed, or the contact is assumed to be between two incompressible materials or an incompressible material and a rigid body.

Assuming the validity of Eq. (18.1), we now consider an axially-symmetric indenter, which is initially pressed into an elastic half-space with the normal force F_N and subsequently loaded by a tangential force F_x in the x-direction. Depending on the tangential loading, the size of the inner stick domain, and with it the sticking contact radius c, will change. Points within this circular domain experience a constant displacement

$$u_x(r) = const. \tag{18.2}$$

The tangential stress must fulfill Coulomb's law of friction:

$$\tau_{zx}(r) \leq \mu p(r) \quad \text{for } 0 \leq r \leq c, \tag{18.3}$$

$$\tau_{zx}(r) = \mu p(r) \quad \text{for } c < r \leq a. \tag{18.4}$$

In Eq. (18.4), we have used the assumptions found in the classical theory of Cattaneo [1] and Mindlin [2], which states that the frictional stresses in the slip

V.L. Popov and M. Heß, *Method of Dimensionality Reduction in Contact Mechanics and Friction*, DOI 10.1007/978-3-642-53876-6_18

domain are all oriented in the direction of the applied tangential force. With the exception of the unrealistic case of $\nu_1 = \nu_2 = 0$, this assumption violates the condition that at every position in the slip domain, the slip is oriented in the direction opposing the tangential stresses. The reason for this is the presence of an additional slip motion perpendicular to the direction of the applied force. For the classical contact of parabolic bodies, however, it could be proven that this component may be neglected [3, 4]. We assume that this approximation is also valid for the generalization of the Cattaneo–Mindlin theory for arbitrary axially-symmetric contacts.

Jäger [5] considered the surface displacement within the contact area as the superposition of differential rigid body displacements, as is exhibited by the flat cylindrical indenter. Using this idea, he could derive the solution of the generalized axially-symmetric normal contact from the stress distribution beneath the flat cylindrical indenter, and with it, the equations from Sneddon [6]. In the same way, he investigated the tangential contact, whereby he took the above mentioned approximations into account, among other things, neglecting the influence of the lateral slip component. In this way, he could prove that the tangential contact problem can be completely reduced to the normal contact problem within the framework of the Cattaneo–Mindlin theory. The tangential stresses result from the coefficient of friction μ multiplied by the difference between the current normal stress distribution and the normal stress distribution that would lead to the (smaller) stick radius c:

$$\tau_{zx}(r) = -\mu\left[p(a,r) - p(c,r)\right]. \tag{18.5}$$

Completely analogously, the following equations are valid for the tangential force and the tangential displacement within the stick domain:

$$F_x = \mu[F_N(a) - F_N(c)], \tag{18.6}$$

$$u_x = \mu\frac{E^*}{G^*}[d(a) - d(c)]. \tag{18.7}$$

Let it be noted that Jäger consequently assumed elastically *identical* materials ($E_1 = E_2 =: E,\ \nu_1 = \nu_2 =: \nu$) in his pioneering work [5], for which the characteristic stiffness ratio in Eq. (18.7) is replaced by

$$\frac{E^*}{G^*} = \frac{2-\nu}{2(1-\nu)}. \tag{18.8}$$

By simply assuming elastically *similar* materials,[1] Ciavarella [7, 8] could show the validity of Eqs. (18.5)–(18.7). Deviating from the procedure of Jäger, Ciavarella's solution was obtained by the comparison of the integrals of the fundamental solutions of Boussinesq [9] and Cerruti [10].

Due to the fact that the axially-symmetric tangential contact with partial slip can be represented by two normal contacts, it must also be exactly mappable using the reduction method. Furthermore, it is in no way necessary to analyze *two*

---

[1] Elastically *similar* materials are characterized by $\beta_D = 0$.

normal contacts, which we will show in the following. Thereby, we assume that the Boussinesq condition (17.17) is met. Then, the following equation results by using Eq. (18.7) and taking into account both Eq. (17.3) and the conditional equation of the form function $g(x)$ of the equivalent profile (17.12):

$$G^* \Delta x\, u_x = \mu\, E^* \Delta x \big[g(a) - g(c)\big], \tag{18.9}$$

where we have additionally multiplied by the spring separation distance Δx. Let us now remember the modeling of the one-dimensional linearly elastic foundation by independent spring elements in the normal and tangential direction, which possess the normal stiffness $\Delta k_z = E^* \Delta x$ and the tangential stiffness $\Delta k_x = G^* \Delta x$. Then, on the left side of (18.9), we have exactly the spring force of a tangential element within the stick contact radius $|x| \le c$. The right side, on the other hand, is characterized by the normal force in the vertical element at the point $|x| = c$ (at the boundary of the stick domain) multiplied with the coefficient of friction. Equation (18.7) of the superposition principle of Jäger is then synonymous with the condition

$$f_x(c) = \mu f_N(c). \tag{18.10}$$

It says clearly that the tangential spring forces in the one-dimensional equivalent model assume the maximum possible value for the force of static friction at the boundary of the stick domain. From this dynamic boundary condition, the stick radius c of the three-dimensional contact can be determined for a given displacement u_x.

In an equally trivial way, we can obtain the connection between the conditional equation for the tangential force (18.6) and the reduction method if we take Eq. (17.10) into account:

$$F_x = \mu \left[2E^* \int_0^a \big[g(a) - g(x)\big]\, \mathrm{d}x - 2E^* \int_0^c \big[g(c) - g(x)\big]\, \mathrm{d}x \right]. \tag{18.11}$$

After splitting the integration domain of the first integral in (18.11) into the subdomains $0 \le x \le c$ and $c < x \le a$ and rearranging the equation, we obtain

$$F_x = 2 \int_0^c \mu E^* \big[g(a) - g(c)\big]\, \mathrm{d}x + 2\mu \int_c^a E^* \big[g(a) - g(x)\big]\, \mathrm{d}x. \tag{18.12}$$

The integrals in (18.12) can be replaced by the expressions in (17.53) and (18.9), where the alternate calculation of the tangential force in the three-dimensional contact is found using the one-dimensional contact:

$$F_x = 2c\, G^* u_x + 2\mu \int_c^a q(x) \mathrm{d}x. \tag{18.13}$$

While the first term in Eq. (18.13) represents the summation of the tangential spring force components in the stick domain $|x| \le c$ displaced by a constant in the x-direction, the second term represents the contribution of the frictional forces during slip in the domain $c < |x| \leq a$. In this domain, Coulomb's law of friction must be locally met, meaning that the one-dimensional, tangential distributed load $q_x(x)$ is proportional to the vertical distributed load $q(x)$ at every point. Until now, it has been proven that the relationships between the tangential force F_x, the tangential displacement u_x, and the stick radius c are exactly mapped by the one-dimensional model.

Finally, let us consider a method for the calculation of the three-dimensional tangential stress distribution from the tangential distributed load in the equivalent system. This piecewise-defined function is

$$q_x(x) = \begin{cases} G^* u_x & \text{for} \quad |x| \leq c \\ \mu q(a,x) & \text{for} \quad c < |x| \leq a \\ 0 & \text{for} \quad |x| > a \end{cases}, \tag{18.14}$$

where it is shown that the vertical distributed load $q(x)$ is dependent on the contact radius a. The constant tangential displacement of the surface within the stick radius can be determined by using Eq. (18.9):

$$G^* u_x = \mu\, q(a,c). \tag{18.15}$$

Continuing in this way, the piecewise-defined force density from (18.14) can also be given in the form

$$q_x(x) = \mu \left[q(a,x) \cdot H(a - |x|) - q(c,x) \cdot H(c - |x|) \right], \tag{18.16}$$

where $H(x)$ denotes the Heaviside function. With this, the tangential distributed load in the one-dimensional model is the difference between the actual vertical distributed load and the distributed load that would lead to the contact half-width c multiplied by the coefficient of friction μ. Applying the (modified) Abel transformation according to (17.55), Eq. (18.16) results in

$$\frac{1}{\pi} \frac{1}{r} \frac{\mathrm{d}}{\mathrm{d}r} \int_r^a \frac{x \cdot q_x(x)}{\sqrt{x^2 - r^2}} \mathrm{d}x = \mu \left[\sigma_{zz}(a,r) - \sigma_{zz}(c,r) \right]. \tag{18.17}$$

According to the superposition principle from Jäger, especially Eq. (18.5), the right side describes the distribution of tangential stress for the three-dimensional contact problem, so that the remaining conditional equation is found. The three-dimensional tangential stress distribution results (completely analogously to the normal stress distribution) from the (modified) Abel transformation of the tangential force density of the one-dimensional linearly elastic foundation[2]:

$$\tau_{zr}(r) = \frac{1}{\pi} \frac{1}{r} \frac{\mathrm{d}}{\mathrm{d}r} \int_r^a \frac{x \cdot q_x(x)}{\sqrt{x^2 - r^2}} \mathrm{d}x = \frac{1}{\pi} \int_r^a \frac{q_x'(x)}{\sqrt{x^2 - r^2}} \mathrm{d}x. \tag{18.18}$$

---

[2] Let it be emphasized that in the special case of non-differentiable profiles, only the first integral expression in (18.18) may be used.

Let it be once again stressed that contacts were investigated that meet the Boussinesq condition (17.17).

References

1. C, Cattaneo, Sul contatto di due corpi elastici: distribuzione locale degli sforzi. *Rendiconti dell'Accademia nazionale dei Lincei.* **27**, pp. 342–348, 434–436, 474–478 (1938)
2. R.D. Mindlin, Compliance of elastic bodies in contact. J. Appl. Mech. **16**(3), 259–268 (1949)
3. K.L. Johnson, Surface interaction between elastically loaded bodies under tangential forces. Proc. R. Soc. **A230**, 531 (1955)
4. R.L. Munisamy, D.A. Hills, D. Nowell, Static axisymmetric hertzian contacts subject to shearing forces. ASME J. Appl. Mech. **61**, 278–283 (1994)
5. J. Jäger, Axi-symmetric bodies of equal material in contact under torsion or shift. Arch. Appl. Mech. **65**, 478–487 (1995)
6. I.N. Sneddon, The relation between load and penetration in the axisymmetric Boussinesq problem for a punch of arbitrary profile. Int. J. Eng. Sci. **3**, 47–57 (1965)
7. M. Ciavarella, Tangential loading of general three-dimensional contacts. J. Appl. Mech. **65**, 998–1003 (1998)
8. M. Ciavarella, Indentation by nominally flat or conical indenters with rounded corners. Int. J. Solids Struct. **36**, 4149–4181 (1999)
9. J. Boussinesq, Application des Potentiels a L'etude de L'equilibre et du Mouvement des Solides Elastiques (1885)
10. V. Cerruti, Ricerche Intorno all'Equilibrio dei Corpie Elastici Isotropi. *Atti della Reale Accademia dei Lincei, Memoriae della Classe de Scienze Fisiche, Matematiche e Naturali.* **13** (1882)

Chapter 19
Appendix 3: Replacing the Material Properties with Radok's Method of Functional Equations

Silvio Kürschner, Valentin Popov, Markus Heß

19.1 Introduction

In Chap. 7, it was shown how the reduction method can be applied to contact problems with elastomers. Here, Radok's principle of functional equations plays an important role. This principle proceeds from a solution of a similar elastic problem which then is carried over to the original problem by replacing the material properties. This method is possible because within the framework of linear theory, the geometric, material specific, and loading specific influences can be decoupled to a certain degree.

In this appendix, it will be shown in detail how with Radok's method of functional equations the replacement of the material properties should be carried out. In this chapter, we assume that we are looking for the solution to a contact problem with an elastomer described by the linear viscoelastic material law. On the other hand, we require that the solution to a similar elastic problem is known.

In the second section, the fundamental solution will be derived for the normal contact problem with a linearly viscous material. In the third section, the simplification for the incompressible linearly viscous model is undertaken, which is considered in Chap. 7. In the fourth section, we show how to use the general viscoelastic material law. In the last two sections, possible ways of simplification are shown.

19.2 The Fundamental Solution for the Linearly Viscous Material Model

In this section, the replacement of the material properties for the linearly viscous material law is shown. The method is very close to that in the publication by Radok [1] and was also published in part in [2]. In order not to make the following explanations too abstract, we consider a concrete problem, namely the

V.L. Popov and M. Heß, *Method of Dimensionality Reduction in Contact Mechanics and Friction*, DOI 10.1007/978-3-642-53876-6_19

deformation of the surface of a linearly viscous half-space being acted upon by a single constant force. If one additionally considers this force as a unit force, the solution is known as the fundamental solution. This, in turn, is the basis of many (numerical) methods, for example, the boundary element method.

Radok's principle of functional equations first requires that a similar elastic problem is solved. In this case, we are looking for the fundamental solution for the normal contact problem with a linearly elastic half-space. This can be found in many textbooks on the theory of elasticity (e.g., [3]):

$$u(r) = \frac{F_N(1-\nu)}{2\pi G r}. \tag{19.1}$$

We express Poisson's ratio ν using the modulus of compression K and the shear modulus G:

$$u(r) = \frac{F(t)}{\pi r} \frac{3K+4G}{2G(6K+2G)}. \tag{19.2}$$

It is assumed that the normal force F_N is applied at time $t = 0$ so that its temporal change can be described as in Chap. 7 with the Heaviside function $H(t)$:

$$F(t) = F_N H(t). \tag{19.3}$$

Now, we consider the isotropic linearly elastic material, which presents the foundation for the similar elastic problem. The stress–strain relationships form the basis of this description, as can be found in textbooks on the theory of elasticity (e.g., [3]):

$$\frac{1}{3}\sigma_{ll}\delta_{ik} + s_{ik} = K\varepsilon_{ll}\delta_{ik} + 2Ge_{ik}. \tag{19.4}$$

The Kronecker delta δ_{ik} and Einstein's summation convention are used. The elastic properties are described by the compression modulus K and the shear modulus G. The stress tensor is denoted by σ, which is separated into the spherical tensor $\sigma_{ll}\delta_{ik}/3$ and the stress deviator $s_{ik} := \sigma_{ik} - \sigma_{ll}\delta_{ik}/3$. This decomposition arises from the separate consideration of pure compression, described by the spherical tensor, and that of pure shear, described by the stress deviator. The strain tensor ε is decomposed in the same way into its spherical tensor and strain deviator e_{ik}. The advantage of this decomposition lies in the possibility of considering the compression and shear separately:

$$\sigma_{ii} = 3K\varepsilon_{ii}, \quad s_{ik} = 2Ge_{ik}. \tag{19.5}$$

As preparation, we now express the right sides of these equations as the series

$$P := \sum_{n=0}^{p} p_n \frac{\partial^n}{\partial t^n} \tag{19.6}$$

and

$$Q := \sum_{n=0}^{\mathrm{q}} q_n \frac{\partial^n}{\partial t^n} \tag{19.7}$$

of linear differential operators with respect to time with constant coefficients p_n, q_n. Both equations from (19.5) consist of only one term of order zero. For the first equation in (19.5), one obtains

$$\sigma_{ii} = P\varepsilon_{ii}, \quad P = 3K \tag{19.8}$$

and for the second,

$$s_{ik} = Qe_{ik}, \quad Q = 2G. \tag{19.9}$$

Radok's procedure fundamentally allows that also the left sides of Eq. (19.5) are expressed as series of time-dependent differential operators in the same way. In this way, integral relationships between stress and strain can be taken into account. For reasons of clarity, we forgo the generalization, which is unnecessary here.

In the next step, the solution to the similar elastic problem (19.2) is subjected to the Laplace transformation $\mathcal{L}\{u\}(s) = \int_0^\infty u(t)e^{-st}\mathrm{d}t$, for which the evolution of the loading (19.3) must be taken into account:

$$u^*(s) := \mathcal{L}\{u\}(s) = \frac{F_N}{\pi rs}\frac{3K + 4G}{2G(6K + 2G)}. \tag{19.10}$$

Thereby, we have denoted the Laplace transformed function u with a star and will also use this notation in the following considerations. In the Laplace domain, the material properties are expressed according to (19.8) and (19.9) by the respective differential operators:

$$u^*(s) = \frac{F_N}{\pi rs}\frac{P + 2Q}{Q(2P + Q)}. \tag{19.11}$$

Next, we consider the stress–strain relations for the isotropic, linearly viscous material, which is the actual problem to be solved. This can be found, for instance, in [4]:

$$\frac{1}{3}\sigma_{ll}\delta_{ik} + s_{ik} = \tilde{K}\varepsilon_{ll}\delta_{ik} + \zeta\dot{\varepsilon}_{ll}\delta_{ik} + 2\eta\dot{e}_{ik}. \tag{19.12}$$

In order to avoid confusion, the quantities already used for the elastic application are denoted with a tilde. Also here, the stress tensor σ and strain tensor ε are decomposed into the spherical tensor and the deviator. Furthermore, the time derivative of the strain tensor appears, which is denoted as $\dot{\varepsilon}$. The material constants are the modulus of compression $\tilde{K}$, the volume viscosity ζ, and the shear viscosity η. The separate consideration of compression and shear provides

$$\sigma_{ii} = 3\tilde{K}\varepsilon_{ii} + 3\zeta\dot{\varepsilon}_{ii}, \quad s_{ik} = 2\eta\dot{e}_{ik}. \tag{19.13}$$

The right sides of these equations are also expressed in series of differential operators with respect to time. To prevent confusion, we denote the appearing symbols with a tilde. In the case of the first equation from (19.13), a term of zero and first order are to be taken into account, respectively:

$$\sigma_{ii} = \tilde{P}\varepsilon_{ii}, \quad \tilde{P} = 3\tilde{K} + 3\zeta\frac{\partial}{\partial t} \tag{19.14}$$

and in the case of the second, only one term of first order:

$$s_{ik} = \tilde{Q} e_{ik}, \quad \tilde{Q} = 2\eta \frac{\partial}{\partial t}. \tag{19.15}$$

The preparatory work is finished and the properties of the elastic material in the solution can now be replaced with those of the linearly viscous medium. This is done by replacing the differential operators P and Q by $\tilde{P}$ and $\tilde{Q}$ in Eq. (19.11):

$$z^*(s) := u^*(s)\Big|_{\substack{P\mapsto\tilde{P}\\ Q\mapsto\tilde{Q}}} = \frac{F_N}{\pi r s} \frac{\tilde{P}^* + 2\tilde{Q}^*}{\tilde{Q}^*\left(2\tilde{P}^* + \tilde{Q}^*\right)} \tag{19.16}$$

and subsequently substituting the properties of the viscous material (in the form of the Laplace transformed Eqs. (19.14) and (19.15):

$$z^*(s) = \frac{F_N}{4\pi r \eta s^2} \frac{3\tilde{K} + 3\zeta s + 4\eta s}{\left(3\tilde{K} + 3\zeta s + \eta s\right)}. \tag{19.17}$$

To avoid confusion, we denote the solution to the viscous problem in the Laplace domain with z^*.

The remaining task consists of taking the reverse transformation into the time domain: $\mathcal{L}^{-1}\{z^*(s)\} = \frac{1}{2\pi i}\int_{\gamma-i\infty}^{\gamma+i\infty} e^{st} z^*(s)\mathrm{d}s$ (where γ is a real number that ensures the convergence of the integral). This is possible using tables of Laplace transforms, for example, those found in [5]. For this purpose, Eq. (19.17) must be split:

$$z^*(s) = \frac{F_N}{4\pi r \eta}\left[\frac{\omega}{s^2(s+\omega)} + \frac{3\zeta + 4\eta}{3\zeta + \eta}\frac{1}{s(s+\omega)}\right], \quad \omega := \frac{3\tilde{K}}{3\zeta + \eta}. \tag{19.18}$$

Using the reverse transformation $\mathcal{L}^{-1}\{z^*(s)\}$, the following is obtained:

$$z(r,t) := \mathcal{L}^{-1}\left\{z^*(s)\right\} = \frac{F_N}{4\pi r}\left[\frac{t}{\eta} + \frac{1}{\tilde{K}}\left(1 - e^{-\omega t}\right)\right]. \tag{19.19}$$

There are two influences that may be noticed in the solution. First, there exists a linear term that is only influenced by the shear viscosity. The second term shows an exponential behavior. The amplitude of this term is determined by the compressibility and the characteristic time by the ratio of the elastic and viscous parameters in Eq. (19.18).

19.3 The Fundamental Solution for the Linearly Viscous, Incompressible Material Model

In this section, the respective solution is derived for the incompressible model, which is the topic of Chap. 7. After the preparatory work in the previous section, the necessary simplifications are easy to find. By allowing the modulus of compression to tend towards infinity $K \to \infty$, one obtains the result for the incompressible case directly from Eq. (19.19):

$$z(r,t) = \frac{F_N t}{4\pi\eta r}. \tag{19.20}$$

One also obtains the same result if incompressibility is forced on the solution to the similar elastic problem, by substituting $\nu = 1/2$ directly into Eq. (19.1). We have already used the resulting equation in Chap. 7 as a starting point. Through this, the rearrangements following the equation are drastically simplified.

19.4 Applying the Reduction Method to the General Linearly Viscoelastic Material Model

In this section, we provide the derivation of the reduction method for general viscoelastic materials. In the process, however, we restrict ourselves to the linear theory as done thus far. This theory is limited to small deformations. For the sake of clarity, we now consider a concrete example, namely the description of the normal contact of a rigid indenter with a viscoelastic half-space using the reduction method. The problem itself is not especially of interest but it can be carried over to other cases completely analogously, for example, to tangential or rolling contacts. More complicated is the generalization to the contact between two deformable bodies. Here, the problem lies not in the reduction method, but rather in the complicated description of the behavior of the material. In principle, however, such problems are able to be solved as well (see, for example [6]).

We describe the behavior of the viscoelastic material by the relaxation function, which we have thus far separated into pure compression and pure shear [7]:

$$\sigma_{ii}(t) = \int_{\tau=0}^{t} K(t-\tau)\dot{\varepsilon}_{ii}(\tau)\mathrm{d}\tau, \tag{19.21}$$

$$s_{ik}(t) = 2\int_{\tau=0}^{t} G(t-\tau)\dot{e}_{ik}(\tau)\mathrm{d}\tau. \tag{19.22}$$

At this point, we assume that the shear relaxation function $G(t)$, also known as the time-dependent shear modulus, is related to the shear angle and not the strain tensor, analogously to the elastic case. Here, we follow the considerations of Lee and Radok [8]. From this convention, a factor 2 results in Eq. (19.22). This fact, however, is handled in literature in various ways. If the time-dependent shear modulus is based directly on the strain tensor, then this must be taken into account in Eq. (19.22) and in the following results.

With the conventional notation for the occurring (one-sided) convolution integrals

$$(f * g)(t) := \int_{\tau=0}^{t} f(t-\tau)g(\tau)\mathrm{d}\tau, \tag{19.23}$$

we can write both expressions as

$$\sigma_{ii}(t) = (K * \dot{\varepsilon}_{ii})(t), \quad s_{ik}(t) = 2(G * \dot{e}_{ik})(t) \tag{19.24}$$

and now simply conduct a Laplace transformation:

$$\sigma_{ii}^{*}(s) = sK^{*}(s)\varepsilon_{ii}^{*}(s), \quad s_{ik}^{*}(s) = 2sG^{*}(s)e_{ik}^{*}(s). \tag{19.25}$$

Analogously to Eqs. (19.14) and (19.15), we can interpret these as

$$\sigma_{ii}^{*}(s) = \tilde{P}^{*}(s)\varepsilon_{ii}^{*}(s), \quad \tilde{P}^{*}(s) = sK^{*}(s), \tag{19.26}$$

$$s_{ik}^{*}(s) = \tilde{Q}^{*}(s)e_{ik}^{*}(s), \quad \tilde{Q}^{*}(s) = 2sG^{*}(s). \tag{19.27}$$

In contrast to the previous considerations, the viscoelastic behavior of the material is not described by a series of linear differential operators, but rather by the relaxation function.

After we have described the viscoelastic material in this way, we turn to the procedure of Radok in the next step: Identifying a similar elastic problem. In this case, the similar elastic problem is the normal contact between a rigid indenter and an elastic half-space described by the reduction method. The results can be taken from Sect. 3.1. The half-space is mapped to a chain of independent spring elements. For every individual element, the following relation is valid for the force on the spring f_N and its deformation u:

$$f_N(t) = E^{*}\Delta x \cdot u(t). \tag{19.28}$$

As previously, we denoted the width of the spring element as Δx and the effective modulus of elasticity E^{*}. The product $E^{*}\Delta x$ is obviously the spring stiffness of the element. Now, we take into account that one contact partner is rigid and describe the elastic behavior of the other partner using the compression modulus K and the shear modulus G. The resulting equation is the solution to the similar elastic problem:

$$f_N(t) = \frac{2G(6K+2G)}{3K+4G}\Delta x \cdot u(t). \tag{19.29}$$

Now, we assume that $u(t) = 0$ for $t < 0$, conduct a Laplace transformation of the equation, and replace the elastic constants according to Eqs. (19.8) and (19.9). In this way, we obtain

$$f_N^{*}(s) = \frac{Q(2P+Q)}{P+2Q}\Delta x \cdot u^{*}(s). \tag{19.30}$$

From this equation, we can determine the viscoelastic solution by replacing P with $\tilde{P}^{*}$ and Q with $\tilde{Q}^{*}$

$$f_N^{*}(s) = \frac{\tilde{Q}^{*}(s)\left(2\tilde{P}^{*}(s) + \tilde{Q}^{*}(s)\right)}{\tilde{P}^{*}(s) + 2\tilde{Q}^{*}(s)}\Delta x \cdot z^{*}(s), \tag{19.31}$$

substituting the relaxation function according to (19.26) and (19.27),

$$f_N^*(s) = \frac{2sG^*(s)(2sK^*(s) + 2sG^*(s))}{sK^*(s) + 4sG^*(s)} \Delta x \cdot z^*(s) \tag{19.32}$$

and rearranging

$$f_N^*(s) = 4\Delta x \frac{G^*(s)(K^*(s) + G^*(s))}{K^*(s) + 4G^*(s)} \cdot \left(sz^*(s)\right). \tag{19.33}$$

Using the reverse transformation into the time domain, we obtain the relationship between the normal force and the deformation for the general viscoelastic material:

$$f_N(t) = 4\Delta x (V * \dot{z})(t) = 4\Delta x \int\limits_{\tau=0}^{t} V(t-\tau)\dot{z}(\tau)\mathrm{d}\tau, \tag{19.34}$$

where

$$V(t) := \mathcal{L}^{-1}\left\{ \frac{G^*(s)(K^*(s) + G^*(s))}{K^*(s) + 4G^*(s)} \right\} \tag{19.35}$$

is the Laplace reverse transformation of the resulting fraction. This contains both relaxation functions.

By comparing Eq. (19.34) with (19.28), it is noticeable how the description of the general viscoelastic contact problem is undertaken within the framework of the reduction method: In the linearly elastic foundation, the linear spring elements are replaced with force law according to Eqs. (19.34) and (19.35).

At this point, however, we have steered clear of the main difficulty. This consists in the reverse transformation according to Eq. (19.35). In most cases, in which describing the behavior of the material with the relaxation function is sensible, the reverse transformation (19.35) causes remarkable difficulties.

In the following two sections, we will demonstrate with which assumptions the solution may be simplified.

19.5 Simplification: The Incompressible, Viscoelastic Material Model

In many cases the considered elastomer can be viewed, at least approximately, as being incompressible. We will investigate such a case in this section. We start with Eq. (19.35) and write

$$\begin{aligned} \frac{G^*(s)(K^*(s) + G^*(s))}{K^*(s) + 4G^*(s)} &= \left(\frac{K^*(s) + 4G^*(s)}{G^*(s)(K^*(s) + G^*(s))} \right)^{-1} \\ &= \left(\frac{1}{G^*(s)} + \frac{3}{K^*(s) + G^*(s)} \right)^{-1}. \end{aligned} \tag{19.36}$$

Now, it is taken into account that for an incompressible material, $K^* \to \infty$. Then, the second fraction tends to zero and we obtain[1]

$$V(t) = G(t) = \mathcal{L}^{-1}\left\{G^*(s)\right\}. \tag{19.37}$$

In this way, Equation (19.34) is simplified to

$$\Delta F_N(t) = 4\Delta x \int\limits_{\tau=0}^{t} G(t-\tau)\dot{z}(\tau)\mathrm{d}\tau. \tag{19.38}$$

By comparing Eq. (19.38) with (19.28), it is recognizable how the formulation of the incompressible viscoelastic material can be conducted within the framework of the reduction method. The spring elements of the linearly elastic foundation are replaced by a force law according to Eq. (19.38).

19.6 Simplification: Approximation of the Relaxation Function by Discrete Models

In this section, an additional way of handling the relaxation function is shown. Hereby, we restrict ourselves, however, to the general procedure without going into further detail. Gross showed already in [9] that the relaxation functions K and G can by approximated by a generalized Maxwell element or equivalently by a generalized Kelvin–Voigt element. These elements can be described by a few known functions for which a Laplace transformation can be simply conducted. When these functions are inserted into Eq. (19.35), rational functions in the Laplace domain result. These, in turn, may be reformed into a few types of standard functions using partial fraction decomposition and transformed back into the time domain using tables of Laplace transforms. In this way, the generalized viscoelastic material law can be approximated with a generalized Maxwell model or Kelvin–Voigt model. The remaining problem, however, consists of finding the poles of the rational functions. For details, let the reader be referred to [7, 9–11]. A relatively current application may be found, for instance, in [12].

References

1. J.R.M. Radok, Quart. Appl. Math. **15**, 198 (1957)
2. S. Kürschner, A.E. Filippov, Phys. Mesomech. **15**, 270–274 (2012)
3. L.D. Landau, E.M. Lifschitz, *Lehrbuch der Theoretischen Physik, Band VII Elastizitätstheorie*, 1st edn. (Akademie, Berlin, 1965)

---

[1] The mathematically sound way consists of taking the incompressibility into account in Eq. (19.29) and only then, taking the Laplace transformation. It is, however, easy to see that this procedure leads to the same result.

4. L.D. Landau, E.M. Lifschitz, *Lehrbuch Der Theoretischen Physik, Band VI Hydrodynamik*, 5. überarb. Aufl. (Akademie Verlag, 1991)
5. I.N. Bronstein, K.A. Semendjajew, G. Musiol, H. Mühlig, *Taschenbuch Der Mathematik*, 5. überarb. u. erw. Aufl. (Harri Deutsch, 2000)
6. W. Yang, J. Appl. Mech. **33**, 395 (1966)
7. R.M. Christensen, *Theory of Viscoelasticity: An Introduction* (Academic Press, New York, 1971)
8. E.H. Lee, J.R.M. Radok, J. Appl. Mech. **27**, 438 (1960)
9. B. Gross, *Mathematical Structure of the Theories of Viscoelasticity* (Hermann, Paris, 1953)
10. A.C. Pipkin, *Lectures on Viscoelasticity Theory* (Springer, Berlin, 1972)
11. D.R. Bland, *Theory of Linear Viscoelasticity* (Pergamon, Oxford, 1960)
12. M. Vandamme, F.J. Ulm, Int. J. Solids Struct. **43**, 3142 (2006)

Chapter 20
Appendix 4: Determining Two-Dimensional Power Spectrums from One-Dimensional Scans

Valentin L. Popov and Markus Heß

20.1 Introduction

The power spectra of rough surfaces are necessary “input parameters” for the calculation of contact and frictional properties. The power spectrum of a randomly rough surface can be determined using the Fourier transform of a measured two-dimensional surface topography. The experimental determination of the entire surface topography, for instance, with an atomic force microscope can, however, be very time intensive. Therefore, it begs the question, whether or not it is possible to determine the entire two-dimensional power spectrum from a limited number of one-dimensional scans. For isotropically randomly rough surfaces, all of the necessary information is, in fact, already contained in the one-dimensional scans of the surface. These can be used to obtain the required surface information more quickly and with less hassle.

20.2 Definitions

The two-dimensional power spectrum of a surface is defined as

$$C_{2\mathrm{D}}(\vec{q}) = \frac{1}{(2\pi)^2} \int \left\langle z(\vec{r}) z\left(\vec{0}\right) \right\rangle e^{-i\vec{q}\cdot\vec{r}} \mathrm{d}^2 r, \tag{20.1}$$

where $\vec{r}$ is the two-dimensional radius vector. $z(\vec{r}) = z(x, y)$ is the surface profile defined over the rectangular area $x \in [0, L_x)$, $\mathrm{y} \in \left[0, L_y\right)$ with the discretization step sizes Δx, Δy and with a mean of zero, so that $\langle z(\vec{r})\rangle = 0$; here, $\langle . \rangle$ denotes the average over the statistical ensemble. $\vec{q} = \left(q_x, q_y\right)$ is the wave vector. We assume that the surface topography is randomly rough and statistically homogeneous and isotropic. Under these conditions, the power spectrum is only dependent on the

V.L. Popov and M. Heß, *Method of Dimensionality Reduction in Contact Mechanics and Friction*, DOI 10.1007/978-3-642-53876-6_20

magnitude $q = \sqrt{q_x^2 + q_y^2}$ of the wave vector $\vec{q}$. Individual realizations of the randomly rough surface with the given power spectrum were generated with the help of the expression

$$z(\vec{r}) = \sum_{q_x=-\pi/\Delta x}^{\pi/\Delta x} \sum_{q_y=-\pi/\Delta y}^{\pi/\Delta y} B_{2D}(\vec{q}) \exp(i(\vec{q} \cdot \vec{r} + \phi(\vec{q}))) \tag{20.2}$$

with a random phase $\phi(\vec{q}) = -\phi(-\vec{q})$, which exhibits a uniform distribution over the interval $[0, 2\pi)$ and

$$B_{2D}(\vec{q}) = \frac{2\pi}{\sqrt{L_x L_y}} \sqrt{C_{2D}(\vec{q})} = \bar{B}_{2D}\,(-\vec{q}). \tag{20.3}$$

The summation in (20.2) is done with the discretization step sizes $\Delta q_x = 2\pi/L_x$ and $\Delta q_y = 2\pi/L_y$, in the respective directions.

We define the power spectrum $C_{1\mathrm{D}}(q)$ similarly to a one-dimensional “surface,” or a rough line

$$C_{1\mathrm{D}}(q) = \frac{1}{2\pi} \int \langle z(x) z(0) \rangle e^{-iqx} \mathrm{d}x. \tag{20.4}$$

The “line topography” in the one-dimensional case is calculated as follows with the help of the power spectrum:

$$z(x) = \sum_{q=-\pi/\Delta x}^{\pi/\Delta x} B_{1D}(q) \exp(i(qx + \phi(q))), \tag{20.5}$$

with

$$B_{1D}(q) = \sqrt{\frac{2\pi}{L} C_{1D}(q)} = \bar{B}_{1D}\,(-q), \tag{20.6}$$

the discretization step size $\Delta q = 2\pi/L$, and the phase $\phi(q) = -\phi(-q)$, which is uniformly distributed over the interval $[0, 2\pi)$.

20.3 Relationship Between the One-Dimensional and the Two-Dimensional Power Spectra

Let $z(x, y)$ be a rough surface that is generated with the power spectrum $C_{2D}(q)$:

$$z(x, y) = \sum_{q_x=-\pi/\Delta x}^{\pi/\Delta x} \sum_{q_y=-\pi/\Delta y}^{\pi/\Delta y} B_{2D}\left(\sqrt{q_x^2 + q_y^2}\right) \exp\left(i\left(q_x x + q_y y + \phi\left(q_x, q_y\right)\right)\right). \tag{20.7}$$

We consider a linear cross-section through this surface. Because the surface is statistically homogeneous, every cross-section is statistically equivalent so that the cross-section at $y = 0$ may be taken without reducing the generality:

$$z(x,0) = \sum_{q_x=-\pi/\Delta x}^{\pi/\Delta x} \sum_{q_y=-\pi/\Delta y}^{\pi/\Delta y} B_{2D}\left(\sqrt{q_x^2+q_y^2}\right) \exp\left(i\left(q_x x + \phi\left(q_x, q_y\right)\right)\right). \tag{20.8}$$

This is a rough line with the length L_x and the discretization step size Δx. To determine the power spectrum of this line using the definition (20.4), we write

$$\begin{aligned} C_{1D}(q) &= \frac{1}{2\pi} \int \langle z(x,0) z(0,0) \rangle e^{-iqx} \mathrm{d}x \\ &= \frac{1}{2\pi} \int \sum_{q_x,q'_x=-\pi/\Delta x}^{\pi/\Delta x} \sum_{q_y,q'_y=-\pi/\Delta y}^{\pi/\Delta y} B_{2D}\left(\sqrt{q_x^2+q_y^2}\right) B_{2D}\left(\sqrt{q_x'^2+q_y'^2}\right) \\ &\quad \left\langle \exp\left(i\left(q_x x + \phi\left(q_x, q_y\right)\right)\right) \exp\left(i\left(\phi\left(q'_x, q'_y\right)\right)\right) \right\rangle e^{-iqx} \mathrm{d}x. \end{aligned} \tag{20.9}$$

Due to the fact that the mean $\left\langle \exp\left(i\left(q_x x + \phi\left(q_x, q_y\right)\right)\right) \exp\left(i\left(\phi\left(q'_x, q'_y\right)\right)\right) \right\rangle$ always vanishes, with the exception of the cases $q_x = -q'_x$ and $q_y = -q'_y$, we obtain

$$C_{1D}(q) = \frac{1}{2\pi} \int \sum_{q_x=-\pi/\Delta x}^{\pi/\Delta x} \sum_{q_y=-\pi/\Delta y}^{\pi/\Delta y} \left| B_{2D}\left(\sqrt{q_x^2+q_y^2}\right) \right|^2 e^{iq_x x} e^{-iqx} \mathrm{d}x. \tag{20.10}$$

In the discrete case, the integral should be understood in the sense of a discrete sum:

$$\int (\ldots) \mathrm{d}x \Rightarrow \sum (\ldots) \Delta x. \tag{20.11}$$

Therefore, the following identity is valid:

$$\int e^{iq_x x} e^{-iqx} \mathrm{d}x \Rightarrow \sum \left(e^{iq_x x} e^{-iqx}\right) \Delta x = \delta_{q_x,q} L_x. \tag{20.12}$$

It follows that

$$C_{1D}(q) = \frac{L_x}{2\pi} \sum_{q_y=-\pi/\Delta y}^{\pi/\Delta y} \left| B_{2D}\left(\sqrt{q^2+q_y^2}\right) \right|^2 = \sum_{q_y=-\pi/\Delta y}^{\pi/\Delta y} C_{2D}\left(\sqrt{q^2+q_y^2}\right) \frac{2\pi}{L_y}. \tag{20.13}$$

By taking the relation $\Delta q_y = 2\pi/L_y$ into account and writing the sum in the form of an integral, we obtain

$$C_{1D}(q) = \int_{-\pi/\Delta y}^{\pi/\Delta y} C_{2D}\left(\sqrt{q^2+q_y^2}\right) \mathrm{d}q_y. \tag{20.14}$$

In the domain of small wave vectors

$$q \ll q_{y,\max} = \frac{\pi}{\Delta y}, \tag{20.15}$$

this equation can be written in the following form using the substitution of $\tilde{q} = \sqrt{q^2 + q_y^2}$:

$$C_{1\mathrm{D}}(q) = 2\int\limits_q^\infty \frac{C_{2D}(\tilde{q})\tilde{q}d\tilde{q}}{\sqrt{\tilde{q}^2 - q^2}}. \tag{20.16}$$

This relationship was derived in 1973 by Nayak [1]. The solution of this integral equation with respect to $C_{2D}(q)$ is known in the closed integral form [2] as

$$C_{2D}(q) = \frac{1}{\pi}\int\limits_q^\infty \sqrt{\tilde{q}^2 - q^2}\left\{\frac{C'_{1D}(\tilde{q})}{\tilde{q}} - \frac{C''_{1D}(\tilde{q})}{\tilde{q}^2}\right\}\mathrm{d}\tilde{q} = -\frac{1}{\pi}\int\limits_q^\infty \frac{C'_{1D}(\tilde{q})}{\sqrt{\tilde{q}^2 - q^2}}\mathrm{d}\tilde{q}. \tag{20.17}$$

20.4 One-Dimensional and Two-Dimensional Power Spectra for Randomly Rough, Self-Affine Surfaces

For self-affine fractal surfaces, we can calculate the integrals (20.16) and (20.17) analytically very easily. The power spectrum of a self-affine surface has the form

$$C_{2D}(q) = Aq^{-2(H+1)}. \tag{20.18}$$

Insertion into (20.16) results in

$$C_{1\mathrm{D}}(q) = \zeta(H) \cdot qC_{2D}(q), \tag{20.19}$$

with

$$\zeta(H) = 2\int\limits_1^\infty \frac{\xi^{-2H-1}}{\sqrt{\xi^2 - 1}}\mathrm{d}\xi = \sqrt{\pi}\frac{\Gamma\left(\frac{1}{2} + H\right)}{\Gamma(1 + H)}. \tag{20.20}$$

Here, $\Gamma(x)$ is the gamma function. This dependence is presented graphically in Fig. 20.1.

Insertion of Eq. (20.19) into Eq. (20.17) for the back transformation results in

$$C_{2D}(q) = C_{2D}(q)\sqrt{\pi}\frac{\Gamma\left(\frac{1}{2} + H\right)}{\Gamma(1 + H)}\frac{(1 + 2H)}{\pi}\int\limits_1^\infty \frac{\xi^{-2H-2}}{\sqrt{\xi^2 - 1}}\mathrm{d}\xi. \tag{20.21}$$

Due to the identity

$$\sqrt{\pi}\frac{\Gamma\left(\frac{1}{2} + H\right)}{\Gamma(1 + H)}\frac{(\frac{1}{2} + H)}{\pi}\frac{\sqrt{\pi}\Gamma(H + 1)}{\Gamma(H + \frac{3}{2})} \equiv 1, \tag{20.22}$$

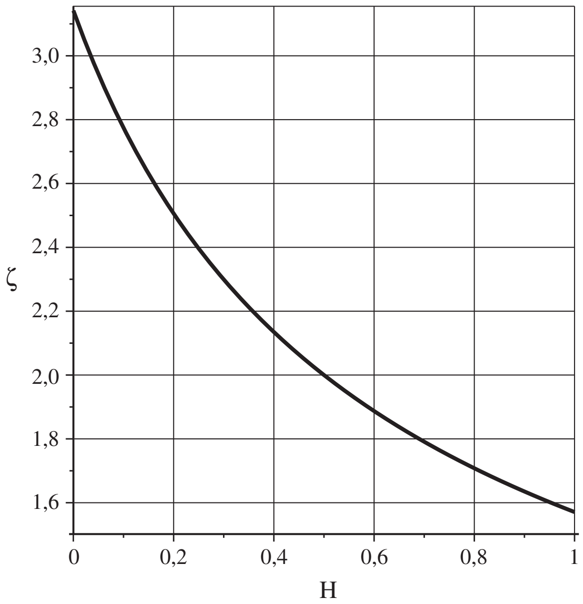

Fig. 20.1 Dependence of the factor $\zeta(H)$ (20.20) on the Hurst exponent H

Equation (20.21) is, as expected, identically met.

For the interval of practically relevant values of Hurst exponents $H \cong 0.5 \ldots 0.75$, one can assume an approximately constant value for the factor: $\zeta \simeq 2$.

$$C_{1D}(q) \approx 2qC_{2D}(q) \tag{20.23}$$

This is also the rule that is used over this interval of Hurst exponents for the application of the method of dimensionality reduction for the conversion of three-dimensional spectral densities to one-dimensional spectral densities (see Fig. 10.9) so that the method of dimensionality reduction can simply use the profile from the one-dimensional cross-section *as a first order approximation* without the need to convert the spectral densities!

References

1. P.R. Nayak, Some aspects of surface roughness measurement. Wear **26**, 165–174 (1973)
2. R. Bracewell, *The fourier transform and its applications* (McGraw-Hill, New York, 1965)

Index

V.L. Popov and M. Heß, , *Method of Dimensionality Reduction in Contact Mechanics and Friction*, DOI 10.1007/978-3-642-53876-6